Imperial College London

Department of Materials

Theory and Simulation of Moiré Graphene Multilayers

Zachary A. H. Goodwin

Supervisors: Dr Johannes Lischner and
Professor Arash A. Mostofi

Submitted in part fulfilment of the requirements for the degree of
Doctor of Philosophy in Materials

16th of September 2021

The work presented in this thesis was conducted at Imperial College London by myself between October 2018 and September 2021 under the supervision of Dr. Johannes Lischner and Prof. Arash A. Mostofi. The work of other authors has been acknowledged and cited accordingly throughout.

The copyright of this thesis rests with the author. Its contents are licensed under a Creative Commons Attribution-Non Commercial-No Derivatives 4.0 International Licence (CC BY-NC-ND 4.0). Under this licence, you are free to copy and redistribute the thesis, on the condition that it is appropriately attributed and for the licence of this work to be made clear to others. This licence prevents the contents of this thesis being used for commercial purposes, and if you remix, transform or build-upon this thesis it prevents the distribution of this modified material.

Abstract

Graphene has been hailed as a material which is going to revolutionise myriad technologies due to its extraordinary stability, mechanical strength yet flexibility, and remarkable transport properties. Furthermore, it was recently discovered that if two graphene layers are stacked and twisted relative to one another, referred to as twisted bilayer graphene (tBLG), correlated insulating states and superconductivity are observed, even though graphene does not intrinsically display these properties. These phases only emerge at twist angles close to the "magic angle" of 1.1°, and by tuning the temperature and doping level, the system can undergo electronic phase transitions between these states.

I studied electron interactions and electronic screening in tBLG and other moiré graphene multilayers. I found that in the absence of external and internal electronic screening, the on-site Hubbard parameter of the flat bands of tBLG scales linearly with twist angle. Upon considering internal screening, this linear scaling breaks down, where the Hubbard interaction energy decreases more rapidly towards the magic angle owing to increased screening. Moreover, external screening, from proximity to metallic gates which dope tBLG, was found to substantially affect these Hubbard interactions, owing to the moiré length scale of the magic-angle being comparable to the distances to the metallic gates. For a sufficiently small separation to these gates, I predicted that the correlated insulating states should be screened-out and the superconducting phase should be stabilised.

Long-ranged Hartree interactions were found to induced doping-dependent band-flattening in tBLG that was predicted to increase the magic-angle range of tBLG. For moiré graphene multilayers, the role of these Hartree interactions were found to sensitively depend on the stacking sequence of the structure: systems with alternating twist angles have similar interaction-driven band flattening, but systems where there are also adjacent layers that are aligned have no such interaction-driven band flattening.

Acknowledgements

The research presented in this thesis would not have been possible without numerous people who directly collaborated with me on work presented in this thesis and those who have supported me, academically and personally, throughout my PhD. I wish to acknowledge their contributions.

Firstly, I wish to thank my supervisors Johannes Lischner and Arash Mostofi for their patience, guidance and encouragement throughout my PhD. Members of the Mostofi-Lischner research group are thanked for their insightful comments and for creating a lively atmosphere in which to work. In particular, I would like to thank Valerio Vitale and Fabiano Corsetti for their lasting collaboration on several projects.

Cohorts of the TSM CDT are thanked for creating a stimulating environment in which to develop, and for the wisdom passed down from prior cohorts. In particular, I would like to thank my Cohort and Daniele Dini for their support.

I would like to thank Lennart Klebl and Ammon Fischer, and their supervisor Dante Kennes for a particularly fruitful and enjoyable collaboration. I also wish to thank Christoph Karrasch for stimulating discussions.

I would like to thank Alexei Kornyshev for all of the opportunities, energy and guidance throughout my time at Imperial. I also wish to extend thanks to Pedro de Souza, Micheal McEldrew, and their supervisor Martin Bazant, for the highly interesting collaborations and their support during the course of my PhD.

I wish to acknowledge the unwavering support from family and friends throughout my PhD.

I acknowledge the financial support through a studentship in the Centre for Doctoral Training on Theory and Simulation of Materials at Imperial College London funded by the EPSRC (EP/L015579/1).

Dedicated to A. R. H. Goodwin.

Contents

1 Introduction **14**

2 Methods **49**

2.1 Commensurate moiré graphene multilayers 50

2.2 Structural relaxations 54

2.3 Density functional theory 56

2.3.1 Linear-scaling DFT 57

2.4 Non-interacting atomistic tight-binding 57

2.4.1 Slater-Koster hopping parameters 60

2.4.2 On-site energies 61

2.4.3 Hamiltonian in second quantisation 61

2.4.4 Coulomb interaction of p_z orbitals 62

2.4.5 Valley polarisation 63

2.5 Wannier functions 64

2.5.1 Wannier functions from atomistic tight-binding 68

2.5.2 Wannier function centres 70

2.5.3 Wannier functions of tBLG 71

2.6 Screened interactions 71

2.6.1 Internal screening 72

2.6.2 External screening 76

2.7 Interacting atomistic Hamiltonians 77

2.7.1 Hartree interactions in atomistic tight-binding 78

2.7.2 Hubbard interactions in atomistic tight-binding 80
2.7.3 Constrained Hubbard calculations 81
2.7.4 Hubbard parameters of Wannier functions 82
2.8 Spin susceptibility 84

3 Screening of electron-electron interactions in twisted bilayer graphene 85

3.1 Flat band electronic structure 88
3.1.1 Wannier functions of flat bands 88
3.2 Internal screening 90
3.2.1 Polarizability and screened interaction 90
3.2.2 Hubbard parameters 93
3.2.3 Discussion 94
3.3 External screening 97
3.3.1 Hubbard parameters 98
3.3.2 Correlated insulators 99
3.3.3 Superconductivity 101

4 Hartree interactions and magnetic order of twisted bilayer graphene 102

4.1 Hartree interactions in twisted bilayer graphene 105
4.1.1 Band structure 105
4.1.2 DOS and LDOS 109
4.1.3 Environmental screening 112
4.2 Importance of Hartree interactions for magnetic order 115
4.2.1 Band structures 116
4.2.2 Magnetic phase diagram 117
4.2.3 Discussion of phase diagram 120
4.3 Hubbard calculations 123
4.3.1 Leading instability 124
4.3.2 Excited antiferromagnetic instabilities 126
4.3.3 Ferromagnetic order 128

5 Moiré graphene multilayers beyond twisted bilayer graphene 131
5.1 Alternating twist angle structures 133
5.1.1 Twisted trilayer graphene 133
5.1.2 Double twisted bilayer graphene 137
5.2 Moiré structures with twisted and aligned layers 140
5.2.1 Twisted double bilayer graphene 140
5.2.2 Mono-trilayer graphene 151
6 Conclusions and Outlook 160

List of Figures

1.1 Electronic band structure of graphene 15

1.2 Schematic demonstration of the atomic structure of twisted bilayer graphene . . 16

1.3 Schematic of twisted bilayer graphene electronic structure 18

1.4 Schematic of twisted bilayer graphene corrugation 22

1.5 Wannier functions of the flat bands of twisted bilayer graphene 23

1.6 Atomic and electronic structure of twisted double bilayer graphene 41

1.7 Atomic and electronic structure of mono-trilayer graphene 44

1.8 Atomic and electronic structure of twisted trilayer graphene 46

2.1 Schematic of graphene lattice 51

2.2 Schematic demonstration of how to construct commensurate structures 52

2.3 Schematic demonstration of bilayer graphene systems with different stacking order 54

2.4 Sign convention of valley polarisation operator 64

3.1 Band structure, width and gaps of twisted bilayer graphene near the magic angle 88

3.2 Wannier orbitals of the flat bands of twisted bilayer graphene 89

3.3 Internal screening of twisted bilayer graphene 91

3.4 Internally screened Hubbard parameters of twisted bilayer graphene 94

3.5 Twist angle sensitivity of electron correlations in twisted bilayer graphene 96

3.6 External screening of Hubbard parameters of twisted bilayer graphene 97

3.7 Critical gate separation for screening of correlated insulating states in twisted bilayer graphene 99

4.1 Hartree theory electronic structure of twisted bilayer graphene 106

4.2 Characteristics of doping and twist angle dependent electronic states of twisted bilayer graphene 107
4.3 Doping-dependent densities of states of twisted bilayer graphene 110
4.4 Doping-dependent local densities of states of twisted bilayer graphene 110
4.5 Environmental dependence of Hartree band structure of twisted bilayer graphene 113
4.6 Characteristics of Hartree potential of twisted bilayer graphene 114
4.7 Hartree theory band structures of twisted bilayer graphene 117
4.8 Critical Hubbard parameter for the onset of magnetic order in twisted bilayer graphene 118
4.9 Leading magnetic instabilities of twisted bilayer graphene 119
4.10 Magnetic phase diagram of twisted bilayer graphene 120
4.11 Electronic structure of leading antiferromagnetic instability of twisted bilayer graphene 125
4.12 Electronic structure of nodal antiferromagnetic order of twisted bilayer graphene 126
4.13 Electronic structure of honeycomb antiferromagnetic order of twisted bilayer graphene 127
4.14 Ferromagnetic order of twisted bilayer graphene 129

5.1 Hartree theory electronic structure of twisted trilayer graphene 134
5.2 Characteristics of twisted trilayer graphene Hartree potential 135
5.3 Electronic band structure of twisted trilayer graphene from DFT 137
5.4 Hartree theory band structure of double twisted bilayer graphene 138
5.5 Characteristics of Hartree potential of double twisted bilayer graphene 139
5.6 Electronic band structure of double twisted bilayer graphene from DFT 139
5.7 Hartree theory band structure of twisted double bilayer graphene 141
5.8 Hartree potential of twisted double bilayer graphene 142
5.9 Electronic structure of twisted double bilayer graphene in a perpendicular electric field 143
5.10 Electronic structure of twisted double bilayer graphene from DFT 145
5.11 Hartree potential of twisted double bilayer graphene at charge neutrality 146

5.12 Layer-dependent contribution to Hartree potential and number of excess electrons of twisted double bilayer graphene 146
5.13 Local potential of twisted double bilayer graphene from DFT 149
5.14 Electronic structure of mono-trilayer graphene 152
5.15 Density of states of mono-trilayer graphene 153
5.16 Hartree theory electronic structure of mono-trilayer graphene 154
5.17 Magnetic order of mono-trilayer graphene 155
5.18 Magnetic phase diagram of mono-trilayer graphene 156
5.19 Magnetic phase diagram of magic angle mono-trilayer in electric field 158

List of Tables

3.1 Characteristic screening parameters of twisted bilayer graphene 92

4.1 Hartree potential fit parameters 114

Chapter 1

Introduction

The discovery of graphene

Carbon, in its pure form, has several well-known allotropes. In three dimensions (3D), diamond is known for its mechanical strength, and graphite for its high electrical conductivity and use in pencils [1, 2]. In the opposite limit, molecular or zero-dimensional (0D) carbon comes in the form of the fullerenes [1, 2], where the carbon atoms form a closed surface, similar to a balloon. Intermediate to these regimes, carbon nanotubes are a one-dimensional (1D) form of carbon and two-dimensional (2D) carbon comes in the form of graphene[†]. The existence of free-standing graphene, a single layer of carbon atoms arranged in a honeycomb lattice was not thought to be possible, as it was presumed to be structurally unstable with respect to other allotropes [1, 2].

To the surprise of many, graphene was first isolated and characterised by Novoselov *et al.* [4] from mechanical exfoliation of graphite. Since graphene is a 2D material, its properties in-plane and out-of-plane are quite different. One important property of a material is how it screens electrostatic fields. In-plane fields created from edge-contacts are, eventually, screened, which preserves the charge neutral state in the bulk of the graphene. Out-of-plane fields created from a back-gate, however, causes the number of electrons in graphene to globally change[‡]. Novoselov *et al.* [4] demonstrated that the conductivity of graphene was highly dependent on the electrostatic gating, consistent with a semi-metal [1].

[†] Note that other allotropes of 2D carbon have also been predicted [3].

[‡] In contrast, 3D materials cannot be electrostatically gated.

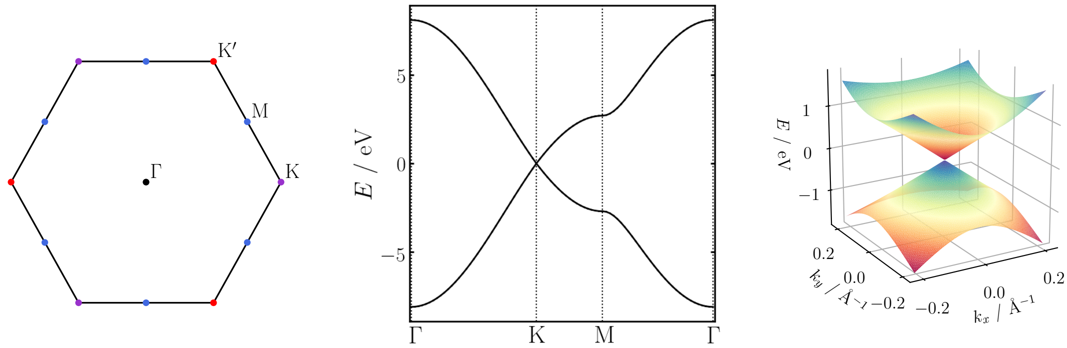

Figure 1.1: Electronic band structure of graphene along the high symmetry path (middle), the high symmetry points of which have been indicated in the hexagonal Brillouin zone (left), and a surface plot close to the Dirac point (right). The electronic structure is calculated with the nearest-neighbour model of graphene with a hopping parameter of $t = -2.7$ eV [1]. The crystal momentum in the surface plot (left) is relative to the Dirac cone at K.

Even though the first experimental realisation of graphene was only in 2004, a theoretical model of the electronic structure of graphene was first developed by Wallace in 1947 [1, 5]. It was noted by Wallace that the electronic structure of graphene has an unusual semi-metallic character [5], where the valence and conduction bands have a linear dispersion which touch at the K and K′ points at of the first Brillouin zone, as seen in Fig. 1.1 (middle). This feature is referred to as a Dirac cone, a surface plot of which is shown in Fig. 1.1 (right). Interestingly, the low-energy electrons in graphene behave as massless Dirac fermions, which move with a large (Fermi) velocity* [1, 2]. This gives rise to many interesting electronic phenomena in graphene, such as anomalous quantum Hall effect, high electron mobility and Klein tunnelling [1, 2].

In its normal state, then, graphene exhibits many interesting phenomena [1, 2]. Naturally, theoretical predictions of broken symmetry phases in graphene were also made [1, 6–10]. At charge neutrality, for example, antiferromagnetic order could exist in graphene, which would break C_2 and lift the degeneracy at the Dirac point [7]. In experiments of intrinsic graphene, however, no such effects have been reported [11]. Moreover, superconductivity does not appear to be intrinsic to graphene either [7].

Therefore, efforts turned to engineering the properties of graphene through charged defects [12], periodic potentials [13], strain [14], suspending graphene [15, 16], alignment to substrates [17–21], and stacking several layers of graphene [22–27], for example. In fact, the latter approaches provided quite fruitful methods for engineering strongly correlated phases in graphene-based systems. For example, Bernal-stacked bilayer graphene [28] and rhombohedral trilayer graphene [26, 27] exhibit signatures of strong correlations as the density of states at the Fermi level is finite [1, 7]. In these systems the crystallographic axes of the graphene layers are aligned, but more generally, a relative twist angle can be introduced. For two graphene sheets, this creates what is referred to as twisted bilayer graphene.

---

*The Fermi velocity of graphene is $v_F \approx 1 \times 10^6$ ms^{-1}, which is approximately 300 times smaller than the speed of light [1].

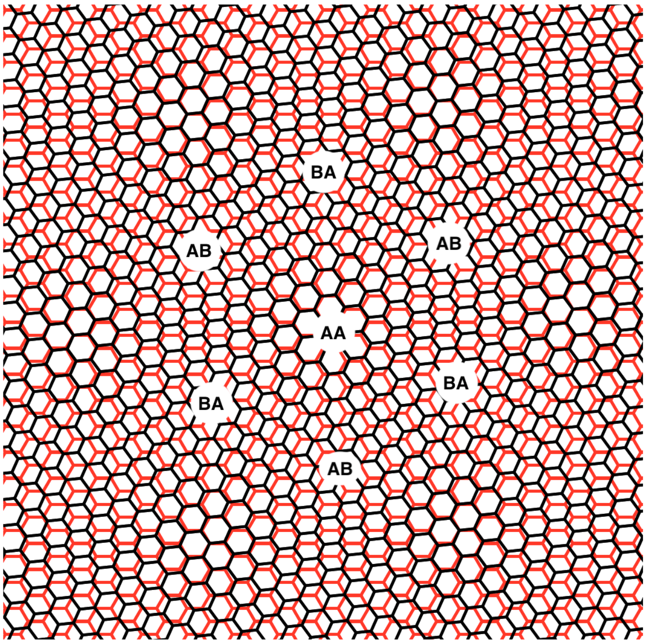

Figure 1.2: Schematic demonstration of the atomic structure of (a commensurate) twisted bilayer graphene at a twist angle of ∼6°. The top, rotated graphene layer is shown in black and the bottom, unrotated graphene layer is shown in red. Different stacking sequences of the bilayer have been indicated.

Magic angle of twisted bilayer graphene

The atomic and electronic structure of twisted bilayer graphene (tBLG) was first theoretically investigated by Lopes dos Santos *et al.* [29]. A schematic of the atomic structure of tBLG with a twist angle of ∼6° is shown in Fig. 1.2. As can be seen, there is an emergent honeycomb moiré pattern* on a larger length scale than the underlying honeycomb lattice of graphene.

---

*A moiré pattern is a term given to an interference effect caused by overlapping several patterns which differ slightly. When the pattern is initially identical, a moiré pattern can either be created through one being stretched relative to another or from rotational misalignment.

This moiré pattern is characterised by the stacking order of the bilayer changing in real space. The AA stacking regions create a triangular lattice, while the AB and BA stacked regions form triangular lattices that can be interpreted as "moiré sublattices" of a moiré honeycomb pattern, similar to the two carbon atoms (sublattice A and B) in the unit cell of graphene.

Upon rotating one graphene sheet relative to another, it is not guaranteed that spatial periodicity will always be achieved [30][*]. In fact, only certain twist angles generate structures which exhibit exact spatial periodicity[†], as first derived in Ref. 29 for tBLG. The analysis demonstrated that smaller twist angles are associated with larger moiré unit cells, and therefore, also larger numbers of atoms in the moiré unit cell. These commensurate structures can be investigated using atomistic electronic structure methods, but it was noted in Ref. 29 that even modest twist angles of 2.1° had 2884 atoms in the unit cell which makes *ab initio* methods impractical, motivating the development of simpler approaches.

In the absence of interlayer coupling between the graphene layers of tBLG, there are two copies of the graphene electronic structure rotated in momentum space relative to each other, as seen in Fig. 1.3. Upon switching on the interlayer coupling between these two rotated graphene sheets, it was demonstrated [29] that the low-energy states of one graphene layer most strongly couple to only a handful of low-energy states (at crystal momenta which differ to the first graphene layer by integer multiples of moiré reciprocal lattice vectors) of the other graphene layer. Therefore, an effective low-energy Hamiltonian only consisting of these minimal terms could be constructed to investigate the electronic structure at low energies and large twist angles. In contrast to Bernal stacked bilayer graphene (where the electronic dispersion is quadratic at low energies [1]), it was found that the low-energy electronic structure of tBLG exhibits linear Dirac cones at the Fermi level. Moreover, using perturbation theory (which was valid down to a twist angle of $\sim 3°$), it was demonstrated that the Fermi velocity of these Dirac cones was renormalised to smaller values.

This continuum model of Lopes dos Santos *et al.* [29] was further developed [33, 34] to be applicable to small twist angles ($< 3°$) and for incommensurate structures. For small

---

[*] A notable example of which is the twist angle of 30°, where a quasi-crystal forms with no spatial periodicity [31].

[†] Details of a similar method which is employed here is outlined in Ref. 32 and the Methods.

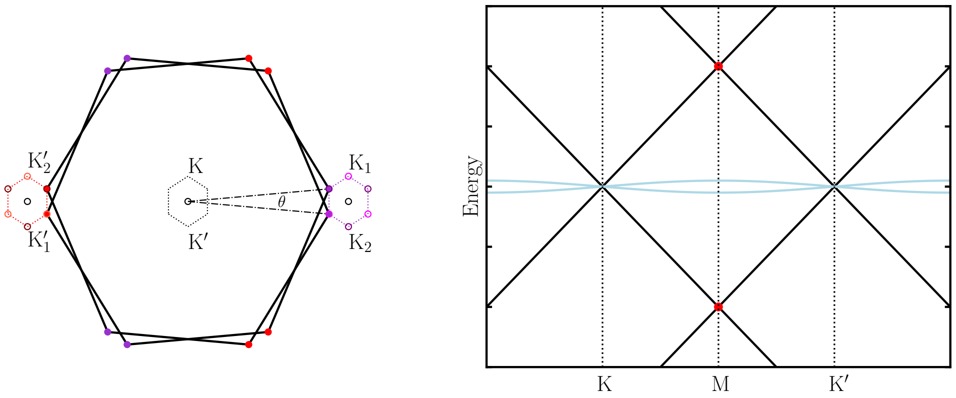

Figure 1.3: Schematic of moiré Brillouin zone of twisted bilayer graphene (left) and low-energy electronic structure (right). (left) - the Brillouin zone of the individual graphene layers, which are rotated by θ with respect to each other, are indicated by the large black hexagons, with purple and red circles denoting the K and K$'$ points of these graphene layers, respectively. The K valley of moiré Brillouin zone of tBLG originates from the K valley of graphene layer 1 and the K valley of graphene layer 2, i.e. K_1 and K_2, respectively. The Dirac cones from K_1 and K_2 form the K and K$'$ points of the moiré Brillouin zone, as indicated by the magenta and dark purple open circles, respectively. On the hand, the K$'$ valley of tBLG originates from the the K$'$ valley of graphene layer 1 and the K$'$ valley of graphene layer 2, i.e. K'_1 and K'_2, respectively. The Dirac cones from K'_1 and K'_2 form the K$'$ and K points of the moiré Brillouin zone, as indicated by the dark red and light red open circles, respectively. (right) - the low-energy electronic structure (right), is for a single valley of tBLG, say the K valley. The Dirac cone located at K of the moiré Brillouin zone comes from layer 1, while the Dirac cone at K$'$ originates from layer 2. In the absence of interlayer tunnelling, these graphene Dirac cones cross at M of the moiré Brillouin zone, as indicated by the red circles. In the presence of interlayer tunnelling, the Fermi velocity of these Dirac cones can be strongly renormalised, forming the flat electronic bands, as shown in light blue.

twist angles, the momentum difference between the K-point of layer 1 and layer 2 is much smaller than the momentum difference between the K and K$'$ points of a single graphene layer. Therefore, to a reasonable approximation, the K and K$'$ points do not couple to each other in the low-energy electronic structure of tBLG, giving rise to valley separation in tBLG. As depicted in Fig. 1.3 (left), the electronic structure of a single valley of tBLG originates from the hybridisation of the same valley from each graphene sheet, i.e. the K-valleys of the graphene layers form a single valley in tBLG. The other valley, originating from the K$'$ points of the graphene layers, is related through time reversal symmetry. This means that tBLG has a valley symmetry (in the normal state), with valley degeneracies in parts of the moiré Brillouin zone of tBLG. This additional degree of freedom, the valley degree of freedom, has key differences to that of graphene[*].

These Dirac cones of one valley cross at an energy of $\hbar v_F \Delta K$, where v_F is the Fermi velocity of graphene and ΔK is the momentum shift of these Dirac cones [35]. Upon including interlayer coupling, characterised by the interlayer coupling parameter $w \approx 0.1$ eV [36], the Dirac cones undergo an avoided crossing and generate a pair of van Hove singularities (VHS) at energies $\pm(\hbar v_F \Delta K - 2w)$ [35], as schematically shown in Fig. 1.3 (right). At large angles ($\sim 5°$), these VHS are separated by large energy gaps, but for smaller twist angles the energy gap between these VHS reduces as the momentum difference between the two Dirac cones decreases. At a critical twist angle, referred to as the *magic angle* [33], there comes a point where the momentum misalignment between these Dirac cones matches the hybridisation of the layers, and the separation between the VHS vanishes. At this magic twist angle the Fermi velocity of the low-energy Dirac cones were found to vanish, which causes the electronic bands to become extremely flat in the Brillouin zone with a concomitant increase in the density of states (DOS) [32–34, 37]. In fact, Bistritzer and MacDonald [33] predicted that a set of magic angles should appear[†], with the largest one occurring at a twist angle of $\sim$1.05°.

At a similar time, Trambly de Laissardière *et al.* [32, 37], Shallcross *et. al.* [39] and Suárez Morell *et al.* [40] investigated tBLG with atomistic tight-binding models, and found that the Fermi velocity of the low-energy Dirac cones was strongly reduced at twist angles smaller than 5° [40–42], and an almost vanishing Fermi velocity was found close to $\sim$1°. Moreover, Trambly de Laissardière *et al.* [32, 37] also predicted that the local density of states (LDOS) of these low-energy states is predominantly localised on the AA stacking regions of the moiré unit cell [32, 42, 43].

Early experimental work was able to realise these remarkable electronic properties of tBLG [44–49]. Samples of tBLG were grown using chemical vapour deposition (CVD), which resulted in highly uniform samples with low strain and twist angle variation [44–47, 49]. This CVD growth of tBLG did not permit control over the twist angle which was obtained, however [35].

These tBLG samples were experimentally investigated using scanning tunnelling microscopy

---

[*] In graphene, the K and K′ valley are also related by time reversal symmetry, but they do not share the same crystal momentum. To convert from one valley to another in graphene, a large crystal momentum is required. Whereas in tBLG, there is a valley degeneracy, with zero momentum transitions being possible.

[†] The existence of magic-angle states has been further formalised [38].

(STM) [44–49], a technique that measures the differential conductance locally, which is proportional to the LDOS. Real space maps of the LDOS at a given Fermi level from STM demonstrated that the low-energy states were indeed predominantly located in the AA regions of the moiré unit cell. For a tBLG sample with a twist angle of 1.8°, two large peaks in the LDOS of the AA region where reported with an energy separation of 85 meV, consistent with the picture of a pair of van Hove singularities emerging in the low-energy electronic structure [44]. For smaller angles, the energy separation between these VHS reduced further. At an angle of 1.16°, the STM measurements found that these two VHS merged to form a single peak with a width of only ∼32 meV with a pseudo-gap of ∼12 meV suggesting the onset of correlated-insulating states [44]. These early experimental observations demonstrated the tunability of the low-energy electronic structure of tBLG with twist angle.

Atomic reconstruction of twisted bilayer graphene

Up to this point, theoretical studies of tBLG considered the atomic positions to be rigid, being defined by a pristine graphene lattice of each layer and a constant interlayer separation between the layers. The moiré pattern of tBLG has stacking sequences of the bilayer range from AA to AB/BA, as seen in Fig. 1.2. Importantly, the interlayer spacings of these stackings are known to be approximately 3.6 Å and 3.35 Å, respectively [24]. Therefore, it might be expected that the atomic positions in the moiré lattice do not retain this flat configuration.

An early theoretical work using *ab initio* methods by Uchida *et al.* [50] demonstrated that the interlayer spacing between the two graphene layers was, in fact, not constant throughout the moiré unit cell [51]. Rather, for angles smaller than 10° (structures down to 2° were investigated), significant variations (0.1-0.2 Å) in the interlayer separation occurred [50]. While for angles larger than this, the interlayer separation was relatively constant throughout the moiré unit cell with a value of 3.42 Å. In the AA region of the moiré unit cell, it was found that the interlayer separation would increase to values of 3.6 Å in the limit of small angles, whereas the interlayer separation in the AB/BA regions decreased to values of 3.35 Å. This atomic corrugation effect, as schematically shown in Fig. 1.4, was found to be accurately reproduced by a cosine series with the shortest seven Fourier components [50]*.

Later, several works investigated these atomic corrugation effects in tBLG using empirical force fields [54–57]. This method is significantly cheaper than *ab initio* calculations, which permitted the investigation of small twist angles ($< 2°$), where significant in-plane relaxations were also found [54–56]. In particular, these works demonstrated that the atoms in each layer rotate around the AA regions in opposite directions, causing the area of the AB/BA regions to grow at the expense of the AA regions [54–56, 58]. This occurs because the AB stacking configuration is lower in energy than the AA stacking configuration, and therefore, the total energy is lowered by increasing the area of AB stacking [56]. While each atom can undergo significant in-plane displacements (of the order of 0.5 Å at small angles [56]), the changes in the bond lengths from equilibrium are still quite modest, with changes of the order of $\sim$0.1% [54, 59]. Therefore, the strain in the graphene layers remains relatively low.

In what is described above, the atoms in each layer move in opposite directions out-of-plane, which is referred to as the breathing mode. At small twist angles ($< 1°$), additional types of atomic reconstruction become energetically favourable in tBLG. Specifically, a bending mode can onset where the layers instead move in the same direction, causing a buckling of the whole system [55, 60].

These atomic reconstruction effects have important consequences for the low-energy electronic structure of tBLG. Using an atomistic tight-binding model, Nam and Koshino [58], and Gargiulo and Yazyev [56] demonstrated that the flat electronic bands near the Fermi level separate in energy from all other remote bands, as seen in Fig. 1.4, with small energy gaps between the flat bands and all others (near the magic angle) [61–65]. The atomic reconstruction also affects the Fermi velocity renormalisation of these low-energy Dirac bands, which can clearly be seen in Fig. 1.4.

This result motivated the development of a continuum model to reproduce these effects. Instead of a single parameter, w, describing the interlayer coupling between the two graphene layers, the magnitudes of the tunnelling matrix elements could be tuned [36, 66–68]. It was found that a two-parameter model, one parameter $w_0 \approx 0.08$ eV represents the interlayer

---

[*] Later *ab initio* calculations showed that this simple corrugation picture was over-simplified [52, 53].

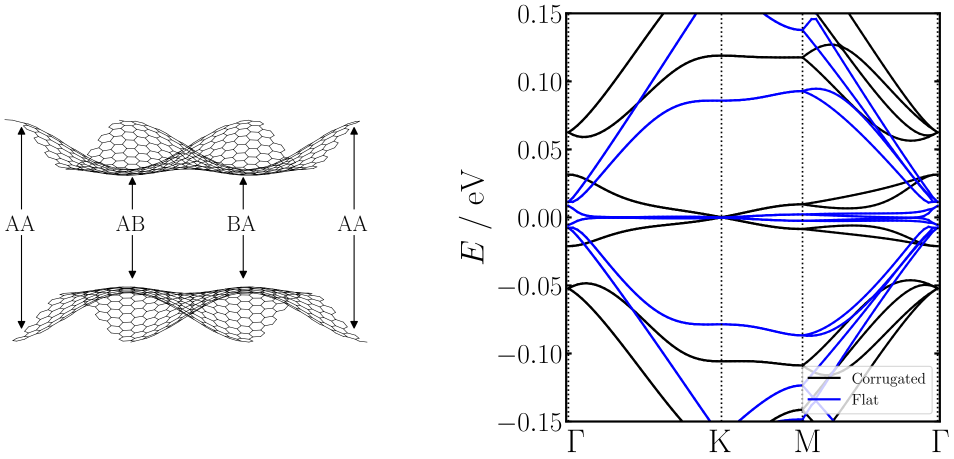

Figure 1.4: Schematic of out-of-plane atomic corrugation effects in twisted bilayer graphene (left) and the affect this has on the low-energy electronic structure (right). Note the schematic structure has greatly exaggerated the out-of-plane displacements to make the larger interlayer spacing in the AA regions compared to the AB/BA regions obvious. The z-coordinates of the schematic were generated using the cosine approximation (see Methods). The electronic structure of 1.3° tBLG was calculated with pristine graphene layers, with no in-plane or out-of-plane corrugation. The corrugated structure was generated from empirical force fields, as discussed in the Methods.

tunnelling in the AA region and the other parameter $w_1 \approx 0.1$ eV the tunnelling in the AB/BA regions, could reproduce the effects from these atomic relaxations (despite the atomic positions not explicitly being included in the calculations) [66, 68]. The continuum model was further developed by Carr *et al.* [69], using a $\mathbf{k} \cdot \mathbf{p}$ expansion of the atomistic tight-binding model, which reproduces the atomistic model with remarkable accuracy. An interesting feature of the model is that it only predicts a single magic angle at ∼1.1° [69].

Wannier functions of the isolated flat bands of twisted bilayer graphene

Since the low-energy electronic states are separated in energy from all other states, this motivated the development of Wannier Hamiltonians to describe these isolated flat bands*. In total, there are four (spin-degenerate) bands in tBLG (in the normal state). This means that there are four Wannier functions which describe these states. To reproduce the degeneracies at high symmetry points of these flat bands[*], a number of symmetry analyses [68, 71–73][†] showed that the Wannier functions must be centred on the AB/BA regions of the moiré unit cell. Therefore, the Wannier orbitals create a honeycomb lattice, with two of these Wannier orbitals located on the AB region, while the other two are located on the BA region of the moiré unit cell [74, 75]. This result appeared counter-intuitive, since the LDOS of these flat bands are almost entirely centred on the AA regions of the moiré unit cell [32]. If the Wannier orbitals were centred on the AA regions with s orbitals, which might be intuitively expected from the LDOS, the eigenstates at Γ would be a singlet, which is not consistent with the observed band structures [71]. Using an atomistic tight-binding method, Kang and Vafek [73] generated the Wannier functions of these flat bands from a symmetry adapted Wannierisation procedure [76] (to ensure the Wannier functions were located on the AB/BA regions). The resulting flat band Wannier functions have a peculiar three-lobe structure from the closest AA regions to a AB (or BA) region, as seen in Fig. 1.5.

---

*In the absence of energy isolated bands, the disentanglement procedure is required [70].

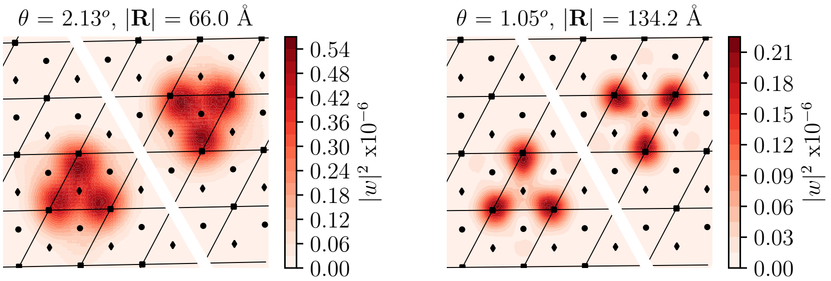

Figure 1.5: Wannier functions of the flat bands of twisted bilayer graphene, for the indicated twist angles. The AA regions are shown by squares, and the AB and BA regions are shown by diamonds and circles, respectively. Reproduced from Ref. 75.

Within a single valley of the continuum model, where there are only two isolated bands in the low-energy spectrum, it was shown that the Wannier functions of these bands have a fragile topology [72, 77–80]. The Berry curvature within a single valley of graphene is the same, but the two valleys (K and K′) have the opposite curvature. For graphene, this means Wannier functions of the bands of the p_z orbitals can be constructed because there is an overall cancellation of the Berry curvature. In a single valley of tBLG, however, the K and K′ points of the moiré Brillouin zone have the same Berry curvature, since they both derive from the same valley of graphene. Therefore, these bands have a finite Chern number, which prevents the generation of well-localised Wannier functions. To alleviate this fragile topology, additional bands must be included [80, 81]. The two valleys of tBLG can be mixed and Wannier functions of these four bands can be generated, which is essentially the approach used by the atomistic tight-binding formalism [73–75].

---

[*] Namely, at the Γ and M point two doublets were found, and at the K/K′ points a four-fold degeneracy was found [71].

[†] An interesting finding from atomistic models is the emergent D_6 symmetry of structures which only have D_3 in the underlying atomic structure at small relative twist angles ($\sim 5°$ or lower). Moreover, relaxed structures without explicit symmetries would also hold this 6-fold rotational symmetry [64].

On the other hand, if it is desired to keep the valley symmetry, additional bands must be included from higher/lower-energy states. An 8-band model was proposed by Carr *et al.* [81], from a projection method onto the bands of a single valley from the $\mathbf{k}\cdot\mathbf{p}$ continuum model [69]. The Wannier orbitals with an s-character of these flat bands were centred on the AA regions of the moiré unit cell [81], which offered a more natural approach to think about these electronic states. A similar approach was proposed by Po *et al.* in a phenomenological 6-band and 10-band model [80], which retained all of the necessary symmetries, where the orbitals of the model have well-defined atomic analogues.

The tear and stack revolution

To experimentally investigate the predictions of flat electronic states, a method for reliably fabricating a desired twist angle was required. Early experiments utilised CVD to grow tBLG structures [44–49], or a single graphene sheet was folded onto itself using the tip of an atomic force microscope (AFM) [82, 83]. While these fabrication methods would generate a tBLG structure, there was a lack of controllability and reproducibility. Therefore, a method to controllably and reproducibly fabricate a tBLG device with a known twist angle was desired.

The experimental breakthrough for fabricating moiré materials came with the invention of the "tear and stack" method [84]. To outline this method, the steps to construct tBLG shall briefly be described. Starting from a graphene flake on a SiO_2 substrate (for example), a hexagonal boron nitride (hBN) substrate supported from above would be manoeuvred over and then lowered onto approximately half of the graphene flake. Because of graphene's affinity to hBN over SiO_2, upon lifting the hBN substrate far enough away from the SiO_2 substrate, the graphene flake would tear in half, with part of the graphene stuck to SiO_2 and the other part to hBN*. This resulted in the generation of two graphene flakes, with aligned crystallographic axes. The graphene-hBN structure could then be translated to reside above the graphene flake on SiO_2, and then a relative twist could be controllably introduced between the two structures. Finally, the graphene-hBN structure could be lowered onto the graphene-SiO_2 structure to generate the tBLG. This method permitted a twist angle control of $\sim$0.1°. Further processing steps to contact and encapsulate the device were required for the desired measurement technique [85].

Using the tear and stack method, Cao *et al.* fabricated a tBLG device and used transport measurements to experimentally probe the material [86]. After preparing a tBLG sample, it was contacted at the edges, and a top and back gate were added. The edge contacts were used to measure the conductivity through the device [85]. As tBLG is a 2D material, the top and back electrostatic gates can change the doping level (the number of electrons per unit cell) through electrostatic forces alone. Using electrostatic gates, the surface density of electrons can be varied by up to $\pm 10^{13}$ cm^{-2}, and owing to the large unit cells of small twist angle structures, this carrier density is sufficiently large to completely fill/empty the flat bands of tBLG [86]. Therefore, this electrostatic gating can be used to investigate the conductivity in tBLG as a function of doping level, which provides information about the low-energy electronic structure of tBLG.

For a large twist angle sample ($> 3°$), the conductivity was found to have the characteristic V-shape of Dirac cones [4] as a function of doping away from charge neutrality. For a smaller twist angle of 1.8°, additional features appear in the conductivity as a function of doping level [86]. Upon doping the tBLG device to $\pm 2\times 10^{12}$ cm^{-2}, past the V-shaped feature near charge neutrality, the conductivity peaks and plateaus off until values of $\pm$7-8$\times 10^{12}$ cm^{-2}, where strong insulating states were found [86, 87]. The thermal activation gaps of these insulating states were found to be $\sim$40 meV, with these insulating states being apparent even at relatively large temperatures ($\sim$100 K). These insulating states were identified to be consistent with the trivial band insulating features that occur upon reaching doping levels of $\nu = \pm 4$ electrons per moiré unit cell (measured from charge neutrality - the addition of electrons is denoted by positive numbers, with negative values indicating the removal of electrons) when atomic reconstruction effects are included in the electronic structure [86].

---

*Further development of the fabrication method to the "cut and stack", where the graphene flake would initially be cut in two before this procedure was undertaken. Cutting instead of tearing the graphene flake in two reduces the strain endured by the graphene flake, which improves the uniformity of the twist angle.

Furthermore, the work of Cao *et al.* [86] demonstrated that there was a reduction in the Fermi velocity of these bands relative to graphene*, and an extra valley degeneracy factor of 2 of tBLG relative to graphene was apparent from the Landau levels [86]. Therefore, the early work of Cao *et al.* [86] was consistent with prior theoretical predictions of tBLG at twist angles above the magic angle.

Strong correlations in magic-angle twisted bilayer graphene

In 2018, Cao *et al.* [88] reported the first conclusive results of correlated phases in magic angle tBLG, as determined by electrical transport measurements. Initially, interaction-induced insulating states appeared when the flat electronic states were doped by $\nu = \pm 2$ electrons per moiré unit cell at temperatures of ∼4 K for a twist angle of 1.08° [88]. At twist angles further from the magic angle, in large perpendicular magnetic fields (∼6 T) and for larger temperatures, the measured resistance for these doping levels increased to values similar to the "normal" metallic state [88]. These correlated insulating states were interpreted as Mott-like states, since the wavefunctions of the flat electronic bands exhibit a strong localisation on the AA regions of the moiré unit cell. The Mott states occur when the electron interaction energy becomes dominant over the kinetic energy of the electrons [88]. While the exact nature of these correlated insulating states was not conclusively demonstrated by Cao *et al.* [88], it was, however, clear that Cao *et al.* provided the first conclusive evidence of strong electron correlations in magic angle tBLG.

Shortly after this, Cao *et al.* [89] also observed that superconductivity was found in proximity to the correlated insulating states at $\nu = \pm 2$. These superconducting phases were found upon both electron and hole doping on either side of these insulating states at temperatures of up to ∼1 K [89]. Importantly, a number of key experimental signatures were reported to demonstrate

---

[*] By fitting the temperature dependence of the Shubnikov-de Haas (SdH) oscillation amplitude to the Lifshitz-Kosevich formula, an estimate for the Fermi velocity can be extracted. In addition, another estimate can come from fitting the V-shape of the capacitance of the device [86].

that this is a robust phase of tBLG [89]. Naturally, the first characteristic of superconductivity is the observation of zero resistance which sharply onsets as the temperature is reduced to a critical value. In addition, at low temperatures (∼0.7 mK), a sharp onset of resistive behaviour occurs when the applied current reaches a threshold value [89].

Overall, the phase diagram of magic angle tBLG reported by Cao *et al.* [88, 89] was similar to that of the high-temperature superconducting cuprates, which have an unconventional mechanism for superconductivity [90]. The cuprate materials also have a correlated insulating state flanked by superconducting phases, with strange metallic behaviour at higher temperatures[*]. The analogy between tBLG and the cuprates was further strengthened by reports of strange metallic behaviour in tBLG [91, 92], for doping levels close to $\nu = \pm 2$ at temperatures up to room temperature, although it was later shown that magic-angle samples were not necessary for its observation [92].

These initial results of magic-angle tBLG, which were verified shortly afterwards by Yankowitz *et al.* [93][†], indicated that strong correlations in a graphene-based system could be controllably realised. In contrast to other strongly correlated materials, such as the cuprates[‡], doping in tBLG can be continuously and reproducibly varied through electrostatic gating, and other physical parameters can be readily tuned too (as discussed later) [88, 89]. This generated huge interest in both the theoretical and experimental communities, since tBLG suggested that it could be the key to understanding high temperature unconventional superconductivity [89].

Theoretical understanding of correlated phases in twisted bilayer graphene

In the interpretation of the experimental results of magic-angle tBLG, it was initially suggested that the insulating states could be Mott-like [88]. It was theoretically proposed by Padhi *et al.* [94], however, that the insulating phases were, in fact, a Wigner crystal[§]. This conclusion was drawn through computing the ratio of the kinetic energy to the potential energy for approximate dispersion relations and screened Coulomb interactions [94]. For the estimates made, it was found that only doping levels of $\nu = 2$ and $\nu = 3$ electrons per moiré unit cell would yield a Wigner crystal (on a honeycomb and Kagome lattice, respectively), which, at the time, was partially consistent with the experimental observations [88]. In addition, it was argued that a dynamical criterion for the Mott-transition was only fulfilled for large twist angles $\sim 2°$ [94].

---

[*] A strange metal is referred to one in which the resistivity of a material is linear-in-T at low temperatures, when it should have a quadratic temperature dependence (if it was a Fermi liquid).

[†] Note that Yankowitz *et al.* [93] did more than merely confirm the results of Cao *et al.* [88, 89], but the discussion of their novel results are deferred until later.

[‡] Where the doping level is chemically changed through altering the chemistry of the sample, which results in significant disorder and additional unknowns in the experiments.

[§] A Wigner crystal in 2D occurs when the potential energy of the electrons, which are assumed to reside in a neutralising background, becomes dominant over the kinetic energy. When this ratio reaches a critical value, the electrons condense into a triangular lattice, for example, to minimise the Coulomb repulsion between electrons.

Another early theoretical work by Guinea and Walet [95] demonstrated that the energy associated with long-ranged electron interactions was the dominant energy scale of magic-angle tBLG. For twist angles close to the magic angle, the moiré length scale is approximately $L_\mathrm{m} \approx a/\theta$, where a is the lattice constant of graphene and θ is the twist angle (in units of radians). Since the LDOS is mostly localised on the AA regions of the moiré unit cell, the Coulomb energy can be approximated by point-like interactions between these regions. For a twist angle of $\sim 1°$, which corresponds to a moiré length scale of $L_\mathrm{m} \approx 10 - 20$ nm, with a dielectric constant of $\epsilon = 4$, the Coulomb interaction energy is found to be $V \approx 50$ meV [95]. On the other hand, the on-site Hubbard interactions parameter, U, of the p_z orbitals which describe the π bands of graphene can be considered. Projecting the wavefunctions of the moiré system generates an effective interaction of the scale $U_\mathrm{eff} \sim 1$ meV [95]. Clearly, then, the long-ranged Coulomb interaction is the dominant energy scale in the system, being several times the bandwidth which can be ~ 10 meV at the magic angle [95].

This motivated Guinea and Walet [95] to investigate the effects of these long-ranged electron-electron interactions using a continuum model. Their analysis revealed that only the six shortest Fourier components of the interaction needed to be included, which generated a potential energy that varied with the same periodicity as the moiré unit cell [95]. This arose because electrons added/removed from tBLG are predominantly added/removed from the AA regions of the moiré unit cell [32], causing a peak/trough in the potential on these regions. This modulated Hartree potential caused significant band deformations to the low-energy electronic structure [95]*.

These Hartree interactions cannot explain the correlated insulating states of tBLG, however. The next natural interaction to include in a continuum model is the exchange interaction. Xie and MacDonald [66] were the first[*] to report results of a self-consistent Hartree-Fock continuum model. At charge neutrality, gapped states were predicted to occur over a wide range of twist angles, provided the interaction strength was large enough[†]. Generally, these insulating states broke the valley projected $C_2\mathcal{T}$ symmetry [66], which can be achieved through either breaking C_2 or time reversal symmetry ($\mathcal{T}$). At the time, no insulating states at charge neutrality were experimentally found in magic angle tBLG.

---

*These band deformations shall be discussed in more detail later.

For all other integer doping levels in the flat bands of tBLG, insulating states were created through breaking the spin and/or valley symmetry [66]. These broken symmetry phases could only be found at twist angles close to the magic angle, unlike the gapped states at charge neutrality. For insulating states at ±2 electrons per moiré unit cell, the valley and/or spin symmetry needs to be broken [66]. Whereas, for ±1 and ±3 electrons per moiré unit cell, the spin *and* valley symmetry must be broken to create an insulating state [66].

These theoretical works treated electron correlations on a mean-field level, which is known to break down in the strongly correlated limit. Methods which can treat strong correlations often need a Hubbard model description of the system. As previously mentioned, Wannier Hamiltonians were constructed for the flat bands of tBLG [68, 73], which describe the kinetic energy contribution to the Hubbard model. The interactions parameters of electrons in these Wannier orbitals were also determined by a number of groups [68, 75, 96]. Due to the Wannier orbitals' peculiar three-lobed structure, the electron interactions beyond the on-site interaction were non-negligible. The on-site Hubbard parameter of the Wannier functions can be considered as the interaction of 3 "lobes" of charges of $e/3$ located at the three AA regions of the moiré unit cell, where there are "intralobe" and "interlobe" contributions to the on-site interaction [68]. For the on-site Hubbard interaction, there are 3 intralobe interactions, which are the dominant contribution to the interaction [68]. While for the Coulomb interaction between Wannier functions located on adjacent AB and BA sites, there are still two intralobe interactions, meaning that the magnitude of nearest-neighbour interaction is approximately 2/3 of the on-site interaction [68]. Furthermore, the next two possible interactions still have an intralobe contribution to the interaction, which means these interactions are approximately 1/3 the on-site interactions, and therefore, always significant in tBLG [68].

---

[*] For a review of other works, see Results Chapter 2.

[†] This was characterised through the fine structure constant of tBLG, $\alpha^* = e^2/\epsilon\hbar v_F^*$, where ϵ is the dielectric constant and v_F^* is the renormalised Fermi velocity of the flat bands of tBLG. If $\alpha^* > 0.4$, insulating states were found at charge neutrality.

Therefore, methods which study strong correlations in tBLG must actually employ an extended Hubbard model for accurate descriptions of the interactions. An example of an exact diagonalisation investigation into an extended Hubbard model of tBLG was performed by Ochi *et al.* [97] at $\nu = -2$ electrons per moiré unit cell. In the limit of the interaction strength going to zero, the theory predicted no flavour symmetry breaking (flavour being defined as the combination of the valley and spin degree of freedom), with the system remaining metallic [97]. In the opposite limit, a "spin and valley-ferromagnetic" state was found to be the ground state, i.e. the system had polarised into a single flavour (one combination of spin and valley) [97]. For intermediate interaction strengths, the ground state becomes quite sensitive to the details of the calculation [97]. An interesting example is when the electrons partially fill two of the flavours, leaving the other two completely empty. This would yield a Dirac dispersion, but since the Dirac cone weakly screens long-ranged electron interactions, the Fermi velocity of the Dirac cones can anomalously increase, causing a suppression of the DOS near the Dirac point [97]. It was suggested that this, in addition to proximity to VHS, could make this state appear to be an insulator [97].

For the origin of the superconducting phase, many theoretical proposals have been put forward [98]. The condensation of the superconducting phase, a "glue" which binds the electrons is required, i.e. an attractive interaction between electrons [99]. In conventional superconductors, such as aluminium, the attractive interaction which binds Cooper pairs originates from electron-phonon interactions. Unconventional mechanisms, on the other hand, have attractive interactions from electronic origins. Another important question is whether the superconducting phase competes with the correlated insulating state, or if its existence is required for the superconducting phase to emerge. The initial experiments of Cao *et al.* [89] suggested an unconventional mechanism, similar to the cuprates, where the superconducting phase arises in proximity to insulating states.

Despite this indication, many works still investigated the possibility of a conventional mechanism of the superconducting phase [65, 100–103]. It was demonstrated using a tight-binding model that there is strong electron-phonon coupling in tBLG, especially for twist angles near the magic angle and doping levels near the VHS (i.e. where the DOS is large) [65]. Moreover, the estimates of the transition temperatures of the superconducting phase were of the order of ∼10 K [65, 100], which was not far off from the 1 K superconducting transition temperature reported in the experiments of Cao *et al.* [89]. The doping dependence of the transition temperature was predicted to be much broader than what was observed in experiments, however [100]. Instead of superconducting domes close to $\nu = \pm 2$ electrons per moiré unit cell, it was predicted that the superconducting phase could have transition temperatures of ∼10 K at most doping levels in the flat bands of tBLG, which would compete with the insulating states at $\nu = \pm 2$ [100].

Many different origins of unconventional superconductivity were proposed [104], ranging from electron-assisted hopping [95] to collective excitations [105]. An interesting example of this was the Kohn-Luttinger instability proposed by Gonzàlez and Stauber [106]. An attractive interaction was found from highly anisotropic screening that is provided by nearly perfect nesting of the VHS [106]. Moreover, at angles close to the magic angle, it was found that the number of VHS would double from 6 to 12, which further enhances this mechanism [106]. Their results indicated that a superconducting phase emerges for doping levels slightly away from the VHS, where a spin density wave insulating state was found at large interaction strengths [106]. In a similar spirit, Fischer *et al.* [107] found that spin-fluctuation-induced superconductivity can occur at non-integer fillings in proximity to magnetic order which occurs at integer doping levels.

These theories for different possible mechanisms for insulating and superconducting states are constructed and independently evaluated, however, meaning that while indications of possible mechanisms are possible, identifying the leading instability is difficult. A method which can simultaneously treat multiple possible instabilities and identify the leading instability without bias is the functional renormalisation group. While this method is formally a weak coupling method, with magic-angle tBLG presumably being well in the strong coupling regime, some success came from this method. A study by Kennes *et al.* [108] demonstrated, using a simplified Hubbard model of tBLG[*], that a Mott-like insulating state at -2 electrons per moiré unit cell was obtained at high temperatures, with an unconventional superconducting phase at the same doping level but at lower temperatures [108]. At larger interaction strengths, a Mott-like insulating state was also found to emerge at charge neutrality [108]. Their theoretically prediction phase diagram had similarities to the initially experimentally obtained one by Cao *et al.* [88, 89], and also gave indications of further correlated states.

Tuning twisted bilayer graphene

These experiments and theoretical studies worked hand-in-hand to generate further excitement in the field, and the burgeoning field of twistronics [110] started to branch out in myriad directions [111]. There were three main directions in which the field progressed since the works of Cao *et al.* [88, 89]. One direction of study was to further tune tBLG through applied hydrostatic pressure [112], alignment with substrates [113] and proximity to the electrostatic gates [114]. Another direction was to further understand the phases of tBLG through different experimental methods. Finally, moiré graphene multilayers beyond tBLG were investigated[†]. Each of these directions shall be summarised in turn.

One of the first experiments after Cao *et al.* [88, 89] was by Yankowitz *et al.* [93], where tBLG was further tuned through hydrostatic pressure. By applying hydrostatic pressure to tBLG, the layers are squeezed closer to each other, which causes the interlayer separation to decrease. This increases the hybridisation energy of the layers, which causes the magic angle to increase slightly [112, 117]. Yankowitz *et al.* [93] found that a 1.27° twist angle device, which does not have robust correlated insulating states or superconductivity at low temperatures, can be tuned to exhibit correlated insulating states and superconductivity after the application of a 2.21 GPa hydrostatic pressure[‡]. Specifically, correlated insulating states were found at $\nu = \pm 2$

---

[*] The dispersion was assumed to be two copies (from the valley symmetry) of an ideal graphene dispersion [71] with only nearest-neighbour hopping, t. Moreover, interactions were only treated through an on-site Hubbard interaction, U. As discussed in the main text, there are long-ranged interactions of the Wannier orbitals of tBLG. It has been shown [109] that long-ranged interactions can be included in an effective way through the reduction of the on-site Hubbard parameter. Therefore, the ratio of U/t was the single parameter of the model.

[†] In fact, twistronics [110] has moved to other 2D materials beyond graphene, such as transition metal dichalcogenides [115] and germanium selenide [116], for example. These materials shall not be reviewed here, however.

[‡] Also found for a pressure of 1.33 GPa.

electrons per moiré unit cell, as found by Cao *et al.* [88, 89], but in addition to these, resistive peaks at doping levels of +1 and +3 electrons per moiré unit cell were also found [93]. In addition, superconductivity was reported for the 1.27° device at 2.21 GPa for doping levels of $-2-\delta$, where δ is a small positively defined number [93]. In fact, the shift of the magic angle to larger values was first theoretically predicted by Carr *et al.* [112] and Chittari *et al.* [117] before the experimental measurements of Yankowitz *et al.* [93].

In the experiments of Yankowitz *et al.* [93], for a twist angle of 1.14° without applied pressure, the phase diagram of magic angle tBLG was reported to have some differences to the one measured by Cao *et al.* [88, 89]. Correlated insulating states were found at +2 and +3 doping levels, but a well-developed insulating state was not observed at the -2 doping level*. Moreover, superconductivity was found between the +2 and +3 insulating states, but not at $2-\delta$ doping levels. Perhaps the most significant difference between Yankowitz *et al.* [93] and Cao *et al.* [88, 89] was the presence of an extended superconducting dome between -2 and -3, without the presence of a well-developed insulating state. Upon turning on a positive displacement field, a correlated insulating state at -2 develops, suppressing the superconducting phase. Whereas, a negative displacement field further strengthened the superconducting phase at -2. The effect of displacement field on the electronic structure of tBLG was predicted to be quite weak†, which suggested these observations might be a consequence of twist angle disorder. Overall, the experiments of Yankowitz *et al.* [93] suggested that the phase diagram of tBLG was significantly more complex than originally thought.

This was most clearly demonstrated by experiments of Lu *et al.* [120]. Importantly, Lu *et al.* [120] introduced an additional step in the fabrication of their tBLG devices. After performing the tear-and-stack method, a relatively small pressure was applied to the device to "squeeze-out" air bubbles between the graphene layers in tBLG [120]. This resulted in a tBLG sample

---

[*] Note that this is in the absence of a displacement field.

[†] The effect of an electric field on the electronic structure was first predicted by Lopes dos Santos *et al.* [29]. It was shown that the Dirac cones of the low-energy states at K and K′ (of the moiré Brillouin zone) would shift up/down in energy. This is occurs because the Dirac cone at K originates from one of the layers, while the K′ Dirac cone originates from the other layer for a single valley. Since an electric field causes the layers to have different energies, the Dirac cones from these layers are shifted in energy relative to each other [118]. The opposite effect happens to the other valley of tBLG. While the electronic structure is not drastically changed by an electric field, it was shown that the magnetic order of magic angle tBLG could be tuned from antiferromagnetic to ferromagnetic with an applied electric field [11, 119], which suggests that these observations could have been intrinsic to tBLG.

with a highly uniform twist angle of ∼1.10°, with variations of less than 0.02°*. This device was reported to have resistive features which were consistent with correlated insulating states at all integer doping levels from -3 to $+3$ electrons per moiré unit cell, i.e. all integer doping levels inside the flat bands [120]. In contrast to the previous works [88, 89, 93], an insulating state was also observed at charge neutrality, which was found to be the strongest insulating state of them all [120]. This was attributed to the fact that in previous devices twist angle heterogeneity and strain mask the onset of correlated insulating states at charge neutrality [120]. In the presence of a ∼4 T perpendicular magnetic field, the insulating state at $\nu = -1$ exhibited strong hysteretic behaviour consistent with a field stabilised orbital magnet [120].

Furthermore, the device of Lu *et al.* [120] exhibited superconducting domes between doping levels of -3 and -2, -1 and 0, 0 and 1, and 1 and 2. The transition temperatures of some of these superconducting domes were ∼3 K [120], which was higher than previous devices [89, 93]. Interestingly, the appearance of superconducting domes does not correspond to energies where the DOS is largest [120], as could have been suggested for the devices of Cao *et al.* [89]. Instead, superconducting domes close to charge neutrality were found, where the DOS is low in the flat bands owing to the Dirac dispersion [120]. This, with the fact that the superconducting domes were always in proximity to correlated insulating states, suggested that the origin of superconductivity in their device could have been from an unconventional mechanism.

The debate about the origin of the superconductivity mechanism was further heated by the observations of superconducting phases without correlated insulating states. In experiments performed by Saito *et al.* [121] and Stepanov *et al.* [122], it was demonstrated that the proximity of the tBLG sample to the electrostatic gates could screen-out these correlated insulating states†. These gates are essential for doping tBLG devices, with all previous experiments using hexagonal boron nitride (hBN) substrates with thicknesses of 10-60 nm to separate tBLG from these gates [88, 89, 93, 120]. At these separations from tBLG, the gates can dope tBLG, but

---

[*] This was confirmed through comparing the resistive features of the tBLG sample through multiple different contacts on the device. In addition, their data did not show the phase coherent Fraunhofer interference patterns, which are a consequence of phase separation between normal and superconducting regions [120].

[†] Qualitatively similar results were also reported later by Liu *et al.* [123] where a tBLG device was separated from a Bernal stacked bilayer graphene with an extremely thin hBN layer. The screening environment from the Bernal stacked bilayer graphene could also be changed through electrostatic gating, which permitted further control of the dielectric environment.

the effect of screening from the induced image charges is minimal. It was only when a hBN substrate with a thickness of ∼5 nm, [121, 122] which is shorter than the moiré length scale of magic-angle tBLG, was used to fabricate a device that the effect of screening could be observed in magic angle tBLG. In fact, this was first theoretically predicted to occur by Goodwin *et al.* [75, 114].

The superconducting domes in the absence of correlated insulating states ranged over a wide range of doping levels [121, 122]. These observations[*] suggested that the superconducting phase was from a conventional mechanism [122], and that the correlated insulating states are competing instabilities to the superconducting phase. While the superconducting domes were found for both electron and hole doped systems, the peak in the critical transition temperatures did not coincide well with the VHS that occur close to $\nu = \pm 2$, which should occur if the mechanism is conventional. Instead, the superconducting domes had the highest transition temperatures at filling levels closer to ±1 or ±3 [121, 122]. In fact, there are some unconventional mechanisms of superconductivity which do not require correlated insulating states. For example, the spin-fluctuation-induced superconductivity from the Hubbard interaction of the p_z orbitals does not require insulating states, but only magnetic order to be present [125]. Moreover, the Hubbard interaction of these atomic orbitals will not be strongly screened by the gates, which indicates that magnetic order could still onset [126].

Another way in which tBLG can be tuned is through crystallographic alignment with the substrate, as performed by Sharpe *et al.* [127] and Serlin *et al.* [128]. In the other experiments, a large relative twist angle between the hBN substrates and tBLG was introduced to ensure that the substrate was decoupled from tBLG [88, 89, 93, 120]. By aligning hBN to tBLG, the C_2 symmetry of tBLG is broken [113]. This causes an insulating state to emerge at charge neutrality, which is not driven by correlations, but by the alignment to the substrate. In addition, (correlated) insulating states were observed only for the electron-side bands, with the insulating state at $\nu = 3$ being particularly stable [127, 128]. Further analysis revealed that this insulating state exhibits hysteretic resistance in a magnetic field, which indicates the onset of ferromagnetic order [127, 128]. For a strong insulating state to occur at $\nu = 3$, the valley and spin degrees of freedom must be broken. This indicated that this insulating state should be a Chern insulator*, owing to an unequal population of the valleys.

---

[*] Superconductivity without correlated insulating states was also reported by Arora *et al.* [124] in a tBLG device in proximity to WSe_2 for twist angles from 0.97° to as low as 0.79°.

Further experimental findings of twisted bilayer graphene

Next, the study of strongly correlated phases in tBLG through methods other than transport measurements, and effects beyond correlated insulating states and superconductivity shall be summarised. The use of STM measurements shall first be outlined, before moving on to additional results from transport experiments, electron compressibility measurements, amongst other techniques.

To investigate tBLG with an STM, the tear-and-stack method had to be modified to expose one side of tBLG, making it accessible to the STM tip. This challenge was overcome quickly, and devices with a single back gate were constructed to investigate the doping dependence of tBLG [129–133]. Importantly, STM is an experimental technique that can measure a quantity which is directly proportional to the LDOS. Therefore, this method can provide direct insight into the local electronic structure of tBLG.

For angles around 1-3°, two large peaks close to the Fermi energy in the LDOS of the AA regions were reported, consistent with earlier work [44–49]. As the angle is decreased from large angles $\sim 3°$ to small angles $\sim 0.8°$, significantly smaller than the magic angle predicted by Bistritzer and MacDonald [33], Kerelsky *et al.* [129] reported a monotonic decrease in the separation of these two peaks, which correspond to the VHS of the flat bands. This indicated a discrepancy between the experimental results and the prior electronic structure calculations, which predicted the separation of the VHS to vanish at the magic angle of 1.05° [33]. The discrepancy suggested that the minimum in the bandwidth, i.e. the Fermi velocity of these bands, actually occurred at angle of $\sim 0.8°$ [129]. In fact, it is well known that electronic structure methods based of DFT underestimate the Fermi velocity of graphene, with experiments and GW calculations indicating a Fermi velocity which is ~20-30% larger [129, 134]. Interestingly, despite the Fermi velocity of the flat bands not being minimal at 1.1°, the experiments still reported this angle to be the magic-angle of the system, as defined by the observation of correlated phases (which shall be shortly discussed) [129].

---

*The existence of Chern insulating states shall be discussed in more detail later.

At angles just slightly above the magic angle (1.15° and 1.72°, respectively), Kerelsky *et al.* [129] and Xie *et al.* [130] reported pinning of the VHS as a function of doping level in the flat bands. Starting from a Fermi energy below the flat bands of tBLG (completely empty flat bands), increasing the Fermi energy causes a rigid shift of the LDOS of the flat bands, with the valence-side VHS peak being significantly larger than the conduction-side [129, 130]. This rigid-shift is consistent with a non-interacting picture. Upon doping inside the flat bands, the Fermi energy rapidly reaches the valence-side VHS, and is pinned there for a wide range of doping levels, significantly larger than expected from non-interacting theories [129, 130]. Only when the doping level has reached $\nu \approx -2$ electron per moiré unit cell does the Fermi level pinning cease, and the LDOS exhibits the characteristic V-shape of the Dirac cones [129, 130]. The Fermi level passes through the Dirac cone feature of the flat bands, but becomes pinned again upon reaching the conduction-side VHS until the flat bands are completely filled [129, 130]. At these Fermi energies, the peaks of the valence and conduction VHS are comparable, which is in contrast to the case when the bands were completely empty [129, 130].

These experiments suggested that there is a sensitive doping-dependence of the electronic structure of tBLG in the normal state. In fact, this was first predicted by Guinea and Walet [95] using a mean-field Hartree theory based on a continuum model of tBLG. This motivated others to theoretically study electron-electron interactions and Fermi level pinning from Hartree theory in tBLG using various models. For example, Cea *et al.* [135] employed the continuum model, Rademaker *et al.* [136] and Goodwin *et al.* [137] used the atomistic tight-binding model, and Calderón and Bascones [138] employed the local 8-orbital model [81] of the flat bands.

Experiments performed by Xie *et al.* [130] indicated the break-down of mean-field approximations at an angle of 1.01°. For doping levels where the bands were completely filled or empty, the LDOS comprised of two peaks, corresponding to the VHS. However, for doping levels inside the flat bands, the LDOS underwent drastic distortions, changing significantly with doping level, even at non-integer values [130]. At most doping levels, the LDOS looked completely different from a singe-particle calculation, as three or four well defined peaks were often present [130]. The only exception was at charge neutrality, where two peaks occurred in the LDOS, although with a separation several times larger than that was found in empty/filled bands [130]. This indicated the formation of a correlated insulating state at charge neutrality with a large gap [130], much larger than those reported from transport experiments [120]. The calculations performed by Xie *et al.* [130] demonstrated that these observations were not consistent with mean-field calculations, even with symmetry breaking, but required strong correlations to be accounted for using exact diagonalization of a phenomenological model of the flat bands.

In contrast, the experiments of Kerelsky *et al.* [129], Jiang *et al.* [131], Choi *et al.* [139] and Zhang *et al.* [140] found that their spectra where much closer to the single-particle picture for angles near the magic angle. Moreover, they all reported that upon doping the flat bands by ±2 electrons per moiré unit cell, the VHS at these doping levels would split into two peaks, indicating the onset of a broken symmetry phase [129, 131, 139, 140]. At this doping level, real-space maps of the LDOS at the Fermi energy demonstrated that these correlated phases exhibit nematic ordering. Namely, the (approximate) C_3 rotational symmetry exhibited in the AA regions of the moiré unit cell was broken, leaving only an (approximate) C_2 rotational symmetry at these points [129, 131, 139, 140]. While this rotational symmetry breaking could occur because of residual strain in tBLG, it was noted by Choi *et al.* [139] that the effects of strain were not sufficiently large enough to explain the extent of the symmetry breaking, which indicates that this rotational symmetry breaking originates from interaction-driven nematic ordering. It was also noted that the nematic order could be stabilised by the strain as in some of the experiments the nematic axis and strain were aligned [129].

In fact, using transport experiments, Cao *et al.* [141] also found signs of nematicity [142, 143]. At high temperatures (∼10 K), anisotropic features in the "normal state" were observed at $\nu = -2 - \delta$ (again δ is defined as a small, positive number) in the resistivity [141]. Lowering the temperature causes this anisotropic response to strengthen and shift towards doping levels closer to $\nu = -2$, where it eventually intersects the superconducting dome at doping levels just under the correlated insulating state. Where these phases intersect in $\nu - T$ space, a reduction in the superconducting transition temperature was observed [141]. Upon applying a perpendicular magnetic field of 0.5 T, the superconducting phase was suppressed, and it was found that the anisotropic state persists at low temperatures. Therefore, this anisotropic "normal phase" competes with the superconducting phase [141]. Moreover, nematic characteristics were observed in the superconducting phase, the axis of which was highly sensitive to the doping level [141]. These findings suggest that nematicity is a "normal"-state property of tBLG [141].

Further insight into tBLG came through STM [144, 145], local electronic compressibility measurements [146], and transport experiments [147, 148], where Chern numbers of $C = \pm 1, \pm 2, \pm 3$ at doping levels of $\nu = \pm 3, \pm 2, \pm 1$ were observed. In transport experiments [147, 148], this can be deduced from the observation of the quantised Hall conductance, while in STM [144, 145] and local electronic compressibility [146], this comes from the magnetic field dependence of the gap. These observations were interpreted as spin and valley polarised Chern insulators, which validate the topological nature of the bands which was theoretically predicted. Moreover, Xie *et al.* [149] found evidence of fractional Chern insulators and Stepanov *et al.* [150] found evidence for Chern insulators in zero magnetic field at $\nu = 1$. While evidence for zero-field Chern insulators was observed upon aligning tBLG to hBN at $\nu = 3$ [127, 128], which comes from explicit breaking of C_2 from the alignment, these later observations where a direct consequence of interactions, rather than a secondary effect.

These observations suggested a clear sequence of symmetry breaking transitions. Using STM and local electronic compressibility measurements, respectively, Wong *et al.* [151] and Zondiner *et al.* [152] reported the observation of a cascade of phase transitions, where Dirac-like features emerge as integer doping levels in the flat bands are reached. For example, starting from charge neutrality with all four flavours equally populated, consider adding electrons to the system [151, 152]. Close to when a single additional electron per moiré unit cell has been added beyond charge neutrality, a symmetry breaking phase transition occurs, causing the electrons to fill one of the flavours, returning the other flavours to the Dirac-point, resulting in Dirac features in the electronic compressibility measurements [97, 151, 152]. This transition was observed to occur upon reaching each integer filling, although it was more pronounced in the electron-doped systems, giving rise to a "cascade of Dirac revivals" [151, 152]. Interestingly, these features arose for relatively high temperatures of ∼30 K, indicating that this Dirac cascade is the high-temperature parent state from which the strongly correlated phases emerge at low temperatures [151, 152].

Using local and global electronic compressibility and entropy measurements, evidence of the Pomeranchuk effect in magic angle tBLG was reported by Rozen *et al.* [153] and Saito *et al.* [154]. Pomeranchuk [155] first predicted the counterintuitive effect of ^{3}He freezing upon heating, owning to the high excess spin entropy in the solid phase in comparison to the liquid phase. In magic angle tBLG, an electronic analogue of the Pomeranchuk effect was found to occur close to $\nu = \pm 1$ electrons per moiré unit cell [153, 154]. At low temperatures, the electrons were found to have Fermi liquid-like behaviour, which transitions to a free moment phase with a large entropy at higher temperatures [153, 154]. Interestingly, this free moment phase was observed to exist at low temperatures (~ 3 K) without a thermodynamic gap, i.e. it remains metallic [153, 154]. The resistive peaks at $\nu = 1$ in most transport experiments were always significantly less developed, which can presumably be attributed to this electronic Pomeranchuk effect [155].

Finally, many other experiments on tBLG have also revealed interesting effects. For example, superconducting quantum interference device measurements have been used to map out the twist angle disorder [156] and local magnetic structure of tBLG [157], angle-resolved photoemission spectroscopy with nanoscale resolution has directly probed the electronic structure of magic angle tBLG [158, 159], collective excitations have been probed using AFM [160], and enhancements to thermoelectricity [161] have also been found. The summary here is naturally not exhaustive, and it is clear that this is not the end of the story for tBLG.

Overall, this part of the Introduction has provided some insight and evidence that strong correlations give rise to many intriguing effects in magic angle tBLG. At the point of writing, it is clear that there remains to be some experimental discrepancies between different measurements, and that the origin of (some of) these reported phases further divides the theoretical community that aims to understand these observations. It has, however, generated enormous excitement, causing many others to explore moiré materials beyond tBLG.

Twisted double bilayer graphene

In terms of moiré graphene multilayers [162], one of the first systems to be investigated after tBLG was twisted double bilayer graphene (tDBLG), where instead of stacking and twisting two graphene layers, two Bernal stacked graphene bilayers were stacked and twisted relative to each other, as seen in Fig. 1.8. The electronic structure of Bernal stacked bilayer graphene consists of parabolic bands which touch at the Fermi level of the neutral system [1]. In 2D, this gives rise to a finite DOS at the Fermi level, in contrast to graphene where the DOS vanishes at the Fermi level [32]. There has, in fact, been reports of strong correlations in Bernal stacked bilayer graphene [24], which would intuitively suggest it is a good candidate of strong correlations as a moiré material. Moreover, Bernal stacked bilayer graphene is quite sensitive to perpendicular electric fields [1], which breaks the inversion symmetry, causing a gap to open up where the parabolic bands touch.

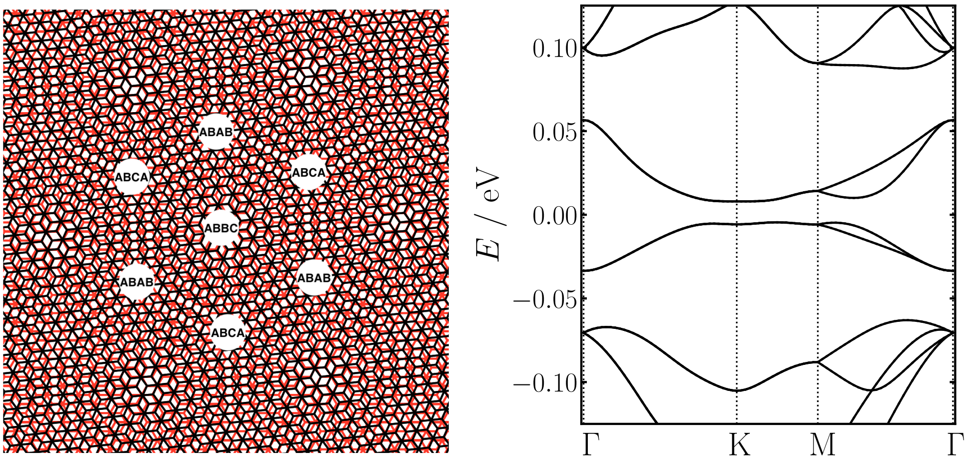

Figure 1.6: Moiré pattern of twisted double bilayer graphene (left). Electronic structure of twisted double bilayer graphene (right) at a twist angle of 1.7° calculated from the atomistic tight-binding model. A relaxed structure was utilised for the atomic positions, and no additional on-site potentials were included.

Theoretically, the electronic structure of tDBLG was investigated using *ab initio* methods [163–165], atomistic tight-binding approaches [163] and the low-energy continuum models [166]. The latter approaches found that tDBLG also exhibits a magic angle, albeit at a slightly larger angle of ∼1.3° in comparison to tBLG [163, 167]. The flat electronic states of tDBLG were found to resemble those of tBLG, as seen in Fig. 1.8, with the key difference being the presence of parabolic bands (touching) at the K/K′ points instead of a Dirac cone*. As alluded to earlier, the electronic structure of tDBLG was found to be extremely sensitive to perpendicular electric fields [166, 168], owing to the sensitivity of each Bernal bilayer to the field.

Using the tear-and-stack method†, Shen *et al.* [169], Liu *et al.* [170], Burg *et al.* [171] and Cao *et al.* [172] fabricated magic-angle tDBLG and investigated its properties using transport experiments. In the absence of a perpendicular displacement field, trivial band insulating states were found upon completely filling/emptying the isolated flat bands [169–172]. In the presence of a perpendicular displacement field, a strong insulating state occured at charge neutrality, owing to inversion symmetry breaking of the Bernal bilayers [1]. In addition, a correlated insulating state was found to occur upon the addition of $\nu = +2$ electrons per moiré unit cell (in the presence of a finite displacement fields) at a temperature of ∼4 K [169–172]. The gaps associated with these correlated insulating states were found to increase upon application of an in-plane magnetic field, suggesting these states have a ferromagnetic character [169–173]. These transport experiments also found indications of superconductivity‡, and in the presence of ferromagnetic order, the mechanism could well be unconventional [174].

Using STM experiments, Zhang *et al.* [175] and Liu *et al.* [176] investigated the correlated phases of tDBLG at the magic angle. The observations of these local measurements were found to be consistent with the transport measurements. Correlated insulating states were only found upon doping tDBLG by +2 electrons per moiré unit cell, and a perpendicular displacement field is always present in the single-gated devices upon doping [175, 176]. The electronic structure of tDBLG was found to be sensitive to the doping level, which changes with the back-gate voltage. This effect, however, is not intrinsically due to the doping level change in tDBLG [177]. A continuum model calculation by Pantaleón *et al.* [178] showed that Hartree interactions are quite weak in the normal state of tDBLG, and therefore, these doping-dependent changes to the electronic structure are solely caused from changes to the perpendicular displacement field [177].

---

[*] Note this was actually for large angles where this feature was evident. At angles closer to the magic angle, the features of the electronic structure is not so clear, and depend sensitively on the model.

[†] Note that the tear and stack method naturally creates and AB-AB quad-layer system. While a AB-BA system is also possible, this system is harder to fabricate. In fact, calculations have shown there is little difference between these two [166].

[‡] This is not well agreed upon, however [98].

In addition, Rubio-Verdé *et al.* [177] found evidence of nematic order in tDBLG close to the magic-angle from STM experiments. Similar to tBLG, a breaking of the C_3 rotational symmetry occurred, which was found not to be associated with strain in the material. In fact, it was also not induced through changes in the perpendicular displacement field, and was observed for a range of doping levels in the flat electronic states (but not the remote bands) [177]. At very small twist angles of tDBLG, Kerelsky *et al.* [179] found evidence of strong correlations in the ABCA stacking regions but not the ABAB stacking regions.

Also at large twist angles, tDBLG was found to exhibit interesting properties in transport experiments performed by Rickhaus *et al.* [164, 180]. At an angle of 2.36° in moderate displacement fields, tDBLG was found to exhibit charge density waves [180]. These states could be realised in this system, in contrast to tBLG, because of the nesting which can be achieved in the electronic structure of tDBLG in the presence of a displacement field. In addition, at a large twist angle, but in the absence of a displacement field, their transport experiments revealed the existence of a gap at charge neutrality [164]. While the predictions of the continuum model and atomistic tight-binding theories indicated there should be a quadratic band touching at charge neutrality, DFT calculations were found to have a small gap at charge neutrality [163–165].

In theoretical calculations of Haddadi *et al.* [163] and Rickhaus *et al.* [164], the existence of a gap at charge neutrality was interpreted as the presence of a “intrinsic symmetry polarisation” or a “crystal field”, respectively. This crystal field is an intrinsic potential difference which occurs in this quad-layer system, as the outer layers are inequivalent to the inner layers*. The outer layers were found to have a larger potential energy than the inner layers, which suggested that the electrons accumulate on the inner layers of the quad-layer system [163–165]. To reproduce the DFT calculations, it was found that the potential felt by the electrons on the inner layers used in a tight-binding calculation needed to be approximately 30 meV lower on the inner layer relative to the outer layers [163–165]. The origin of this field is not well understood, however.

---

[*] The outer layers in a DFT calculation either face a vacuum, or a substrate such as hBN. Whereas, the inner layers only have adjacent graphene layers. Therefore, the graphene layers are in chemically different environments.

Twisted mono-bilayer graphene

In a similar spirit, a moiré graphene multilayer comprising of a monolayer of graphene twisted relative to a Bernal-stacked bilayer graphene, the structure of which is shown in Fig. 1.7, referred to as mono-bilayer graphene or AtAB, has also been investigated in some depth. This material is conceptually interesting, as it was not *a priori* evident if it was going to behave more similar to graphene, bilayer graphene, a trilayer graphene, or even something entirely different.

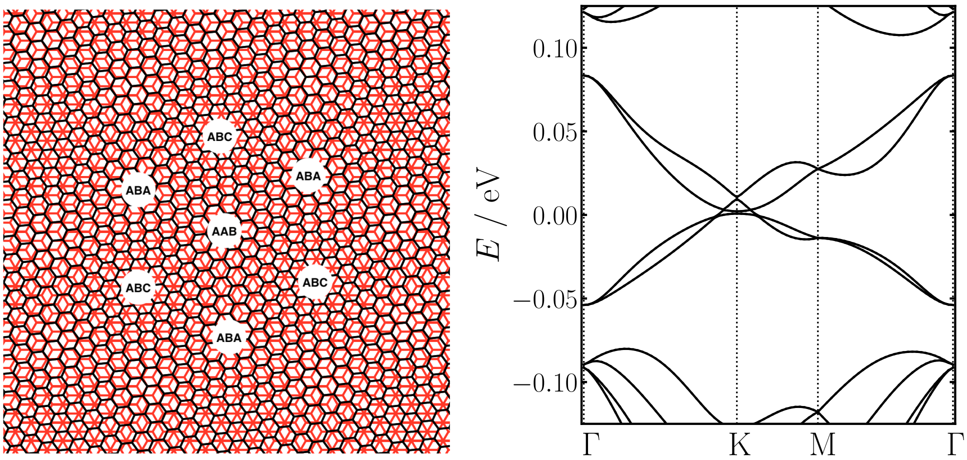

Figure 1.7: Moiré pattern of mono-trilayer graphene (left). Electronic structure of mono-trilayer graphene (right) at a twist angle of 1.7° calculated from the atomistic tight-binding model. A relaxed structure was utilised for the atomic positions, and no additional on-site potentials were included.

It was shown using a continuum model [181, 182] that the electronic structure of AtAB is similar to that of tBLG, as seen in Fig. 1.7. A magic angle was found to occur at a twist angle of ∼1.2°, where the isolated flat bands reach a minimum bandwidth [181, 182]. Instead of there being a set of Dirac cones with a valley degeneracy at the K/K′ points (as is the case for tBLG), there is a set of parabolic bands from the AB bilayer and a Dirac cone from the monolayer [182]. Within the low-energy electronic structure of a single valley of the continuum model approximation, the K-points of the moiré Brillouin zone host a Dirac cone from the twisted graphene layer, and the K′-points have a set of parabolic bands from the Bernal bilayer; with the other valley having the opposite ordering of the K/K′ points for the features in the electronic structure, because of time reversal symmetry [182]. This is an interesting difference to the cases of tBLG and tDBLG, where the K/K′ points within a valley had the same features in the electronic structure. Similar to these materials, the low-energy electronic structure of AtAB was found to be topologically non-trivial [181, 182]. In the presence of an electric field, the electronic structure deforms drastically, presumably because the inversion symmetry of the bilayer is broken [181, 182].

Using transport experiments, Chen *et al.* [183], Polshyn *et al.* [184] and Shi *et al.* [185] found evidence of strong correlations in this moiré material near its magic angle, which was quite sensitive to the sign of the displacement field which was applied. At charge neutrality, semi-metallic behaviour was found at small displacement fields, which transitions to a trivial band insulator when the displacement field is large enough [183–185]. For the hole-doped system, independent of displacement field, no evidence of interaction-induced broken symmetry phases was found [183–185]. This observation is similar to tDBLG [169–172], but is not consistent with the measurements of tBLG [98]. For a displacement field which lowers the energy of the AB bilayer with respect to the twisted graphene layer, a correlated insulating state at $\nu = 2$ electrons per moiré unit cell is reported over a narrow range of displacement fields, again consistent with the reports of tDBLG [183]. Moreover, evidence of ferromagnetism was found at $\nu = 1$ when the displacement field lowers the energy of the AB bilayer [183]. On the other hand, for displacement fields which lower the energy of the twisted graphene sheet relative to the AB bilayer, the system becomes more similar to tBLG [183]. Resistive peaks at each electron-doped integer doping are found. While transport experiments did not find conclusive evidence of superconductivity, STM experiments of Shi *et al.* [185] found a superconducting gap at non-integer fillings (between $\nu = 1$ and $\nu = 2$) in the presence of a displacement field.

Twisted trilayer graphene

These moiré graphene multilayers, namely tDBLG and AtAB, have adjacent layers of graphene in which the crystallographic axes are aligned and twisted, i.e. Bernal stacked bilayer graphene. The experimental community was able to quickly fabricate such moiré materials, as the moiré material could be constructed in a single step, similar to tBLG. It was theoretically proposed by Khalaf *et al.* [186], however, that perhaps a more interesting moiré graphene trilayer (and quad-layer) system might exist if there are no adjacent layers of graphene where the crystallographic

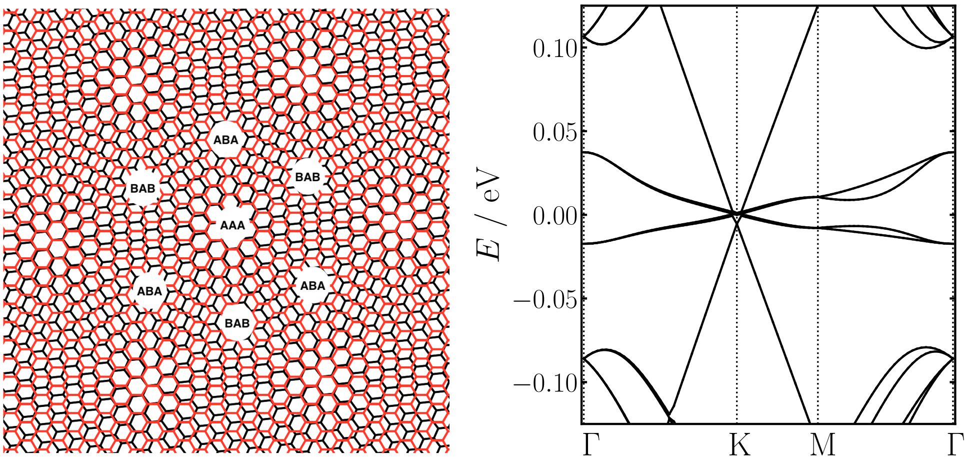

Figure 1.8: Moiré pattern of twisted trilayer graphene (left). Electronic structure of twisted trilayer graphene (right) at a twist angle of 1.7° calculated from the atomistic tight-binding model. A relaxed structure was utilised for the atomic positions, and no additional on-site potentials were included.

axes are aligned, i.e. Bernal or rhombohedral stacked graphene layers. More specifically, they proposed a moiré graphene multilayer where the twist angle alternates by $\pm\theta$ between adjacent sheets[*], since this protects the $C_2\mathcal{T}$ symmetry, which is present in tBLG, but not tDBLG or AtAB [186]. Actually, this symmetry only holds for these alternating-twist-angle structures if the graphene layers which are not adjacent are aligned, and do not have a relative shift of positions, i.e. they are "AA" stacked. For twisted trilayer graphene (tTLG), Carr *et al.* [190] demonstrated that the lowest energy structure occurs when the middle layer of an AAA[†] stack is twisted relative to the encapsulating graphene layers. Therefore, starting from an initial AAB/BBA/ABC stack and twisting the middle layer causes the structure to have a larger energy than if the initial stacking was AAA [190]. This occurs because in the AAA system, upon twisting the middle layer, the moiré patterns of the upper and middle graphene layer, and the lower and middle graphene layer align, permitting coherent reconstruction effects [190]. Therefore, it is this "AtAtA" system, as seen in Fig. 1.8, which we refer to as tTLG and continue to summarise.

It was found, from a minimal continuum model, that the low-energy electronic structure of tTLG can be mapped onto a tBLG and graphene layer that are decouple from each other [186]. Therefore, the low-energy electronic structure consists of a Dirac cone with a large Fermi velocity, and a set of flat electronic bands which are analogous to tBLG [126, 190–193], as shown in Fig. 1.8. One key difference between the flat bands of tTLG and tBLG is that the magic angle of tTLG is $\sqrt{2}$ larger than in tBLG. Therefore, the magic angle of tTLG occurs at approximately 1.5°. It was also shown that the LDOS is peaked in the AAA regions of the moiré unit cell, with a larger weight on the middle layer relative to the outer layers for the wavefunctions of the flat electronic bands at the edge of the hexagonal moiré Brillouin zone [126, 194, 195]. It was theoretically shown by Fischer *et al.* [126] that tTLG exhibits similar effects from Hartree interactions as tBLG. In contrast to tBLG, however, tTLG was predicted to be quite sensitive to a perpendicular electric field. It was found by Lopez-Bezanilla and Lado [192] that the two VHS of the flat bands merge at a critical electric field, causing a massive enhancement of the DOS.

---

[*] Generally, the twist angles do not need to be symmetric, which leads to multiple moiré patterns, which can also have interesting effects [187–189].

[†] The relative shift of the middle layer to the encapsulating outer layers is actually inconsequential, as this simply shift the positions of the different stacking orders. Therefore, an ABA starting configuration is equivalent.

It was found by Park *et al.* [196] and Hao *et al.* [197] that magic-angle tTLG is perhaps the most correlated and tunable moiré graphene multilayer fabricated to date. In the absence of a displacement field, the results of their transport experiments resembled those of tBLG. In particular, resistive peaks near integer doping levels per moiré unit cell[*], and robust superconductivity was observed between $\nu = -3$ and $\nu = -2$ [196, 197]. Note that while signatures of superconductivity have been found in moiré graphene multilayers other than tBLG, tTLG is the only other system where its existence is not debated. Moreover, signatures of the Dirac revival features were also observed [196].

In the presence of a perpendicular displacement field, the superconducting phase was found to be further stabilised. In fact, Hao *et al.* [197] reported an additional superconducting dome to appear at $\nu = +2$ and $\nu = +3$ in the presence of a large displacement field. While Park *et al.* [196] actually found superconducting domes between these fillings in the absence of a displacement field, they also reported superconducting domes to appear between $\nu = 1$ and $\nu = 2$. Moreover, the largest critical transition temperature for superconductivity was found in the presence of a moderate displacement field [196, 197]. Interestingly, their transport experiments indicated that these superconducting phases were bounded by VHS [196]. Therefore, the superconductivity appears to occur at doping levels where the DOS is not the largest, which suggests an unconventional mechanism for superconductivity [196]. It was later found by Cao *et al.* [198] that superconductivity in magic-angle tTLG close to $\nu = -2$ in a displacement field violates the Pauli limit for conventional spin-singlet superconductivity. In other words, superconductivity was only destroyed by an in-plane magnetic field of 8 T, which is 2-3 times larger than expected for a conventional spin-singlet superconductor [198]. At even larger in-plane fields (of $\sim$10 T), the superconducting phase is stable again, indicating re-entrant superconductivity [198]. These measurements suggest that superconductivity in tTLG is not a conventional spin-singlet mechanism [198].

---

[*] Note that these were not referred to correlated insulating states, however, since the dispersive Dirac cone persists.

Trends in moiré graphene multilayers

It appears, then, that moiré graphene multilayers with alternating twist angles between adjacent graphene layers are a more promising route to study strong correlations than moiré graphene multilayers in which there are adjacent layers that are aligned. In this spirt, some researchers have started to make predictions of the trends of these different systems. In other words, the qualitative differences between these two classes of moiré graphene multilayers, and how these properties change with the number of graphene layers. For example, Choi and Choi [199] have studied the electron-phonon coupling of various moiré graphene multilayers. Their results clearly show that alternating twist angle structures exhibit significantly stronger coupling than ones with adjacent aligned layers [199]. Moreover, from comparing tBLG and tLTG, one might wonder if moiré graphene multilayers with more layers are more promising. Moiré materials in 3D has been theoretically studied by Cea *et al.* [200] and Xian *et al.* [201].

In summary, moiré graphene multilayers have been shown to exhibit a wide range of interesting phenomena. Given the recent experimental advances and activity in the theoretical community, it is timely to investigate these materials. In this work, we take the perspective of an atomistic model. In this approach, there are two length scales: the length scale associated with the underlying graphene layers, and the longer moiré length scale arising from twisting. Here we investigate the interplay of these two length scales.

Chapter 2

Methods

Atomistic methods have exclusively been used to investigate moiré graphene multilayers in the work described here [30]. The advantage of atomistic methods is that the interplay between the carbon-carbon bond length and the moiré length scale can be investigated. These methods, however, are typically significantly more computationally expensive than others, such as continuum model approaches [30]. As such, the computational expense of the methods restricts our analysis of moiré graphene multilayers to have only one moiré pattern from a twist angle (down to ∼1°, which is sufficient to probe magic angle systems), with systems of up to 4 layers[†]. Furthermore, we do not account for any disorder effects [202], such as heterostrain [203, 204], defects [205, 206], or consider any additional moiré patterns created from the substrates [20, 21, 113, 207].

This chapter has the following structure. Firstly, we outline the convention used to define the lattice structure of moiré graphene multilayers with a single twist angle. We then briefly give details of the methods employed to model the atomic reconstruction effects of these materials. Next we describe the methods used to investigate the electronic properties of moiré graphene multilayers. Starting with a brief summary of the employed *ab initio* methods, we move onto describing the "non-interacting" atomistic tight-binding method (since this is the main starting point for our calculations). We then describe how to calculate the Wannier functions and screened interactions from this model. Finally, we move onto including interactions in this model, where we outline an atomistic Hartree tight-binding theory, an atomistic Hubbard tight-binding theory, and the extended Hubbard model of the flat bands. Details of the spin susceptibility calculations carried out in a collaboration with Lennart Klebl and Dante Kennes are also provided [208].

[†] When there are more than two layers in the moiré graphene multilayer, multiple twist angles can exist. Such structures often have unit cells with length scales that are extremely long [187]. The atomistic methods cannot be employed with reasonable computational expense to investigate these systems, owing to the number of atoms being too large, as beyond 20,000 atoms these atomistic methods become prohibitively expensive.

2.1 Commensurate moiré graphene multilayers

In pristine graphene, the primitive unit cell contains two atoms, with all other atoms in an infinite sheet of graphene being reached by translations given by the unit cell vectors ($\mathbf{a}_1$ and $\mathbf{a}_2$ are defined later), as demonstrated in Fig. 2.1 [1]. These two atoms in the unit cell belong to different sublattices, referred to as the A and B sublattice, as indicated by red and black circles, respectively, in Fig. 2.1. Individually, each of these sublattices form a triangular lattice, but when considered together they form a honeycomb lattice. Since graphene is a 2D material, we shall use the convention of defining it to be in the $x-y$ plane throughout. When considering more than one layer of graphene, the layers reside at different values of z.

For two (or more) layers of graphene, additional degrees of freedom arise from the relative registry between the layers and the alignment of the crystallographic axes of each graphene layer [209]. In the case of perfect alignment of the crystallographic axes, or a symmetry equivalent structure, only the stacking registry remains as a degree of freedom. As the lattice vectors of each graphene layer are identical (in the absence of strain), the unit cell of bilayer graphene is the same as that of graphene [1, 24]. When there is not perfect alignment between crystallographic axes of each graphene layer (but still ignoring strain), translational symmetry is not always present. Translational symmetry is only present when there is a relative twist angle between the two graphene sheets that can be expressed in terms of integer multiples of graphene unit cell vectors [29, 32, 37]. These are referred to as commensurate structures, where the relative twist angle between the two graphene sheets generates a honeycomb moiré pattern with a well defined length scale that is larger than the length scale of the underlying graphene honeycomb lattice.

Since moiré graphene multilayers with only a single twist angle are considered here, the

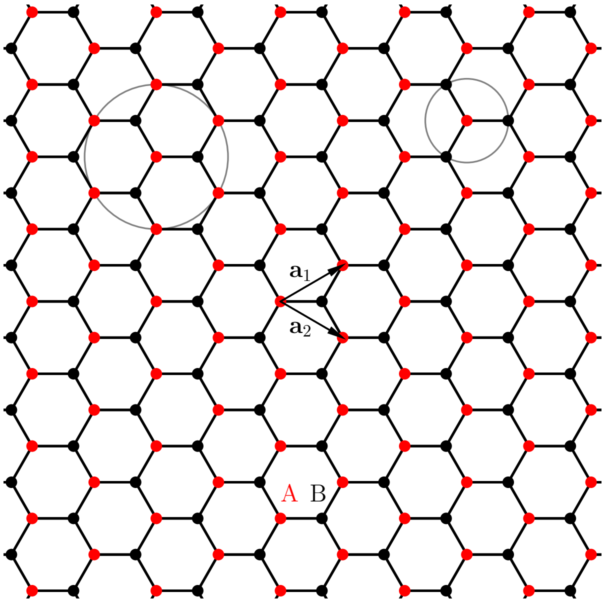

Figure 2.1: Schematic of graphene lattice demonstrating the different sublattices (as shown by red for A and black for B), the lattice vectors of graphene ($\mathbf{a}_1$ and $\mathbf{a}_2$), the nearest neighbour carbon atoms (as shown, a sublattice A carbon has only sublattice B carbon atoms for nearest neighbours), and next nearest neighbour atoms (as shown, a sublattice A carbon has only sublattice A carbon atoms for next nearest neighbours).

method for defining commensurate moiré structures of Trambly de Laissardière *et al.* [32, 37] was employed*. In this method, one starts with a graphene multilayer system with all graphene lattice vectors being aligned (different stacking configurations can be considered, but this does not affect the definition of the commensurate moiré structure). A twist angle with a commensurate moiré structure is created through choosing a vector

$$\boldsymbol{V}(m,n) = m\mathbf{a}_1 + n\mathbf{a}_2, \tag{2.1}$$

where $\mathbf{a}_1$ and $\mathbf{a}_2$ are the lattice vectors of graphene [1] given by

$$\mathbf{a}_1 = \frac{a_0}{2}\begin{pmatrix}\sqrt{3}\\ -1\end{pmatrix}, \qquad \mathbf{a}_2 = \frac{a_0}{2}\begin{pmatrix}\sqrt{3}\\ 1\end{pmatrix}, \tag{2.2}$$

---

*See also Ref. 29.

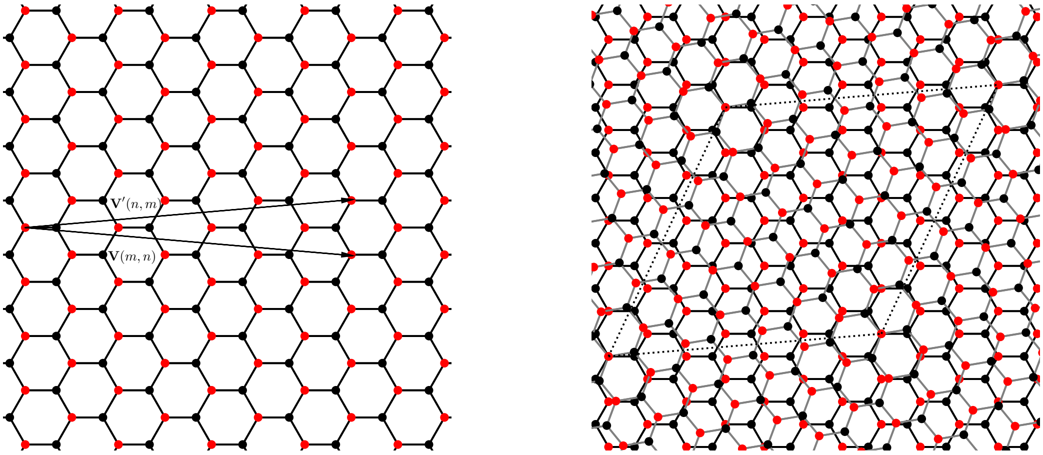

Figure 2.2: Schematic demonstration of how to construct commensurate unit cells when a relative twist angle exists between two graphene sheets. (left) - Defining vector which generates a commensurate structure, as explained in the text for $n = 3$ and $m = 4$. (right) - Corresponding commensurate moiré unit cell, with black dashed line indicating the moié unit cell. Again, grey lines correspond to bonds between atoms in the top, twisted layer, with black lines corresponding to bonds in the bottom, untwisted layer.

with a_0 denoting the lattice parameter of graphene, and n and m are non-equal integers which multiply these graphene lattice vectors. The origin of this vector is chosen as the rotation center, and a layer of graphene is rotated such that the lattice point at $\boldsymbol{V}(m, n)$ now resides at $\boldsymbol{V}'(n, m)$. This procedure is demonstrated in Fig. 2.2. The commensurate moiré lattice vectors are given by

$$\boldsymbol{R}_1 = n\mathbf{a}_1 + m\mathbf{a}_2, \qquad \boldsymbol{R}_2 = -m\mathbf{a}_1 + (n+m)\mathbf{a}_2. \tag{2.3}$$

These vectors connect the intrinsic length scale associated with the atomic structure of graphene to the moiré length scale that is constructed through introducing a twist angle between graphene sheets. Here we only consider $m = n + 1$ structures.

The number of atoms in the moiré unit cell is given by

$$N = 2N_l(n^2 + nm + m^2), \tag{2.4}$$

where N_l is the number of layers in the moiré graphene multilayer (with a single twist angle).

Therefore, the total number of atoms increases approximately quadratically with n and m, but linearly in the number of layers in the moiré graphene multilayer.

The corresponding twist angle, θ, for the commensurate moiré structure is

$$\cos\theta = \frac{n^2 + 4nm + m^2}{2\left(n^2 + nm + m^2\right)}. \tag{2.5}$$

For increasingly large values of n and m, and small values of the difference between these integers, the twist angle tends to zero, as both numerator and denominator tend towards the same value ($\sim 6n^2$, if $m \approx n$ for large n). The moiré length scale [95] can be connected to the twist angle through

$$L_m = \frac{a_0}{2\sin(\theta/2)}. \tag{2.6}$$

Therefore, at small angles, the moiré length scale increases as $a_0\theta^{-1}$, which is a key relationship.

The reciprocal space vectors [209] of a crystal are determined by

$$\boldsymbol{R}_i \cdot \boldsymbol{G}_j = 2\pi\delta_{ij}, \tag{2.7}$$

where δ_{ij} is a Kronecker delta function. For 2D structures, the reciprocal lattice vectors are given by

$$\boldsymbol{G}_1 = \frac{2\pi\boldsymbol{R}_2 \times \boldsymbol{e}_z}{|\boldsymbol{R}_1 \times \boldsymbol{R}_2|}, \qquad \boldsymbol{G}_2 = \frac{2\pi\boldsymbol{e}_z \times \boldsymbol{R}_2}{|\boldsymbol{R}_1 \times \boldsymbol{R}_2|}. \tag{2.8}$$

Therefore, the reciprocal lattice vectors become shorter with the decreasing twist angle.

In the above description, commensurate moiré graphene multilayers were defined, but the convention does not require information about the origin of the rotation and the relative stacking of the layers. To generate a moiré graphene multilayer, this information is required, with different choices leading to moiré structures with different symmetries. In Fig. 2.2 we display the convention which is used throughout. For layers which are being twisted relative to each other, we initially stack the layers in an AA configuration, and choose an axis of rotation which passes through atoms in both layers and that is perpendicular to the graphene sheets.

This generates structures with D_3 symmetry, but there is an emergent D_6 symmetry at small angles [64].

2.2 Structural relaxations

The moiré pattern causes the stacking order of the graphene multilayer to change throughout the moiré unit cell: there are regions where adjacent layers have AA, AB/BA and saddle point stacking, as shown in Fig. 2.3. These regions have different energies and interlayer spacings [1, 24, 210], which causes the atomic positions of a (suspended) moiré graphene multilayer to change from the pristine coordinates outlined in the previous section. As summarised in the Introduction, these atomic reconstructions lower the energy in the system and only introduce modest strain of approximately 0.1% in the graphene layers [54, 59], and are important for the electronic properties of moiré graphene multilayers.

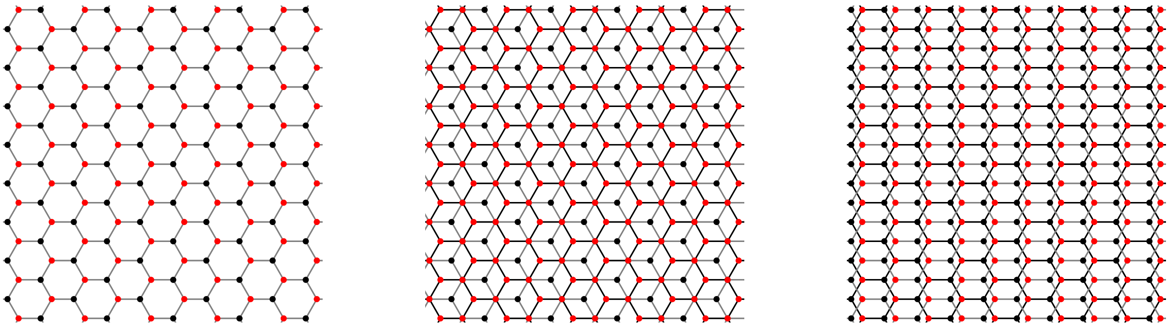

Figure 2.3: Schematic demonstration of bilayer graphene systems with different stacking order: AA (left), AB (middle) and saddle (right). Again, sublattice A is indicated in red and sublattice B in black, with bonds of the top layer being shown in grey and bonds in the bottom layer being shown in black.

To include atomic reconstruction effects of the moiré graphene multilayer, we employ several approaches: (1) - approximate expressions for the z-displacements to mimic relaxations effects. (2) - empirical force fields to obtain the minimum energy structure. Both of these methods were employed here for tBLG (which approach was taken will be stated, in a footnote, each time different results are presented), while for other moiré graphene multilayers only the latter approach was taken.

For tBLG at twist angles down to (approximately) 1°, it was found to a good accuracy [42, 50, 54, 55, 67], the z-displacements of the carbon atoms followed the expression

$$z(\mathbf{r}_{xy}) = d_0 + d_1 \sum_{i=1,2,3} \cos(\mathbf{G}_i \cdot \mathbf{r}_{xy}), \tag{2.9}$$

where $\mathbf{r}_{xy}$ are the (pristine) in-plane $x-y$ coordinates and $\mathbf{G}_i$ are the shortest 3 reciprocal lattice vectors ($\mathbf{G}_3 = \mathbf{G}_1 + \mathbf{G}_2$), and $d_0 = (d_{AA} + 2d_{AB})/3$ and $d_1 = 2(d_{AA} - d_{AB})/9$, with d_{AB} and d_{AA} corresponding to the chosen interlayer spacing in the AB and AA regions, respectively [68]. The exact values of d_{AB} and d_{AA} depend on the twist angle. As shown by Uchida *et al.* [50], the magnitude of the corrugation parameters changes with twist angle according to $\exp\{-0.009\theta^2\}$ [implemented in Eq. (2.9) through $d_{AA} = d_{AB} + (d_{AA} - d_{AB})\exp\{-0.009\theta^2\}$].

For graphene-based systems, there are well known and tested empirical potentials to describe the intralayer and interlayer interactions [54, 55, 67]. For the intralayer potential, we utilised the AIREBO potential [211], which contains three main contributions [212]

$$E^{\mathrm{AIREBO}} = E^{\mathrm{REBO}} + E^{\mathrm{LJ/M}} + E^{\mathrm{TORS}}. \tag{2.10}$$

Here E^{REBO} is the REBO bonding energy contribution between carbon atoms that are separated by less than 2 Å (therefore only nearest neighbours), which is the main chemical bonding contribution to the potential [212]. The $E^{\mathrm{LJ/M}}$ term is either a Lennard-Jones (LJ) or Morse (M) intermolecular potential which contains information about the short-ranged repulsion and attraction between carbon atoms [212]. Finally, E^{TORS} is a torsional component which describes how the energy changes with respect to the rotation of bonds [212]. The AIREBO potential can describe quite well the structures which graphene can form, but to obtain accurate structures with more than one layer an interlayer potential also needs to be included. Here we utilised the Kolmogorov-Crespi (KC) [213] potential which can accurately describe the registry-dependent interlayer interactions between graphene layers.

These potentials are implemented in the LAMMPS software package [214], which was used to relax the structures (using the FIRE minimisation algorithm [215]) of tBLG and other moiré graphene multilayers. A cut-off distance of 2.5 Å was used for the AIREBO-Morse potential, and a cut-off distance of 20 Å was used for the KC potential. The equilibrium set of atomic positions, τ_i, for a moiré graphene multilayer would then be used in the atomistic methods to calculate the electronic structure.

2.3 Density functional theory

Density functional theory (DFT) is a widely used method to investigate the properties of materials [99, 216, 217]. In principle, DFT is an exact formalism, which determines the ground state energy and electron density of a material through solving a set of one-electron Kohn-Sham [218] equations

$$[\hat{T} + \hat{V}_{\text{KS}}] \left|\phi_i\right\rangle = \varepsilon_i \left|\phi_i\right\rangle . \tag{2.11}$$

Here $\hat{T}$, $\hat{V}_{\text{KS}}$, $\left|\phi_i\right\rangle$ and ε_i are the kinetic energy operator, the Kohn-Sham potential, the Kohn-Sham one-electron wavefunctions and the Kohn-Sham energies, respectively. The Kohn-Sham potential, which is the effective potential felt by the "non-interacting" electrons in the presence of all other electrons, is given by

$$\hat{V}_{\text{KS}} = \hat{V}_{\text{ext}} + \hat{V}_{\text{H}} + \hat{V}_{\text{xc}}, \tag{2.12}$$

where $\hat{V}_{\text{ext}}$ is the external potential which contains the information of the atomic nuclei, $\hat{V}_{\text{H}}$ is the Hartree potential and $\hat{V}_{\text{xc}}$ is the exchange-correlation potential. The latter is not exactly known, however, and needs to be approximated. There are many approximations to the exchange-correlation potential, with varying degrees of accuracy and computational expense. In addition, the exact $\hat{V}_{\text{ext}}$ is often approximated as a pseudopotential [99, 216]. This latter approximation is more controllable and accurate, and reduces the computational cost of the calculation [99, 216].

For large systems, such as small twist angle moiré graphene multilayers, the use of accurate electronic structure methods, such as GW [216, 219], is not reasonably accessible. Therefore, performing DFT calculations with the local density approximation or generalised gradient approximation functionals is typically the route to investigate the electronic structure of these materials [217, 220]. Even with these "cheap functionals", the cost of performing a conventional plane-wave electronic structure calculation scales as $\mathcal{O}(N_e^3)$, where N_e is the number of electrons [221]. Thus, even performing a calculation for a relatively large twist angle structure can be extremely computationally expensive. There are, however, electronic structure methods which take advantage of the "nearsightedness of electronic matter" [222, 223], which can permit a linear scaling with the number of electrons (for large systems) [224].

2.3.1 Linear-scaling DFT

ONETEP [222, 224] is linear-scaling DFT code which was employed to efficiently investigate the electronic structure of moiré graphene multilayers with relatively large unit cells (∼3,000 atoms). In ONETEP, $\mathcal{O}(N_e)$ scaling is achieved through the optimisation of a minimal set of non-orthogonal generalised Wannier functions (NGWFs) [222, 224]. These local orbitals are expanded in terms of periodic basis functions, which permits "plane wave accuracy" to be achieved [222, 224]. For detailed reviews of the specifics of ONETEP, the reader is referred to Refs. 222, 224.

For graphene based systems, we utilise 4 NGWFs per carbon atom to calculate the electronic structure of moiré graphene multilayers. The PBE exchange-correlation functional [225] with projector-augmented-wave pseudopotentials [226, 227] was utilised for these calculations with a kinetic energy cut-off of 800 eV. The ensemble-DFT approach was used because of the metallic nature of the studied systems [228, 229]. We perform these calculations using the positions generated from the classically relaxed moiré graphene multilayers described in Section 2.2. With the ONETEP code, we are able to study the electronic band structure [230] of systems with twist angles as low as 2.45° with up to 4 layers.

2.4 Non-interacting atomistic tight-binding

In the tight-binding approximation, it is assumed that the electronic structure of a material can be treated perturbatively to the comprising atomic states [216, 231, 232]. Therefore, the total Hamiltonian, $\hat{H}$, is approximated as the sum of contributions from the isolated atoms, $\hat{H}_{\text{atom}}$, and a perturbative term from the bringing the atoms from isolation into a material, $\Delta\hat{V}_{\text{tb}}$. The time-independent Schrödinger equation to be solved for a crystal is then

$$[\hat{H}_{\mathrm{atom}} + \Delta\hat{V}_{\mathrm{tb}}] \left|\psi_{n\mathbf{k}}\right\rangle \approx \hat{H} \left|\psi_{n\mathbf{k}}\right\rangle = \varepsilon_{n\mathbf{k}} \left|\psi_{n\mathbf{k}}\right\rangle . \tag{2.13}$$

Here $\varepsilon_{n\mathbf{k}}$ and $\left|\psi_{n\mathbf{k}}\right\rangle$ are the eigenvalues and associated Bloch eigenstates, with n corresponding to a band index and $\mathbf{k}$ is the crystal momentum (both of which are good quantum numbers for the atomistic methods employed here). Note we suppress the spin index σ when there is a spin degeneracy for clarity of notation.

The assumption of the electronic structure of a crystal being described as a perturbation from atomic states means that the Bloch eigenstates can be expressed as a linear combination of atomic states [216, 231, 232]. Since the electronic structure of graphene near the Fermi energy can be approximated with only the p_z atomic orbitals of carbon [1], we shall only need to consider one type of orbital in the employed tight-binding method. Therefore, the Bloch states are given by

$$\left|\psi_{n\mathbf{k}}\right\rangle = \sum_{i} c_{n\mathbf{k}i} \left|\chi_{\mathbf{k}i}\right\rangle , \tag{2.14}$$

where $\left|\chi_{\mathbf{k}i}\right\rangle$ and $c_{n\mathbf{k}i}$ are, respectively, the atomic states which are being linearly combined and the associated coefficients which describe the weight of each atomic orbital to the Bloch state, with the index i corresponding to an atom in the moiré unit cell. The atomic states can be expressed as

$$\left|\chi_{\mathbf{k}i}\right\rangle = \frac{1}{\sqrt{N_{\mathrm{k}}}} \sum_{\mathbf{R}} e^{i\mathbf{k}\cdot\mathbf{R}} \left|\phi_z(\mathbf{r} - \boldsymbol{\tau}_i - \mathbf{R})\right\rangle , \tag{2.15}$$

where N_{k}, $\mathbf{R}$, $\phi_z(\mathbf{r})$ and $\boldsymbol{\tau}_i$ are, respectively, the number of unit cells in the crystal, the lattice vectors of the unit cell (defined in Section 2.1), the p_z atomic orbitals of carbon (the expression for which shall be introduced later) and the position of each carbon atom in the unit cell of the moiré material (these are determined from Sections 2.1 and 2.2). Inserting the atomic states into the linear combination yields

$$|\psi_{n\mathbf{k}}\rangle = \frac{1}{\sqrt{N_{\mathrm{k}}}} \sum_i c_{n\mathbf{k}i} e^{i\mathbf{k}\cdot\mathbf{R}} \left|\phi_z(\mathbf{r} - \boldsymbol{\tau}_i - \mathbf{R})\right\rangle . \tag{2.16}$$

This form of the Bloch states have the convenient property of the coefficients being periodic with respect to reciprocal lattice vectors, $c_{n\mathbf{k}i} = c_{n\mathbf{k}+\mathbf{G}i}$.

Having established the Hamiltonian and trial Bloch wavefunction, we insert the trial Bloch wavefunction of Eq. (2.14) into the Hamiltonian of Eq. (2.13) and pre-multiply by $\langle\chi_{\mathbf{k}j}|$. This yields a set of N equations to be solved

$$\sum_i [\langle\chi_{\mathbf{k}j}|\hat{H}|\chi_{\mathbf{k}i}\rangle - \varepsilon_{n\mathbf{k}} \langle\chi_{\mathbf{k}j}|\chi_{\mathbf{k}i}\rangle] c_{n\mathbf{k}i} = 0. \tag{2.17}$$

This is achieved by diagonalising the Hamiltonian in matrix form for each value of $\mathbf{k}$, which yields the eigenvalues and coefficients of the Bloch eigenstates.

The second term in Eq. (2.17) is the overlap of the atomic orbitals, $\langle\chi_{\mathbf{k}j}|\chi_{\mathbf{k}i}\rangle$. Using Eq. (2.15) we have for the overlap

$$\langle\chi_{\mathbf{k}j}|\chi_{\mathbf{k}i}\rangle = \frac{1}{N_{\mathrm{k}}} \sum_{\mathbf{R}\mathbf{R}'} e^{i\mathbf{k}\cdot(\mathbf{R}-\mathbf{R}')} \left\langle\phi_z(\mathbf{r} - \boldsymbol{\tau}_j - \mathbf{R}^{'})|\phi_z(\mathbf{r} - \boldsymbol{\tau}_i - \mathbf{R})\right\rangle . \tag{2.18}$$

Introducing the transformation $\Delta\mathbf{R} = \mathbf{R} - \mathbf{R}'$ and shifting the coordinates with $\mathbf{r}' = \mathbf{r} - \mathbf{R}'$ yields

$$\langle\chi_{\mathbf{k}j}|\chi_{\mathbf{k}i}\rangle = \sum_{\Delta\mathbf{R}} e^{i\mathbf{k}\cdot\Delta\mathbf{R}} \left\langle\phi_z(\mathbf{r}' - \boldsymbol{\tau}_j)|\phi_z(\mathbf{r}' - \boldsymbol{\tau}_i - \Delta\mathbf{R})\right\rangle = \sum_{\Delta\mathbf{R}} e^{i\mathbf{k}\cdot\Delta\mathbf{R}} S_{ji\Delta\mathbf{R}}, \tag{2.19}$$

where $S_{ji\Delta\mathbf{R}}$ is the overlap matrix between orbitals located at j and $i\Delta\mathbf{R}$. Generally, $S_{ji\Delta\mathbf{R}}$ is not a diagonal matrix, but often off-diagonal terms are ignored as the contributions are typically smaller, such that only the diagonal terms ($S_{ji\Delta\mathbf{R}} = I$) are retained in the Hamiltonian.

The first term in Eq. (2.17) is the Hamiltonian matrix elements. Performing a similar analysis, we arrive at

$$\langle\chi_{\mathbf{k}j}|\hat{H}|\chi_{\mathbf{k}i}\rangle = \sum_{\Delta\mathbf{R}} e^{i\mathbf{k}\cdot\Delta\mathbf{R}} [\delta_{ij}\delta_{\Delta\mathbf{R},0}\varepsilon_i + t(\boldsymbol{\tau}_i - \boldsymbol{\tau}_j - \Delta\mathbf{R})\delta_{\boldsymbol{\tau}_i,\boldsymbol{\tau}_j+\Delta\mathbf{R}}]. \tag{2.20}$$

Here ε_i is the on-site energy of atom i, and $t(\mathbf{r})$ is the tunnelling matrix element between atom

i and j, which is often referred to as the hopping of electrons between atoms. In the two-centre tight-binding model, the hopping parameters only depend on the coordinates of the two carbon atoms. In the following section, the details of these hopping parameters are given in full.

2.4.1 Slater-Koster hopping parameters

The hopping parameters $t(\mathbf{r})$ between atoms i and j are determined using the expressions derived by Slater and Koster based on the two-centre approximation [233]. The Slater-Koster equations determine how the hopping parameters change as a function of separation and orientation of the two orbitals. The expression for the hopping between two p_z orbitals is given by

$$t(\mathbf{r}) = t_\pi e^{q_\pi(1-|\mathbf{r}|/a)} F(\mathbf{r}) \sin^2\varphi + t_\sigma e^{q_\sigma(1-|\mathbf{r}|/d)} F(\mathbf{r}) \cos^2\varphi. \tag{2.21}$$

Here $t_{\pi/\sigma}$, $q_{\pi/\sigma}$, a, d, φ and $F(\mathbf{r})$ are, respectively, the magnitudes of the π/σ hopping parameters, the decay lengths of the π/σ hopping parameters, the pristine carbon bond length ($a = a_0/\sqrt{3}$), interlayer spacing, the angle of inclination between the two orbitals and an additional function for the truncation of hopping parameters [37].

The two structural parameters, a and d are typically based on the lattice constant of graphene and the smallest interlayer spacing between adjacent graphene layers, respectively. Given these parameters, the remaining parameters ($t_{\pi/\sigma}$ and $q_{\pi/\sigma}$) are chosen to best fit a DFT calculation of graphene, AB bilayer graphene and AA bilayer graphene [32, 37], or alternatively chosen to fit the electronic structure of a moiré graphene multilayer of interest [163]. In the former case, a graphene calculation is used to determine t_π, since there are no σ hoppings for flat graphene [1]. The π hopping parameter is chosen to obtain the correct Fermi velocity of graphene, $v_\mathrm{F} = 3\hbar t_\pi a/2$, assuming that the intralayer decay parameter (of flat graphene) is such that the second nearest neighbour hopping is $0.1t_\pi$. Based on this, assuming the same decay $q_\pi/a = q_\sigma/d$, the AB and AA bilayer calculations are used to determine the σ hopping parameter.

Here we mainly employ the parameters of Trambly de Laissardière *et al.* [32, 37], where $t_\pi = -2.7$ eV and $t_\sigma = 0.48$ eV. In each calculation, the parameters of the model will be stated.

We further assume that all of the p$_z$-orbitals are aligned with the z-axis, ignoring any tilting effects from atomic reconstruction (as the effect was shown to be negligible [64]). We take $F(\mathbf{r})$ to be a Heaviside step function with a cut-off of $3-10$ Å, which is taken for numerical efficiency as the hopping parameters after third nearest neighbour become insignificantly small [64].

2.4.2 On-site energies

The other contribution to the tight-binding Hamiltonian is the on-site energy of each p$_z$ orbital, ε_i. The total energy in the tight-binding formalism is arbitrary, which means an on-site energy contribution (to all p$_z$ orbitals) is chosen such that the Fermi energy is at zero energy [32, 37]. For moiré graphene multilayers studied here, there are three other contributions to the on-site energy in the atomistic model: (1) - Electrostatic energy contributions from perpendicular electric fields. (2) - Intrinsic differences in layer environments (for systems with more than two layers) which are included through layer-dependent on-site energies [163, 164]. (3) - Electron interactions, such as Hartree interactions [136]. The former (1) is included through the electrostatic potential energy an electron feels in the field through $\propto E \cdot z$. Since the variations of the displacements of the z positions within a layer are small in comparison to the interlayer separation, electric fields are often included through a layer-dependent on-site potential. The layer-dependent on-site energies of (2) were reviewed in the Introduction. The inclusion of electron-electron interactions (3) is discussed in Section 2.7.1.

2.4.3 Hamiltonian in second quantisation

A convenient and transparent formulation of the tight-binding approximation can be established using second quantisation [234], where the Hamiltonian reads

$$\hat{\mathcal{H}}_0 = \sum_i \varepsilon_i \hat{c}_i^\dagger \hat{c}_i + \sum_{\mathbf{R}\mathbf{R}'} \sum_{ij} t(\boldsymbol{\tau}_i + \mathbf{R}' - \boldsymbol{\tau}_j - \mathbf{R}) \hat{c}_{\mathbf{R}j}^\dagger \hat{c}_{\mathbf{R}'i}, \tag{2.22}$$

where $\hat{c}_i^\dagger$ and $\hat{c}_i$ are, respectively, the electron creation and annihilation operators associated with the p$_z$-orbital on atom i. The Fourier transformation of the field operators to/from momentum space are given by

$$\hat{c}_{\mathbf{k}i} = \frac{1}{\sqrt{N_\mathrm{k}}} \sum_{\mathbf{R}} e^{-i\mathbf{R}\cdot\mathbf{k}} \hat{c}_{\mathbf{R}i} \qquad \hat{c}_{\mathbf{R}i} = \frac{1}{\sqrt{N_\mathrm{k}}} \sum_{\mathbf{k}} e^{i\mathbf{R}\cdot\mathbf{k}} \hat{c}_{\mathbf{k}i}. \tag{2.23}$$

The non-interacting Hamiltonian in reciprocal space is then

$$\hat{\mathcal{H}}_0 = \sum_i \varepsilon_i \hat{c}_i^\dagger \hat{c}_i + \sum_{\mathbf{k}} \sum_{\Delta\mathbf{R}} \sum_{ij} t(\boldsymbol{\tau}_i - \boldsymbol{\tau}_j - \Delta\mathbf{R}) e^{-i\Delta\mathbf{R}\cdot\mathbf{k}} \hat{c}_{\mathbf{k}j}^\dagger \hat{c}_{\mathbf{k}i}. \tag{2.24}$$

For crystals, this is the form of the Hamiltonian that is commonly used.

2.4.4 Coulomb interaction of p_z orbitals

The pseudo-hydrogenic p_z orbital which is utilised for the atomistic tight-binding model of moiré graphene multilayers is given by

$$\phi_z(\mathbf{r}) = \phi_z(r, \tilde{\theta}) = \frac{\cos\tilde{\theta}}{4\sqrt{2\pi}\tilde{a}_\mathrm{B}^{3/2}} \frac{r}{\tilde{a}_\mathrm{B}} e^{-r/2\tilde{a}_\mathrm{B}}, \tag{2.25}$$

where $\tilde{\theta}$ is the polar angle in this expression and $\tilde{a}_\mathrm{B}$ is the effective Bohr radius of the pseudo-hydrogenic p_z orbital (related by $\tilde{a}_\mathrm{B} = a_\mathrm{B}/Z_\mathrm{eff}$ to the Bohr radius, a_B, and the effective charge of the nucleus, $Z_\mathrm{eff} \approx 3.18$ [235]). This pseudo-hydrogenic function was used to derive the Slater-Koster hopping expressions [233]. It is also required when evaluating a number of response functions or when considering interactions. In this section, expressions which rely on evaluating an integral of the p_z orbital shall be derived, such that it is not repeated.

A common object which needs to be evaluated is the Coulomb scattering element of the p_z orbitals, as given by

$$\langle \phi_z(\mathbf{r}) | e^{\pm i\mathbf{q}\cdot\mathbf{r}} | \phi_z(\mathbf{r}) \rangle, \tag{2.26}$$

where $\mathbf{q}$ is a crystal momentum. The result [235] is well known to be

$$\langle \phi_z(\mathbf{r}) | e^{\pm i\mathbf{q}\cdot\mathbf{r}} | \phi_z(\mathbf{r}) \rangle = I(\mathbf{q}) = \Big[1 + (|\mathbf{q}|\tilde{a}_\mathrm{B})^2\Big]^{-3}. \tag{2.27}$$

Since the effective Bohr radius is of the order of 3× smaller than the Bohr radius, and the moiré unit cells have small Brillouin zones because of the large real space structure, it is often sufficient to take $\langle \phi_z(\mathbf{r}) | e^{\pm i\mathbf{q}\cdot\mathbf{r}} | \phi_z(\mathbf{r}) \rangle = 1$.

The on-site Hubbard parameter for p$_z$ orbitals is given by

$$U = \langle \phi_z(\mathbf{r})\phi_z(\mathbf{r}') | W(\mathbf{r}, \mathbf{r}') | \phi_z(\mathbf{r}')\phi_z(\mathbf{r}) \rangle \,. \tag{2.28}$$

Let us assume $W(\mathbf{r}, \mathbf{r}') = V(\mathbf{r} - \mathbf{r}')$, where we assume a bare potential, and introduce the Fourier transform of the Coulomb potential

$$U = \frac{1}{(2\pi)^3} \int d\mathbf{q} V(\mathbf{q}) \langle \phi_z(\mathbf{r}') | e^{-i\mathbf{q}\cdot\mathbf{r}'} | \phi_z(\mathbf{r}') \rangle \langle \phi_z(\mathbf{r}) | e^{i\mathbf{q}\cdot\mathbf{r}} | \phi_z(\mathbf{r}) \rangle \,. \tag{2.29}$$

Using Eq. (2.27), we arrive at

$$U = \frac{1}{(2\pi)^3} \int d\mathbf{q} V(\mathbf{q}) I(\mathbf{q})^2. \tag{2.30}$$

Introducing the Coulomb potential explicitly, and evaluating the angular dependence, we obtain

$$U = \frac{1}{2\pi^2} \frac{e^2}{\epsilon_0} \int_0^\infty dq I(q)^2 = \frac{1}{2\pi} \frac{e^2}{\epsilon_0 \tilde{a}_{\mathrm{B}}} \frac{63}{512} \approx 21 \text{ eV}. \tag{2.31}$$

This is approximately equal to what is reported in literature for a bare Coulomb interaction (17 eV) of the p$_z$ orbitals of graphene [236].

2.4.5 Valley polarisation

In the tight-binding formalism, unlike the continuum model, the valley index is not an explicit quantum number. However, in the tight-binding formalism, the valley polarisation can be computed from the valley operator introduced by Lado and co-workers [192, 205, 237]

$$\hat{\mathcal{V}} = \frac{i}{3\sqrt{3}} \sum_{\langle\langle ij \rangle\rangle} \eta_{ij} \sigma_z^{ij} \hat{c}_i^\dagger \hat{c}_j. \tag{2.32}$$

Here $\langle\langle ij \rangle\rangle$ is a summation over second nearest neighbours, $\eta_{ij} = \pm$ is a sign associated with clock-wise or anti-clockwise hopping between second nearest neighbours, and $\sigma_z^{ij} = \pm$ is the Pauli matrix associated with the sublattices of graphene (sign difference between A and B). To clearly demonstrate the structure of $\eta_{ij}\sigma_z^{ij}$, Fig. 2.4 displays the sign convention [192, 205, 237].

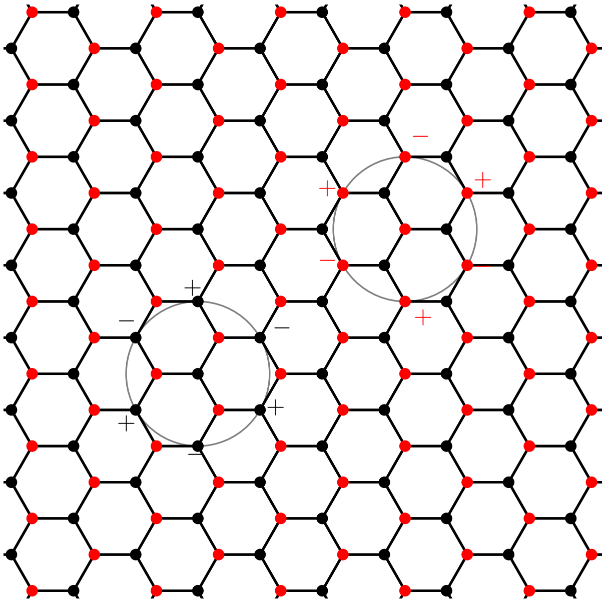

Figure 2.4: Schematic demonstration of the sign convention of $\eta_{ij}\sigma_z^{ij}$ for each sublattice.

Taking the expectation value of the valley operator yields a value of ±1 for perfectly polarised states, but a value closer to zero means there is some valley mixing.

For a non-degenerate state, the valley index can be calculated through

$$\langle\psi_{n\mathbf{k}}|\hat{\mathcal{V}}|\psi_{n\mathbf{k}}\rangle = \frac{i}{3\sqrt{3}} \sum_{\Delta\mathbf{R}} \sum_{\langle\langle ij\rangle\rangle} e^{i\Delta\mathbf{R}\cdot\mathbf{k}} \eta_{ij}\sigma_z^{ij} c^*_{n\mathbf{k}i} c_{n\mathbf{k}j} . \tag{2.33}$$

In the case of degenerate states, a valley matrix must be constructed

$$\langle\psi_{n\mathbf{k}}|\hat{\mathcal{V}}|\psi_{m\mathbf{k}}\rangle = \langle\mathcal{V}\rangle^{\mathbf{k}}_{nm} , \tag{2.34}$$

and diagonalised for each **k**-point to obtain the valley polarisation. The unitary transformation which diagonalises this matrix can be used to obtain the valley polarised states.

2.5 Wannier functions

Bloch states are the natural form of wavefunctions in periodic systems, since they are the eigenstates of the Hamiltonian which commutes with the lattice translation operator [216, 231].

These extended wavefunctions are characterised by a (unit cell) periodic function multiplied by a crystal periodic plane wave

$$|\psi_{n\mathbf{k}}\rangle = e^{i\mathbf{k}\cdot\mathbf{r}} |u_{n\mathbf{k}}\rangle \,. \tag{2.35}$$

There are, however, different representations of the states, such as the Wannier functions [70, 238, 239]. In the Wannier representation (for an isolated band), the Fourier transform of the Bloch eigenstates (for a given band index n) is taken

$$|w_{n\mathbf{R}}\rangle = \frac{1}{\sqrt{N_{\mathrm{k}}}} \sum_{\mathbf{k}} e^{-i\mathbf{k}\cdot\mathbf{R}} |\psi_{n\mathbf{k}}\rangle \,, \tag{2.36}$$

which generates a localised Wannier function, $|w_{n\mathbf{R}}\rangle$, in unit cell $\mathbf{R}$ of the crystal*. The Wannier function is localised in real space, but it is no longer an eigenstate of the Hamiltonian [70]. Despite this, since Wannier functions are unitary transformations of the Bloch states, they can still provide a valid description of the electronic structure.

There are, however, issues with the generation of Wannier functions, as they are non-unique functions [70]. The issue of non-uniqueness arises from the "gauge freedom" of Bloch states

$$|\tilde{\psi}_{n\mathbf{k}}\rangle = e^{i\phi_n(\mathbf{k})} |\psi_{n\mathbf{k}}\rangle \,, \tag{2.37}$$

where $\phi_n(\mathbf{k})$ is a real and periodic function in $\mathbf{k}$-space $[\phi_n(\mathbf{k}+\mathbf{G}) = \phi_n(\mathbf{k}) + 2\pi]$ [70]. While this complex number changes the exact values of the Bloch wavefunctions, it does not affect the physical observables of the system, and therefore, $|\tilde{\psi}_{n\mathbf{k}}\rangle$ and $|\psi_{n\mathbf{k}}\rangle$ are essentially equivalent [70]. However, changing the gauge of the Bloch states can result in completely different Wannier functions [70]. In particular, to generate localised Wannier functions, one needs the Bloch states to have a "smooth gauge" in $\mathbf{k}$-space, since the Fourier transform of a smooth function in $\mathbf{k}$-space is well localised in real-space [70]. Therefore, the extent of localisation of the Wannier functions is highly dependent on how smooth the gauge is [70].

For a manifold of J bands, which are isolated in energy from all other bands, where internal band crossings and degeneracies can occur, the issue with the gauge invariance remains [70].

---

[*] Note that there are periodic images of these Wannier functions, the separation of which is determined by the number of $\mathbf{k}$-points in the Fourier transform

However, since traces of the manifold are invariant with respect to unitary transformations [70], one can generalise the "gauge transformation" to

$$|\tilde{\psi}_{n\mathbf{k}}\rangle = \sum_{m=1}^{J} U_{mn}^{(\mathbf{k})} |\psi_{m\mathbf{k}}\rangle \,, \tag{2.38}$$

where $U_{mn}^{(\mathbf{k})}$ is a unitary matrix for each $\mathbf{k}$-point (that is also periodic in $\mathbf{k}$-space). Note that these gauge transformed Bloch states are also not generally eigenstates of the Hamiltonian, with n in $|\tilde{\psi}_{n\mathbf{k}}\rangle$ no longer explicitly corresponding to a band index. To obtain the Wannier functions of the manifold of J bands, the following unitary transformation is made

$$|w_{n\mathbf{R}}\rangle = \frac{1}{\sqrt{N_{\mathrm{k}}}} \sum_{\mathbf{k}} \sum_{m} e^{-i\mathbf{k}\mathbf{R}} U_{mn}^{(\mathbf{k})} |\psi_{m\mathbf{k}}\rangle \,. \tag{2.39}$$

Typically, a smooth gauge for the Bloch states can be generated through projection of these states onto an initial guess for what the Wannier function should be, $|g_n\rangle$ [70]. This projection is given by

$$|\phi_{n\mathbf{k}}\rangle = \sum_{m=1}^{J} |\psi_{m\mathbf{k}}\rangle \langle\psi_{m\mathbf{k}}|g_n\rangle \,, \tag{2.40}$$

where the following matrix is introduced

$$A_{mn}^{\mathbf{k}} = \langle\psi_{m\mathbf{k}}|g_n\rangle \,. \tag{2.41}$$

As shall be discussed later, this is one of the key objects which needs to be specified for the generation of Wannier functions. The Löwdin-orthonormalised Bloch-like states

$$|\tilde{\psi}_{n\mathbf{k}}\rangle = \sum_{m=1}^{J} |\phi_{m\mathbf{k}}\rangle \, (S_{\mathbf{k}}^{-1/2})_{mn} \tag{2.42}$$

can be generated from the overlap matrix

$$(S_{\mathbf{k}})_{mn} = (A^{\mathbf{k}\dagger} A^{\mathbf{k}})_{mn}. \tag{2.43}$$

The states of Eq. (2.42), which are unitary transformed from the original Bloch states, now have a smooth gauge, and well localised Wannier functions can be generated from them [70].

The Wannier functions generated from Eq. (2.42) would, however, still depend on the initial guess that was used to generate them [70]. To fix this issue, the $U_{mn}^{(\mathbf{k})}$ can be optimised subject to some criterion. One of the most commonly used criterions is to maximally localise the Wannier functions [70, 239]. The spread, Ω, of the Wannier functions is defined by

$$\Omega = \sum_n \Big[\langle w_{n\mathbf{0}} | r^2 | w_{n\mathbf{0}} \rangle - | \langle w_{n\mathbf{0}} | \mathbf{r} | w_{n\mathbf{0}} \rangle |^2 \Big], \tag{2.44}$$

which is minimised with respect to $U_{mn}^{(\mathbf{k})}$ to generate the maximally localised Wannier functions [70]. The spread of the Wannier functions can be decomposed into two parts

$$\Omega = \Omega_I + \tilde{\Omega}. \tag{2.45}$$

Here Ω_I is the gauge invariant part

$$\Omega_I = \sum_n \Big[\langle w_{n\mathbf{0}} | r^2 | w_{n\mathbf{0}} \rangle - \sum_{m\mathbf{R}} | \langle w_{m\mathbf{R}} | \mathbf{r} | w_{n\mathbf{0}} \rangle |^2 \Big], \tag{2.46}$$

and the gauge dependent part is given by

$$\tilde{\Omega} = \sum_n \sum_{m\mathbf{R} \neq n\mathbf{0}} | \langle w_{m\mathbf{R}} | \mathbf{r} | w_{n\mathbf{0}} \rangle |^2. \tag{2.47}$$

It is solely the minimisation of the this gauge dependent spread which determines the maximal localisation of the Wannier functions [70].

The definition of the position operator takes the form

$$\langle w_{m\mathbf{R}} | \mathbf{r} | w_{n\mathbf{0}} \rangle = i \frac{V}{(2\pi)^3} \int d\mathbf{k} e^{i\mathbf{k}\cdot\mathbf{R}} \langle u_{m\mathbf{k}} | \nabla_{\mathbf{k}} | u_{n\mathbf{k}} \rangle \,. \tag{2.48}$$

To compute this, one discretises the derivatives on the finite grid of **k**-points and uses

$$\nabla | u_{n\mathbf{k}} \rangle \approx \sum_{\mathbf{q}} w_q \mathbf{q} [| u_{n\mathbf{k}+\mathbf{q}} \rangle - | u_{n\mathbf{k}} \rangle], \tag{2.49}$$

where $\mathbf{q}$ is a vector connecting two points and w_q is a geometric weighting factor [70]. Therefore, the only other essential piece of information is the overlap of the unit cell periodic parts of the Bloch states

$$M_{mn}^{\mathbf{k},\mathbf{q}} = \langle u_{m\mathbf{k}} | u_{n\mathbf{k}+\mathbf{q}} \rangle \,. \tag{2.50}$$

Provided $M_{mn}^{\mathbf{k},\mathbf{q}}$ and $A_{mn}^{\mathbf{k}}$ are specified, the generation of maximally localised Wannier functions can be achieved as a post-processing step using the Wannier90 [238] code (for more information of the minimisation algorithm see Refs. 70, 239). Therefore, these matrices can be generated from the atomistic tight-binding formalism to generate Wannier functions of isolated flat bands of moiré graphene multilayers.

2.5.1 Wannier functions from atomistic tight-binding

In the employed tight-binding formalism, as summarised in Section 2.4, the unit-cell periodic function can be expressed as

$$|u_{n\mathbf{k}}\rangle = \frac{1}{\sqrt{N_\mathrm{k}}} \sum_i \sum_{\mathbf{R}} c_{n\mathbf{k}i} e^{i\mathbf{k}\cdot(\mathbf{R}-\mathbf{r})} \, |\phi_z(\mathbf{r} - \boldsymbol{\tau}_i - \mathbf{R})\rangle \,. \tag{2.51}$$

The matrix elements of $M_{mn}^{\mathbf{k},\mathbf{q}}$ can be calculated from inserting the above expression into Eq. (2.50) to give

$$\begin{aligned} \langle u_{m\mathbf{k}} | u_{n\mathbf{k}+\mathbf{q}} \rangle = \frac{1}{N_\mathrm{k}} \sum_{ij} \sum_{\mathbf{R}\mathbf{R}'} c_{m\mathbf{k}i}^{*} c_{n\mathbf{k}+\mathbf{q}j} e^{-i\mathbf{k}\cdot\mathbf{R}} e^{i(\mathbf{k}+\mathbf{q})\cdot\mathbf{R}'} \\ \times \langle \phi_z(\mathbf{r} - \boldsymbol{\tau}_i - \mathbf{R}) | e^{-i\mathbf{q}\cdot\mathbf{r}} | \phi_z(\mathbf{r} - \boldsymbol{\tau}_j - \mathbf{R}') \rangle \,. \end{aligned} \tag{2.52}$$

Shifting coordinate systems with the transformation $\mathbf{r}' = \mathbf{r} - \mathbf{R}$, we have

$$\langle u_{m\mathbf{k}} | u_{n\mathbf{k}+\mathbf{q}} \rangle = \sum_{ij} \sum_{\mathbf{R}''} c_{m\mathbf{k}i}^{*} c_{n\mathbf{k}+\mathbf{q}j} e^{i(\mathbf{k}+\mathbf{q})\cdot\mathbf{R}''} \, \langle \phi_z^{*}(\mathbf{r}' - \boldsymbol{\tau}_i) | e^{-i\mathbf{q}\cdot\mathbf{r}'} | \phi_z(\mathbf{r}' - \boldsymbol{\tau}_j - \mathbf{R}'') \rangle \,, \tag{2.53}$$

where $\mathbf{R}'' = \mathbf{R}' - \mathbf{R}$. Assuming contributions only come from the overlap of the same orbital yields

$$\langle u_{m\mathbf{k}}|u_{n\mathbf{k}+\mathbf{q}}\rangle = \sum_i c^*_{m\mathbf{k}i} c_{n\mathbf{k}+\mathbf{q}i} e^{i\mathbf{q}\cdot\boldsymbol{\tau}_i} I(\mathbf{q}), \tag{2.54}$$

where $I(\mathbf{q})$ was defined in Eq. (2.27). Note that the $e^{i\mathbf{q}\cdot\boldsymbol{\tau}_i}$ phase factor comes from making the integral independent of the position of each atom. Since the tight-binding coefficients are periodic in **k**-space, which Brillouin zone $\mathbf{k}+\mathbf{q}$ resides in is not a concern.

To calculate $A^{\mathbf{k}}_{mn}$, an initial guess for the Wannier function is required. Here we outline how the matrix $A^{\mathbf{k}}_{mn}$ is constructed based on two types of initial guesses.

The first type of initial guess is based on fixing the gauge of the Bloch states to be real and positive where the Wannier function should be localised [68]. Upon Fourier transforming those Bloch states, a well localised Wannier function should be generated, since the Bloch states constructively interfere at this location. This initial guess (for a Wannier function at $\mathbf{R}=0$) is given by

$$|g_n\rangle = \frac{1}{\sqrt{N_\mathrm{k}}} \sum_{\mathbf{k}'} U^{\mathbf{k}'}_{np} |\psi_{p\mathbf{k}'}\rangle . \tag{2.55}$$

The overlap element with the Bloch states can then be readily calculated

$$\langle \psi_{m\mathbf{k}}|g_n\rangle = \frac{1}{\sqrt{N_\mathrm{k}}} \sum_{\mathbf{k}'} U^{\mathbf{k}'}_{np} \langle \psi_{m\mathbf{k}}|\psi_{p\mathbf{k}'}\rangle . \tag{2.56}$$

From the orthonormality of Bloch states, we arrive at

$$\langle \psi_{m\mathbf{k}}|g_n\rangle = U^{\mathbf{k}}_{nm}. \tag{2.57}$$

Another approach is to use the Γ-point Bloch state and a real-space cut-off to localise the Bloch state [73]. The guess for the Wannier function is then given by

$$|g_n\rangle = \sum_{n'} f(\mathbf{r}-\mathbf{r}_i) |\psi_{n'\Gamma}\rangle , \tag{2.58}$$

where $f(\mathbf{r}-\mathbf{r}_i)$ is a Gaussian function centred at $\mathbf{r}_i$. The task now is to calculate the $A^{\mathbf{k}}_{mn}$ matrix

$$\langle \psi_{m\mathbf{k}} | g_n \rangle = \sum_{n'} \langle \psi_{m\mathbf{k}} | f(\mathbf{r} - \mathbf{r}_i) | \psi_{n'\Gamma} \rangle \, . \tag{2.59}$$

Introducing the Bloch states, we arrive at

$$\langle \psi_{m\mathbf{k}} | g_n \rangle = \frac{1}{N_\mathrm{k}} \sum_{n'} \sum_{\mathbf{R}\mathbf{R}'} \sum_{ij} c^*_{m\mathbf{k}i} c_{n'\Gamma j} e^{-i\mathbf{k}\cdot\mathbf{R}} \langle \phi_z(\mathbf{r} - \boldsymbol{\tau}_i - \mathbf{R}) | f(\mathbf{r} - \mathbf{r}_i) | \phi_z(\mathbf{r} - \boldsymbol{\tau}_j - \mathbf{R}') \rangle \, . \tag{2.60}$$

Furthermore, assuming that the only non-vanishing contributions come from the same p_z orbital, and that the Gaussian function is slowly varying (on the scale of the p_z orbital - since the decay length is taken to be of the order of $|\mathbf{R}|$ this is a reasonable approximation) such that it can be brought outside of the integral. After evaluating these assumptions, we have

$$\langle \psi_{m\mathbf{k}} | g_n \rangle = \frac{1}{N_\mathrm{k}} \sum_{n'} \sum_{\mathbf{R}} \sum_{i} c^*_{m\mathbf{k}i} c_{n'\Gamma i} e^{-i\mathbf{k}\cdot\mathbf{R}} f(\boldsymbol{\tau}_i + \mathbf{R} - \mathbf{r}_i). \tag{2.61}$$

2.5.2 Wannier function centres

To construct the Wannier functions for a manifold of J bands, the final key piece of information is the centres of the Wannier functions. Having the centres of the Wannier functions in the correct position is key because, if they are not, the Wannier functions might not be a faithful representation of the electronic band structure [68, 71–73]. Moreover, the Wannier functions which are (the most) maximally localised might not actually occur in the positions which are required to reproduce the electronic structure. This has motivated the development of methods where the symmetry, and therefore centre, of the Wannier functions can be enforced [76], and a selective localisation method where the centres of some Wannier functions are constrained [240]. These constrained minimisation procedures ensure a faithful representation of the electronic structure at the cost of increasing the spread of the Wannier functions (slightly).

Both methods are implemented in Wannier90 v3.0 [238]. The symmetry adapted Wannier functions requires the specification of an additional matrix for how the Bloch states of the band manifold transform under the symmetry representations of the point group [76]. This method was not employed here. The selective localisation of Wannier functions with constrained centres was employed here instead [240]. It has been found that by constraining the centre of a Wannier function to a point which has a certain point group symmetry produces a Wannier function which transforms as an irreducible representation of that point group [240]. Therefore, Wannier functions with the correct symmetry can also be generated with this selective localisation method by only specifying the centre of the Wannier functions. Note that this comes at the cost of only being able to generate a sub-set of the Wannier functions for a manifold. For example, in a four band system only two Wannier functions can be generated if their centres are constrained. Further details of this method see Ref. 240.

2.5.3 Wannier functions of tBLG

For tBLG, the Wannier function centres were found to reside on the AB/BA sites of the moiré unit cell [68, 71–73]. Therefore, two Wannier functions (of the total of four) could be generated with the selective localisation procedure. Both methods for generating initial guesses were utilised [68, 73]. A 30×30 set of **k**-points were utilised for the generation of the Wannier functions.

2.6 Screened interactions

To investigate the interacting properties of a material, it is important to know the screened Coulomb potential between the electrons of interest [216]. Screening can arise intrinsically from the material, and in moiré graphene multilayers the screened interaction between different layers, i.e. interlayer compared to intralayer, could be important. Moreover, when developing a downfolded Hamiltonian, the electrons should interact with each other accounting for degrees of freedom that are not included in the downfolded Hamiltonian [236, 241–243]. Screening can also arise from external sources, such as the supporting dielectric substrate [244] or proximity to metallic gates [245]. Methods to determine screening based on these sources shall be outlined in this section.

2.6.1 Internal screening

We are interested in the static internal screening of moiré graphene multilayers. Since the screening of graphene is known to be relatively isotropic [235, 246], we shall mainly employ the convention for isotropic systems and note how to investigate anisotropic screening could be investigated. These moiré materials comprise of at least two layers of graphene, which means that these materials can have non-vanishing thicknesses. Therefore, we shall outline the theory for screening which accounts for the finite width of graphene and the different layers in the moiré material, and investigate if these terms are needed [247–251].

The extended-zone scheme [99] shall be utilised and local field effects neglected under the assumption that the polarizability only depends on $\mathbf{r} - \mathbf{r}'$. Hence, the dielectric response is a function of $\mathbf{q} + \mathbf{G}$ rather than a matrix of $\mathbf{G}$ and $\mathbf{G}'$ as a function of $\mathbf{q}$, where $\mathbf{q}$ and $\mathbf{G}$ are the wave vector in the first Brillouin zone and reciprocal lattice vector, respectively [252]. The screened interaction in Fourier space between electrons in layers l and l' in the random phase approximation (RPA) [247–251] is then given by

$$W_{ll'}(\mathbf{q} + \mathbf{G}) = \epsilon_{ll'}(\mathbf{q} + \mathbf{G})^{-1} v_{ll'}(\mathbf{q} + \mathbf{G}), \tag{2.62}$$

where $\epsilon_{ll'}(\mathbf{q} + \mathbf{G})$ is the static isotropic dielectric matrix which describes screening between layers, and $v_{ll'}(\mathbf{q} + \mathbf{G})$ is the 2D Fourier transform of bare Coulomb interaction between layers l and l'. The static dielectric function which describes screening between layers l and l' for an isotropic moiré graphene multilayer is

$$\epsilon_{ll'}(\mathbf{q} + \mathbf{G}) = \epsilon_0 \delta_{ll'} - \sum_m v_{lm}(\mathbf{q} + \mathbf{G}) \Pi^0_{ml'}(\mathbf{q} + \mathbf{G}). \tag{2.63}$$

Here ϵ_0 is the permittivity of free space and $\Pi^0_{ml'}(\mathbf{q}+\mathbf{G})$ is the independent particle polarizability from layers m and l' [247–251]. The 2D Coulomb potential, taking into account the finite width of graphene, is

$$v_{lm}(\mathbf{q} + \mathbf{G}) = \frac{e^2}{2\epsilon_0 |\mathbf{q} + \mathbf{G}|} e^{-|\mathbf{q}||z_m - z_l|} F_{lm}(\mathbf{q} + \mathbf{G}). \tag{2.64}$$

Interactions between electrons in different sheets is account for by the exponential term, where

$|z_m - z_l|$ is the distance between layers of the moiré graphene multilayer [235, 250]. Here $F_{lm}(\mathbf{q}+\mathbf{G})$ is a form factor that takes into account the finite width of the graphene sheets [250].

The independent particle polarizability of Bloch states, also known as the Alder-Wiser equation [216, 252], which can be derived from time-independent perturbation theory, is given by

$$\Pi^0_{ll'}(\mathbf{q}+\mathbf{G}) = \frac{2}{V}\sum_{\mathbf{k}}\sum_{nn'} \frac{f(\varepsilon_{n\mathbf{k}}) - f(\varepsilon_{n'\mathbf{k}+\mathbf{q}})}{\varepsilon_{n\mathbf{k}} - \varepsilon_{n'\mathbf{k}+\mathbf{q}}} \langle \psi_{n\mathbf{k}l} | e^{-i(\mathbf{q}+\mathbf{G})\mathbf{r}} | \psi_{n'\mathbf{k}+\mathbf{q}l} \rangle \\ \times \langle \psi_{n'\mathbf{k}+\mathbf{q}l'} | e^{i(\mathbf{q}+\mathbf{G})\mathbf{r}'} | \psi_{n\mathbf{k}l'} \rangle \,. \quad (2.65)$$

The summation occurs over all possible transitions between n and n', which have Fermi occupations of $f(\varepsilon_n)$ and $f(\varepsilon_{n'})$, respectively. Here, V is the crystal area, which is related to the number of $\mathbf{k}$-points in the summation over the first Brillouin zone; the summation over spin has been explicitly performed which yields the factor of 2.

Further simplifications can be made to the study of screening in moiré graphene multilayers. There is a general expression for $F(\mathbf{q}+\mathbf{G})$ [250], but typically this is a small effect and it can be approximated by 1 in the first instance. Moreover, in moiré graphene multilayers where there are not large separations between layers and the twist angle is sufficiently small, such that only small values of $\mathbf{q}$ are of interest, another reasonable approximation is to take $e^{-|\mathbf{q}||z_m - z_l|} \approx 1$ [253]. This causes the formalism to reduce down from a matrix form to a function, which treats the moiré graphene multilayer as a 2D material without different layers. In this limit, the screened interaction is given by

$$W(\mathbf{q}+\mathbf{G}) = \frac{v(\mathbf{q}+\mathbf{G})}{\epsilon(\mathbf{q}+\mathbf{G})}, \quad (2.66)$$

where the dielectric function is given by

$$\epsilon(\mathbf{q}+\mathbf{G}) = \epsilon_0 - v(\mathbf{q}+\mathbf{G})\Pi^0(\mathbf{q}+\mathbf{G}). \quad (2.67)$$

Moreover, the limit of zero temperature can be taken, which permits the summation over n

and n' to be simplified to a summation over all occupied valence states (v) and unoccupied conduction states (c). In this limit, the polarizability is given by

$$\Pi^0(\mathbf{q}+\mathbf{G}) = \frac{4}{V}\sum_{\mathbf{k}}\sum_{cv}\frac{|\langle\psi_{c\mathbf{k}+\mathbf{q}}|e^{i(\mathbf{q}+\mathbf{G})\mathbf{r}'}|\psi_{v\mathbf{k}}\rangle|^2}{\varepsilon_{v\mathbf{k}}-\varepsilon_{c\mathbf{k}+\mathbf{q}}}. \tag{2.68}$$

Hence, a scattering element needs to be determined in the atomistic tight-binding model. A similar derivation was performed in Section 2.5, and therefore, it shall not be repeated. The employed result is

$$\langle\psi_{c\mathbf{k}+\mathbf{q}}|e^{i(\mathbf{q}+\mathbf{G})\mathbf{r}}|\psi_{v\mathbf{k}}\rangle = \sum_i c^*_{c\mathbf{k}+\mathbf{q}i}c_{v\mathbf{k}i}e^{i(\mathbf{q}+\mathbf{G})\cdot\boldsymbol{\tau}_i}I(\mathbf{q}+\mathbf{G}) \tag{2.69}$$

where $I(\mathbf{q}+\mathbf{G})$ is defined by Eq. (2.27). To be consistent with neglecting the layer separations, $I(\mathbf{q}+\mathbf{G})\approx 1$.

Internal screening for downfolded Hamiltonian

In the construction of a downfolded Hamiltonian, such as a Wannier model of the flat electronic bands of moiré graphene multilayers, screening from the other electronic states should also be included. This can be achieved with what is called the constrained RPA (cRPA) approach, where the interaction between electrons in the bands of interest are screened by all transitions apart from between the bands of interest [236, 241–243]. This ensures that screening from states of interest are not double counted - once from the screened interaction and again from a solution of the interacting model of the bands of interest*.

In the cRPA approach [241–243], the total RPA polarizability is partitioned into two contributions

$$\Pi^0(\mathbf{q}+\mathbf{G}) = \Pi^f(\mathbf{q}+\mathbf{G}) + \Pi^r(\mathbf{q}+\mathbf{G}), \tag{2.70}$$

where Π^f denotes the polarizability contribution from electronic transitions between the bands of interest (the superscript f is used to denote transitions between flat bands, as these are the states of most interest in moiré graphene multilayers), and Π^r are the rest of the transitions which is the cRPA polarizability. Note that Π^r contains transitions from all other states to the unoccupied states of interest, and also transitions from the occupied states of interest to all other unoccupied states [241–243].

---

*Note that this method still has limitations [254], and tends to overestimate screening.

The total screened interaction can be written as

$$W(\mathbf{q}+\mathbf{G}) = [1 - \Pi^f(\mathbf{q}+\mathbf{G})W^r(\mathbf{q}+\mathbf{G})]^{-1}W^r(\mathbf{q}+\mathbf{G}), \tag{2.71}$$

where

$$W^r(\mathbf{q}+\mathbf{G}) = [1 - \Pi^r(\mathbf{q}+\mathbf{G})v(\mathbf{q}+\mathbf{G})]^{-1}v(\mathbf{q}+\mathbf{G}) \tag{2.72}$$

is the cRPA screened interaction between electrons in the bands of interest. With the cRPA dielectric function being defined as

$$\epsilon^r(\mathbf{q}+\mathbf{G}) = \epsilon_0 - v(\mathbf{q}+\mathbf{G})\Pi^r(\mathbf{q}+\mathbf{G}). \tag{2.73}$$

Internal screened interaction in real space

The screened interaction in real space is calculated via a 2D Fourier transform according to

$$W(\mathbf{r}) = \frac{1}{(2\pi)^2}\int d\mathbf{q}\frac{v(\mathbf{q})}{\epsilon(\mathbf{q})}e^{-i\mathbf{q}\cdot\mathbf{r}}. \tag{2.74}$$

As the polarizability is assumed to be isotropic, the angular part of the Fourier transform can be carried out analytically

$$W(r) = \frac{e^2}{4\pi\epsilon_0}\int_0^\infty dq\frac{J_0(qr)}{\epsilon(q)}, \tag{2.75}$$

where q and r denote the magnitudes of the in-plane momentum and the in-plane distance, respectively, and J_0 is a Bessel function of the first kind with zeroth order.

The polarizability of moiré graphene multilayers exhibit two main regimes: at large momenta (i.e. those larger than twice the length of the primitive reciprocal lattice vectors), the responds similar to decoupled graphene layers, whereas at small momenta, there can be significant deviations from the graphene response [255, 256]. Therefore, the integral of Eq. (2.75) can be separated into two parts

$$
\begin{aligned}
W(r) &= \frac{e^2}{4\pi\epsilon_0}\left[\int_0^{2|\mathbf{G}|} dq \frac{J_0(qr)}{\epsilon(q)} + \int_{2|\mathbf{G}|}^{\infty} dq \frac{J_0(qr)}{\epsilon(q)}\right] \\
&= W_{\mathrm{s}}(r) + W_{\mathrm{l}}(r),
\end{aligned}
\tag{2.76}
$$

The first contribution, W_{s}, stems from the response at small wavevectors, which can be numerically integrated and readily converged. The second contribution, W_{l}, is the contribution from large momenta, which is essentially that of decoupled graphene layers. Since the dielectric function is approximately a constant in the latter regime, $\epsilon(q \gtrsim 2|\mathbf{G}|) \approx \epsilon_{\mathrm{ni}}$, the integral can be transformed to

$$
W_{\mathrm{l}} = \frac{e^2}{4\pi\epsilon_0\epsilon_{\mathrm{ni}} r}\left[1 - \int_0^{2|\mathbf{G}|r} dy J_0(y)\right],
\tag{2.77}
$$

which can also be readily evaluated. This circumvents the difficult problem of converging an integral of J_0 which is highly oscillatory. Note provided the cut-off point is chosen in the graphene regime, the exact point at which this integral is split into two makes no difference to the final result [256].

2.6.2 External screening

As summarised in the Introduction, external screening comes from proximity to metallic gates and the supporting dielectric substate. To include the effects of these gates, a number of approximations are taken: (1) - The metallic gate is considered to be a perfectly flat, ideal metallic conductor. (2) - The dielectric substrate can be considered on the level of an effective dielectric constant [244]. (3) - The distance to the metallic gate from the moiré graphene multilayer is significantly longer than the thickness of the moiré material, such that the moiré graphene multilayer can be considered as having no width. (4) - When there are two metallic gates, the moiré material resides exactly between the two of them [257]. We shall outline the so-called single and double metallic gate interactions in real-space [245].

For a single metallic gate [245] located underneath the moiré graphene multilayer, the screened Coulomb interaction between charges is given by

$$W(\mathbf{r}) = \frac{e^2}{4\pi\epsilon_0\epsilon}\left[\frac{1}{|\mathbf{r}|} - \frac{1}{|\mathbf{r} - 2\xi\boldsymbol{e}_z|}\right]. \tag{2.78}$$

Here ξ is the (shortest) distance from the moiré graphene multilayer to the ideal metallic gate, and $\boldsymbol{e}_z$ is the unit vector in the z direction. This screened interaction can be derived from the method of image charges, where the second term in the equation is the "image charge" located $-\xi\boldsymbol{e}_z$ underneath the interface between the metallic gate and the dielectric substrate. At large separations of electrons in the moiré graphene multilayer, the screened interaction decays as $\propto 1/|\mathbf{r}|^2$ which is shorter ranged than the bare Coulomb potential.

For a double metallic gate interaction [245, 257], the screened interaction reads as

$$W(\mathbf{r}) = \frac{e^2}{4\pi\epsilon_0\epsilon}\sum_{m=-\infty}^{\infty}\frac{(-)^m}{|\mathbf{r} + 2m\xi\boldsymbol{e}_z|}. \tag{2.79}$$

Here m is an integer which corresponds to an image charge in the infinite set of images which are created through image charges in one metallic gate inducing images charges in the opposite metallic gate. At large separations ($|\mathbf{r}| \gg \xi$) [245] of electrons in the moiré graphene multilayer, the screened interaction can be approximated as

$$W(\mathbf{r}) = \frac{e^2}{2\pi\epsilon_0\epsilon}\frac{e^{-\pi|\mathbf{r}|/\xi}}{\sqrt{|\mathbf{r}|\xi}}. \tag{2.80}$$

Therefore, the electron interactions are exponentially screened at large distances.

2.7 Interacting atomistic Hamiltonians

In the previous sections, we have outlined methods to investigate the "non-interacting" Hamiltonian, $\mathcal{H}_0$, at charge neutrality in the normal state (no broken symmetries) [99]. To investigate the effects of doping and the possible broken symmetry phases, the interactions between electrons must also be accounted for. The Hamiltonian with interactions then reads

$$\mathcal{H} = \mathcal{H}_0 + \mathcal{H}_{int}, \tag{2.81}$$

where $\mathcal{H}_{int}$ is the interacting contribution that accompanies the "non-interacting" contribution. In this section, different approximations for $\mathcal{H}_{int}$ are outlined. The effect of doping the normal state is investigated with an atomistic tight-binding theory which accounts for Hartree interactions [95]. Also in an atomistic tight-binding approach, we investigate magnetic ordering in a Hubbard model [11]. For a $\mathcal{H}_0$ which only accounts for the flat bands of interest in the moiré graphene multilayers, we investigate $\mathcal{H}_{int}$ in the Wannier representation.

2.7.1 Hartree interactions in atomistic tight-binding

In second quantisation, Hartree interactions are included through [99]

$$\mathcal{H}_{int} = \frac{1}{2}\sum_{\sigma\sigma'}\sum_{\mathbf{R}\mathbf{R}'}\sum_{ij} W_{ij\mathbf{R}\mathbf{R}'}\hat{c}^{\dagger}_{i\mathbf{R}\sigma}\hat{c}^{\dagger}_{j\mathbf{R}'\sigma'}\hat{c}_{j\mathbf{R}'\sigma'}\hat{c}_{i\mathbf{R}\sigma}. \tag{2.82}$$

Taking the mean-field limit of the operators in the normal state [99], the long-ranged electron-electron interaction contribution to the Hamiltonian can be included through an on-site term to the atomistic tight-binding model

$$\varepsilon_i = \langle \phi_z(\mathbf{r}-\boldsymbol{\tau}_i)|V_{\mathrm{H}}(\mathbf{r})|\phi_z(\mathbf{r}-\boldsymbol{\tau}_i)\rangle\,, \tag{2.83}$$

where $V_{\mathrm{H}}(\mathbf{r})$ is the Hartree potential. The Hartree potential is determined from the electron density $n(\mathbf{r})$ and the screened electron-electron interaction $W(\mathbf{r})$, as seen by

$$V_{\mathrm{H}}(\mathbf{r}) = \int d\mathbf{r}' W(\mathbf{r}-\mathbf{r}')[n(\mathbf{r}') - n_0(\mathbf{r}')], \tag{2.84}$$

where $n_0(\mathbf{r})$ is a reference electron density of the uniform system. The electron density is determined through

$$n(\mathbf{r}) = \sum_{n\mathbf{k}} f_{n\mathbf{k}}|\psi_{n\mathbf{k}}(\mathbf{r})|^2, \tag{2.85}$$

where $f_{n\mathbf{k}} = 2\Theta(\varepsilon_{\mathrm{F}} - \varepsilon_{n\mathbf{k}})$ is the spin-degenerate occupancy with ε_{F} denoting the Fermi energy. Inserting the Bloch states gives

$$n(\mathbf{r}) = \sum_j n_j \chi_j(\mathbf{r}), \tag{2.86}$$

where $\chi_j(\mathbf{r}) = \sum_{\mathbf{R}} \phi_z^2(\mathbf{r} - \boldsymbol{\tau}_j - \mathbf{R})$ and the total number of electrons on the j-th p$_z$-orbital in the unit cell being determined by $n_j = \sum_{n\mathbf{k}} f_{n\mathbf{k}} |c_{n\mathbf{k}j}|^2 / N_\mathrm{k}$.

The reference density is taken to be that of a uniform system, $n_0(\mathbf{r}) = \bar{n} \sum_j \chi_j(\mathbf{r})$, where $\bar{n}$ is the average of n_j over all atoms in the unit cell, which is related to the filling per moiré unit cell ν through $\bar{n} = 1 + \nu/N$, where N is the total number of atoms in a moiré unit cell [136]. This reference density is taken to prevent over-counting the intrinsic graphene Hartree contribution which should be included in the Slater-Koster hopping parameters that are fitted to DFT band structures [32, 37].

In our atomistic model, we neglect contributions to the electron density from overlapping p$_z$-orbitals that do not belong to the same carbon atom, which is equivalent to treating $\phi_z^2(\mathbf{r})$ as a Kronecker delta function. Therefore, we calculate the Hartree on-site energies using

$$\varepsilon_i = \sum_{j\mathbf{R}} (n_j - \bar{n}) W_{\mathbf{R}ij}, \tag{2.87}$$

where $W_{\mathbf{R}ij} = W(\mathbf{R} + \boldsymbol{\tau}_j - \boldsymbol{\tau}_i)$. If $\mathbf{R} = 0$ and $i = j$, we set $W_{0,ii} = U/\epsilon_\mathrm{bg}$ with $U = 17$ eV [236], where ϵ is the background dielectric constant of the interaction. The screened interaction is taken to be the double metallic gate interaction from Section 2.6.2, or simply be a Coulomb interaction $W_{\mathbf{R}ij} = e^2/4\pi\epsilon_0\epsilon|\mathbf{R} + \boldsymbol{\tau}_j - \boldsymbol{\tau}_i|$.

To obtain the mean-field solution of the Hartree atomistic tight-binding, a linear mixing scheme is employed and in each iteration the Fermi energy is determined from enforcing the total number of electrons to be $N + \nu$. To converge the electron density, a Monkhorst-Pack $\mathbf{k}$-point grid, which includes the Γ-point, of at least 4×4 is required. Typically, 6×6 to 12×12 grids were utilised. For each calculation, the $\mathbf{k}$-point grid sampling and dielectric environment shall be stated. Initially, we perform a tight-binding calculation without an on-site energy from Hartree interactions. This permits the "non-interacting" Hartree potential to be found. This initial potential was rescaled by a scalar (0.1-1) to obtain a better initial guess to the converged solution based on experience. For all proceeding iterations, a linear mixing parameter of 0.1-0.01

was taken to mix in the new iteration with that of the previous mixed iteration. A convergence criterion in the Hartree potential or electron density was used to decide when to finish the calculation. Typically, the eigenvalues can be converged to 0.1 meV or better within less than 100 iterations. Due to the lack of smearing in the calculation, smaller mixing values are larger numbers of iterations were sometimes required to smooth-out the "flickering" potential that prevents the calculation from converging to this threshold.

2.7.2 Hubbard interactions in atomistic tight-binding

In second quantisation, the collinear Hubbard interaction contribution to the atomistic tight-binding Hamiltonian [11, 99] is given by

$$\mathcal{H}_{int} = \frac{1}{2}\sum_{\sigma\sigma'}\sum_{i} U\hat{c}^{\dagger}_{i\sigma}\hat{c}^{\dagger}_{i\sigma'}\hat{c}_{i\sigma'}\hat{c}_{i\sigma}. \tag{2.88}$$

Taking the mean-field limit the on-site energy is determined by the mean-field Hubbard interaction

$$\varepsilon_{i\sigma} = U\left\langle \phi_z(\mathbf{r}-\boldsymbol{\tau}_i)|n_{\sigma'}(\mathbf{r})|\phi_z(\mathbf{r}-\boldsymbol{\tau}_i)\right\rangle, \tag{2.89}$$

where U is the Hubbard parameter of the carbon atoms, and $\langle n_{i\sigma'}\rangle$ is the mean-field electron density on atom i with the spin σ' being the opposite to σ.

The electron density can be determined from the Bloch eigenstates according to

$$\begin{aligned} n_\sigma(\mathbf{r}) &= \sum_{n\mathbf{k}} f_{n\mathbf{k}\sigma}|\psi_{n\mathbf{k}\sigma}(\mathbf{r})|^2 \\ &= \sum_{j} n_{j\sigma}\chi_j(\mathbf{r}), \end{aligned} \tag{2.90}$$

where $f_{n\mathbf{k}\sigma} = \Theta(\varepsilon_{\mathrm{F}} - \varepsilon_{n\mathbf{k}\sigma})$ is the occupancy of state $\psi_{n\mathbf{k}\sigma}$ and $n_{j\sigma} = \sum_{n\mathbf{k}\sigma} f_{n\mathbf{k}\sigma}|c_{n\mathbf{k}\sigma j}|^2/N_{\mathrm{k}}$ is the total number of electrons in the j-th orbital with spin σ.

$$\varepsilon_{i\sigma} = Un_{i\sigma'}. \tag{2.91}$$

The Hubbard parameter, U, for the on-site interactions of the p_z orbitals shall be considered as a parameter of the model.

The magnetic order parameter is defined by

$$\zeta_i = \frac{n_{i\uparrow} - n_{i\downarrow}}{n_{i\uparrow} + n_{i\downarrow}}, \tag{2.92}$$

which is used to characterise the ordering. Ferromagnetic or ferrimagnetic order has a non-zero $\sum_i \zeta_i$, but for antiferromagnetic order this summation is zero.

To obtain a self-consistent solution, a very similar procedure to the Hartree theory is taken. Therefore, we shall not repeat the details that are the same. Practically the only difference in these mean-field Hubbard calculations is that a Hamiltonian for the up and down spin need to be diagonalised in each iteration. When determining the Fermi energy, the total electron density is again forced to be $N + \nu$, but this does not restrict the spin densities to be the same.

2.7.3 Constrained Hubbard calculations

To investigate excited magnetic states, constrained calculations must be performed. Several approximate methods were employed to investigate these states. These methods utilised an analytical form for the magnetic order, $\zeta_i^{(j)}$ [where (j) is an index denoting the type of magnetic order]. Since we are investigating collinear magnetic order with the periodicity of a moiré unit cell, i.e. $q = 0$ instabilities, this significantly restricts the type of magnetic order that can occur. To generate the scale of the ordering, one can simply project the ordering onto the magnetic order parameter

$$A_j = \frac{\sum_i \zeta_i \cdot \zeta_i^{(j)}}{\sum_i \zeta_i^{(j)} \cdot \zeta_i^{(j)}}. \tag{2.93}$$

The on-site energy term is then given by

$$\varepsilon_{i\sigma} = \pm \frac{U}{2} \zeta_i^{(j)}. \tag{2.94}$$

A self-consistent solution is obtained through a linear mixing of the spin densities. Alternatively, a non-self-consistent route to determine the ground state is through computing the total energy

$$E^{(j)} = \frac{1}{N_\mathrm{k}} \sum_{n\mathbf{k}\sigma} f_{n\mathbf{k}\sigma} \varepsilon^{(j)}_{n\mathbf{k}\sigma} + \frac{U}{4} \sum_i \zeta_i^{(j)} \zeta_i^{(j)} \tag{2.95}$$

as a function of A_j in order to determine the A_j which corresponds to the minimum in the energy. As the on-site energies only depend on the product of U and $\zeta_i^{(j)}$, this can mean the space of $U - A_j$ can be explored efficiently.

2.7.4 Hubbard parameters of Wannier functions

In second quantisation, the Wannier-Hubbard interaction contribution to the Hamiltonian reads [99]

$$\mathcal{H}_{int} = \frac{1}{2} \sum_{\sigma\sigma'} \sum_{\{n_i\}} \sum_{\{\mathbf{R}_i\}} U_{\sigma\sigma',\{n_i\},\{\mathbf{R}_i\}} \hat{c}^\dagger_{n_4\mathbf{R}_4\sigma} \hat{c}^\dagger_{n_3\mathbf{R}_3\sigma'} \hat{c}_{n_2\mathbf{R}_2\sigma'} \hat{c}_{n_1\mathbf{R}_1\sigma}. \tag{2.96}$$

Here the Hubbard parameters associated with Wannier functions are given by

$$U_{\sigma\sigma',\{n_i\},\{\mathbf{R}_i\}} = \langle w_{n_4\mathbf{R}_4\sigma}(\mathbf{r}) w_{n_3\mathbf{R}_3\sigma'}(\mathbf{r}') | W(\mathbf{r},\mathbf{r}') | w_{n_2\mathbf{R}_2\sigma'}(\mathbf{r}') w_{n_1\mathbf{R}_1\sigma}(\mathbf{r}) \rangle\,. \tag{2.97}$$

The generated Wannier functions are in the normal state, and therefore, we drop the spin index from now.

The general form of the Wannier functions is

$$|w_{n\mathbf{R}}\rangle = \frac{1}{\sqrt{N_\mathrm{k}}} \sum_{m\mathbf{k}} e^{-i\mathbf{k}\cdot\mathbf{R}} U^{(\mathbf{k})}_{nm} |\psi_{m\mathbf{k}}\rangle\,, \tag{2.98}$$

as described in detail in Section 2.5. Inserting the Bloch states into the Wannier function gives

$$|w_{n\mathbf{R}}\rangle = \frac{1}{N_\mathrm{k}} \sum_{m\mathbf{k}} \sum_{i\mathbf{R}'} e^{i\mathbf{k}\cdot(\mathbf{R}'-\mathbf{R})} c_{m\mathbf{k}i} U^{(\mathbf{k})}_{nm} |\phi_z(\mathbf{r} - \boldsymbol{\tau}_i - \mathbf{R}')\rangle\,. \tag{2.99}$$

If we then introduce a new set of coefficients, we have

$$|w_{n\mathbf{R}}\rangle = \sum_{i\mathbf{R}'} c_{n\mathbf{R}\mathbf{R}'i} |\phi_z(\mathbf{r} - \boldsymbol{\tau}_i - \mathbf{R}')\rangle\,, \tag{2.100}$$

where

$$c_{n\mathbf{R}\mathbf{R}'i} = \frac{1}{N_\mathrm{k}} \sum_{m\mathbf{k}} U^{(\mathbf{k})}_{nm} e^{i\mathbf{k}\cdot(\mathbf{R}'-\mathbf{R})} c_{m\mathbf{k}i}. \tag{2.101}$$

Hence, the atomistic Wannier functions of the bands can be expressed as a linear combination of atomic orbitals too.

The p_z orbitals are highly localised on each carbon atom, so it is often approximated that they do not overlap significantly. This means that we approximate these p_z^2 orbitals as Kronecker delta functions, and work on a grid which is composed of the centres of the carbon atoms of the moiré graphene multilayer. Under this approximation, the integral of the Wannier function squared is given by

$$\langle w_{n\mathbf{R}} | w_{n\mathbf{R}} \rangle = \sum_{i\mathbf{R}'} c^*_{n\mathbf{R}\mathbf{R}'i} c_{n\mathbf{R}\mathbf{R}'i} = 1. \tag{2.102}$$

We restrict our analysis to the Coulomb Hubbard parameters, such that $\mathbf{R}_4 = \mathbf{R}_1$ and $\mathbf{R}_3 = \mathbf{R}_2$. Therefore, the object which needs to be calculated is

$$U_{n_1\mathbf{R}_1 n_2\mathbf{R}_2} = \int\int d\mathbf{r}d\mathbf{r}' |w_{n_1\mathbf{R}_1}(\mathbf{r})|^2 W(\mathbf{r},\mathbf{r}') |w_{n_2\mathbf{R}_2}(\mathbf{r}')|^2. \tag{2.103}$$

Inserting the expressions for the Wannier functions and assuming translational invariance, our final equation is

$$U_{n_1\mathbf{R}_1 n_2\mathbf{R}_2} = \sum_{\mathbf{R}\mathbf{R}'} \sum_{ij} |c_{n_1\mathbf{R}_1\mathbf{R}i}|^2 |c_{n_2\mathbf{R}_2\mathbf{R}'j}|^2 W_{i\mathbf{R}j\mathbf{R}'}, \tag{2.104}$$

where $W_{i\mathbf{R}j\mathbf{R}'} = W(\mathbf{R} + \boldsymbol{\tau}_j - \mathbf{R}' - \boldsymbol{\tau}_i)$. If $\mathbf{R} = \mathbf{R}'$ and $i = j$, we set $W_{0,ii} = U/\epsilon$ with $U = 17$ eV [236].

The form of Eq. (2.104) has a clear physical meaning. The summations of the coefficients represent the fractional charges of the Wannier functions that reside on each of the p_z orbitals. The total interaction of the Wannier functions is simply given by the sum of all of these interactions.

2.8 Spin susceptibility

Following Refs. 125, 208 to analyse the magnetic ordering tendencies of graphitic moiré systems*, we calculate the spin susceptibility $\chi_{ij}(\boldsymbol{q}, q_0)$ in its long-wavelength, static limit $\boldsymbol{q} = q_0 = 0$

$$\hat{\chi} = \hat{\chi}(\boldsymbol{q} = 0, q_0 = 0) = \frac{T}{N_{\boldsymbol{k}}} \sum_{\boldsymbol{k}, k_0} \hat{G}(\boldsymbol{k}, k_0) \hat{G}^T(\boldsymbol{k}, k_0). \tag{2.105}$$

The Matsubara Green's function reads $\hat{G}(\boldsymbol{k}, k_0) = [ik_0 - \hat{H}(\boldsymbol{k})]^{-1}$ with the non-interacting part of the Hamiltonian $\hat{H}(\boldsymbol{k})$. Since we approximate the interacting part of the Hamiltonian by a local Hubbard interaction, the renormalised interaction reads

$$\hat{W} = \frac{U^2 \hat{\chi}}{1 + U\hat{\chi}}. \tag{2.106}$$

Employing Stoner's criterion, we find an ordered state if the smallest eigenvalue χ^0 of the matrix $\hat{\chi}$ reaches $-1/U$, or, vice versa, we can investigate the critical interaction strength $U_\mathrm{c} = -1/\chi^0$ below which the system will go into an ordered state. The eigenvector corresponding to the eigenvalue χ^0 is proportional to the system's magnetisation in its ordered state. The numerical evaluation procedure is identical to the one presented in Ref. 125 – we use $N_{k_0} = 500$ Matsubara frequencies and $N_{\boldsymbol{k}} = 24$ momentum points at a temperature of $T = 10^{-4}\,\mathrm{eV}$.

---

*This method was implemented and executed by Lennart Klebl on joint projects.

Chapter 3

Screening of electron-electron interactions in twisted bilayer graphene

The observation of strongly correlated phases in magic angle tBLG [88, 89] generated significant attention, as summarised in the Introduction. In particular, these observations piqued the interest of the theoretical community, as the mechanism for superconductivity was suggested to be unconventional in nature [89], which has been a long-studied problem in context of the cuprates [90]. There are, however, many methods, with drastically different assumptions, that a theorist can utilise to make predictions for the broken symmetry phases of tBLG. Specifically, methods often differ in their treatment of electron-electron interactions. In a material, the bare Coulomb interaction is screened, and an accurate description of screening is challenging, with simplifying assumptions often being taken [99, 231].

One method that has been utilised numerous times to investigate the phase diagram of tBLG is the Hartree-Fock theory based on the continuum model [66, 143, 258–261]. It is well known, however, that Hartree-Fock can lead to unphysical results, such as a diverging Fermi velocity in metals [216], because the Coulomb interaction in the exchange term is not screened [99, 231]. In these works [66, 143, 258–261] the exchange was sometimes screened by an internal dielectric constant with a fairly modest value [66], approximately twice the static response of graphene at charge neutrality [235, 246]. Stauber and Kohler [262] calculated the static random phase approximation (RPA) dielectric function from a continuum model and found a massive enhancement in screening for twist angles close to the magic angle, however. Therefore, a detailed understanding of the RPA response function of tBLG is required if accurately screened exchange interactions are to be used in calculations.

Internal electronic screening is also important for the construction of Wannier Hamiltonians [68, 72–75, 96] of the flat bands[*], as screening from bands excluded in the Wannier Hamiltonian renormalises the interaction between flat band electrons [256]. In the context of the construction of low-energy Hamiltonians, it has been shown that the constrained random phase approximation (cRPA), in which transitions among the low-energy bands are excluded in the polarizability, should be used for the screened interactions between electrons in the flat bands [236, 241–243]. This is to ensure that screening of the electrons in the flat bands is not double-counted [241]. Recently, Pizarro *et al.* [255] calculated the static cRPA polarizability of undoped tBLG at a single twist angle of 1.05° using a continuum model, where a dielectric function with a magnitude approximately twice the response of graphene was found.

Another important source of screening can originate from external factors. The surrounding dielectric environment is controlled by the device setup. For gated tBLG devices, the potential created by an electron in the tBLG is reduced by the image charge(s) in the metallic gate(s) [73, 96, 245]. The strength of the resulting effective interaction between electrons in the tBLG is determined by the separation of the metallic gate(s) from tBLG, which can be experimentally controlled via the thickness of a dielectric spacer. In the experimental devices, there has been significant variations in the device setup. For example, Cao *et al.* [88, 89] used devices in which the tBLG was encapsulated by hexagonal boron nitride (hBN) slabs of 10-30 nm thickness with gold gates above/below tBLG. In contrast, Yankowitz *et al.* [93] used thicker hBN slabs (30-60 nm) sandwiched between two graphite gates, and the device of Lu *et al.* [120] only had a single graphite gate separated from the tBLG by a hBN layer of ~ 10 nm thickness. Therefore, understanding how external screening influences the electron interactions is extremely important for understanding the phase diagrams of these tBLG devices.

In this chapter, results for how electrons interact and screen in tBLG is outlined. In Section 3.1, the Wannier functions of the low energy states of tBLG are briefly presented, as these orbitals are used in the subsequent sections. Next the internal screening of tBLG is investigated, where the screened interactions of electrons in the flat band states are presented. Subsequently, the role of external screening on the electron interactions of these states is investigated. This chapter is mainly based on three papers which have been published. In the first of these, Ref. 75 [Goodwin *et al.* Phys. Rev. B 100:121106(R) 2019], was where the Wannier functions of the flat bands were generated, and initial results for the interaction between these states were presented[*]. Section 3.1 on the Wannier functions and flat bands of tBLG is based on Ref. 75. Section 3.2 focuses on internal screening and the interaction parameters screened by internal responses of these states, and is heavily based on Ref. 256 [Goodwin *et al.* Phys. Rev. B 100:245424 2019]. Finally, Section 3.3 investigates the effect of external screening on these states, and is substantially based on Ref. 114 [Goodwin *et al.* Phys. Rev. B 101:165110 2020].

---

[*] Which can be used in methods such as quantum Monte Carlo [263], functional renormalisation group [108] and exact diagonalization [97], as reviewed in the Introduction.

These works were done in collaboration with other members of the Mostofi-Lischner group. Therefore, the contributions of my collaborators shall be explicitly described, with everything else being what I contributed (a brief description also given). Fabiano Corsetti contributed an initial code for the atomistic tight-binding model of graphitic based-systems (based on previous work of graphene with large unit cells [264]), which I generalised to account for atomic corrugation effects of tBLG. Valerio Vitale contributed in the development of the interface with Wannier90-3.0 [238], with particular help in the use of the selective localisation procedure. Arash Mostofi and Johannes Lischner initiated these projects, guided their progression and significantly helped in writing the papers. I wrote codes to interface with Wannier90-3.0 [238], to calculate the static polarizability of tBLG and the screened interactions, and the Hubbard parameters of the flat bands. I generated all results presented in this chapter.

---

[*] These results shall not be summarised in full for brevity, as the latter papers investigate this aspect in more depth

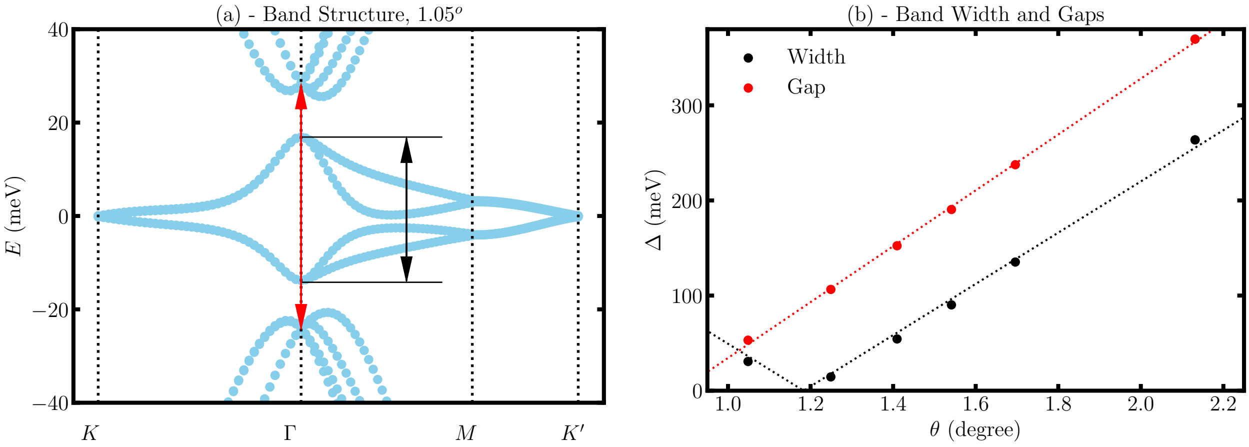

Figure 3.1: (a) - Band structure of tBLG for a twist angle of 1.05°. The black arrow indicates the width of the flat bands, and the red arrow denotes the energy gap between non-flat bands at Γ. (b) - Bandwidths of flat bands [black arrow in (a)] and band gaps at Γ between non-flat bands [red arrow in (a)] as function of twist angle.

3.1 Flat band electronic structure

Fig. 3.1 shows the electronic band structure* of tBLG at a twist angle of 1.05°, which exhibits four flat bands near the Fermi level that are separated from all other bands by energy gaps. The undoped system is a semimetal as the flat valence and conduction bands touch at the K and K′ points of the moiré Brillouin zone. As the twist angle approaches the magic angle ($\theta = 1.18°$ in our calculations), the width of the flat bands decreases, see black circles in Fig. 3.1(b). Also, the energy gaps that separate the non-flat bands decrease as the twist angle is reduced, see red circles in Fig. 3.1(b). Note that in a narrow twist-angle window (1.12-1.20°), we find qualitatively different band structures with a metallic character for undoped tBLG (similar band structures are shown in Refs. 69 and 65).

3.1.1 Wannier functions of flat bands

To obtain a Wannier-transformed Hamiltonian that reproduces the symmetries of the band structure of tBLG, as summarised in the Introduction, the Wannier functions must be centred at the AB or the BA positions of the moiré unit cell [68, 71–73]. We use the approach of

---

*The structure was generated from pristine tBLG with corrugation effects being approximated by the cosine series. The tight-binding parameters for these calculations were $a = 1.42$ Å, $d = 3.35$ Å, $q_\pi = 7.43$ and $q_\pi = 3.14$, with a cylindrical Heaviside step function with cut-off of third nearest neighbour in-plane being used to truncate hopping parameters.

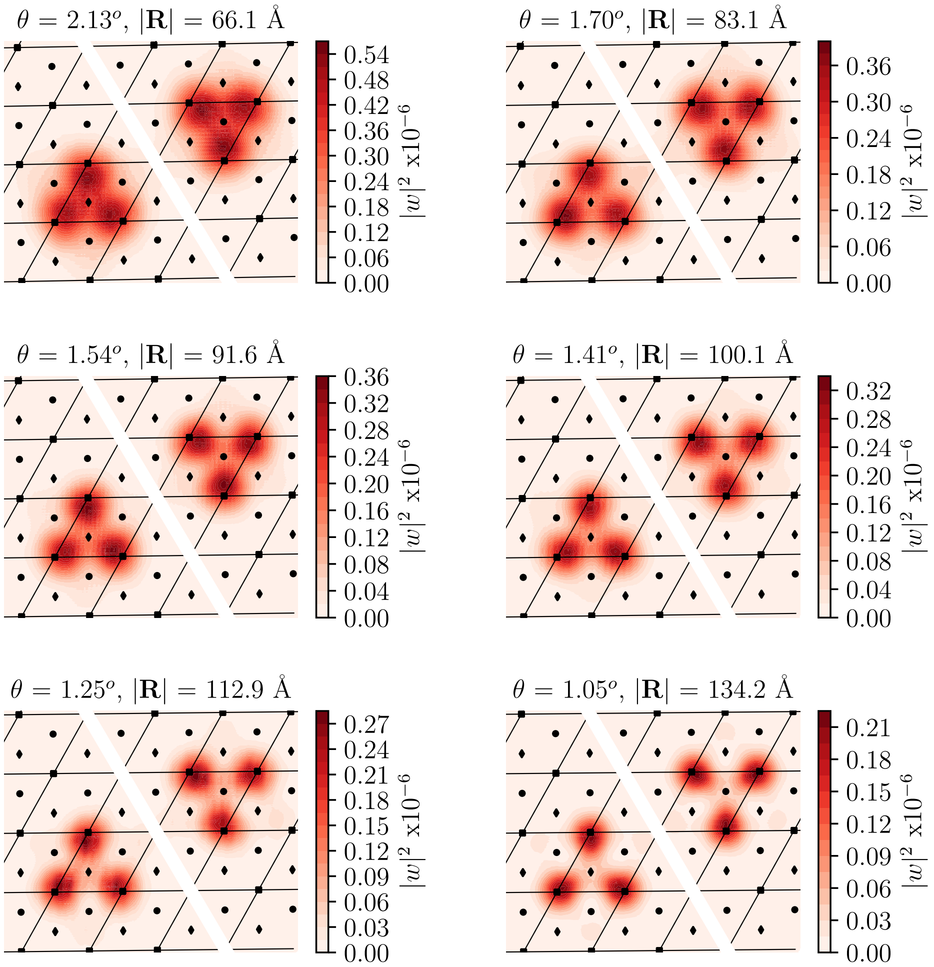

Figure 3.2: Flat-band Wannier functions of tBLG at several twist angles, as indicated in the title of each sub-plot. Shown is the square modulus of the coefficients of the Wannier functions on each carbon atom. The squares, diamonds and circles denote the centres of the AA, AB and BA regions of tBLG, respectively.

Ref. 240 to selectively localise two Wannier functions with constrained centres, one on each of these positions, as outlined in the Methods. Note that the method of Ref. 240 only permits the calculation of two of the four Wannier functions if their centres are constrained. If all four Wannier functions are required the symmetry constrained method must instead be used [76].

In Fig. 3.2 we display the obtained Wannier functions on the AB and BA positions of the moiré unit cell at a number of twist angles. In agreement with previous work [68, 72–74], we find the Wannier functions exhibit three lobes that reside on the closest AA regions of the moiré unit cell, with very little weight on the AB/BA positions where the Wannier functions are centred. For smaller twist angles, as the moiré length scale increases, the lobes which reside on the AA regions become increasingly separated. These Wannier functions shall be utilised in the subsequent sections to study the Hubbard interactions of the flat bands.

3.2 Internal screening

3.2.1 Polarizability and screened interaction

Figure 3.3(a) shows the RPA polarizability of tBLG as function of crystal momentum (in the extended zone scheme) for several twist angles in the vicinity of the magic angle. For these twist angles, we find that $\Pi_0^{\mathrm{RPA}} \propto q/v_{\mathrm{F}}$ at small wavevectors as expected from the linear dispersion of the flat bands near K and K′. The slope of Π_0^{RPA} at small $\mathbf{q}$ depends sensitively on twist angle [262] because of the strong renormalisation of the Fermi velocity, $v_{\mathrm{F}}(\theta)$, which approaches zero at the magic angle [32, 33, 37]. At wavevectors larger than the second reciprocal lattice vector of the moiré lattice, Π_0^{RPA} of tBLG is very similar to that of decoupled graphene sheets [255]. In particular, it is linear in wave vector with a slope that is determined by the *unrenormalised* Fermi velocity of graphene [255].

Cutting out transitions between flat bands from the RPA yields the cRPA polarizability, which is displayed in Fig. 3.3(b). The cRPA polarizability is highly isotropic and quadratic in $|\mathbf{q}|$ for small $\mathbf{q}$. This is characteristic of 2D semiconductors [265], such as molybdenum disulfide [266], and a consequence of the finite energy gap for electronic transitions in the cRPA. The polarizability at small wavevectors increases with decreasing twist angle because the energy gap between the non-flat bands decreases [63, 75], as seen in Fig. 3.1(b). It was found that

$$\Pi_0^{\mathrm{cRPA}} \approx \frac{a|\mathbf{q}|^2}{1+b|\mathbf{q}|} + \frac{c|\mathbf{q}|^2}{1+d|\mathbf{q}|^3} \tag{3.1}$$

fits the cRPA polarizability remarkably well, where a, b, c and d were fitting parameters. In the limit of small $\mathbf{q}$ we recover the correct quadratic dependence, and for large $\mathbf{q}$ this formula recovers the linear dependence as the second term is only finite for relatively small $\mathbf{q}$. Not all the parameters are free, however. In the large $\mathbf{q}$ limit, the gradient must be twice that of graphene, which puts a constraint on a and b. Furthermore, we found little doping dependence

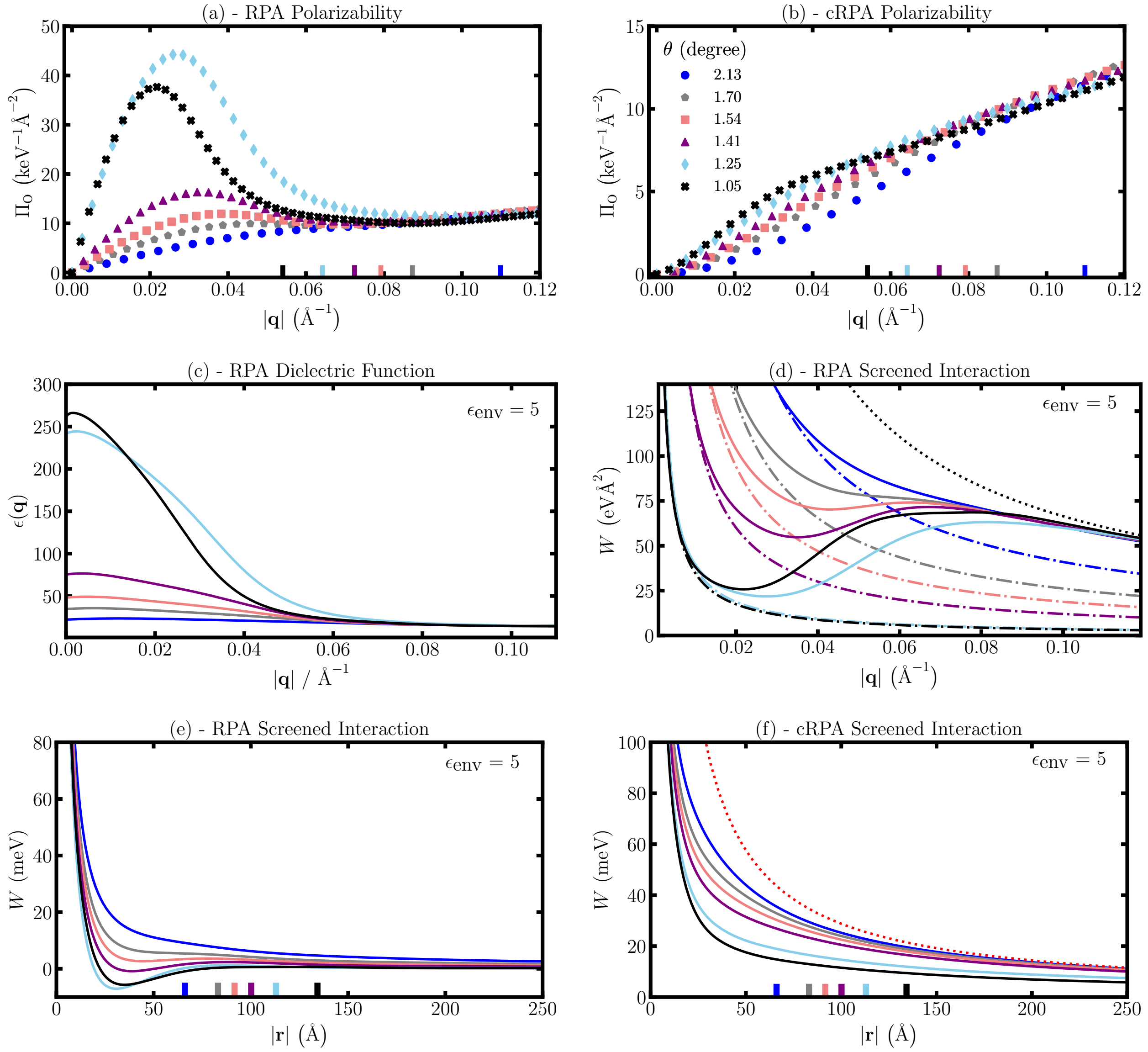

Figure 3.3: (a) and (b): RPA and cRPA polarizability of tBLG as a function of momentum transfer (in the extended zone scheme) for several twist angles near the magic angle. Vertical stubs indicate the magnitude of the moiré reciprocal lattice vectors for each twist angle. (c) - RPA dielectric function of tBLG encapsulated in hBN as a function of wavevector. (d) - RPA screened interaction of tBLG encapsulated in hBN in momentum space (solid lines). Dash-dotted lines denote the long wavelength limit, and the dotted line denotes the screened interaction divided by a dielectric constant with contributions from non-interacting graphene bilayers and hBN. (e) and (f): RPA and cRPA screened interaction in real space for tBLG encapsulated by hBN (solid lines). The red dash-dotted line indicates bare the Coulomb interaction. Vertical stubs denote moiré lattice constant for each twist angle.

of the cRPA polarizability, especially near the magic angle.

Table 3.1 shows the twist-angle dependent value of the screening parameter $\alpha(\theta)$, obtained from fitting the quadratic polarizability at small **q**, that enters the widely used Keldysh model for the dielectric function of 2D semiconductors, $\epsilon(q) = 1 + \alpha q$ [265] (note in this section,

ϵ is used to denote total or just internal dielectric responses, with ϵ_{env} being used to denote external dielectric responses). At small twist angles, we find a dramatic increase of the screening parameter reaching values of more than 1000 Å. This indicates that the Coulomb interaction is screened already for very small wavevectors (those larger than $1/\alpha$). At crystal momenta larger than the first moiré reciprocal lattice vector, Π_0^{cRPA} also becomes linear in $|\mathbf{q}|$ and very similar to the polarizability of uncoupled graphene bilayers [255].

θ / degree	ϵ (RPA)	α / Å (cRPA)
2.13	18.1	155.4
1.70	30.6	255.2
1.54	44.1	327.8
1.41	71.4	430.4
1.25	237.5	889.3
1.05	256.3	1292.0

Table 3.1: Long wavelength dielectric constants of tBLG from linear fits to Fig. 3.3(a) (with ϵ_{env} is taken to be 1) and Keldysh parameters from quadratic fits to Fig. 3.3(b) as a function of twist angle.

The RPA dielectric functions (in the extended zone scheme) are displayed in Fig. 3.3(c). For angles close to the magic angle, the large linear slope of the polarizability at small wave vectors gives rise to a large dielectric constant. At larger wave vectors, the reduced slope of Π_0^{RPA} results in a significantly smaller dielectric constant. The crossover between these two regimes of approximately constant dielectric functions occurs on the scale of the first two reciprocal moiré lattice vectors. Table 3.1 shows the resulting long-wavelength dielectric constants $\epsilon(\theta)$ of tBLG in air ($\epsilon_{\text{env}} = 1$). All angles exhibit enhanced dielectric constants relative to decoupled graphene bilayers ($\epsilon_{\text{ni}} = 8.86$ [1, 262], where the subscript is to denote it being the non-interacting case). Near the magic angle, the dielectric constant of tBLG increases dramatically and reaches values larger than 250 - a factor of 20 larger than decoupled graphene bilayers [262].

The RPA screened interaction in momentum space of tBLG encapsulated by a dielectric substrate ($\epsilon_{\text{env}} = 5$) is shown in Fig. 3.3(d). The effective interaction crosses over from a strongly screened small wave vector regime to a less strongly screened large wave vector regime. As a consequence of this crossover, the interaction exhibits a well-like feature for twist angles near the magic angle. Fig. 3.3(e) shows the interaction after Fourier transformation to real space. At several twist angles near the magic angle, the screened interaction in real space exhibits an *attractive region*. Specifically, the minimum of the screened interaction occurs near 40 Å with a well depth of up to $\sim$ 10 meV. At larger separations, the screened interaction decays as $1/(\epsilon(\theta)|\mathbf{r}|)$, i.e. it is repulsive and significantly weaker than the screened interaction of uncoupled graphene bilayers. At small separations, the screened interaction of tBLG is similar to that of uncoupled bilayers.

Fig. 3.3(f) shows the real-space cRPA screened interaction. At small distances, the interaction is similar to that of uncoupled graphene bilayers, while at large distances it proportional to $1/(\epsilon_{\text{env}}|\mathbf{r}|)$, i.e., the bare interaction screened by the dielectric constant of the environment (red dotted line). The distance at which the crossover between these two regimes occurs is determined by the twist-angle dependent Keldysh parameter $\alpha(\theta)$ [265], see discussion above.

3.2.2 Hubbard parameters

The increased internal screening combined with the emergence of attractive regions in the RPA interaction leads to a significant reduction of the on-site and extended interaction parameters [75]. Fig. 3.4(a) shows the screened on-site Hubbard parameters, V_{00}, as function of twist angle for different values of the environmental dielectric constant ϵ_{env}, and compares them to the linear fits to the on-site Hubbard parameters calculated with a Coulomb potential screened by a dielectric constant with contributions from the environment and uncoupled bilayers (solid lines). In contrast to the case of screening from a constant dielectric response [75], the RPA on-site Hubbard parameters are relatively small near the magic angle (only a few meV instead of tens of meV [75]), and they are a non-linear functions of twist angle.

Similarly, the extended Hubbard parameters for tBLG, shown in Fig. 3.4(c), are strongly reduced near the magic angle compared to the case of screening from a constant [75]. The calculated Hubbard parameters are well described by an analytical Ohno-like [267] expression $V(r) = V_{00}/\sqrt[4]{1 + (V_{00}/W_{\text{RPA}}(r))^4}$, where $W_{\text{RPA}}(r)$ denotes the screened RPA interaction in the long wavelength limit and r is the separation between Wannier function centres.

The Hubbard parameters obtained from the cRPA interaction are shown in Figs. 3.4(b) and (d). The on-site Hubbard parameters from the cRPA interaction, as displayed in Fig. 3.4(b),

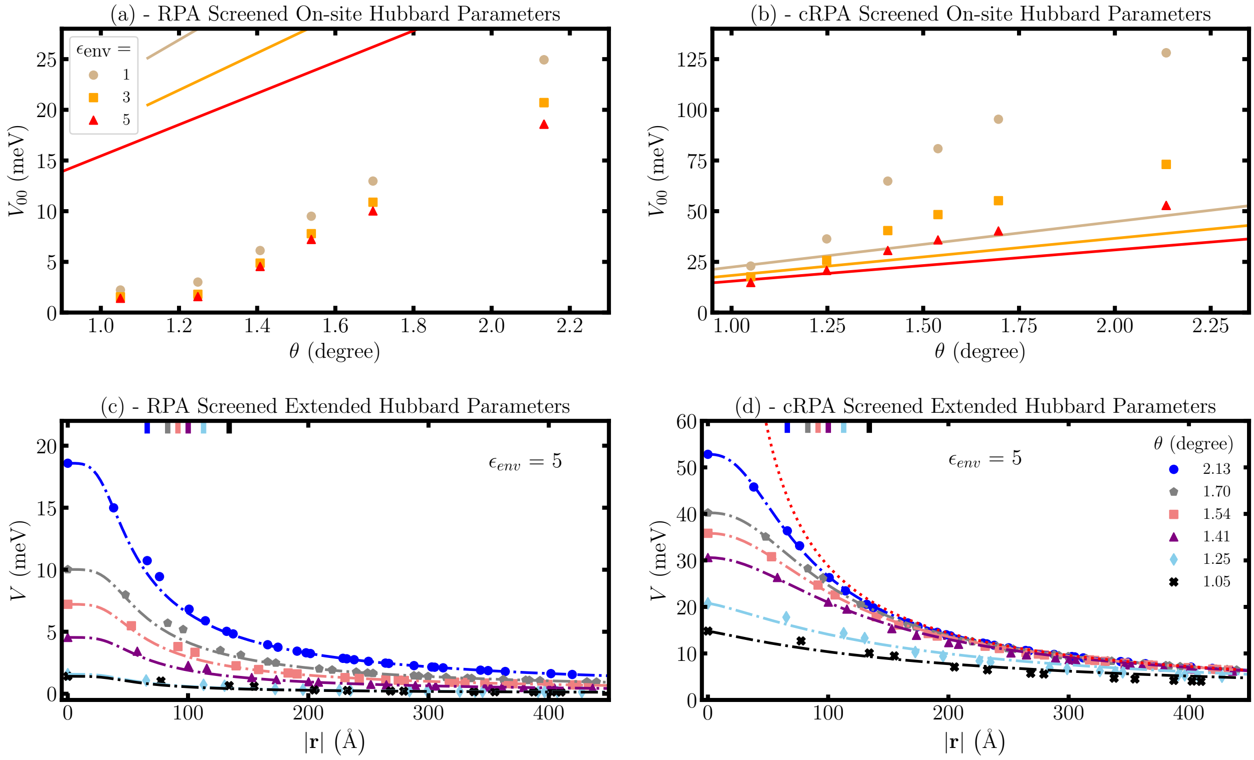

Figure 3.4: (a) and (b): RPA and cRPA screened on-site Hubbard parameters (symbols) as a function of twist angle for several environmental dielectric constants. Solid lines denote fits to bare on-site Hubbard parameters from Ref. 75 divided by a dielectric constant with contributions from environmental screening plus decoupled graphene bilayers. (c) and (d): RPA and cRPA screened extended Hubbard parameters (symbols) as a function of Wannier function separation for several twist angles. Dash-dotted lines denote generalised Ohno potential fits; the dotted red line denotes the hBN screened Coulomb potential and vertical stubs denote the size of the moiré lattice vector.

are approximately one order of magnitude larger than the RPA values, but again display a non-linear dependence on twist angle (when the external screening environment is not present). In contrast, the simplified screening model exhibits a linear dependence [75]. The extended cRPA Hubbard parameters, shown in Fig. 3.4(d), approach the bare Coulomb interaction divided by the environmental dielectric constant (red dotted line) at large Wannier function separations, and are well-described by the analytical Ohno-like [267] model $V(r) = V_{00}/\sqrt[n]{1 + (V_{00}/W_{\text{env}}(r))^n}$, where the exponent n is fitted for each twist angle separately and $W_{\text{env}}(r) \propto 1/(\epsilon_{\text{env}} r)$ [256].

3.2.3 Discussion

Attractive regions in the screened interaction are also found in the two-dimensional and three-dimensional electron gas where they are a consequence of Friedel oscillations [268]. These real-space oscillations of the induced charge density are caused by the discontinuity of the Bloch state occupancy at the Fermi level in k-space. Importantly, undoped graphene and undoped tBLG (at the twist angles we study) do not exhibit Friedel oscillations because the density of states at the Fermi level vanishes*. Instead, the attractive regions in tBLG have a different origin: they are caused by the abrupt change of the band velocity as a function of the band energy which gives rise to the peaks in the RPA polarizability, see Fig. 3.3(a). At small wave vectors, the RPA polarizability exhibits a large slope as a consequence of the strongly renormalised Fermi velocity of the flat bands [32, 33, 37, 262]. At larger wave vectors, the slope of Π_0^{RPA} reflects the unrenormalised Fermi velocity of uncoupled graphene sheets [255]. Fourier transformation of the resulting screened interaction to real space then results in oscillatory behaviour and attractive regions.

The screened interaction influences many properties of tBLG. For example, it determines the interaction of charged defects with the electrons in tBLG which can be studied with transport measurements and scanning tunnelling spectroscopy and microscopy techniques [264, 269]. Moreover, photo-excited electron-hole pairs interact via the screened interaction giving rise to excitonic effects in the optical properties of tBLG [270]. Attractive regions in the screened interaction can also induce electronic phase transitions. It is well known that Friedel oscillations in 2D and 3D electron gases can give rise to Cooper pairing and superconductivity via the Kohn-Luttinger mechanism [106, 271, 272]. Similarly, superconductivity due to polarisation induced electron pairing has been suggested to occur in long organic molecules with polarizable side chains [273–275]. Finally, electrons can reduce their potential energy by localising in the attractive regions of the screened interaction leading to the formation of charge density waves. The resulting energy gaps could explain the recently observed correlated insulator behaviour in undoped tBLG [120]. Our calculations demonstrate that internal screening strongly reduces the on-site Hubbard parameter, see Fig. 3.4(c). For graphene, Jung and MacDonald have shown that this favours the formation of charge density waves [9].

Spin density waves have also been suggested as candidates for the correlated insulator states [11, 104, 108, 263, 276–278]. These phases are expected to occur when the ratio of the

---

*Recall, however, that we do find metallic band structures of undoped tBLG for certain twist angles, and tBLG away from charge neutrality might be expected to exhibit such oscillations.

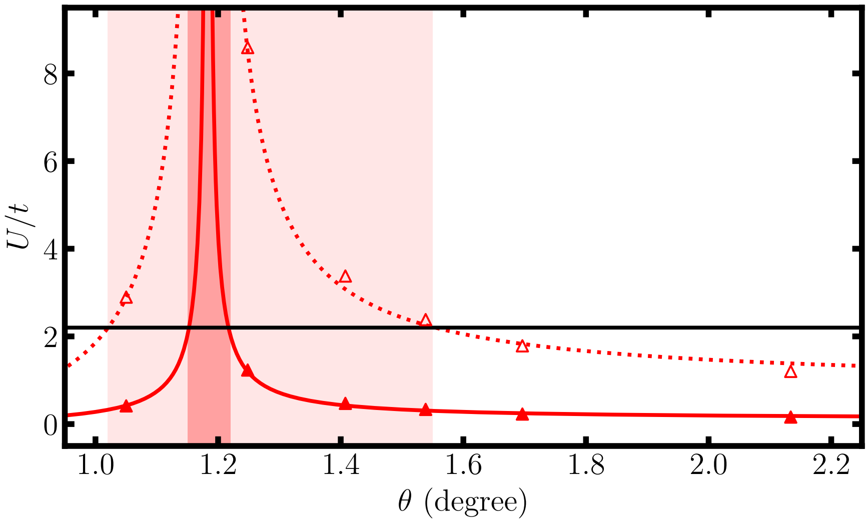

Figure 3.5: U/t of tBLG as function of twist angle (open symbols) with U being the cRPA on-site Hubbard parameter and t denoting the hopping parameter. Closed symbols indicate U^*/t (with U^* denoting the difference between the on-site and the nearest-neighbour cRPA Hubbard parameters) which is a better measure of electron correlations in systems with long-range interactions [109].

on-site Hubbard parameter V_{00} (commonly denoted as U) and the hopping integral t is large. Based on Quantum Monte Carlo calculations, Scalettar *et al.* [279] suggested that undoped tBLG undergoes a transition to a spin density wave at a U/t value of about two. This agrees well with the critical value of $U/t = 2.2$ obtained for Bernal stacked bilayers [280]. Here, we use a critical value of $U/t = 2.2$, but stress that our qualitative conclusions do not depend on the precise choice for this value. As discussed above, the on-site Hubbard parameter that enters a downfolded Hamiltonian for the flat-band electrons should be screened by all transitions except those between flat bands. Fig. 3.5 shows the ratio of U calculated within the cRPA and the hopping parameter (approximated as $\Delta/6$ [75]) as function of the twist angle. U/t exceeds the critical value of 2.2 in a significant twist-angle range ($\theta = 1.02°$ to $\theta = 1.52°$ corresponding to the light shaded region in the figure). It is well known, however, that long-ranged interactions reduce electron correlations. This effect can be approximately incorporated by replacing V_{00}^{cRPA} by $U^* = V_{00} - V_{01}$, i.e. the difference between the on-site and nearest neighbour Hubbard parameters [75, 109]. The resulting measure for the strength of electron correlations U^*/t exceeds the critical value only in a very narrow range of twist angles (dark shaded region in the figure) indicating that spin density wave states can only be found in a narrow twist-angle

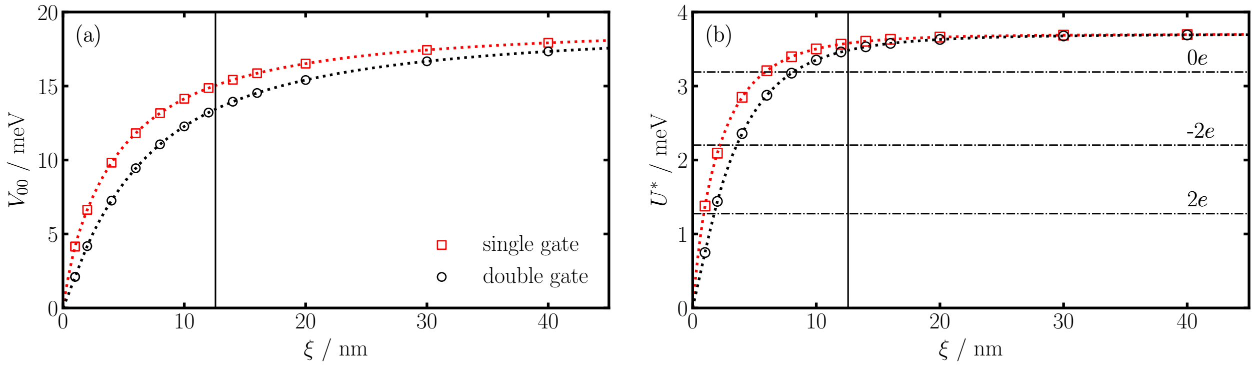

Figure 3.6: (a) - On-site Hubbard parameter V_{00} as a function of distance between tBLG and the metallic gate(s) ξ for a twist angle of 1.12° for the single-gate and double-gate device. (b) - Long-range corrected on-site Hubbard parameter U^* as a function of ξ for a twist angle of 1.12° for the single-gate and double-gate device. The horizontal dotted-dashed lines denote critical values of U^* obtained by multiplying the critical U^*/t values from atomistic RPA calculations of tBLG [208] with the hopping parameter for neighbouring moiré Wannier functions. Dotted lines through the data points correspond to fits that are used to extract critical gate separations in Fig. 3.7. The solid vertical line denotes to the length of the moiré unit cell.

window [75].

3.3 External screening

Next, we turn to the role of external screening on the cRPA Hubbard parameters of the flat bands of tBLG. The external screening should come from the supporting dielectric substrate (hBN in this case) in addition to the proximity of the metallic gates (which dope tBLG through electrostatic gating). The effect of the dielectric substrate can be assumed to occur through a constant, in addition to the cRPA response function. As shown in Fig. 3.4 the cRPA Hubbard parameters with an environmental dielectric constant of 5 actually changes relatively linearly with the twist angle, which is not far off the values for the environment plus decoupled bilayer response. Therefore, to simplify matters, we introduce the effect of cRPA screening and the environment through a constant (taken to be 10 in this section), and use the analytical equations for the image-charge-induced screening from metallic gates [245].

3.3.1 Hubbard parameters

Figure 3.6(a) shows the on-site Hubbard parameter V_{00} of tBLG as a function of the gate separation ξ for a twist angle of 1.12°, for both single-gate and double-gate device configurations. The largest values of V_{00} are obtained for large gate separations, and there is a substantial reduction in V_{00} as the gate separation decreases below the moiré length (indicated by the vertical line in Fig. 3.6). This can be understood as the image charge contribution arising from the induced charge density at the surface of the gate to reduce the Coulomb interaction between electrons in the tBLG. In the case of the single-gate device, when ξ is small, the electron in the tBLG and its image charge effectively interact with other electrons via a weak dipolar potential (instead of the usual monopole charge-charge interaction). For the double-gate setup, the image charges in both gates give rise to an exponentially screened interaction between electrons in the tBLG. The results for V_{00} in the two different device configurations are qualitatively similar, but the Hubbard parameters are somewhat smaller for the double-gate setup since both of the gates contribute to the screening.

In the Hubbard model [281, 282], electron-electron interactions are assumed to be short-ranged and the strength of electron correlations is usually measured by the ratio of the on-site Hubbard parameter V_{00} and the nearest-neighbour hopping parameter t. A system with long-ranged electron-electron interactions can be mapped onto an effective Hubbard model with an on-site Hubbard parameter $U^* = V_{00} - V_{01}$ (reflecting the energy required to hop from an empty Wannier orbital to an occupied neighbour site [109]), where V_{01} is the interaction between Wannier functions centred on neighbouring AB/BA regions [75, 256]. Figure 3.6(b) shows U^* for tBLG as function of ξ for a twist angle of 1.12° for both device configurations. It can be seen that U^* is significantly smaller than V_{00}, indicating that interactions between neighbouring Wannier functions play an important role even in the presence of metallic gates [75, 256]. This is expected as there is significant overlap between lobes of neighbouring Wannier functions [68, 75]. Similarly to V_{00}, U^* approaches a constant value in the limit of distant gates, but does so more rapidly once ξ becomes larger than the moiré length. Moreover, U^* exhibits a significantly sharper reduction as the distance decreases. Naively, one might expect that the presence of gates should lead to an *increase* in U^* if the screened interaction is sufficiently short-ranged

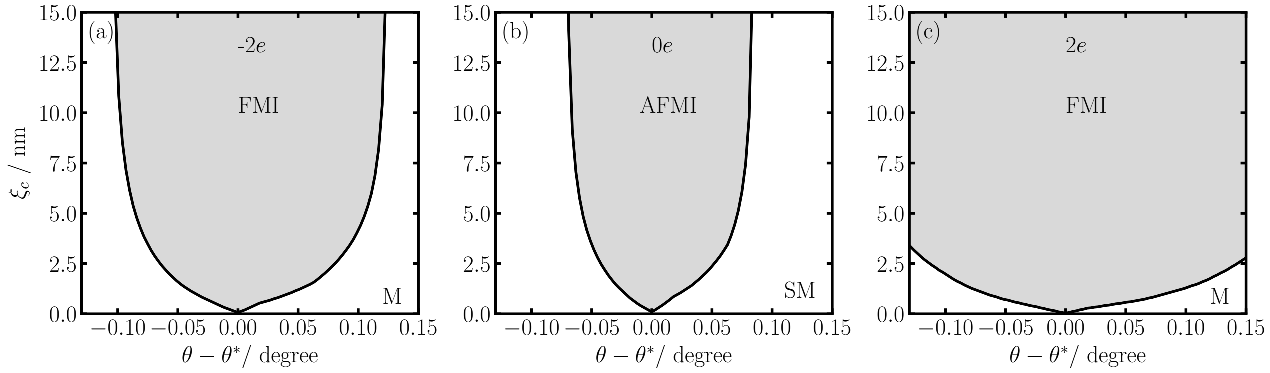

Figure 3.7: Critical value of gate distance as a function of twist angle for (a) two additional electrons per moiré unit cell ($-2e$), (b) charge neutrality ($0e$) and (c) two additional holes per moiré unit cell ($2e$) for a device with a single gate. The grey regions indicate correlated insulator states [either ferromagnetic insulators (FMI) or anti-ferromagnetic insulators (AFMI)], while the white regions denotes either metallic (M) or semi-metallic (SM) phases. Note that we employ the critical U^*/t values obtained from atomistic RPA calculations of tBLG [208].

such that V_{01} is strongly reduced. We find indeed that V_{01} decreases more quickly than V_{00}, but this *relative* reduction of V_{01} compared to V_{00} is not sufficient to overcome the large *absolute* reduction of V_{00} and, therefore, the overall balance is such that U^* decreases with decreasing ξ.

3.3.2 Correlated insulators

When U^*/t reaches a critical value, a phase transition from a (semi-)metallic phase to a correlated insulator state is expected. For tBLG, no consensus has yet been reached regarding the nature of the correlated insulator states, nor the corresponding value of the critical U^*/t. For Bernal stacked bilayer graphene, Quantum Monte Carlo calculations have found a critical value of 2.2 for a phase transition to a gapped antiferromagnetic phase [280]. Recently, Klebl and Honerkamp calculated the phase diagram of tBLG using an atomistic RPA approach [208]. For undoped tBLG (denoted $0e$), they find a transition from a semi-metal to an antiferromagnetic insulator, and for doping levels corresponding to two extra electrons ($-2e$) or holes ($+2e$) per moiré cell, a transition from a metallic phase to a ferromagnetic insulator is predicted. The RPA value for the critical U^*/t in tBLG is smaller than in the Bernal stacked bilayer, and depends both on temperature and doping. Because of the lack of self-energy corrections, the critical U^*/t values from the RPA should be considered as lower bounds [208].

In Fig. 3.6(b), the critical values of U^* for the cases of $0e$, $-2e$ and $+2e$ doping are indicated by horizontal dotted-dashed lines. Here, we have multiplied the critical $U_{\mathrm{p}_z}/t_{\mathrm{p}_z}$ values (where U_{p_z} and t_{p_z} denote the Hubbard and hopping parameters of carbon p_z-orbitals in tBLG) from Klebl and Honerkamp [208] at a temperature $T \approx 0.3$ K with the hopping parameter t between neighbouring Wannier functions (calculated from the width Δ of the flat bands in our atomistic tight-binding model using $t = \Delta/6$, which is the relation between bandwidth and hopping in graphene). While this procedure is not rigorous, we believe that the resulting critical U^*/t values for the flat-band electrons are useful estimates as there is a close connection between atomistic and low-energy Hamiltonians in tBLG [71]. Moreover, we note that our results for the critical gate distances that are derived from the critical U^*/t values are in good agreement with recent measurements [121, 122]. Future work should be carried out to determine the critical U^*/t values of the flat-band electrons in tBLG.

For the single-gate (double-gate) device, as the gate separation is reduced to $\xi_c = 5.86$ nm ($\xi_c = 8.14$ nm), U^* crosses the critical value for zero doping, indicating that tBLG would exhibit a semi-metallic phase at zero doping, but the correlated insulator states at $-2e$ and $+2e$ doping would remain. At $\xi_c = 2.21$ nm ($\xi_c = 3.56$ nm), the critical U^* for $-2e$ doping is crossed and finally, at $\xi_c = 0.89$ nm ($\xi_c = 1.74$ nm) the critical value for $+2e$ doping is reached. For even smaller values of ξ, the tBLG is either metallic or semi-metallic at the doping levels considered here. These results demonstrate that the phase diagram of tBLG can be controlled via the thickness of the dielectric substrate that separates the tBLG from the metallic gates and, hence, determines the degree to which the gate is able to screen electron-electron interactions in tBLG. The critical separations for phase transitions depend on the device configuration, with smaller values for single-gate devices because the screening is weaker than in double-gate devices.

The critical gate separation ξ_c also depends on the twist angle. Fig. 3.7 shows this dependence as a function of twist angle from the magic angle $\theta^* = 1.18°$ for the single-gate device configuration and for three doping levels: $-2e$ (left panel), $0e$ (middle panel) and $+2e$ (right panel) at $T \approx 0.3$ K. For all doping levels, ξ_c decreases as the magic angle is approached. Close to the magic angle, the hopping approaches zero and extremely small values of U^* must be achieved to reach the critical value of U^*/t. This is only possible for very small values of

ξ. Comparing the three doping levels, we find that ξ_c for the undoped system increases most rapidly away from the magic angle. At twist angles larger than 0.1° from the magic angle, the undoped system is always metallic and no phase transition to a correlated insulator phase can be induced. For $-2e$ doping, the critical twist angle window is larger than for zero doping. For $+2e$ doping, a critical thickness can be found for all considered twist angles near the magic angle. At larger temperatures, the critical value of U^*/t is smallest at charge neutrality [208], which means that charge neutrality will require the thinnest hBN slabs to reach the critical value for a phase transition to a (semi-)metallic state.

3.3.3 Superconductivity

The thickness ξ of the dielectric spacer layer also influences the stability of the superconducting state which competes with the correlated insulator states discussed above. To bind electrons into Cooper pairs, the effective electron-electron interaction must contain an attractive part V_{att} (this could arise either from electron-phonon coupling, exchange or spin fluctuations, plasmons or any other glue). The total interaction can be expressed as the sum of the bare Coulomb interaction and V_{att}. The superconducting transition temperature is approximately given by $T_{\mathrm{c}} \propto E_{\mathrm{glue}}/k_B \times \exp(-1/(\lambda - \mu^*))$, where λ describes the coupling of the electrons to the glue (which has an energy scale E_{glue}) and μ^* is the Coulomb pseudopotential, which describes the repulsion due to the bare Coulomb interaction [283] (k_B is the Boltzmann constant). In the presence of metallic gates, the repulsive bare interaction is reduced by the image charge interaction. As a consequence, μ^* is also reduced and has a dependence on the gate separation ξ. The presence of gates, therefore, should enhance the stability of the superconducting phase and increase the superconducting transition temperature, while reducing the stability of the correlated insulator states. Further calculations are required to quantitatively study the competition between superconductivity and correlated insulator states in the presence of metallic gates.

Chapter 4

Hartree interactions and magnetic order of twisted bilayer graphene

Not long after the initial discovery of correlated phases in tBLG [88, 89], Guinea and Walet demonstrated that Hartree interactions are the dominant energy scale in magic-angle tBLG [95]. Using a Hartree continuum model it was shown that the electronic structure is extremely sensitive to the doping level within the flat electronic bands, and that the van Hove singularities (VHS) are pinned at the Fermi level [95]. Interestingly, this is in contrast to graphene, where the electronic structure does not undergo qualitative changes, but electron interactions can renormalise the Fermi velocity [7, 9, 10].

For angles close to, but not exactly at, the magic angle, scanning tunnelling microscopy (STM) studies [129–131, 139] confirmed the predictions of Guinea and Walet [95]. Clear signatures of VHS pinning in the AA regions of tBLG were found from these STM measurements [129–131, 139]. At, or very close to, the magic angle, exchange interactions also become significant and cause the onset of correlated insulating states, which were also clearly seen in the STM experiments [129, 130, 139]. Moreover, close to the correlated insulating state at ±2 doping level, nematic order was observed which clearly broke the (approximate) C_3 rotational symmetry [129, 131, 139].

These findings demonstrated the importance of long-ranged electron-electron interactions for understanding tBLG [98, 111]. Subsequent work by several other groups [135–138] demonstrated that these long-ranged Hartree interactions result in significant interaction driven flattening of the bands (in addition to the band flattening induced by twisting [29, 32, 33, 37]). However, short-ranged electron-electron interactions are also extremely important in understanding strongly correlated systems [99].

The quintessential model for strongly interacting electrons is the Hubbard model [281, 282], in which electrons only interact when they are on the same "site" (typically assumed to be an atom). In tBLG near the magic angle, the moiré pattern results in the emergence of eight flat bands (including a factor of two from spin degeneracy) near the Fermi energy which are separated from all other bands by energy gaps [52, 55, 56, 67, 69]. Starting from atomistic tight-binding approaches[*], Hubbard models for tBLG can be obtained by constructing Wannier functions[†] of the flat bands [73, 75]. The properties of such models have been studied using Quantum Monte Carlo [263], functional renormalisation group [108] and exact diagonalization [97] resulting in many important insights into the origin of superconductivity and correlated insulator states. Instead of using flat-band Wannier functions as a basis, it is also possible to construct atomistic Hubbard models using a basis of carbon p_z orbitals [11, 205, 208, 284].

Accurate models of tBLG should, however, capture both short-ranged and long-ranged electron-electron interactions [125]. Several groups used Hartree-Fock calculations based on a continuum model of the electronic structure [66, 143, 258–261]. These calculations have yielded many useful insights, but they do not capture atomic-scale interactions (such as on-site interactions within carbon p_z-orbitals) and often only include a few bands near the Fermi level with the effect of all other bands being described by an effective dielectric constant. Few groups have attempted to capture the interplay of long-ranged and short-ranged interactions using atomistic calculations: González and Stauber [285, 286] studied the properties of tBLG in different dielectric environments using atomistic Hartree-Fock theory, and Sboychakov *et al.* [287, 288] developed an atomistic Hubbard model with electron-electron interactions up to nearest neighbour. These studies only considered the properties of tBLG at a single twist angle and, therefore, did not study in detail the interplay of long-ranged and short-range interactions as a function of doping and twist-angle.

---

[*] Note that the flat band Wannier functions cannot be constructed from a continuum model of a single valley because of the fragile topology of these bands [72, 77–80]. In that case, additional bands must be included in the Wannierization procedure, either through remote bands of a single valley or from mixing the two valleys [80, 81].

[†] Note that Hubbard models using a basis of flat-band Wannier functions account for some long-ranged interactions because of the large size of the Wannier orbitals [68, 73, 75].

In this chapter, results for how electron interactions affect the magnetic order of tBLG are presented. Initially, the normal state of tBLG is investigated, with a focus on the effects of Hartree interactions when the system is doped, where significant interaction-induced band-flattening occurs. This leads to the investigation of how the interaction-driven band-flattening affects the prevalence of magnetic phases in tBLG. Section 4.1 on Hartree interactions in the normal state of tBLG is heavily based on Ref. 137 [Goodwin *et al.* Electron. Struct. 2:034001, 2020]. While Section 4.2 is mainly based on Ref. 125 [Klebl, Goodwin *et al.* Phys. Rev. B 103:195127, 2021]. The final section of this chapter presents mean-field Hubbard calculations of tBLG. Below I summarise my contribution and those of my collaborators of Refs. 125, 137.

In Ref. 137, I performed practically all of the work that was published. I shall mainly summarise what was done by others, with the remaining work being my own contribution (a brief description shall be given). Valerio Vitale helped to write the initial version of the script for the self-consistency algorithm for numerically evaluating the atomistic Hartree theory. He also helped with discussions of the results. Xia Liang* contributed the relaxed structures which were used in the calculations. Johannes Lischner and Arash Mostofi conceived the project, guided its progression and helped in writing the paper. I wrote all other modules of the code for evaluation of the self-consistency algorithm (generating lattice parameters and importing atomic positions, building and diagonalising the Hamiltonian, finding the Fermi energy, calculating the electron density, and computing the Hartree potential). I also tested and modified the code substantially from the first version on my own, and then generated all results shown in the paper.

In Ref. 125, I was the second author of the paper, with Lennart Klebl being the first author. Lennart performed the calculations of the RPA spin-susceptibility and generated the figures related to those calculations (this was the main novel part of that paper). He also helped write the paper and contributed to discussions. I initiated the project with Lennart following the work described in Ref. 137, after self-consistent Hubbard calculations (some results of which are shown in Section 4.3) proved too computationally demanding to achieve our goals. I contributed

---

[*] A UROP and MEng project student who was predominantly under my supervision.

the figures related to Hartree theory and wrote most of the paper. Dante Kennes, Johannes Lischner and Arash Mostofi helped in the discussion of the results and writing the paper.

It is worth noting that slightly different tight-binding parameters have been used in Section 4.1 compared to Sections 4.2 and 4.3. Whilst this does not qualitatively change any of our conclusions, it does cause a slight change in the magic angle. Therefore, care should be taken when making comparisons between the electronic structure calculations of Section 4.1, and Sections 4.2 and 4.3.

4.1 Hartree interactions in twisted bilayer graphene

4.1.1 Band structure

Figure 4.1 shows the band structures* of tBLG suspended in air† from Hartree theory at six twist angles between $\theta = 1.54°$ and $\theta = 1.05°$. Only the four flat bands closest to the Fermi energy are shown. We refer to the lower two of the flat bands as the flat valence bands and the upper two as the flat conduction bands. These four bands are separated from all other bands by energy gaps that result from the atomic corrugation of tBLG [53, 58, 64, 68, 69, 75]. The width of the flat band manifold is smallest at $\theta = 1.16°$ and we refer to this twist angle as the magic angle.

We first discuss the band structures of undoped tBLG, corresponding to $\nu = 0$ (black curves in Fig. 4.1). The band structures at all twist angles except the magic angle are semi-metallic and feature linear bands at the K and K′ points. As the magic angle is approached, the total width of the flat band manifold decreases rapidly, see Fig. 4.2(a). Interestingly, at charge neutrality, the valence band widths are always smaller than the conduction band widths, see Figs. 4.2(c) and (d).

At the magic angle, the band structure of undoped tBLG is qualitatively different as compared to the other twist angles [65, 69]. In particular, the two valence bands at Γ are pushed

---

*The structure was generated from LAMMPS with a 2.42 Å lattice constant of graphene. The tight-binding parameters for these calculations were $a = 1.39$ Å, $d = 3.35$ Å, $q_\pi = 7.43$ and $q_\pi = 3.14$, with a spherical Heaviside step function with cut-off of 10 Å being used to truncate hopping parameters, which gave a magic angle of tBLG at 1.16°.

†As introduced by a dielectric constant of $\epsilon = 1$. Later we show that a dielectric substrate only leads to small change in the Hartree band structures.

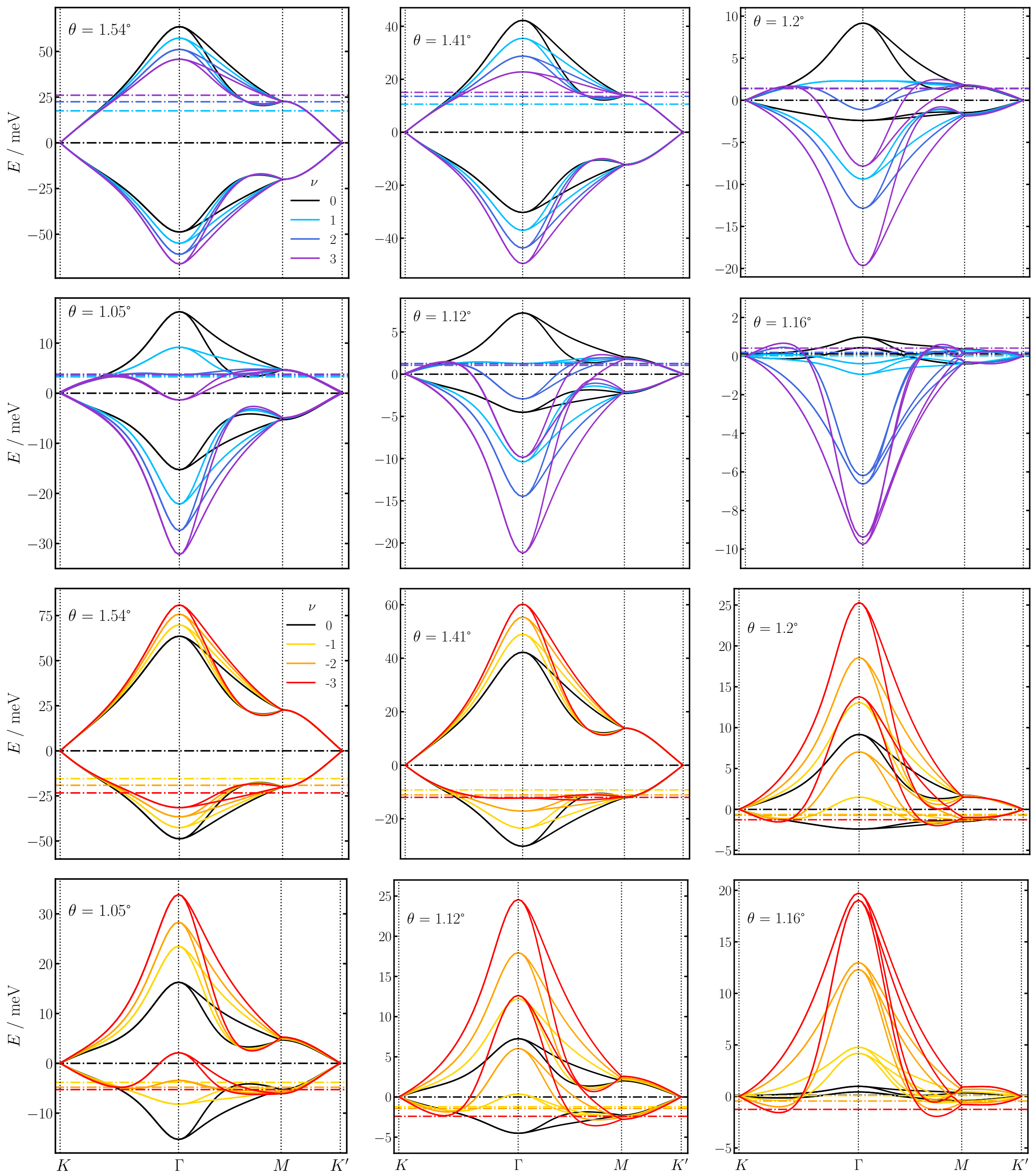

Figure 4.1: Atomistic Hartree band structures of twisted bilayer graphene for various twist angles θ and doping levels ν, assuming Coulomb interaction with dielectric constant of $\epsilon = 1$. Band structures of electron-doped (hole-doped) tBLG are shown in the upper (lower) two rows; the undoped case (black line) is shown in all panels. The Fermi level is denoted by horizontal dash-dotted lines. For clarity, the energy at the K-point is used as reference in all graphs and only the four flat bands near the Fermi level are shown. Note that the width of the flat band manifold, and therefore also the scale of the vertical axis, depends sensitively on the twist angle, as shown in Fig. 4.2. The width of the flat band manifold is smallest at $\theta = 1.16°$.

up and are now higher in energy than the states at K and K′. As a consequence, at this level of theory, tBLG is metallic at the magic angle, even without doping with additional carriers.

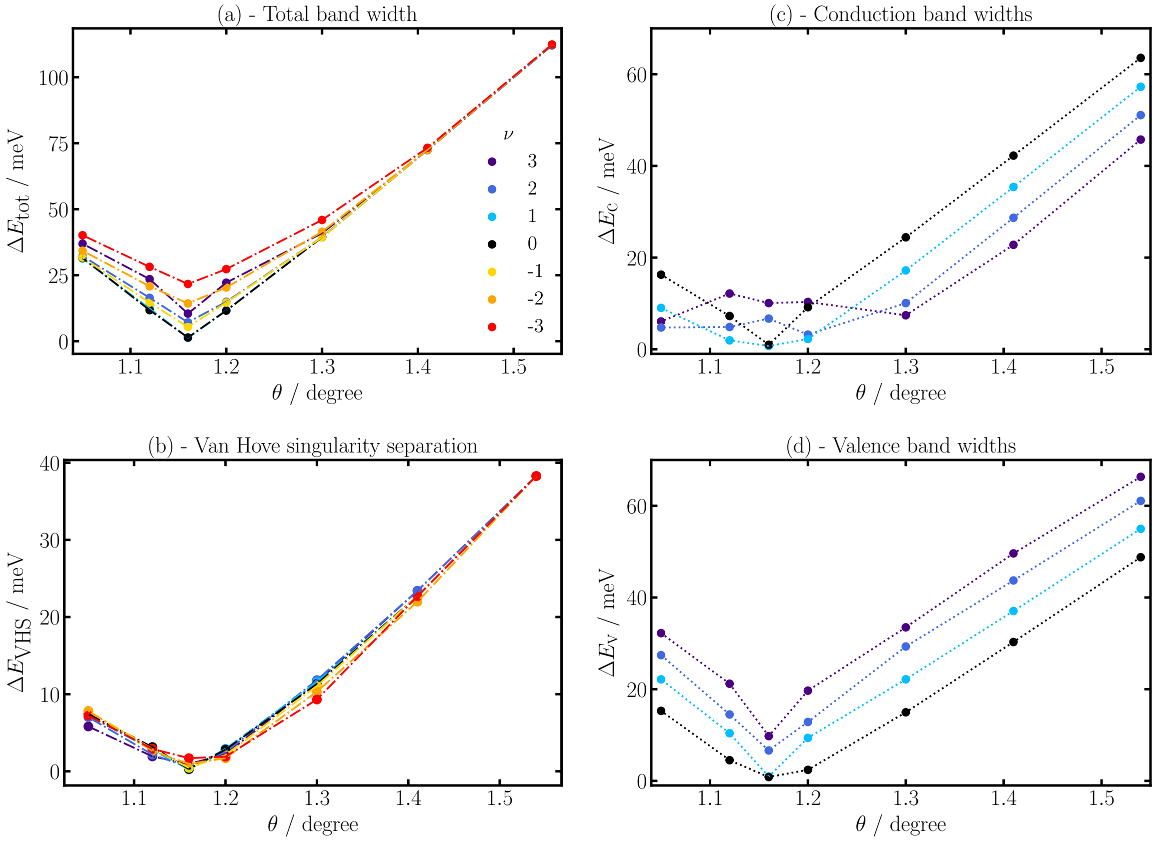

Figure 4.2: (a) - Width of the flat band manifold ΔE_{tot} as a function of twist angle for different doping levels. (b) - Energy separation of the valence and conduction VHS ΔE_{VHS} as function of twist angle for different doping levels. (c) - Width of the flat conduction bands ΔE_{c} as function of twist angle for different doping levels $\nu \geq 0$. (d) - Width of the flat valence bands ΔE_{v} as function of twist angle for different doping levels $\nu \geq 0$. In all cases we assume dielectric screening of $\epsilon = 1$.

The Hartree band structures of undoped tBLG are very similar to the non-interacting tight-binding band structures [95, 136, 137]. This can be understood by analysing the charge density and the corresponding Hartree potential. Without doping each region of the moiré unit cell is approximately charge neutral (when the atomic oscillations are averaged over a region) [136] resulting in a small Hartree potential, as we shall discuss further later.

Figure 4.1 also shows Hartree band structures for electron-doped (upper two rows) and hole-doped (lower two rows) tBLG. In agreement with previous Hartree calculations [95, 135, 136], we observe that doping results in significant changes in the band structures. In contrast, the tight-binding band structures that are widely used to understand the electronic properties of doped tBLG do not change upon doping. Focusing first on the largest twist angle considered, $\theta = 1.54°$, electron doping (corresponding to $\nu = 1$, 2 or 3) flattens the conduction bands, while the valence bands become more dispersive. Figure 4.2(c) shows that the conduction band width decreases by approximately 5 meV for each added electron. However, the valence band width increases by the same amount [Fig. 4.2(d)] and the total band width of the flat band manifold remains constant at this twist angle, as shown in Fig. 4.2(a). For hole doping ($\nu = -1$, -2 and -3), the situation is similar but the valence bands flatten and the conduction bands become more dispersive.

To understand why electron-electron interactions are more relevant for the doped system, we analyse again the charge density and the corresponding Hartree potential (the explanation here follows that outlined by Rademaker *et al.* in Ref. 136). As the local density of states is larger in the AA regions than in the AB/BA regions, additional carriers (both electrons and holes) preferentially localise in the AA regions [136]. This creates a highly non-uniform charge distribution, which gives rise a strong Hartree potential [136]. Fig. 4.6(a) shows that ΔV_{H} (the difference between the Hartree potential in the centres of the AA and AB regions) increases by approximately 30 meV for each added electron. States near the K and K′ points are localised in the AA regions and are pushed up in energy relative to the states at Γ (which have a ring-like shape surrounding the AA regions) for electron-doped systems [136, 289]. In contrast, the K/K′ states are pushed down in energy relative to the Γ-states for hole-doped systems [136].

For smaller twist angles, doping induces even more significant changes in the band structure. At $\theta = 1.41°$, the valence bands are almost completely flat between Γ and M for $\nu = -3$. In contrast, the flattening of the conduction bands upon electron doping is not quite as pronounced at this twist angle. For $\theta = 1.2°$, the Γ-states have moved past the K/K′-states so that the curvature of the conduction band at Γ changes sign at all doping levels (both electron and hole doping) except $\nu = 1$. For this doping level, the conduction band is very flat in the vicinity of the Γ-point. Interestingly, for $\nu = 2$ the width of the conduction bands exhibits a local minimum at $\theta = 1.2°$, see Fig. 4.2(c), and is even smaller than at the magic angle. Similarly, for $\nu = 3$ the width of the conduction bands exhibits a local minimum at $\theta = 1.3°$. This suggests that long-ranged Coulomb interactions between electrons can modify the twist angle at which electron correlation phenomena are strongest and that this may not necessarily be at the magic angle.

These qualitative changes in the band structures of doped tBLG close to the magic angle can be understood by analysing the twist angle dependence of the Hartree potential. Fig. 4.6(a) shows that ΔV_{H} only depends weakly on the twist angle. In contrast, the band widths decrease rapidly as the magic angle is approached and therefore the importance of long-ranged electron-electron increases strongly.

At the magic angle ($\theta = 1.16^\circ$), the band structures of hole-doped tBLG ($\nu = -1$, -2 and -3) look qualitatively similar to the undoped band structure, but with a significantly larger band width. For example, for $\nu = -2$ we find a band width of 13 meV (compared to 1 meV for the undoped system). For electron-doped systems, the conduction bands 'invert' such that both the valence and conduction bands at Γ are at lower energies than the states at K and K$'$.

For twist angles smaller than the magic angle, the band structures of doped tBLG are quite similar to those of twist angles larger than the magic angle. In particular, the band structures at $\theta = 1.12^\circ$ correspond closely to those of $\theta = 1.2^\circ$ (both differ from the magic angle by 0.04°) and the band structures of $\theta = 1.05^\circ$ are similar to those of $\theta = 1.3^\circ$ (which differ from the magic angle by 0.11° and 0.14°, respectively).

4.1.2 DOS and LDOS

Figures 4.3 and 4.4 show the DOS and LDOS[*] from Hartree theory for three twist angles: $\theta = 1.54^\circ$ [panel (a)], $\theta = 1.41^\circ$ [panel (b)] and $\theta = 1.2^\circ$ [panel (c)]. The LDOS is shown both for the AA (solid lines) and AB (dash-dotted lines) regions, averaged over a region around the centre of the respective region[†]. When the tunnelling matrix elements are constant (which is likely a good approximation for the flat bands of tBLG), the LDOS is proportional to the measured tunnelling spectrum and thus directly accessible in experiments. Several STM studies of tBLG have been reported recently [129–131] and we will discuss the similarities and differences of our calculations with these experimental measurements. Below, we analyse each of the three twist angles in turn.

---

[*] In order to calculate the DOS, we sample the first Brillouin zone using approximately 6,000 k-points and represent the contribution from each energy level as a gaussian. A similar procedure is used for the LDOS.

[†] The LDOS is averaged over atoms within a radius of 15 Å [we found that the results do not depend qualitatively on the radius chosen, provided it is larger than the length scale of the carbon-carbon bond length $\mathcal{O}(1$ Å$)$ and smaller than the moiré length scale $\mathcal{O}(10$ nm$)$].

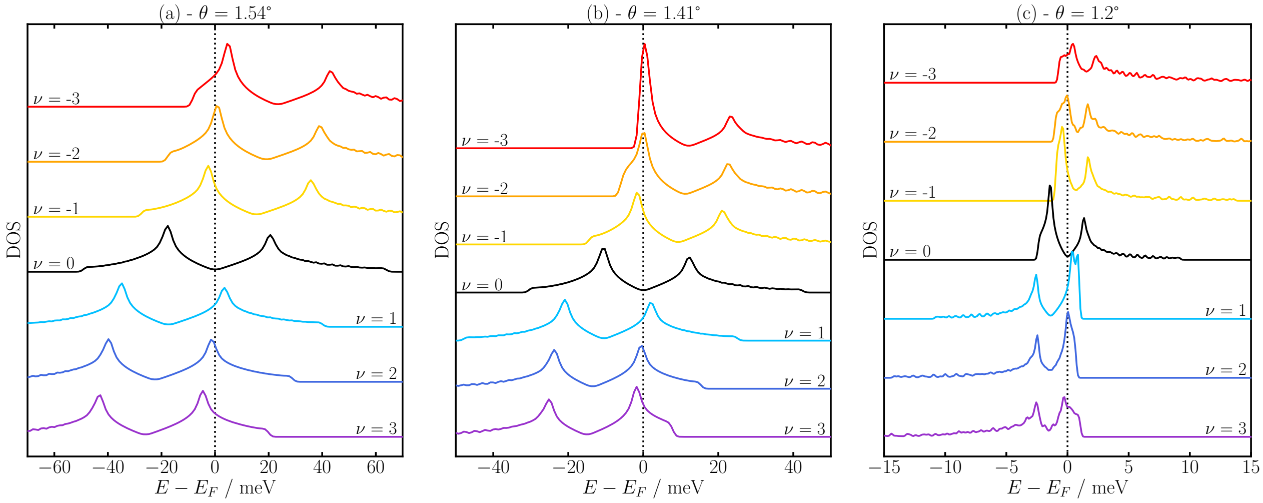

Figure 4.3: Doping-dependent densities of states (DOS) of twisted bilayer graphene (suspended in air) for three twist angles near the magic angle. The dotted vertical line denotes the Fermi level.

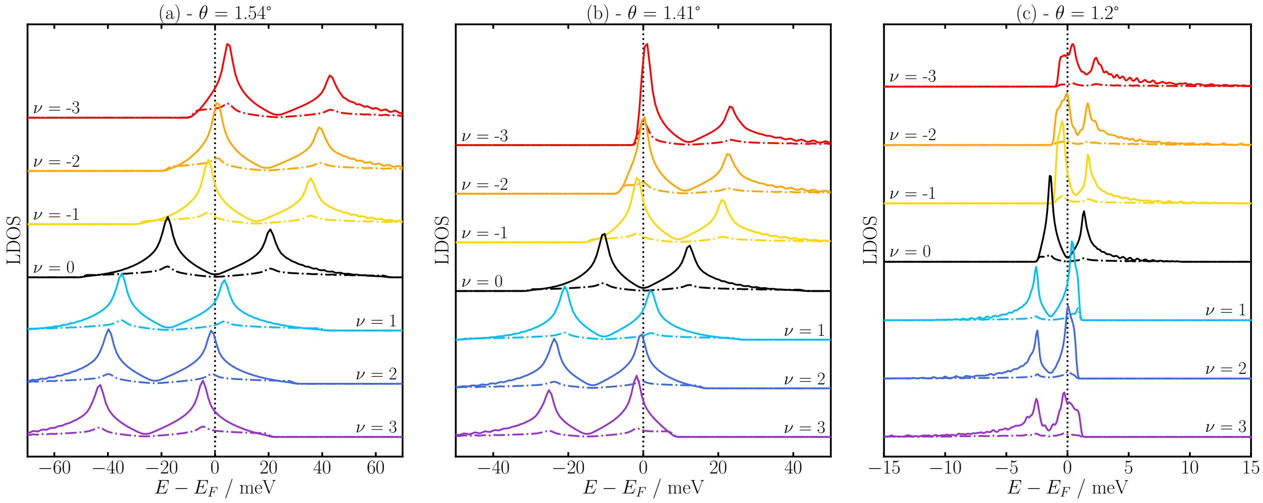

Figure 4.4: Doping-dependent local densities of states (LDOS) in the AA (solid curves) and AB (dash-dotted curves) regions of twisted bilayer graphene (suspended in air) for three twist angles near the magic angle. The dotted vertical line denotes the Fermi level.

For $\theta = 1.54°$, the DOS exhibits two pronounced peaks at all doping levels. At zero doping, these VHS are located at ±20 meV on both sides of the Fermi energy. Comparing the DOS to the LDOS, we find that the dominant contribution to the DOS derives from the AA regions [32]. The LDOS in the AB regions also exhibits small peaks in the vicinity of the VHS. The valence band VHS is somewhat larger than the conduction band one because the valence bands are flatter than the conduction bands, see Fig. 4.1. These findings are in agreement with several recent experimental STM measurements [129–131]. Note, however, that our values for the energy difference between valence and conduction VHS are smaller (for the same twist angle) than the experimental results. In Ref. 129, this was attributed to the use of DFT-derived tight-binding parameters for the intralayer hopping which are about 20 percent smaller than more accurate GW values.

Upon electron doping, the conduction VHS becomes larger while the valence VHS becomes smaller. This is a consequence of the doping-induced band flattening of the conduction bands, while the valence bands become more dispersive, see Fig. 4.1. In contrast, hole doping increases the valence VHS while the conduction VHS becomes smaller. Again, these findings are in agreement with several recent experimental measurements [129, 130] and cannot be explained by tight-binding theory. Note that at this twist angle the Fermi level of the doped system is not pinned at the VHS.

At $\theta = 1.41^\circ$, the separation between the VHS is reduced to 30 meV. Upon hole doping, the difference between valence and conduction band VHS is much clearer than at 1.54°. This is caused by the strong distortion of the doped valence bands resulting in extremely flat valence bands throughout large regions of the Brillouin zone*, see Fig. 4.1. For $\nu = -2$ and $\nu = -3$, we observe that the Fermi level is pinned at the valence VHS. This Fermi level pinning has also been reported in several experimental STM studies and is a consequence of electron-electron interaction induced changes in the band structure. The LDOS in the AA region is again very similar to the DOS. However, we find that the valence peak of the LDOS in the AB regions grows upon hole doping. This is because the wave functions of the flat valence bands are partly localised in the AB regions (in particular, the valence states near Γ). This prediction can be tested by STM measurements and would provide direct evidence of the doping-induced band flattening in Hartree theory. Figure 4.2(b) shows that the separation of the VHS is reduced by hole doping for twist angles larger than the magic angle and increased by electron doping. The opposite trend is observed for twist angles smaller than the magic angle. While this is in qualitative agreement with some experimental measurements, the absolute magnitude of the change in VHS separation is typically smaller than in experiments [44, 46, 47, 49, 87, 129–131, 139, 140].

Besides Fermi level pinning, the enhancement of the DOS at the Fermi level due to the doping-induced flattening of the partially occupied bands is also relevant for understanding broken-symmetry phases, such as correlated insulator or superconducting states [98]. In particular, the values of the transition temperatures to these states are usually very sensitive to the DOS at the Fermi energy [98], DOS(E_F). For example, the superconducting critical transition temperature is given by $T_\mathrm{c} \propto \exp\left(-1/[\mathrm{DOS}(E_\mathrm{F})V]\right)$ with V describing the coupling strength of the electrons to the superconducting glue (e.g., phonons or spin waves). The doping-induced increase of the DOS at the Fermi level should therefore result in a dramatic increase of the critical temperature.

---

*Recall that the distortion of the valence bands is always more pronounced than that of the conduction bands because the valence bands usually have a smaller width.

At $\theta = 1.2°$, very close to the magic angle, the VHS separation is only 5 meV in the undoped system and the valence VHS is much larger than the conduction VHS. Fermi level pinning is observed both for electron and hole doping. In the DOS, the shape of the VHS of the partially filled band is highly asymmetric. In particular, the leading edge of the peak (i.e., the side of the peak facing towards the other VHS) rises more sharply than the trailing edge (i.e., the side facing away from the other VHS). Interestingly, we also observe a double peak in the conduction VHS at $\nu = 1$. The second peak is caused by a peak of the LDOS in the AB regions which does not coincide with the main peak of the LDOS in the AA regions. Again, this double peak structure is caused by the electron-electron interaction induced distortion of the conduction band near Γ. Figure 4.1 shows that the conduction bands are extremely flat near Γ, but have a slightly higher energy than the states at M which give rise to the main peak of the VHS.

4.1.3 Environmental screening

So far, we have presented results for tBLG suspended in air ($\epsilon = 1$). In experiments, however, the tBLG is placed on or sandwiched by a dielectric substrate, typically hexagonal boron nitride (hBN), and the presence of this dielectric environment screens the interaction between electrons in the tBLG [88, 89, 93, 114, 120, 129–131]. In transport experiments, the dielectric substrate separates the tBLG from a metallic gate which is used to control the charge density in the tBLG and the presence of gates further modifies the effective interaction between the electrons in the tBLG.

Figure 4.5(a) compares Hartree band structures of electron-doped tBLG ($\nu = 2$) at $\theta = 1.54°$

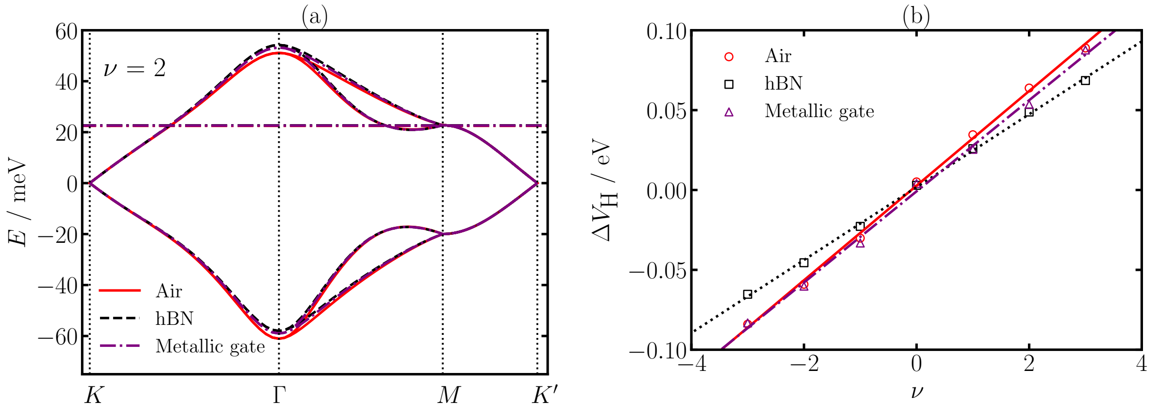

Figure 4.5: (a) - Band structure of electron-doped ($\nu = 2$) twisted bilayer graphene suspended in air ($\epsilon = 1$; red solid lines), encapsulated by hBN ($\epsilon = 3.9$; black dashed lines) and encapsulated by hBN with metallic gates at a distance of 10 Å (purple dash-dotted line). (b) - Corresponding values of ΔV_{H} defined as the difference of the Hartree potential energy in the centres of the AA and the AB regions. The twist angle is $\theta = 1.54°$.

(similar band width to that of the experiments in Ref. 129) with $\epsilon = 1$ (tBLG suspended in air) and $\epsilon = 3.9$ (tBLG sandwiched by thick layers of hBN). Surprisingly, the difference between the two band structures is small on the scale of the band width of the flat bands (similar band widths to those in experiments too). To understand this finding, we analyse the Hartree potentials of the two systems. Fig. 4.5(b) shows ΔV_{H} (the difference between the Hartree potential in the centres of the AA and AB regions) as a function of doping for the two cases. While one might naively expect that the slope of ΔV_{H} should be reduced by a factor of $\epsilon_{\mathrm{bg}} = 3.9$ when the dielectric environment is included, we find that the reduction is much smaller (ΔV_{H} is only reduced by 30% when the dielectric environment is included).

The inclusion of metallic gates on both sides of hBN-encapsulated tBLG at a distance of 10 nm for a twist angle of 1.54° also has little effect on the band structure [Fig. 4.5(a), purple dash-dotted line] because the Hartree potential does not change significantly, as shown in Fig. 4.5(b). It is worth noting that most experiments use larger gate distances than 10 nm which would result in an even smaller effect. Recently, experiments employing very small gate distances reported dramatic changes of the electronic phase diagram and suggested that these were induced by changes in the environmental screening [122]. While further work is required to study the effect of metallic gates for small gate distances and twist angles very close to the magic angle, we stress that the phase diagram is determined by the relative stability

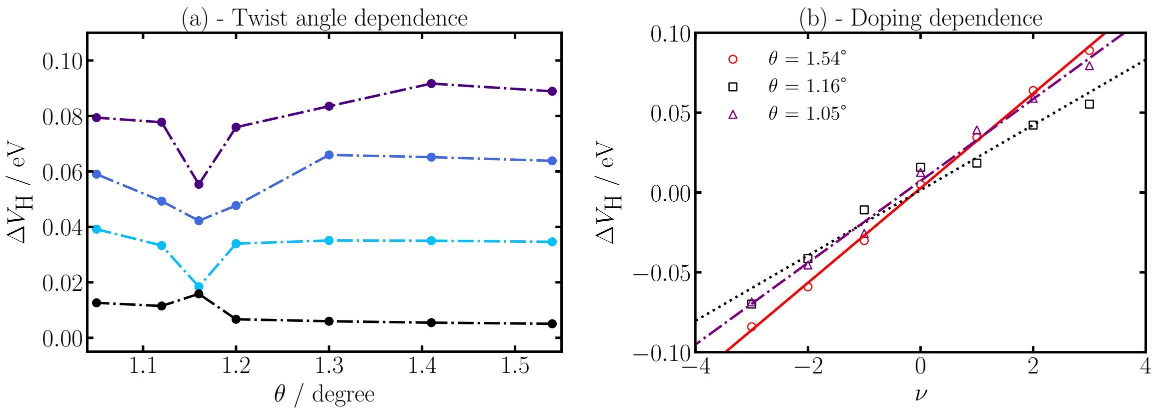

Figure 4.6: (a) - Hartree potential difference ΔV_{H} between the AA and AB region as a function of twist angle for undoped (black) and electron-doped twisted bilayer graphene for $\nu = 1$ (cyan), $\nu = 2$ (blue) and $\nu = 3$ (purple). (b) - ΔV_{H} as function of doping for three twist angles near the magic angle and linear fits obtained from Eq. (4.1).

$\theta°$	V(θ) / meV	$\nu_0(\theta)$
1.54	6.57	−0.080
1.41	6.63	−0.087
1.30	5.98	−0.174
1.20	5.23	−0.192
1.16	—	—
1.12	5.22	−0.236
1.05	5.51	−0.240

Table 4.1: Coefficients for the Hartree potential fit, Eq. (4.1). The magic angle cannot be accurately reproduced with this fit so we do not provide parameters here.

of the competing phase, i.e. the total energy differences. It is possible that relatively small changes in the dielectric screening can change the relative stability of the competing phases and thereby lead to drastic changes in the phase diagram, while only mildly affecting quasiparticle properties.

This surprising robustness of the Hartree band structure of tBLG towards changes in the dielectric environment has two reasons. First, the weakening of the Coulomb repulsion by the dielectric substrate allows for a greater inhomogeneity of the charge density. This results in a larger Hartree potential energy than the one that would have been obtained if the charge density had been frozen in its unscreened configuration. Second, the change in the dielectric environment only leads to small changes in the total screening response because the internal screening of the tBLG is already quite strong [255, 256].

In Fig. 4.6 we show how ΔV_{H} changes as a function of twist angle and doping. It can be seen that there is little change as a function of twist angle (with the exception of the magic angle) and that ΔV_{H} changes approximately linearly with doping. Except at the magic angle, the doping and twist-angle dependent atomistic Hartree potential energy is accurately described by*

$$V_{\mathrm{H}}(\mathbf{r}) \approx V(\theta)(\nu - \nu_0(\theta)) \sum_{j=1,2,3} \cos(\mathbf{G}_j \cdot \mathbf{r}), \tag{4.1}$$

where $\nu_0(\theta)$ is the doping level where the Hartree potential vanishes, $V(\theta)$ is a twist angle dependent energy parameter and $\mathbf{G}_j$ denote the three reciprocal lattice vectors that are used to describe the out-of-plane corrugation of tBLG in Ref. 68. Interestingly, this equation is very similar to the continuum model of Refs. 95, 135, where only the shortest Fourier components are retained in the Hartree potential. Therefore, the continuum model and atomistic model are in excellent agreement. Table 4.1 shows the optimal values of these parameters for the twist angles that we have studied and Fig. 4.6(b) compares the fit to the calculated Hartree potential as function of doping for different twist angles. Using Eq. (4.1) as an on-site energy in a tight-binding calculation allows the determination of Hartree-theory band structures without the need for self-consistent calculations. We believe that this approach is a useful starting point for understanding broken symmetry phases in doped tBLG.

4.2 Importance of Hartree interactions for magnetic order

To investigate magnetic ordering tendencies of tBLG including the effect of long-ranged interactions, we calculate the interacting static spin susceptibility in the normal state using a Hartree theory plus U (Hartree+U) approach. In this approach, Hubbard interactions within the carbon p$_z$-orbitals are captured by adding a Hubbard contribution $U \sum_i n_{i\uparrow} n_{i\downarrow}$, with U denoting the Hubbard parameter and $n_{i\uparrow}$ ($n_{i\downarrow}$) denoting the occupancy of the up (down)-spin p$_z$-orbital on carbon atom i [11], to the Hartree theory [we use Eq. (4.1) with $V(\theta) = 5\,\mathrm{meV}$ and $\nu_0(\theta) = 0$].

---

*Note that Eq. (4.1) assumes that the AA regions reside in the corners of the rhombus-shaped moiré unit cell.

This approach assumes that the spatial range of the exchange interaction is strongly reduced as a result of electronic screening induced by the flat bands [255, 256, 290]. Moreover, it has been shown that models with short-ranged Hubbard-type exchange interactions accurately describe the magnetic phase diagram of graphene and bilayer graphene bilayer [6, 280, 291], which can be viewed as "parent" systems whose ordering tendencies are inherited by the tBLG [208].

4.2.1 Band structures

Figure 4.7 shows the band structures* from Hartree theory at three twist angles near the magic angle ($\theta = 1.41°$, $1.20°$ and $1.05°$) at various doping levels. For comparison, we also show the corresponding tight-binding results. For the two larger twist angles, both the Hartree and tight-binding band structures exhibit Dirac cones at the K and K′ points. While the non-interacting tight-binding band structure does not depend on the doping level, long-ranged electron-electron interactions captured by Hartree theory give rise to a significant doping-dependent distortion of the band structure [95, 135–138]. In particular, Hartree interactions result in a flattening of the doped bands. For example, at $\theta = 1.20°$ and $\nu = 3$ the two higher-energy bands are much flatter than the corresponding tight-binding bands.

The magic angle (defined as the twist angle with the smallest width of the flat band manifold from tight-binding) is found to be 1.05°. At this twist angle, the tight-binding band structure differs qualitatively from the result at larger (and smaller) twist angles. In particular, the lower-energy bands are inverted and have a similar shape to the higher-energy bands. Including long-ranged interactions again results in drastic changes to the band structure with Hartree theory predicting an increase of the overall flat band width when the system is doped. Also, the overall shape of the flat band manifold is flipped when comparing hole-doped and electron-doped systems.

---

*The structure was generated from LAMMPS with a 2.42 Å lattice constant of graphene. The tight-binding parameters for these calculations were $a = 1.39$ Å, $d = 3.2912$ Å, $q_\pi = 7.39$ and $q_\pi = 3.13$, with a spherical Heaviside step function with cut-off of 10 Å being used to truncate hopping parameters, which gave a magic angle of tBLG at 1.05°.

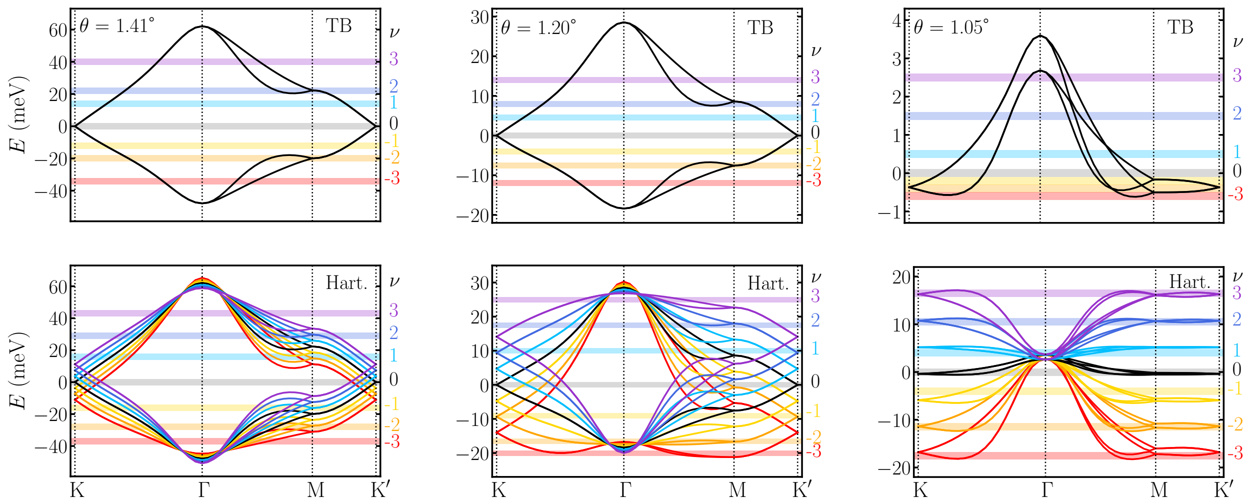

Figure 4.7: Band structures of tBLG at twist angles of 1.41°, 1.20° and 1.05° for integer fillings ν of the flat bands from tight-binding (denoted TB, see upper panels) and Hartree theory (denoted Hart., see lower panels). Fermi levels are indicated by horizontal lines. In contrast to Hartree theory, the tight-binding band structure does not depend on ν. Note that the energy scale on the y-axis is different in each panel. The zero of energy for each plot is taken to be the Dirac point energy from tight-binding.

4.2.2 Magnetic phase diagram

Next, we calculate the interacting spin susceptibility from Hartree+U theory as function of doping at a wide range of twist angles near the magic angle (0.96°, 0.99°, 1.02°, 1.05°, 1.08°, 1.12°, 1.16° and 1.20°). Figure 4.8 compares the critical Hubbard parameter U_c without Hartree interactions (left panel) and with Hartree interactions (right panel) as function of twist angle and doping. To assess if the system undergoes a phase transition, U_c must be compared with the actual value of U for a carbon p_z-orbital. In graphene, Wehling *et al.* [236] and Schuler *et al.* [109] found that $U \approx 4$ eV. We expect that screening from tBLG does not significantly alter this value, as the flat bands mainly screen long-ranged interactions [255, 256]. Therefore, we assume a doping and twist angle independent value of $U \approx 4$ eV in the following analysis.

Without Hartree interactions (left panel of Fig. 4.8), magnetic instabilities are found at twist angles ranging from 0.99° to 1.12°. At the magic angle ($\theta = 1.05°$), instabilities occur at all integer doping levels except $\nu = 2$. At twist angles smaller or larger than the magic angle, instabilities are observed for a smaller set of doping levels. In particular, for $\theta = 0.99°$ and $\theta = 1.12°$, they only occur at $\nu = -1$. In general, the critical Hubbard parameters are smaller for hole doped systems because the lower-energy flat bands are somewhat flatter than

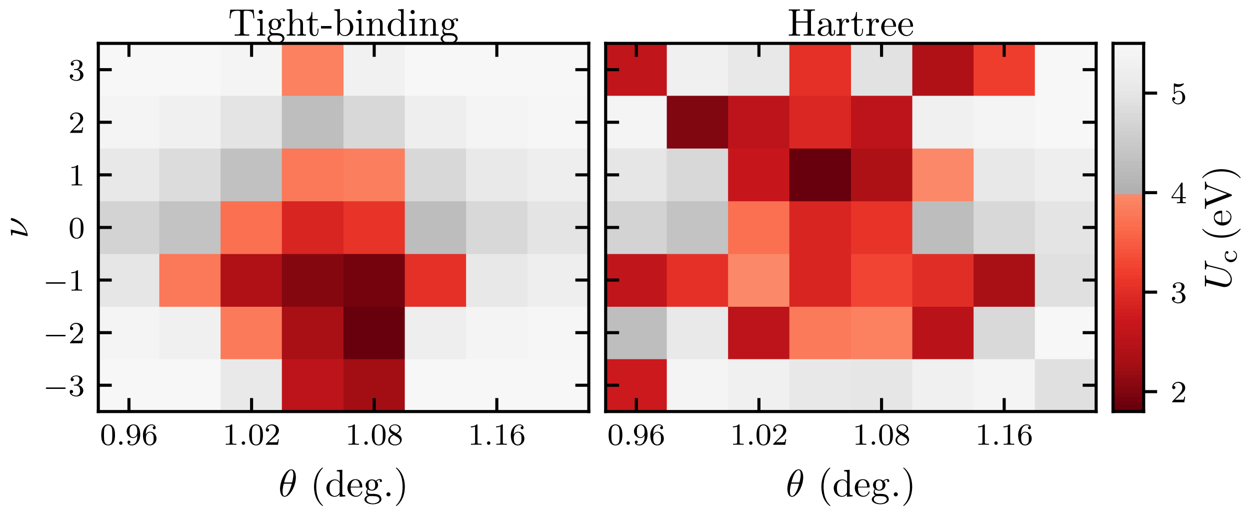

Figure 4.8: Critical Hubbard interaction strength U_c required for the onset of magnetic instabilities as a function of flat band filling ν and twist angle θ. Left panel: without Hartree interactions (tight-binding). Right panel: with Hartree interactions.

the higher-energy ones in tight-binding. For twist angles larger than 1.2°, we find $U_\mathrm{c} \approx 5.5\,\mathrm{eV}$, which is similar to the value predicted for untwisted bilayer graphene [208].

When Hartree interactions are included (right panel of Fig. 4.8), a qualitatively different behaviour of U_c is observed near the magic angle. In particular, the lowest values of U_c are now found for electron-doped systems. Very close to the magic angle, U_c is lowest for $\nu = 1$. At twist angles somewhat smaller or larger than the magic angle, the lowest value of U_c is at $\nu = 2$ and at $\theta = 0.96^\circ$ or 1.16° the minimum is at $\nu = 3$. These findings can be understood from the Hartree theory band structures, as seen in Fig. 4.7, which show that the doping level which gives rise to the flattest bands depends on the twist angle: at the magic angle the flattest bands are found at $\nu = \pm 1$, while at $\theta = 1.20^\circ$ the higher-energy bands are extremely flat at $\nu = \pm 3$. Figure 4.8 also shows that magnetic instabilities occur over a larger twist angle range when long-ranged Hartree interactions are included. Specifically, the Hartree+U approach predicts such instabilities for a twist-angle window from $\theta = 0.96^\circ$ to $\theta = 1.16^\circ$. This larger critical twist angle window is consistent with experimental findings: recent transport and tunnelling experiments reported correlated phases in a twist angle range from 1.0° to 1.2° [98, 141].

Next, we analyse the spatial structure of the magnetic phases: the leading magnetic instabilities are either Ångström scale anti-ferromagnetic with a modulation on the moiré scale (MAFM), Ångström scale anti-ferromagnetic with nodes in the AB and BA regions (NAFM)

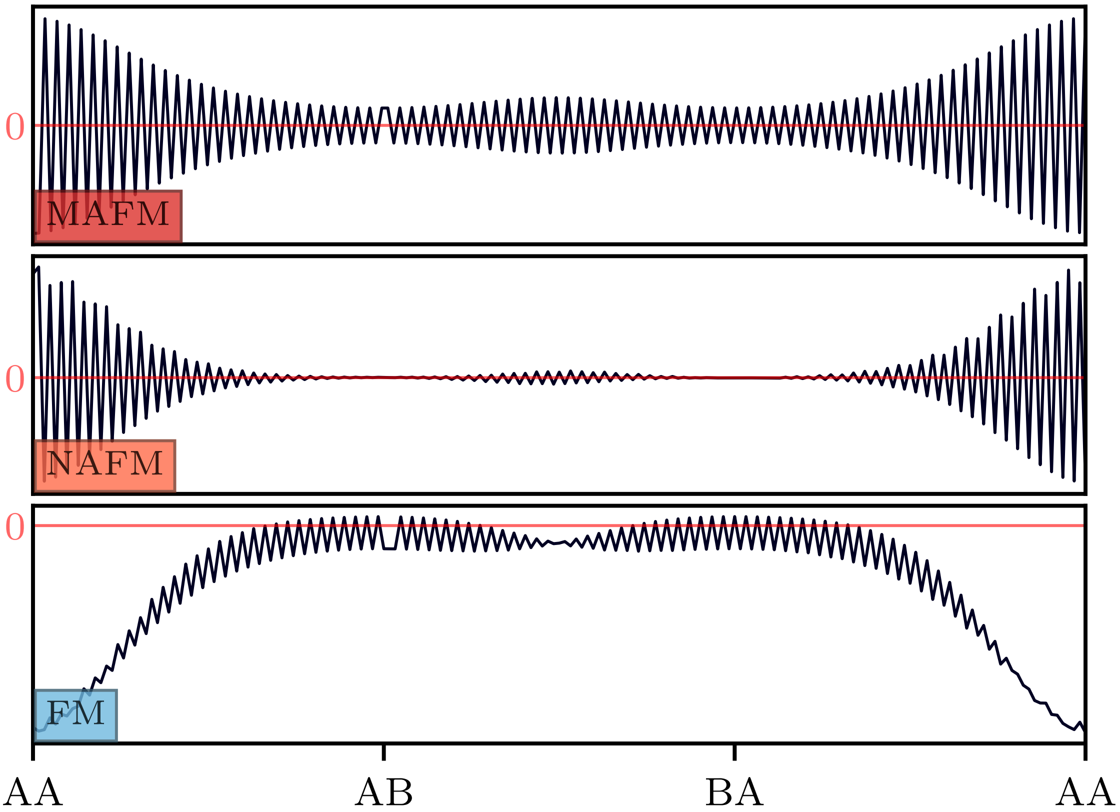

Figure 4.9: Leading magnetic orderings in twisted bilayer graphene near the magic angle. Shown is a line-cut of the magnetic order parameter (spin density) along the diagonal of the rhombus-shaped moiré unit cell. The line-cut is chosen to include the atoms that are closest to the actual line connecting one AA region with the next. Thus, at some point, there will always be a switch from an A sublattice site to yet another A sublattice site which produces a slip in the ordering. Top panel: Ångström scale anti-ferromagnetic with a modulation on the moiré scale (MAFM). Middle panel: Ångström scale anti-ferromagnetic with nodes in the AB and BA regions (NAFM). Bottom panel: mostly ferromagnetic (FM) order.

or mostly ferromagnetic (FM), see Fig. 4.9. Figure 4.10 shows the magnetic phase diagram as function of twist angle and doping near the magic angle. Without Hartree interactions, the hole doped system is typically FM. Ferromagnetism is found to coincide with small values of U_c. In contrast, the undoped and electron doped system always exhibits MAFM, with NAFM only occurring at $\nu = 0$ and $\nu = 1$ at the magic angle.

Dramatic qualitative changes in the magnetic phase diagram are observed when Hartree interactions are included, see right panel of Fig. 4.9. The region of NAFM order in $\nu - \theta$-space is larger, while MAFM is only found for the undoped system at $\theta = 1.02°$ and $\theta = 1.08°$. Everywhere else the ordering is FM. Again, occurrence of FM is correlated with low values of U_c, which occur because of the interplay between the enhancement of the density of states from the long-ranged Hartree interactions upon doping and the enhancement of the density of states

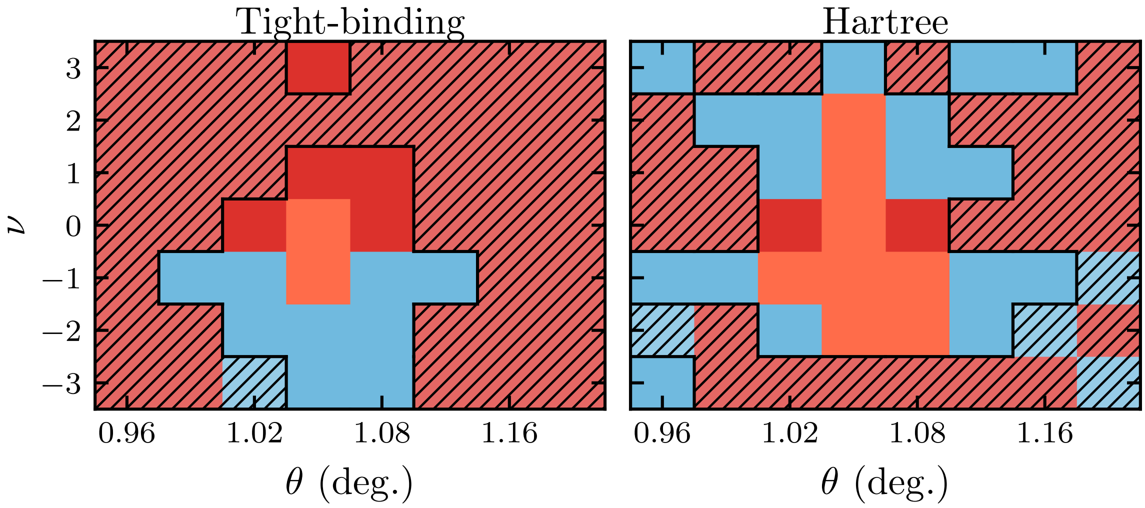

Figure 4.10: Magnetic phase diagram of twisted bilayer graphene as function of flat band filling ν and twist angle θ: blue denotes ferromagnetic order, while red and orange indicate modulated anti-ferromagnetic order and nodal anti-ferromagnetic order, respectively. Left panel: without Hartree interactions (tight-binding). Right panel: with Hartree interactions. Note that magnetic phases with $U_c > 4\,\text{eV}$ are experimentally not relevant (hatched regions).

from changing the twist angle towards the magic angle.

4.2.3 Discussion of phase diagram

Here, we compare our calculated magnetic phase diagram to experimental findings. Many experimental techniques, including transport and tunnelling measurements, probe quasiparticle properties of tBLG. While our approach does not directly yield such properties, our analysis below reveals a strong correlation between the calculated value of the critical Hubbard parameter U_c and the measured quasiparticle gap in the correlated insulator phases, with small values of U_c corresponding to large gaps associated with pronounced resistive peaks in transport experiments. We stress that this correlation cannot be viewed as conclusive evidence that the experimentally observed correlated insulator states have a magnetic origin, because the large density of states at the Fermi which gives rise to the small values of U_c also promotes other instabilities (such as valley-ordered or nematic states).

At charge neutrality, our calculations predict small values of U_c near the magic angle with NAFM/MAFM order. Experimentally, the situation is not clear, however, with some experiments reporting semi-metallic behaviour near the magic angle [88, 89, 93], while others (for very similar twist angles) observe a strong insulating state [120]. These conflicting results could arise from different levels of strain in the samples: Liu *et al.* [143] demonstrated that a C_3 broken symmetry state that is stabilised by strain retains its semi-metallic character because of the topological properties of the flat bands of tBLG.

Next, we consider the effect of doping. While at $\nu = -1$ insulating states are not often observed in experiments, some signatures of insulating states have been found at $\nu = +1$ [92, 93, 123, 147]. This is consistent with our Hartree+U results, which yield lower values of U_c for $\nu = +1$ than for $\nu = -1$. Note that the opposite result is obtained when long-ranged Hartree interactions are neglected.

Experiments typically observe the strongest insulating states at $\nu = \pm 2$ [88, 89, 93, 120]. Without Hartree interactions, our calculations predict no broken-symmetry states at $\nu = +2$. In contrast, Hartree+U theory predicts magnetic states for both $\nu = +2$ and $\nu = -2$. In recent experiments [121, 122], a thin dielectric spacer layer that separates the tBLG from metallic gates was used to enhance the screening of the electron-electron interactions in tBLG [114]. This results in significant changes to the electronic phase diagram with correlated insulator states being "screened out" for most twist angles and doping levels [114]. Interestingly, these experiments often find the insulating state at $\nu = +2$ to be most robust. Naively, one might expect that this system should be described by the magnetic phase diagram obtained without long-ranged Hartree interactions. However, changes in external screening only result in small changes to the Hartree theory band structure [135, 137] and therefore we expect that the Hartree+U result should be more relevant to experiments with thin dielectric spacer layers.

At $\nu = +3$, a strong insulating state is observed in experiments, especially when the tBLG is aligned with the hexagonal boron nitride substrate [127, 128]. In contrast, the $\nu = -3$ insulating state is almost never observed [88, 93, 120, 147]. For insulating phases to emerge at these doping levels both valley and spin symmetries must be broken, i.e., the insulating state must be FM [127, 128]. This is consistent with the Hartree+U results which predict FM order at $\nu = +3$ at several twist angles near the magic angle. Ferromagnetic order at $\nu = -3$ is only found at $\theta = 0.96^\circ$. Without Hartree interactions, our calculations do not predict FM order at $\nu = +3$ and instead we find relatively strong FM states at $\nu = -3$.

Hartree+U theory also predicts that magnetic order at $\nu = +3$ should occur over a relatively large twist angle range, while those at $\nu = +1$ are only found very close to the magic angle. This finding also appears to be consistent with experiments. For example, Yankowitz *et al.* [93] observed an insulating state at $\nu = +3$ for a twist angle of 1.14°, but no insulating state was found at $\nu = +1$. Interestingly, there are also clear signatures of this trend from recent scanning tunnelling microscopy experiments of Choi *et al.* [292]. At large twist angles, they observe that the $\nu = +3$ insulating state occurs before the $\nu = +1$ or $\nu = +2$. At slightly smaller twist angles, an additional insulating state at $\nu = +2$ occurs, with even smaller angles very close to the magic angle exhibiting insulating states for all integer electron doped systems. This observation is in very good agreement with our Hartree+U results. Whereas, without Hartree interactions the opposite trend is observed: the leading instabilities occur closer to $\nu = -1$ for the largest angles away from the magic angle.

In summary, we observe a strong correlation between the critical values of the Hubbard interactions obtained from Hartree+U calculations and the experimentally measured quasiparticle gaps of the correlated insulator states. In contrast, no such correlation is observed when long-ranged Hartree interactions are neglected.

As mentioned above, our current linear-response approach does not yield quasiparticle band structures of the broken-symmetry phases. In principle, such band structures can be obtained from self-consistent Hartree+U calculations, but a qualitative picture can be derived from a symmetry analysis of the spatial structure of the leading magnetic instabilities. Importantly, neither the explicit mean-field calculations nor the symmetry analysis fully capture the effect of strong electron correlations on the quasiparticle band structure. With this caveat in mind, we find that both MAFM and NAFM break the C_2 symmetry of tBLG, and therefore gap the flat band Dirac cone, which means NAFM and MAFM yield insulating states at charge neutrality [208]. Doping the MAFM and NAFM states with electrons or holes does not induce additional gaps and therefore the system is found to be metallic in agreement with explicit Hartree-Fock calculations [261]. The FM instability does not break C_2 (because the slight AFM character of the instability has a node between the AB and BA regions), but the spin degeneracy can be lifted and the bands can split to create an insulating state at charge neutrality. If the bands are spin split and doped away from charge neutrality, the system remains metallic as the C_2 symmetry is not broken. Therefore, this analysis only leads to insulating states at charge neutrality, while the doped magnetic states are found to be metallic. These results are in agreement with another atomistic calculation which found that only retaining Hubbard interactions can only yield insulating states at charge neutrality [287, 288], and also continuum model Hartree-Fock calculations that break C_2 [261]. To overcome the limitations of the current approach, future research should investigate longer-ranged exchange interactions [66, 143, 258, 259, 261, 285] and the influence of ordering tendencies with $\boldsymbol{q} \neq 0$ which could give rise to alternative symmetry breaking mechanisms such as valley [151] and rotational [131] symmetry.

Finally, our Hartree+U results for the magnetic phase diagram also have important implications for superconductivity in tBLG. First, band flattening induced by Hartree interactions enhances the density of states at the Fermi level and therefore increases the transition temperature irrespective of the nature of the superconducting glue. In addition, this mechanism also increases the range of twist angles where superconductivity can be observed [290, 293]. Note that superconductivity is typically observed in the vicinity of correlated insulator states at non-integer doping levels. Naively, one would expect that in this doping regime damped spin fluctuations from the magnetic parent state play an important role. However, Fischer *et al.* [107] recently demonstrated the possibility of pairing by AFM spin fluctuations in the vicinity of a FM phase. Future work will investigate the predictions of Hartree+U theory at non-integer doping levels to realise if long-ranged electron-electron interactions can also facilitate pairing by AFM spin fluctuations [126].

4.3 Hubbard calculations

Finally, mean-field Hubbard calculations of the magnetic instabilities of tBLG are presented*. These mean-field calculations proved to be extremely computationally expensive to perform at the magic angle. Therefore, the results here are limited, and entirely focus on a twist angle of 1.54° at charge neutrality. In such a system, Hartree interactions do not qualitatively change the electronic structure, and therefore, these interactions are also neglected for simplicity. Despite this, constrained calculations are employed to investigate magnetic instabilities that are not leading, which gives insight into the magnetic phases of tBLG, and which could form the basis of future investigation.

---

*The structure was generated from LAMMPS with a 2.42 Å lattice constant of graphene. The tight-binding parameters for these calculations were $a = 1.39$ Å, $d = 3.2912$ Å, $q_\pi = 7.39$ and $q_\pi = 3.13$, with a spherical Heaviside step function with cut-off of 10 Å being used to truncate hopping parameters, which gave a magic angle of tBLG at 1.05°.

Before the discussion of these results, it is interesting to note how magnetic order has been investigated in tBLG. Within tight-binding and DFT calculations, rescaling schemes have typically been employed to efficiently investigate magnetism in tBLG, since performing the calculations explicitly is generally too expensive. For tight-binding calculations [11], flat electronic bands near the Fermi energy can be created at larger twist angles by reducing the π hopping parameter, i.e. effectively changing the magic angle condition. It has been shown in Ref. 284 that this method can give qualitatively correct results, but it does not quantitatively reproduce the full calculation. We performed these rescaled tight-binding calculations too, and found qualitative agreement with the spin-susceptibility calculations, but not quantitative agreement. For DFT calculations [294], the interlayer spacing is rescaled to smaller values (from pressure, for example) to increase the coupling between the layers, which causes the magic angle condition to occur at larger angles. Ferromagnetic order has been found, but the quantitative accuracy of these calculations remains to be validated. Predominately, continuum model calculations are performed to investigate the broken symmetry phases of tBLG. These methods, however, have not shed light onto the real-space structure of the magnetic order.

4.3.1 Leading instability

At charge neutrality with a twist angle of 1.54°, the leading instability is modulated antiferromagnetic (MAFM) order [11, 208]. The critical Hubbard interaction of this system was found to be $U_{\mathrm{c}} \approx 2.06t$ (where $t = 2.7$ eV is the π hopping parameter of graphene in the tight-binding model) from the RPA spin susceptibility [208]. For values of $U < 2t$, the mean-field calculations could not stabilise an ordering with finite magnetic order parameter. Therefore, the critical Hubbard interaction for the onset of magnetic order agrees reasonably well between mean-field and RPA analysis.

In Fig. 4.11, the electronic band structure for the leading instability obtained from the mean-

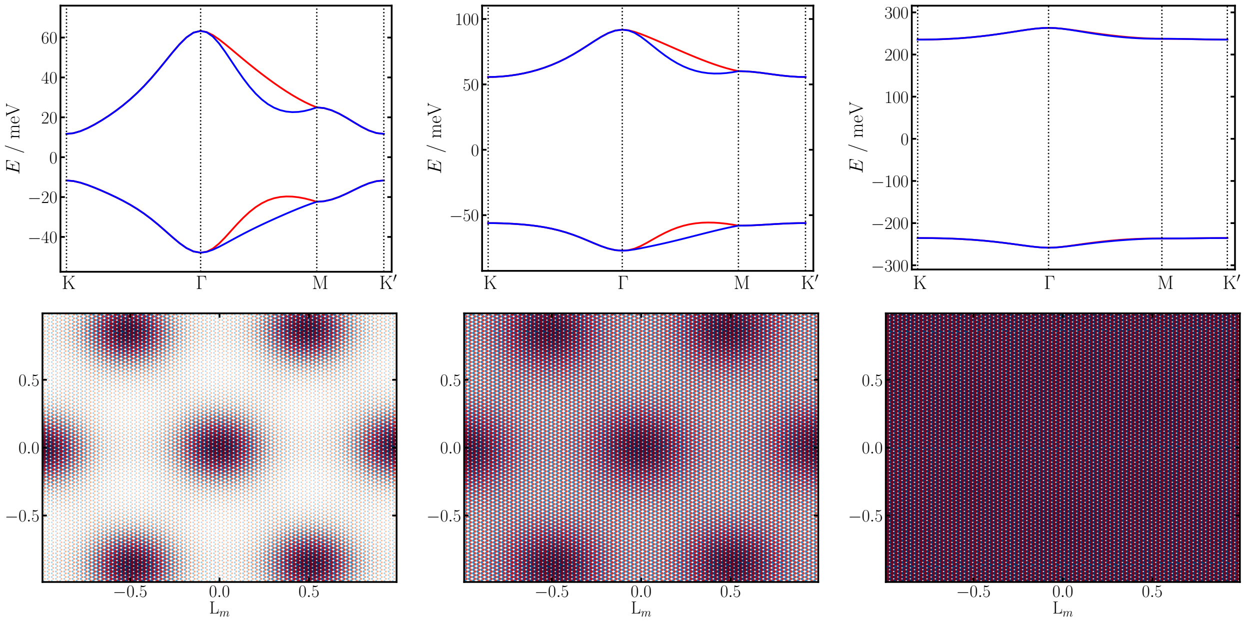

Figure 4.11: Electronic band structure (upper) and corresponding magnetic structure (lower) obtained from the mean-field solution of the atomistic Hubbard model of the MAFM order, which is the leading instability, of 1.54° at charge neutrality for a number of U's [left - $U = 2t$, middle - $U = 2.1t$, right - $U = 2.2t$]. The K and K′ valleys have been denoted by red and blue, respectively. The magnetic structure shows $\zeta = (n_{\sigma'} - n_\sigma)/(n_{\sigma'} + n_\sigma)$ for one layer, where the size of the circle increases with $|\zeta|$ and the colour red/blue corresponds to large positive/negative values of ζ. The size and colour are normalised to the maximum in each case. The magnitude of ζ increases with U. The real-space structure has been normalised by the moiré length scale, L_m, with the AA region located at the origin.

field solution of the Hubbard model at a number of U's is shown. Note that the K and K′ valleys of the flat bands have been determined from the valley operator and coloured in red and blue, respectively, in Fig. 4.11. As discussed in Section 4.3, the MAFM order breaks C_2. Therefore, this ordering gaps out the Dirac cone at the K/K′ points. For $U = 2t$, the gap at the K/K′ points are of the order of 20 meV, as shown in Fig. 4.11(left), which is significantly smaller than the bandwidth at this twist angle. The magnetic order, displayed underneath the electronic band structure, corresponds well to the ordering obtained from the spin-susceptibility calculations. A larger on-site Hubbard parameter of $U = 2.1t$ causes the gap between the K/K′ points to increase to 100 meV, with a concomitant increase in the total bandwidth. The magnetic order is still peaked in the AA regions, but the structure is becoming more uniform throughout the moiré unit cell. Finally, for $U = 2.2t$, the gap between the valence and conduction bands is of the order of 500 meV, where these bands are now extremely flat. The magnetic structure is almost completely uniform throughout the moiré unit cell. A $U = 2.2t$ is not far off what is required to cause an insulating state in graphene [1, 11], which is presumably the origin of the dramatically increasing bandwidth and uniform order.

4.3.2 Excited antiferromagnetic instabilities

The RPA spin-susceptibility gives N, the number of atoms in the moiré unit cell, different magnetic instabilities. At charge neutrality for 1.54° tBLG, none of the instabilities with U_{c} larger than the leading instability could be converged in mean-field. In every case, even for U's much larger than U_{c} for that instability, the ordering would revert to the MAFM order, which was found to be the leading instability in the RPA analysis (for undoped 1.54°). Therefore, to investigate the quasiparticle properties of the excited magnetic instabilities, a constrained mean-field analysis is required, where the form of the magnetic order was fixed but its magnitude could vary.

Nodal antiferromagnetic order

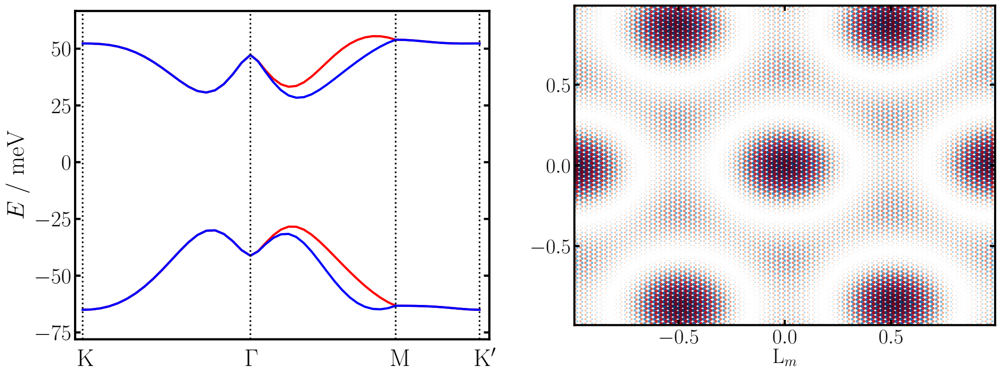

Figure 4.12: Electronic band structure (left) and NAFM magnetic ordering (right) obtained from the constrained mean-field solution of the atomistic Hubbard calculations; at a twist angle of 1.54°, for charge neutrality, with $U = 2.2t$. The K and K′ valleys have been denoted by red and blue, respectively. See caption of Fig. 4.11 for a description of how the magnetic order plot is generated.

The nodal antiferromagnetic order (NAFM) order is found to be a leading instability close to the magic angle, as shown in Fig. 4.10 of Section 4.2. At 1.54° for charge neutral tBLG, it has one of the lowest critical on-site Hubbard interactions $U_{\mathrm{c}} = 2.17(986)t$. The form of NAFM is shown in Fig. 4.12, and is composed of a sublattice oscillation

$$\zeta(1) \approx \begin{cases} \alpha, & \text{if A1 or A2} \\ -\alpha, & \text{if B1 or B2} \end{cases} \tag{4.2}$$

where A/B stand of the sublattices and 1/2 represent each layer, that is modulated throughout the moiré unit cell as given by

$$\zeta(2) \approx \zeta(1) \sum_{i=1,2,3} \cos(\mathbf{G}_i \cdot \mathbf{r}), \tag{4.3}$$

where the reciprocal lattice vectors are again the three shortest moiré vectors, as described in Section 4.1. The constrained mean-field analysis finds α self-consistently through a linear mixing scheme. In Fig. 4.12(left), the constrained mean-field quasiparticle band structure with $U = 2.2t$ is shown. The NAFM order breaks C_2 which causes the Dirac cone at the K/K′ points to be gapped-out, similar to the MAFM order. This ordering also causes an inversion of the conduction and valence bands, such that the K/K′ points are the further in energy from each other in comparison to the states at Γ. This inversion would cause additional features in the LDOS to emerge, which could be detected from STM measurements.

Honeycomb antiferromagnetic order

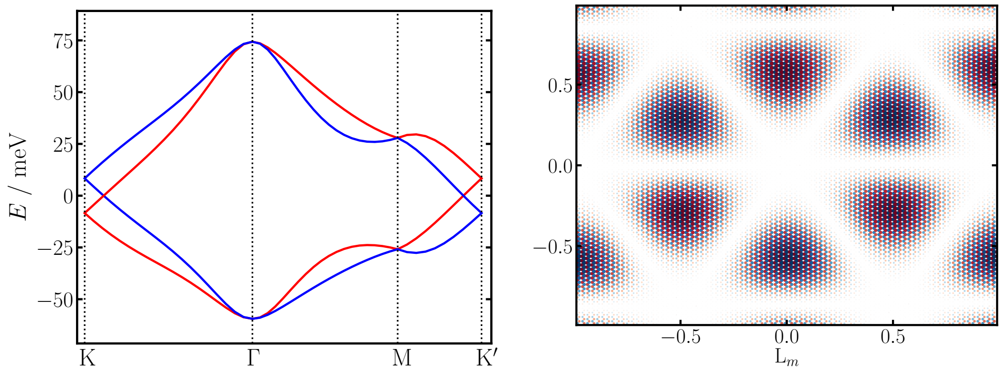

Figure 4.13: Electronic band structure (left) and HAFM magnetic ordering (right) obtained from the constrained mean-field solution of the atomistic Hubbard calculations; at a twist angle of 1.54°, for charge neutrality, with $U = 2.2t$. The K and K′ valleys have been denoted by red and blue, respectively. See caption of Fig. 4.11 for a description of how the magnetic order plot is generated.

Another instability with a critical on-site Hubbard parameter not much larger than the leading instability, $U_\mathrm{c} = 2.17(998)t$, can be described by

$$\zeta(3) \approx \zeta(1) \sum_{i=1,2,3} \sin(\mathbf{G}_i \cdot \mathbf{r}), \tag{4.4}$$

where $\mathbf{G}_3 = -(\mathbf{G}_1 + \mathbf{G}_2)$. This magnetic instability has a sublattice oscillation, in addition to a moiré modulation where the peaks of the magnetic order occur on the AB/BA regions of the moiré unit cell, i.e. it is a honeycomb antiferromagnetic (HAFM) order. This is in contrast to the previously described orderings which are peaked on the AA regions of the moiré unit cell, which might be intuitively expected from the fact the LDOS is localised on the AA regions of the moiré unit cell. Note this ordering was not discussed in the previous sections.

In Fig. 4.13(left), the constrained mean-field quasiparticle band structure with $U = 2.2t$ is shown; the corresponding magnetic structure is shown in Fig. 4.13(right). Interestingly, this magnetic ordering has a drastically different quasiparticle dispersion in comparison to NAFM. While the sublattice symmetry of each layer is broken (in some regions of space), which would gap the Dirac cone of the individual layers, it does not break C_2 on the moiré length scale, owing to the modulation of the sublattice oscillation on the moiré length scale. Therefore, this magnetic ordering does not gap the Dirac cones of the flat bands of tBLG.

Instead it causes the valley degeneracy to be broken throughout most of the moiré Brillouin zone. This splitting of the valleys is analogous to the effect of a perpendicular electric field on the electronic structure [11]. Therefore, this magnetic order should couple to an electric field too, and in fact, we find that this instability is stabilised by a perpendicular electric field. This breaking of the valley degeneracy causes the Dirac cones of the two valleys to be nested, similar to AA stacked bilayer graphene [24, 295]. It is well known that such nesting is particularly susceptible to excitonic instabilities [24]. It has been shown that heterostrain causes a similar splitting of the valleys [143], and also causes the onset of an excitonic gap [296]. Therefore, this instability could also couple to heterostrain too, although we do not investigate this here.

4.3.3 Ferromagnetic order

At a twist angle of 1.54°, ferromagnetic (FM) order is not found close to the leading instability. This ordering tendency only occurs close to the magic angle, as seen in Fig. 4.10 of Section 4.2.

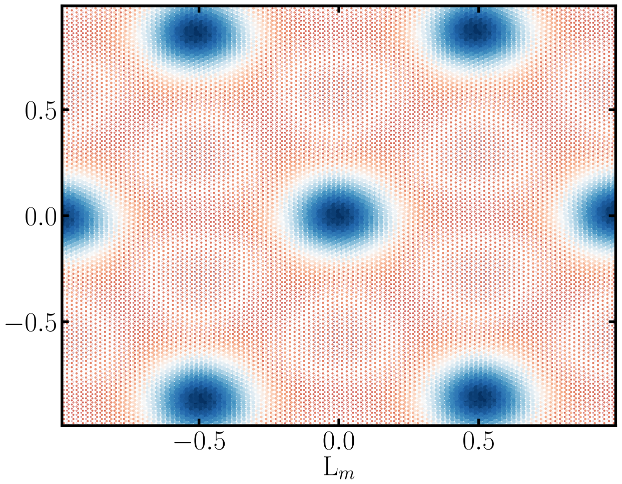

Figure 4.14: Real-space plot of the FM order of tBLG at a twist angle of 1.12° from the spin susceptibility calculations. See caption of Fig. 4.11 for a description of how the magnetic order plot is generated.

In Fig. 4.14 the real-space ordering is shown in full, where it can clearly be seen that the FM order peaks in the AA regions of the moiré unit cell. A feature that becomes more apparent from this plot is the residual AFM order, which can be seen to correspond to HAFM. Therefore, to a reasonable approximation

$$\zeta_{FM} \approx \beta \sum_{i=1,2,3} \cos(\mathbf{G}_i \cdot \mathbf{r}) + \gamma + \zeta(1) \sum_{i=1,2,3} \sin(\mathbf{G}_i \cdot \mathbf{r}), \tag{4.5}$$

where β and γ are additional parameters which need to be obtained in addition to α. Note that $\beta \gg \alpha$ and $\gamma \gg \alpha$, so it could be sufficient to approximate $\alpha = 0$, but $\gamma \approx 3\beta/2$, with the sign of these two parameters being the same.

From inspecting Eq. 4.5 the effect of FM order on the electronic structure can be readily deduced. Since the real-space structure of the FM is analogous to the Hartree potential, it becomes evident that this magnetic structure should distort the electronic structure in a similar manner to the Hartree potential. For the FM order, the up spin will correspond to hole (electron) doping the system and the down spin will correspond to electron (hole) doping. Therefore, the up and down spin bands will be strongly split at the edge of the moiré Brillouin zone, but at the centre of the Brillouin zone the band splitting will be smaller.

Interestingly, other DFT and tight-binding calculations have found FM order which is peaked in the AA regions of the moiré unit cell [11, 294]. The quasi-particle band structure which corresponds to this FM order was clearly demonstrated by Lopez-Bezanilla [294]. For a twist angle of 3.89° with an interlayer spacing of 2.5 Å, magnetic order similar to that shown in Fig. 4.14 was obtained, and the electronic band structure was spin split as previously described. At charge neutrality for this structure, the splitting of the bands was relatively small compared to the bandwidth, and the system remained to be metallic.

Chapter 5

Moiré graphene multilayers beyond twisted bilayer graphene

The observation of strong correlation phenomena in moiré graphene multilayers has driven efforts to understand their electronic structure and behaviour [30, 98, 111]. A key prerequisite for the emergence of correlated states are flat electronic bands that give rise to a high density of states (DOS) at the Fermi level. The total energy of these flat-band electrons is dominated by the contribution from electron-electron interactions, which favours states that break symmetries of the Hamiltonian, opening gaps at the Fermi level to lower the total energy of the electrons [99]. In moiré materials [110], it is possible to "engineer" a high DOS at the Fermi energy through tuning the relative twist angle to values where very flat electronic bands emerge.

In principle the space of graphitic moiré systems is very large, but so far experimental studies have focussed on four systems: twisted bilayer graphene (tBLG) [88, 89, 91–93, 120–122, 124, 127–131, 139, 141, 144, 147, 148, 151, 152, 292], twisted double bilayer graphene (tDBLG) comprised of two AB stacked bilayers [164, 169–172, 177, 179], twisted mono-bilayer graphene (AtAB) [183–185], and different twisted trilayer graphene structures (tTLG) [189, 196–198]. Experimentally, all these systems have been found to exhibit correlated insulator states, and theoretically all of these systems have been predicted to feature flat electronic bands[†]. Of particular interest are tBLG and tTLG (with an alternating twist angle between each graphene sheet) because - in addition to correlated insulator states - robust superconductivity has been observed in these systems [89, 93, 120, 196–198].

[†] tBLG [11, 29, 32, 33, 37, 65, 66, 71, 106–108, 205, 208, 258, 259, 261, 285, 287], tDBLG [59, 165–168, 173, 174], AtAB [181, 182, 187, 191], tTLG [126, 186, 187, 190–195].

In tBLG [95, 135–138], long-ranged electron-electron interactions lead to an additional enhancement of the DOS which increases the robustness of electronic correlations, and could be one reason why robust superconductivity is observed [290, 293]. In contrast, tDBLG requires electric fields to further flatten the electronic bands and increase the DOS to drive the onset of broken symmetry phases [169–172, 183, 185]. Therefore, when investigating new graphitic moiré systems, it is important to investigate both the effect of electron-electron interactions on the band structure in the normal state and the response to external fields.

In this chapter, the effect of electron-electron interactions are investigated in moiré graphene multilayers beyond tBLG. In Section 5.1, moiré graphene multilayers in which there are alternating twists ($\pm\theta$) between adjacent graphene layers are presented. These structures are generalisations of tBLG, and the effects of electron-electron interactions are found to be analogous. In the Section 5.2, moiré graphene multilayers in which there are adjacent layers of graphene which are twisted and also aligned (θ and 0°) are investigated. For this class of moiré graphene multilayers, the effect of electron-electron interactions on the electronic structure are found to be significantly weaker than in tBLG. This chapter is mainly based on three publications. Section 5.1 is based on part of Ref. 126 [Fischer, Goodwin *et al.* arXiv:2104.10176] of tTLG, with additional unpublished results for a quad-layer system too. Section 5.2 is based on two publications. The first part is based on tDBLG of Ref. 297 [Cheung, Goodwin *et al.* arXiv:2111.03019] and the second part is based on the topic of a new mono-trilayer system of Ref. 298 [Goodwin, Klebl *et al.* Phys. Rev. Materials 5:084008 2021].

In Ref. 126, the main focus on the paper was on the unconventional superconductivity of tTLG from spin fluctuations, which was carried out by Ammon Fischer. My contributions to the paper were to determine the atomic structure of tTLG, electronic structure, Hartree interactions, and performing DFT calculations. Lennart Klebl contributed the spin susceptibility calculations which were used for the spin fluctuation calculations. All authors contributed to discussions and writing the manuscript.

In Ref. 297, I co-supervised Christopher Cheung[*] in the study of Hartree interactions in tDBLG. Christopher performed all the Hartree calculations using the code I developed. Valerio Vitale performed the DFT calculations which were used to investigate the electronic band structure and local potential. I plotted and helped to analyse the results from the Hartree calculations performed by Christopher Cheung and DFT calculations performed by Valerio Vitale. Arash Mostofi and Johannes Lischner guided the investigated and significantly contributed to writing the paper.

In Ref. 298, the work was a highly collaborative effort. I instigated the research, and organised most of the work with guidance from Johannes Lischner and Arash Mostofi. I performed all tight-binding and density of states calculations, and helped to analysed the results for the Hartree and magnetic calculations. Vivek Gogtay and Xavier van Gorp[†] utilised the Hartree code I wrote to investigate Hartree interactions in this mono-trilayer graphene, the figures of which I generated. Lennart Klebl performed the spin-susceptibility calculations, generated the figures for these results and also interpreted the results of these calculations. Valerio Vitale performed DFT calculations, which were not used in the manuscript. Xia Liang[‡] generated the atomic structures of these systems. Arash Mostofi, Dante Kennes and Johannes Lischner helped guide the project and significantly contributed to writing the paper.

5.1 Alternating twist angle structures

5.1.1 Twisted trilayer graphene

In this section, a twisted trilayer graphene (tTLG) system is investigated where the middle layer is twisted by θ relative to the encapsulating graphene layers, i.e. between adjacent layers of graphene there is an alternating twist angle of $\pm\theta$. It was shown by Carr *et al.* [190] that the lowest energy structure of tTLG occurs when the encapsulating graphene layers are AA stacked relative to each other. This occurs because the moiré patterns created between the middle and upper graphene layers, and middle and lower graphene layers are coherent, i.e. the

---

[*] Christopher was a UROP student in the summer of 2020. I was substantially involved in his supervision.

[†] Vivek and Xavier were MSci Physics students I helped to supervise in 2020-2021.

[‡] Xia was a UROP and MEng student I supervised in 2019-2020.

AA regions of both moiré patterns share the same $x - y$ positions, which permits significant atomic reconstruction effects [190]. From the mirror symmetry of this structure, the middle twisted layer remains almost entirely flat upon relaxation, but the encapsulating layers have corrugation effects reminiscent of tBLG [190, 192, 195].

As shown in Fig. 5.1, the low-energy electronic structure[*] of tTLG consists of a set of flat bands which are intersected by a Dirac cone with a large Fermi velocity, similar to that of graphene [186, 187, 190, 192]. The flat band states are remarkably similar to those of tBLG [186], as evident from the Dirac cone (with renormalised Fermi velocity) at K/K′, van Hove singularity near M and the different valley degeneracies along the Γ-M and Γ-K paths [192]. In the our tight-binding model (at charge neutrality), the minimum band width of the flat bands occurs at a twist angle of ∼1.54°, which is approximately 0.5° larger than the magic angle of tBLG[†].

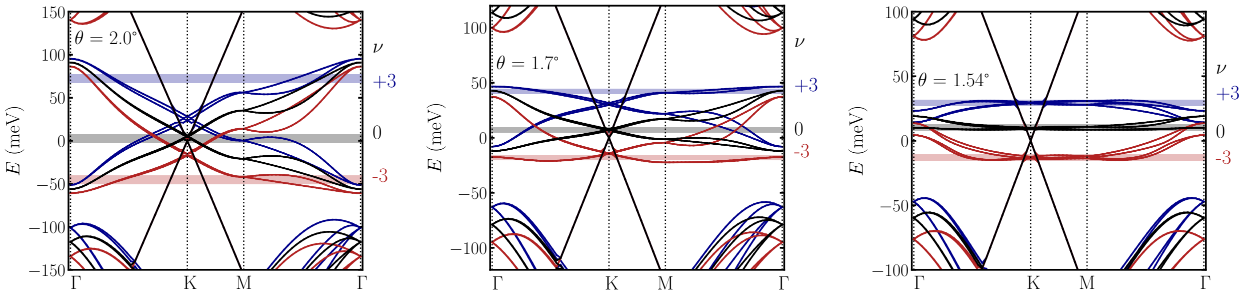

Figure 5.1: Electronic band structure of tTLG along the highly symmetry path from Hartree theory for twist angles of 2°, 1.79° and 1.54°, and doping levels (number of electrons added/removed per moiré unit cell) of 0 and ±3, as indicated.

Moreover, as shown in Fig. 5.1, the dispersion of the flat bands of tTLG are very sensitive to long-ranged electron interactions, analogous to tBLG [126]. The removal of electrons causes the K-point energies of the flat bands to lower relative to the Γ-point, and is accompanied by a global shift of the flat bands relative to the Dirac cone to more negative energies. Conversely, the addition of electrons causes the K-point energies of the flat bands to increase relative to the Γ-point, and shifts the whole flat band manifold to higher energies relative to the Dirac cone. The Dirac cone with its large Fermi velocity is insensitive to long-ranged electron interactions.

---

[*] The structure was generated from LAMMPS with a 2.42 Å lattice constant of graphene. The tight-binding parameters for these calculations were $a = 1.39$ Å, $d = 3.2912$ Å, $q_\pi = 7.43$ and $q_\pi = 3.14$, with a spherical Heaviside step function with cut-off of 10 Å being used to truncate hopping parameters.

[†] According to a minimal model [186], the magic angle of tTLG should occur at $\sqrt{2}$ times the magic angle of tBLG.

The band deformations are completely analogous to those found in tBLG, as discussed in Refs. 95, 135–138.

These strong band deformations arise because of the strongly peaked local density of states (LDOS) in the AAA regions of the moiré unit cell, with the strongest weights on the inner layer [126]. Upon removing (adding) electrons, they are almost entirely taken from (added to) the AAA regions. This localisation of the flat band LDOS gives rise to a strongly varying Hartree potential, similar to tBLG. In Fig. 5.2(c) and (d) the Hartree potential is shown to be strongly peaked in the AAA regions when 3 electrons are removed from 1.61° tTLG. This Hartree potential substantially varies with doping level but does not change significantly with twist angle, as summarised in Fig. 5.2(a) and (b).

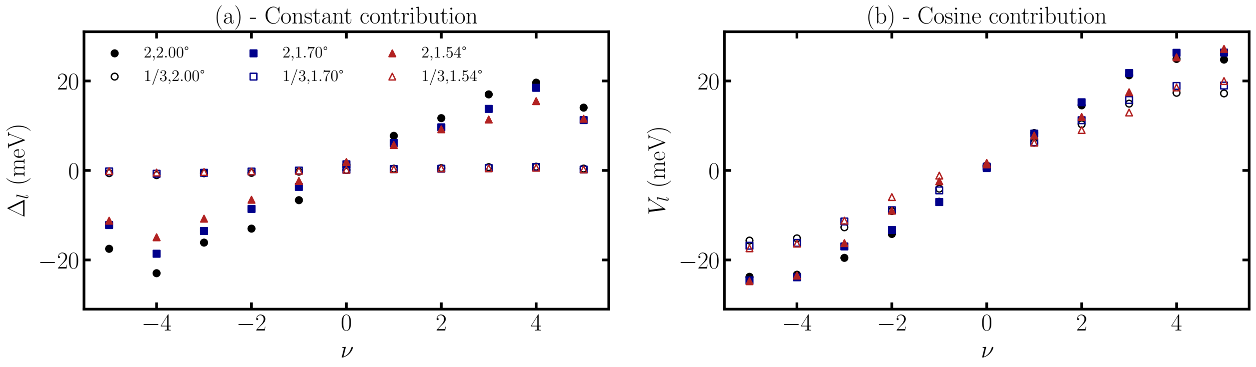

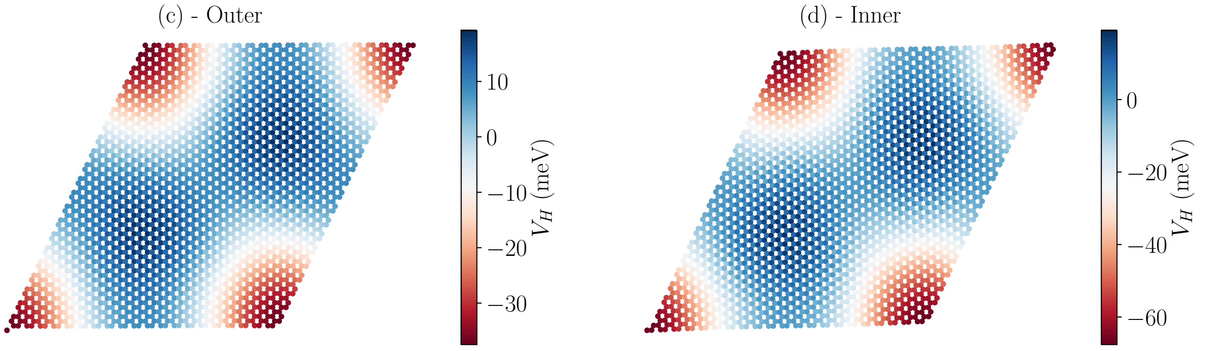

Figure 5.2: (a) - Constant contribution [determined by the mean] to the Hartree potential on each layer as a function of doping level for a number of twist angles. Legend shows the layer (1/3 or 2) and the twist angle convention used for the symbols. (b) - Cosine contribution [determined from Eq. (5.1)] to the Hartree potential on each layer as a function of doping level for several twist angles. (c) - Hartree potential on the outer layers for 1.61° at $\nu = -3$. (d) - Hartree potential on the inner layer for 1.61° at $\nu = -3$.

In Fig. 5.2(a) we plot how the layer-dependent constant contribution to the Hartree potential (Δ_l) changes with doping level for several twist angles. Interestingly, we find that the outer layers (1/3) have an almost zero constant contribution ($\Delta_{1/3} = 0$) for all doping levels and twist angles. However, the central layer (2) has a constant contribution which changes significantly with doping level, but hardly changes with twist angle. When doping within the flat bands, we find that the constant contribution increases when electrons are added, but it becomes more negative when electrons are removed. This occurs because of electrons mainly being added/removed from the central layer. The change in this constant contribution is approximately linear ($\Delta_2 \approx \Delta_2' \nu$) when doping inside of the flat bands. Doping the system outside of the flat bands causes the magnitude of the constant contribution to decrease, which reflects the fact that electrons are now being removed/added from the outer layers where the Dirac cone with large Fermi velocity resides [195].

In Fig. 5.2(b) we plot the scale of the cosine contribution to the Hartree potential, as calculated by

$$V_l(\nu) = \frac{\sum_i V_{\mathrm{H}}(\nu, \boldsymbol{\tau}_{il}) \cdot v_c(\boldsymbol{\tau}_{il})}{\sum_j v_c(\boldsymbol{\tau}_{jl}) \cdot v_c(\boldsymbol{\tau}_{jl})}, \tag{5.1}$$

where

$$v_c(\boldsymbol{\tau}_{il}) = \sum_j \cos(\boldsymbol{G}_j \cdot \boldsymbol{\tau}_{il}). \tag{5.2}$$

Here $\boldsymbol{G}_j$ are the three shortest reciprocal moiré lattice vectors and the summations only run over the atoms in layer l [68]. The scale of the cosine contribution to the Hartree potential is largest on the inner layer (2), as this is where electrons are mainly being added to/removed from. Doping tTLG within the flat bands causes an approximately linear change on the cosine contribution to the Hartree potential ($V_l \approx V_l' \nu$), which is similar to tBLG [95, 135–138]. Upon doping outside of the flat bands, the cosine contribution stops changing significantly as electrons are no longer being added to/removed from the AAA regions.

Naturally, one might ask how the Hartree theory band structure compares against *ab initio* calculations. In Fig. 5.3 the electronic structure from charge neutral DFT calculations of tTLG systems at twist angles of 3.15° and 2.45° are displayed. Overall, the agreement is qualitatively and quantitatively good [192]. The main discrepancy occurs in the relative positioning of the

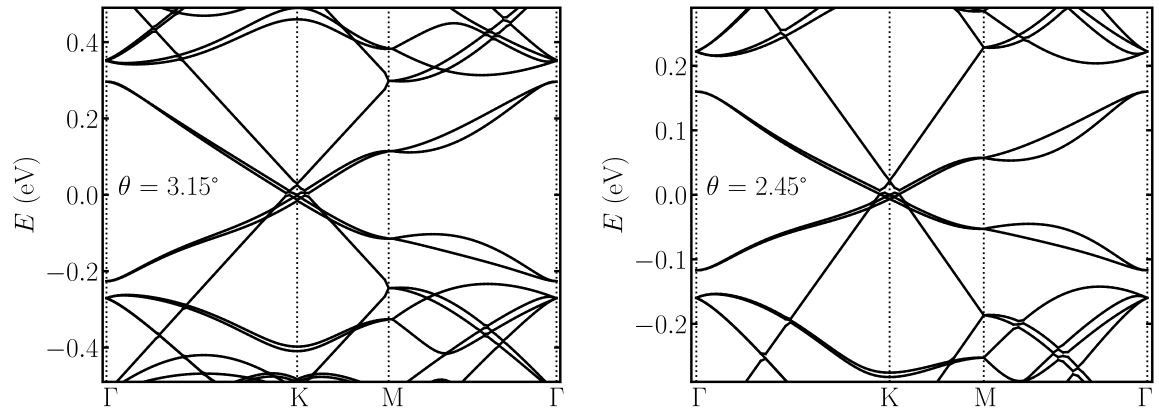

Figure 5.3: Electronic band structure of tTLG along the highly symmetry path from DFT for twist angles of 3.15° and 2.45°, as indicated, at charge neutrality.

flat bands and the Dirac cone (with large Fermi velocity). As seen in Fig. 5.2, tight-binding predicts the flat bands to intersect the Dirac cone with a large Fermi velocity at energies higher than the Dirac point (of the large Fermi velocity Dirac cone). Whereas, the *ab initio* method predicts that the flat bands should intersect at energies lower than the Dirac point. As indicated in Ref. 192 this discrepancy can be rectified through the use of an on-site potential of ~ -35 meV on the inner layer relative to the outer layers. The origin of this layer dependent potential, and the discrepancy between the Hartree theory and DFT, shall be discussed in detail later in the Section 5.2.1 on twisted double bilayer graphene.

5.1.2 Double twisted bilayer graphene

In this section, a quad-layer system with alternating twist angles between adjacent graphene layers is investigated [186]. Starting from an AAAA stack, layers 1/3 (2/4) are rotated relative to 2/4 (1/3), where labels 1-4 correspond to consecutive layers in the graphene multilayer. We refer to this system as double twisted bilayer graphene (DtBLG). Again, there are other possible quad-layer structures from the initial alignment of layers, but these are not considered here as they are assumed to be higher in energy [190].

In Fig. 5.4 the low-energy electronic structure[*] of DtBLG is shown for a number of twist angles (and doping levels, but we shall focus on charge neutrality for now). Similarly to tTLG,

---

[*] The structure was generated from LAMMPS, with a 2.42 Å lattice constant of graphene. The tight-binding parameters for these calculations were $a = 1.39$ Å, $d = 3.35$ Å, $q_\pi = 7.43$ and $q_\pi = 3.14$, with a spherical Heaviside step function with cut-off of 10 Å being used to truncate hopping parameters.

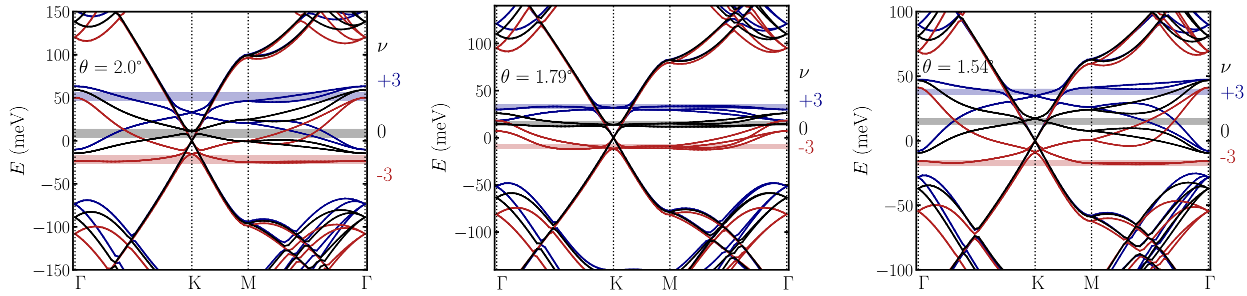

Figure 5.4: Electronic band structure of DtBLG along the highly symmetry path from Hartree theory for twist angles of 2°, 1.79° and 1.54°, and doping levels (number of electrons added/removed per moiré unit cell) of 0 and ±3, as indicated.

the flat bands which emerge are reminiscent of tBLG bands [186] but, for a given twist angle, the Fermi velocity of the bands is smaller in comparison to tBLG (for twist angles above the magic angle of DtBLG). We find that the magic angle of the lowest energy states occurs at an angle of ∼1.79°, which is larger than both tBLG and tTLG[*]. Moreover, these flat bands are not isolated from all other bands but intersect a set of bands which are also reminiscent of tBLG bands (with a larger Fermi velocity than the flattest band). In the tight-binding model, the extremely flat bands cross the other flat bands slightly higher in energy than the Dirac point of the other tBLG-like bands. Interestingly, unlike tTLG, the flattest bands do not simply cross the other bands, but seem to undergo an avoided crossing, to then merge with the other bands asymptotically. In contrast to tTLG, where the Dirac cone that is intersected by the flat bands is not affected by twist angle much, these other tBLG-like bands significantly change with twist angle.

Analogously to tBLG and tTLG, the electronic structure of DtBLG is extremely sensitive to the doping level within Hartree theory. Upon removing electrons, the extremely flat band states near K shift down in energy relative to the states at Γ, in addition to a global shift of the extremely flat bands relative to the other bands. Again, the converse is true for electron-doped systems. The effect of the interactions is most pronounced at the magic angle of 1.79°, where the band width of the lowest states is minimised. Similarly, to the other alternating twist angle structures, the sensitive dependence of the electronic structure arises from the clean localisation of states in real space (where the flattest bands are predominantly located on the AA regions

---

[*] According to a minimal model [186], the magic angle of DtBLG should occur at the golden ratio $(\sqrt{5}+1)/2 \approx 1.62$ times the magic angle of tBLG.

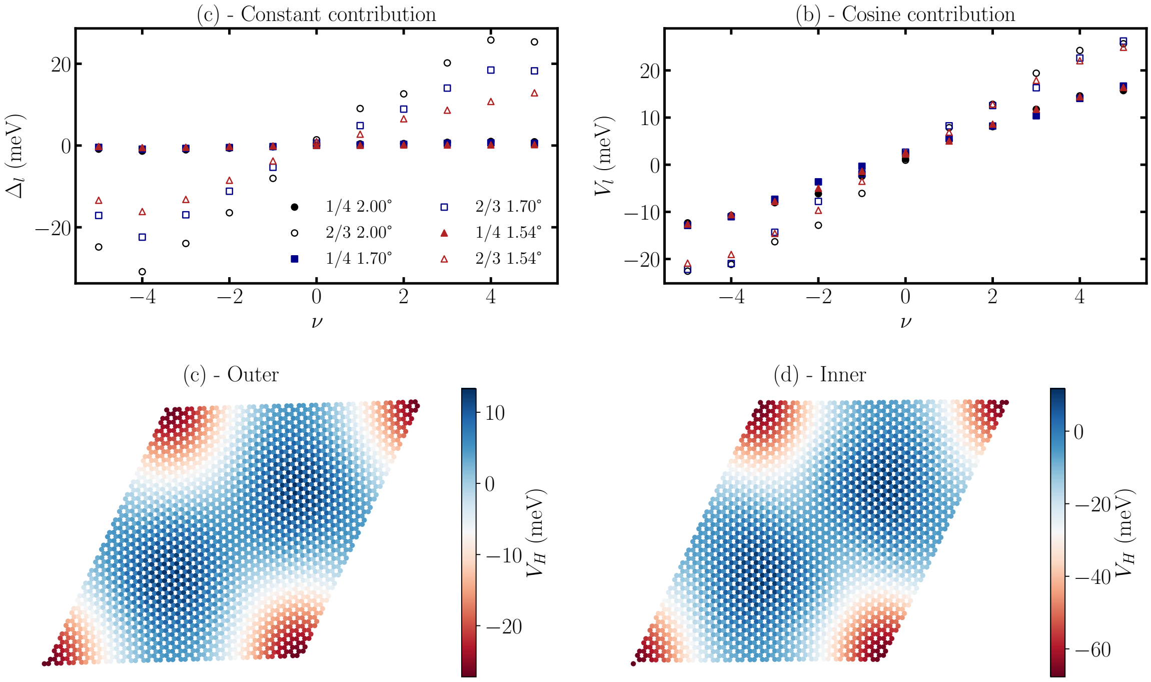

Figure 5.5: (a) - Constant contribution to the Hartree potential on each layer as a function of doping level for a number of twist angles. Legend shows the layer (1/4 or 2/3) and the twist angle convention used for the symbols. (b) - Cosine contribution to the Hartree potential on each layer as a function of doping level for several twist angles. (c) - Hartree potential on the outer layers for 1.61° at $\nu = -3$. (d) - Hartree potential on the inner layer for 1.61° at $\nu = -3$.

of the inner layers) and in the hexagonal Brillouin zone (where states at the edge are mainly localised in the AA regions of the inner layers, with the states at the centre being localised on the AB/BA regions of the inner layers). Therefore, it appears that sensitive doping dependent electronic structures of alternating twist angle moiré structures could be a universal property.

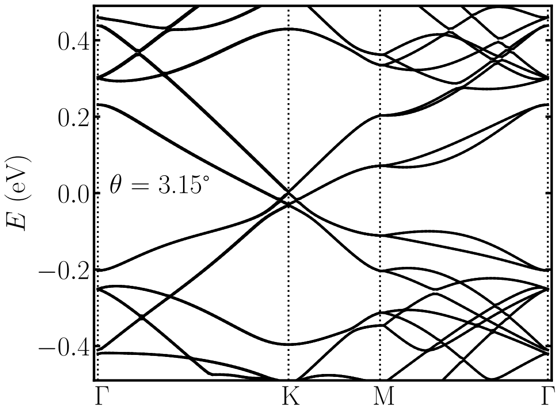

Figure 5.6: Electronic band structure of DtBLG along the highly symmetry path from DFT for a single twist angle of 3.15°.

In Fig. 5.5(a) and (b) the constant and cosine contribution to the Hartree potential as a function of doping level for a number of twist angles are displayed. The results are very similar to tTLG, and therefore, shall not described here. In Fig. 5.5(c) and (d) an example Hartree potential in real space is displayed for 1.61° at $\nu = -3$.

Finally, the electronic structure of DtBLG from DFT for a twist angle of 3.15° is shown in Fig. 5.6. Again, there is good agreement between the DFT and atomistic tight-binding model, with the main difference between the two methods being where the flattest most bands intersect the other tBLG-like bands. In the tight-binding model, we find that the flattest bands intersect the other bands at energies slightly higher than the Dirac point of the more dispersive tBLG-like states. Whereas, DFT finds that the flattest bands intersect the other bands at lower energies than the Dirac point of the other bands. This also suggests the inclusion of an additional on-site potential on the inner two layers (of approximately −30 meV) to obtain better agreement with DFT. This shall be discussed in more detail in Section 5.2.1 for another quad-layer system.

5.2 Moiré structures with twisted and aligned layers

5.2.1 Twisted double bilayer graphene

Here twisted double bilayer graphene (tDBLG) is investigated: a moiré materials composed of Bernal stacked bilayers, where there is a relative twist angle between the two bilayers. For more details of the structure of this system, see Ref. 59.

In tDBLG, a set of four bands emerge in the low energy electronic structure*, which become extremely flat close to the magic angle of ∼1.3° [59, 163, 165–167, 173, 174, 299]. These bands are not entangled with the other bands close to this magic angle as a consequence of the atomic relaxations. The dispersion inherits the quadratic band dispersion of the parent AB bilayers, but there is a band gap at the K and K′ points. In Fig. 5.7 we show the Hartree theory band structure of tDBLG for a twist angle of $\theta = 1.89°$ and for different integer doping levels per moiré unit cell, $-3 \leq \nu \leq 3$, where ν represents the number of electrons ($\nu > 0$) or holes ($\nu < 0$)

---

*The methods for this work can be found in the Methods. The structure was generated from LAMMPS, as outlined in the Methods. The tight-binding parameters for these calculations were $a = 1.39$ Å, $d = 3.35$ Å, $q_\pi = 7.43$ and $q_\pi = 3.14$, with a spherical Heaviside step function with cut-off of 10 Å being used to truncate hopping parameters.

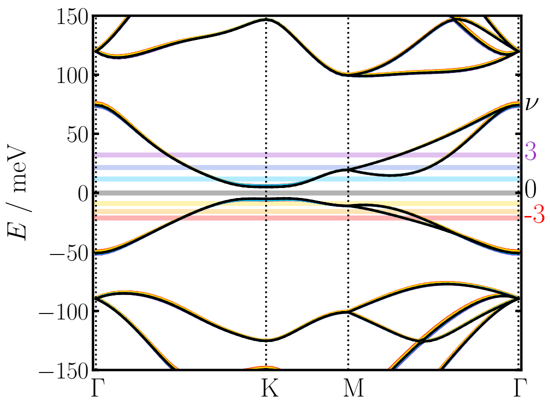

Figure 5.7: Band structure of θ =1.89° tDBLG with $\epsilon_{\mathrm{bg}} = 4$, along the high-symmetry path of the Brillouin zone of the moiré unit cell, for different integer doping levels per moiré unit cell ($-3 \leq \nu \leq 3$), where the horizontal lines denote the Fermi energy at each doping level. The case of charge neutrality is shown in black, and all other integer doping levels are practically identical to it. Note all bands are aligned such that the zero of energy occurs in the middle of the band-gap at the K-point.

added. We have used an effective dielectric constant ϵ_{bg}=4, which corresponds to experiments in which tDBLG is encapsulated in hBN [244]. In stark contrast with tBLG [95, 135–138], it can be seen that the dispersion does not significantly change upon doping (all doping levels have been aligned such that the zero energy occurs at the mid-point between the upper and lower bands at K-point). The bands distort by up to only a few meV relative to the charge neutral case (black lines), which is insignificant compared to the bandwidth of these flat bands.

In tDBLG there are several reasons why the bands do not distort significantly upon doping. Firstly, the strength of the Hartree potential and how it varies with doping is relatively small. In Fig. 5.8, we show the locally-averaged Hartree potential along the diagonal of the moiré unit cell on an outer (left panels) and inner (right panels) graphene layer. We find that the in-plane variation reaches values of ±25 meV on the inner layers, but only of the order of ±10 meV on the outer layers. These variations are significantly smaller than the bandwidth of the flat bands. In contrast, the Hartree potential of tBLG and twisted trilayer graphene (tTLG) reaches values of ±100 meV.

Upon electron doping tDBLG ($\nu > 0$, top panels of Fig. 5.8), a positive peak in the Hartree potential emerges in the AA regions (located 2/3 of the way along the diagonal of the moiré unit cell), and when electrons are removed ($\nu < 0$, bottom panels of Fig. 5.8) this becomes a negative trough. This is due to the flat bands having significant localisation in the AA regions

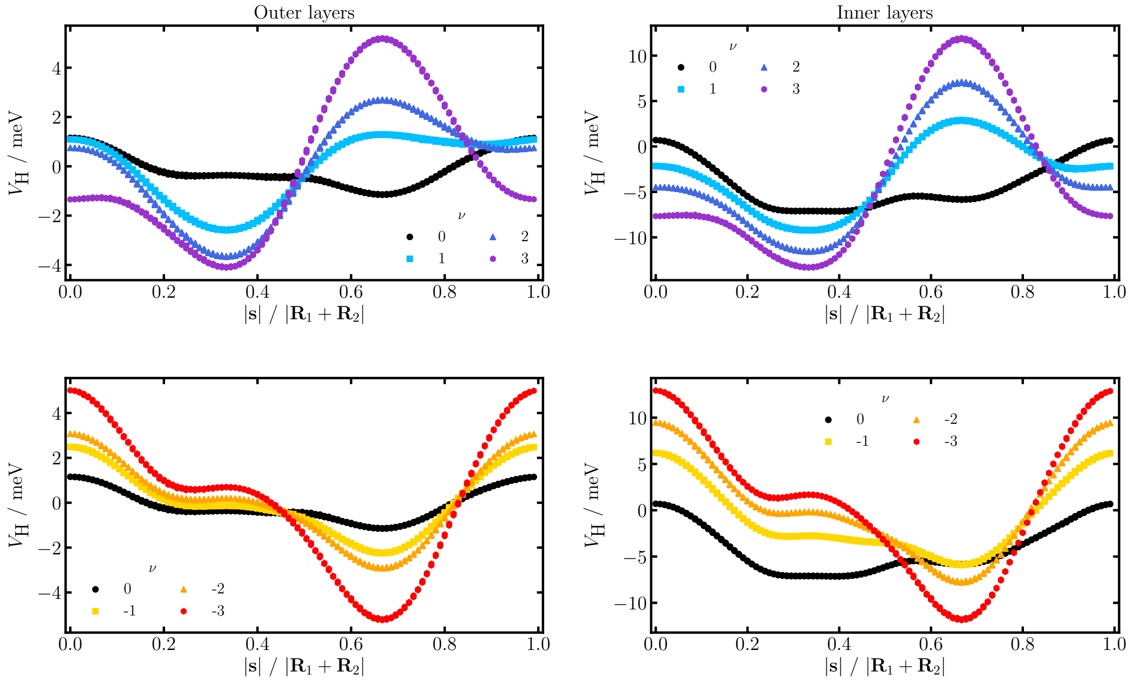

Figure 5.8: Locally-averaged Hartree potential along the diagonal of the moiré unit cell for electron and hole doped tDBLG with θ =1.89° and ϵ_bg = 4. The variable $|\mathbf{s}|$ is the distance from the BA site of the moiré unit cell to a point $\mathbf{s}$ along its long diagonal. The vertical solid lines correspond to BA stacking of the inner layers, dotted-dashed lines to the AB stacking, and dotted lines for AA stacking. The left panels shows results for the outer layers and the right panels are for the inner layers. Results for electron doped systems ($\nu > 0$) are shown in the upper panels and results for hole doped systems ($\nu < 0$) are shown in the lower panels. The Hartree potential in each layer has been locally averaged: the value at each atomic position is obtained by taking the average of the Hartree potentials on that atom its three nearest neighbours. The averaging smooths the oscillations that occur between the two sublattices of each graphene layer.

of the inner layers, similar to tBLG [95, 125, 135–138] and tTLG [126]. However, in contrast to tBLG and tTLG, we do not find a clean separation of electronic states in real and reciprocal space [178]. At the Γ-point, the states are peaked on the AB/BA regions of the inner layers, and the states at the M-point are mainly localised on the AA regions of the inner layers. The localisation of the states at the K-point, however, is not well-separated between these two regions. One of the valley degenerate states is localised on the AA regions of the inner layer, but the other is mainly localised on the outer layer with a small peak in the AB/BA region of the inner layer. Therefore, the in-plane variations of the Hartree potential are not capable of causing significant band deformations in tDBLG*. In tBLG and tTLG, on the other hand, there is a clean separation of states in real and reciprocal space: states at the edge of the hexagonal Brillouin zone are localised on the AA regions of the moiré unit cell in real space, whereas states at the middle of the Brillouin zone are localised on the AB/BA regions of the moiré unit cell. This separation couples with the spatial variations in the Hartree potential to give rise to significant deformations of the electronic band structure and is the main origin of the qualitative difference observed with tDBLG.

---

*A similar explanation was also offered in the continuum model of Ref. 178, where it was noted that the states in the Brillouin zone are not as cleanly separated in tDBLG as they are in tBLG [298].

As we do not observe significant distortions in the bands with doping in tDBLG, this means that we do not expect to observe pinning of the van Hove singularities in tunneling experiments. In fact, recent tunneling experiments have shown that there is, in fact, no pinning of the van Hove singularities in tDBLG [175–177]. The bands were not completely rigid, however, and continuous distortions to the electronic structure were observed with doping. But in the STM experiments doping is accompanied by a concomitant increase in the perpendicular electric field (because of the single-gated devices). In Ref. 177 it was shown that these distortions are well-described by including the effect of a perpendicular electric field.

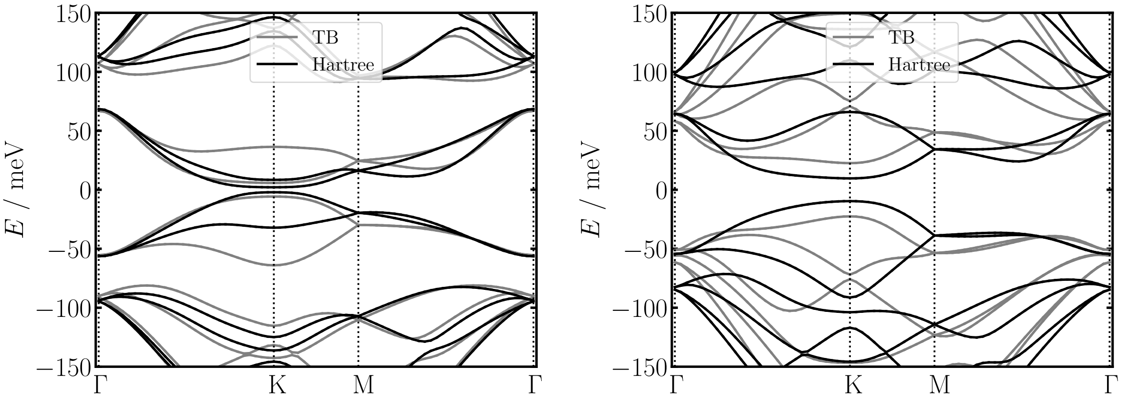

Figure 5.9: Band structure along the high symmetry path of θ =1.89° tDBLG with $\epsilon_{\mathrm{bg}} = 4$ and $\nu = 0$ in an electric field of 10 meVÅ^{-1} (left) and 30 meVÅ^{-1} (right). The results of both the tight-binding approximation (red) and self-consistent Hartree theory (black) calculations are shown.

In Fig. 5.9 we show the Hartree (black) and tight-binding (red) band structures of 1.89° tDBLG at charge neutrality with $\epsilon_{\mathrm{bg}} = 4$ for two different electric field strengths. Upon applying a perpendicular electric field, the gap between the valence and conduction band increases dramatically with the strength of the field. Moreover, the valley degeneracy of both the valence and conduction bands is lifted in the electric field, apart from at the Γ and M points. This splitting of the conduction and valence bands increases substantially with the field, with the valence bands undergoing more significant distortions than the conduction bands.

In the tight-binding approximation (without any additional intrinsic symmetric polarisation fields) the band distortions are significantly more pronounced than in Hartree theory. The electric field causes the system to polarise such that in one of the bilayers there is an enrichment of electrons and in the other bilayer there is a depletion of electrons, with the outer layers exhibiting larger enrichment/depletion than the inner layers. When Hartree interactions are included the Hartree potential opposes the external electric field to reduce its effect.

The extent by which the Hartree potential screens the electric field can be determined by computing an effective dielectric constant for each layer

$$\epsilon^{(\alpha)} = \frac{V_{\text{ext}}^{(\alpha)}}{V_{\text{ext}}^{(\alpha)} + V_{\text{H}}^{(\alpha)}}, \tag{5.3}$$

where $V_{\text{ext}}^{(\alpha)} = \langle E z_i^{(\alpha)} \rangle$ is the average potential due to the electric field in layer α, with E denoting the electric field strength, $z_i^{(\alpha)}$ the z-coordinate of atom i in layer α, and $\langle \cdots \rangle$ an average over i in layer α, and $V_{\text{H}}^{(\alpha)} = \langle V_{\text{H}i}^{(\alpha)} \rangle$ is the averaged Hartree potential in each layer α. For the electric field of 10 $\text{meV}\text{Å}^{-1}$, we found that the average of the dielectric constant in each layer has a value of 2.60, but an electric field of 30 $\text{meV}\text{Å}^{-1}$ only gives a value of 1.94. This reflects the fact that the electrons do not screen larger electric fields as effectively. Note that these values were obtained with $\epsilon_{\text{bg}} = 4$. For free-standing tDBLG, the effective dielectric constant would be slightly larger. It has been found from DFT calculations of different numbers of layers of stacked (untwisted) graphene, that the effective perpendicular dielectric constant is approximately 3 [300, 301]. Therefore, these values of dielectric constant for tDBLG are qualitatively consistent with that found in DFT calculations in layers of stacked (untwisted) graphene.

In Fig. 5.10, we show the band structures of free-standing ($\epsilon_{\text{bg}} = 1$) 2.45° tDBLG, comparing a number of different models. Both panels include the band structure obtained from DFT at charge neutrality as a reference (purple). The left panel also shows the tight-binding band structure (red). We find, as others also have [163], that the tight-binding band structure matches reasonably well with that of DFT. There is, however, a slight discrepancy in the band

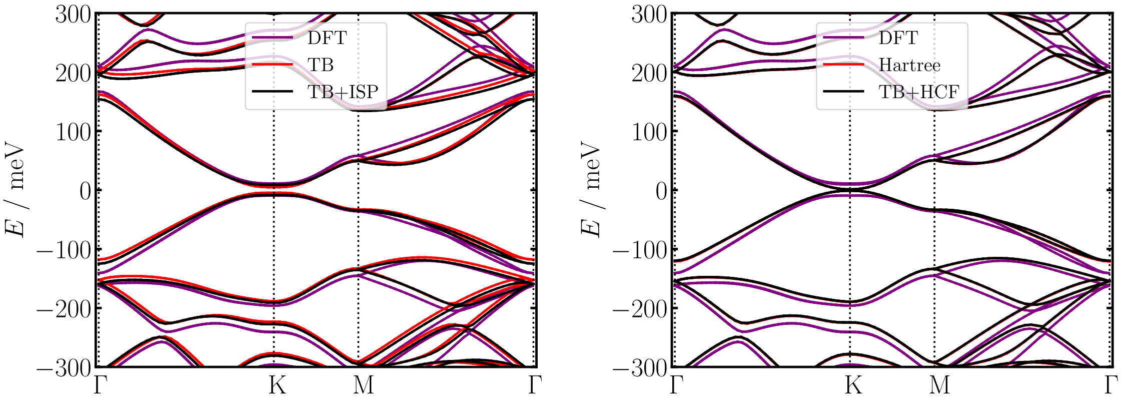

Figure 5.10: Band structure along the high-symmetry path of a θ =2.45° tDBLG with $\epsilon_{\mathrm{bg}} = 1$ and $\nu = 0$. (Left) comparison of DFT with the tight-binding (TB) model (with no layer-dependent potential) and a tight-binding model in which a layer-dependent on-site potential of −30 meV on the inner layers relative to the outer layers is included, which is referred to as the tight-binding plus intrinsic symmetric potential model (TB+ISP). (Right) comparison of DFT with self-consistent Hartree theory and with a tight-binding model in which a layer-dependent on-site potential is included that is determined by the average of the Hartree potential in that layer, the interlayer potential difference resulting from which is 8 meV. This is referred to as the tight-binding plus Hartree crystal field model (TB+HCF).

width of the flat bands and the gap between the conduction and valence bands at the K and K′ points. The difference in the band width is simply a consequence of the chosen decay parameters in the Slater-Koster rules of our tight-binding model, and this does not affect the gap between the bands significantly. As shown in Ref. 163, the tight-binding band gap can be corrected by including an empirical on-site and layer-dependent intrinsic symmetric polarisation (ISP) potential to the tight-binding model, as seen in the TB+ISP band structure (black) in the left panel of Fig. 5.10. The value of −30 meV on the inner layers relative to the outer layers that we have used for the ISP potential is that used in Ref. 163, which was determined by fitting the gap in the band structure at the K-point to that computed with DFT over a range of twist angles. It can be seen that the ISP does not change the band width significantly and gives rise to better quantitative agreement with DFT.

To explore the origin of the ISP, in the right panel of Fig. 5.10, we compare the Hartree band structure (red) to DFT (purple). Compared to the TB bandstructure in the left panel, we find that including long-range electron interactions has a very small effect on the dispersion at charge neutrality, and the most prominent difference is a slight reduction of the gap between the valence and conduction bands at the K and K′ points, where the valence and conduction

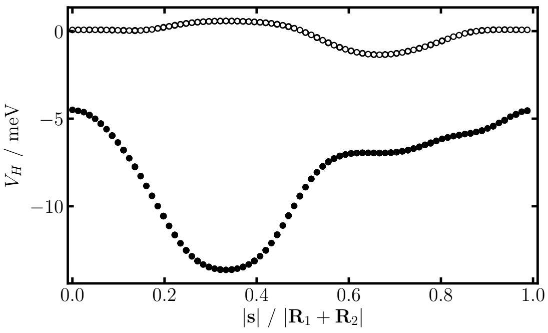

Figure 5.11: Locally-averaged Hartree potential along the diagonal of the moiré unit cell for θ =2.45° with $\epsilon_{\text{bg}} = 1$ at $\nu = 0$. The outer layers are denoted by open circles and the inner layers by filled circles. The variable $|\mathbf{s}|$ is the distance from the BA site of a moiré unit cell along the long diagonal of the unit cell, given by the vector $\mathbf{R}_1 + \mathbf{R}_2$. The vertical solid lines correspond to BA stacking of the inner layers, dotted-dashed lines to the AB stacking, and dotted lines for AA stacking. The value plotted on each atom is the average of the Hartree potential on that atom with the average of the Hartree potentials on the three nearest neighbour atoms.

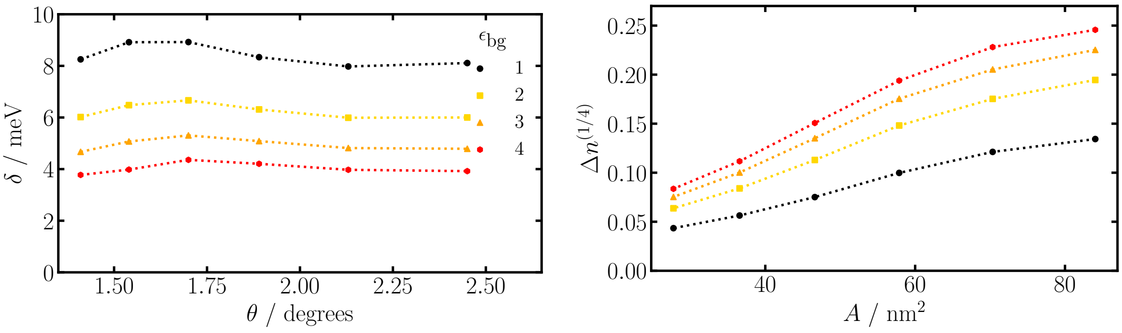

Figure 5.12: (Left) The average Hartree potential difference between the outer and inner layers, δ, for several dielectric constants as a function of twist angle θ. We refer to this quantity as the Hartree crystal field (HCF). (Right) The total excess number of electrons $\Delta n^{(1/4)}$ on one of the outer layers (which we refer to as layers 1 and 4) within the moiré unit cell at various dielectric constants ϵ_{bg} as a function of moiré unit cell area A.

bands now touch. Interestingly, overall, the Hartree band structure appears to be in worse agreement with DFT than the TB results, even without the ISP.

To understand the observed band distortions, we plot the locally-averaged Hartree potential in Fig. 5.11. The Hartree potential has significant variations within the inner layers, whereas it remains approximately constant in the outer layers. Overall, the Hartree potential is more negative on the inner layers than the outer layers; hence, there are more electrons localised on the outer layers than the inner layers. Adapting the definition of Ref. 164 for the crystal field, we define δ to be the difference between the layer-averaged on-site Hartree potential on the outer and inner layers of tDBLG. We refer to this quantity as the Hartree crystal field (HCF) and it is given by

$$\delta = \langle \varepsilon^{\text{el}}_{\text{out}} \rangle - \langle \varepsilon^{\text{el}}_{\text{in}} \rangle, \tag{5.4}$$

where $\langle \varepsilon^{\text{el}}_{\text{out}} \rangle$ and $\langle \varepsilon^{\text{el}}_{\text{in}} \rangle$ are the on-site energies averaged over atoms in the outer and inner layer of a bilayer, respectively. The two bilayers in tDBLG are equivalent by symmetry. In the right panel of Fig. 5.10, we show the band structure from a tight-binding calculation in which δ (taken as 8 meV for $\varepsilon_{bg} = 1$) is added to the outer layers as a layer-dependent on-site energy (referred to as TB+HCF, black lines). Comparing to the self-consistent Hartree approach shown in the same panel (red lines), it can be seen that the band structures almost lie on top of one another except at the K-point where there is a shifting of about 5 meV. Therefore, the in-plane variations of the Hartree potential do not appear to alter the band structure in any way, and it is the average difference between the Hartree potential on the inner and outer layers which determines the (small) band distortions.

Upon including the ISP or Hartree potential, we observe two effects: the Γ-point energies shifts down and a gap opens/closes at the K-point. The former can be understood from the fact that the states at the Γ-point are mainly localised on the inner layers. The latter can be understood from an analysis of the localisation of the states at the conduction and valence sides of the K-point. In the TB model, the conduction states are mainly localised on the inner layers and the valence states are mainly localised on the outer layers. The addition of the ISP or HCF reduces the energy of the conduction states and increases the energy of the valence states. These states cross in energy with an avoided crossing.

The left panel of Fig. 5.12 shows that, for a given ϵ_{bg}, δ remains approximately constant for the twist angles studied here. δ should be directly proportional to the surface charge density of the layers within a bilayer, assuming an idealised parallel plate capacitor model. Therefore, we can understand the twist angle dependence of δ by analysing the number of transferred electrons between the layers of the AB stacked bilayers per moiré unit area. If the number of transferred electrons between the layers of the bilayer remains constant with twist angle, one would expect that δ decreases inversely with the area of the moiré unit cell, and hence as θ^{-2}, as the area of the moiré unit cell scales quadratically with the twist angle. As shown in

Fig. 5.12, we don't observe a θ^{-2} decrease in δ. Therefore, the layer polarisation of the bilayers must increase with decreasing twist angle too. The total number of polarized charges in a layer is calculated from

$$\Delta n^{(\alpha)} = \sum_{j\in\alpha}(n_j - n_0), \tag{5.5}$$

where j runs through all the atoms in one of the layers α. By symmetry Δn is equal and opposite in the outer and inner layer of the bilayers $[\Delta n^{(1)} = -\Delta n^{(2)} = -\Delta n^{(3)} = \Delta n^{(4)}]$. In the right panel of Fig. 5.12 we show how the number of transferred electrons increases with the moiré unit cell area, which explains the approximately constant value of δ over the studied twist angles.

The screened Hartree interaction depends on the dielectric screening due to the environment. The dependence of δ and Δn on ϵ_{bg} is also reported in Fig. 5.12. For a given twist angle, we find that δ reduces as the dielectric constant increases. In experiments, tBDLG is typically encapsulated by thick layers of hBN. Such encapsulation approximately translates to a screened interaction with a dielectric constant of approximately 4 [244]. We find that increasing the dielectric constant from ϵ_{bg}=1 to ϵ_{bg}=4 decreases the magnitude of δ by a factor of two (Fig. 5.12, left panel). A simple $1/\epsilon_{\mathrm{bg}}$ argument would overestimate this by a factor of two. From the right panel of Fig. 5.12, however, we find that the layer polarisation Δn is itself dependent on ϵ_{bg}, as the larger dielectric constant permits more charges to be transferred. The failure of the simple $1/\epsilon_{\mathrm{bg}}$ argument was also shown to be the case for tBLG, where it was argued that tBLG itself already has a large dielectric constant, so increasing the environmental screening by a small amount does not have a large overall effect [137, 256].

In Refs. 163, 164 and 165 it was shown that to obtain DFT accurate low-energy band structures at charge neutrality of free-standing tDBLG, the atomistic tight-binding model which uses the Slater-Koster rules requires a layer-dependent on-site energy. Empirically, it was found that the on-site energy of the inner layers had to be approximately 30 meV lower than that of the outer layers. This is equivalent to the electrons sitting in an electric field which points from inner layers of tDBLG towards the outer layers, which causes the electrons to prefer to reside on the inner layers [164, 165].

We find that the bands predicted by TB+HCF model distort in a very similar manner to those caused by the on-site potential from Refs. 163, 164 and 165. As can be seen from the left panel of Fig. 5.12, the value of δ we obtain from our layer-dependent average of the Hartree potential is approximately one-third of the value found by Ref. 163 for free-standing tDBLG (ϵ_{bg}=1). In our Hartree theory there is an excess of electrons on the outer layers that causes the potential to be larger on the outer layers, which is consistent with the empirically determined ISP. If there were an accumulation of electrons on the inner layers, Hartree theory would give a more positive potential on the inner layers, which is the opposite sign of the ISP that was found in Refs. 163, 164 and 165. Therefore, it does not appear that the Hartree potential alone can fully explain the crystal field.

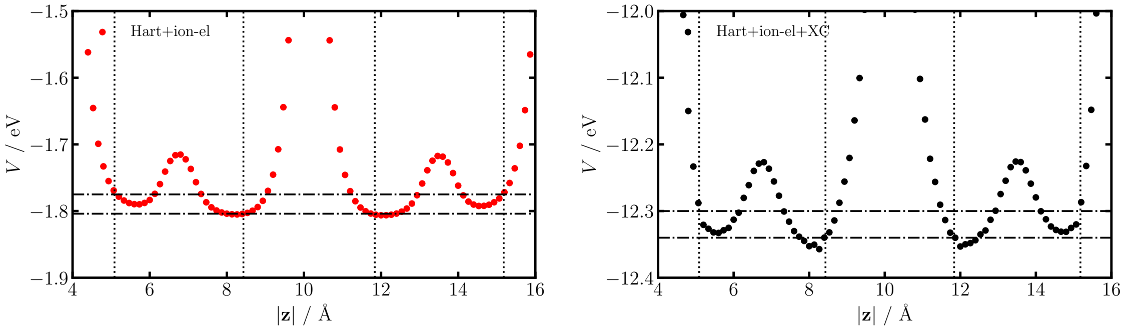

Figure 5.13: (Left) Sum of Hartree potential and ion-electron potential (referred to as the electrostatic potential) from DFT as a function of z (a coordinate perpendicular to the plane of the tDBLG system) in 2.45° tDBLG. (Right) Sum of the electrostatic potential and the local exchange-correlation potential as a function of z in 2.45° tDBLG. In both plots, the potentials are first averaged over the x and y coordinates, and the resulting function of z is smoothed by taking its convolution with a rectangular function of width 3.20 Å. The dotted vertical lines correspond to the z-averaged atomic positions of each layer. The horizontal lines indicate where the potential crosses the z-averaged atomic positions of each layer.

To further investigate the origin of the ISP we perform large-scale first-principles DFT calculations on tDBLG with a twist angle of 2.45°and analyse the Kohn-Sham potential. The Kohn-Sham potential in a DFT calculation has three main contributions: (1) the ion-electron (ion-el) potential, which is often approximated with a pseudo potential; (2) the Hartree contribution from electron-electron (el-el) interactions; and (3) the exchange and correlation contribution. To obtain the on-site energies of the tight-binding model, i.e., what gives rise to the ISP, one needs to integrate the Hamiltonian with the p_z orbital on a carbon atom. The Hamiltonian will have contributions from the kinetic energy and the potential energies. Provided the kinetic energy of the orbitals does not vary between the layers, and it is sufficient to use the local potentials, the local Kohn-Sham potential should give an estimate of the on-site energies of these p_z orbitals. Instead of integrating the potential with the p_z orbitals, we perform spatial averaging of the potential in the x-y plane, and then smooth this resulting potential in the z-direction with a rectangular function. Provided the width of this rectangular function is of the order of an interlayer spacing, reasonable values for the potential difference between the layers are expected.

We find that the ion-el potential is substantially more negative on the inner layers than the outer layers. The inner layers are on average closer to more carbon nuclei than the outer layers, which therefore, produces a more negative potential on the inner layers than the outer layers. Conversely, the Hartree potential is significantly more positive on the inner layers in comparison to the outer layers because the electrons are on average closer to more electrons on the inner layers.

In Fig. 5.13 (left panel), we show the sum of the ion-el and Hartree potential as a function of z, where the potential has been averaged over the x and y directions, and the resulting function of z has been smoothed by taking its convolution with a rectangular function of width 3.20 Å. We find that the sum of these potentials is approximately -30 meV more negative on the inner layers than the outer layers, as indicated with the horizontal lines. This value does not change significantly provided the smoothing function is of the order of the interlayer spacing between adjacent layers. Our atomistic Hartree theory could not capture this value quantitatively. Moreover, if the layer-dependent potential was from charge transfer with just the Hartree potential, we would find more electrons on the outer layers than the inner layers, as found in our tight-binding model (see Fig. 5.12). Ours and other DFT calculations [164, 165] found that there was an accumulation of electrons on the inner layers, however. Therefore, this layer-dependent potential from electrostatic interactions must arise from subtle differences in the ion-el and el-el interactions.

In Fig. 5.13 (right panel) we show the sum of the electrostatic potential and the local part of the exchange-correlation potential, where again the potentials have been smoothed according to the procedure described earlier. When the exchange-correlation potential is included, the precise value of for the difference in potential energy of the inner layers relative to the outer layers has a slight dependence on the width of the smoothing function used, but when the width is of the order of the interlayer spacing we find that including exchange-correlation effects enhance the difference, resulting in values of approximately −40 meV. This is in reasonable agreement with those calculations in Refs. 163, 164 and 165.

5.2.2 Mono-trilayer graphene

In this section, a new mono-trilayer graphene system, where a graphene sheet it is twisted relative to a trilayer graphene (which has aligned layers, i.e. 0°), is investigated. For the trilayer graphene, ABA and ABC stacks are considered since both are experimentally accessible [26, 27]. Recently, ABC trilayer graphene aligned to a hBN substrate has attracted interested because of the reported correlated phases [302–304]. The mono-trilayer system with ABC stacking is ostensibly similar to tBLG and ABC trilayer graphene, which suggests it is a promising candidate for the observation of broken symmetry phases, which motivates us to focus on this moiré material.

In this section, the electronic band structure of graphene twisted on ABC trilayer graphene (referred to as AtABC) and graphene twisted on ABA trilayer graphene (AtABA) is investigated. In Fig. 5.14 the electronic structure[*] of these systems are shown at different twist angles using the atomistic tight-binding approach. For both systems, a set of extremely flat electronic bands emerges as the twist angle approaches the magic-angle of 1.16°.

At twist angles larger than the magic angle (2.0° and 1.47°), the band structure of AtABA [in Fig. 5.14 (top panels)] exhibits a set of four bands with a bandwidth of the order of 100 meV. Two of these form a Dirac cone at the K-point while the other two have a parabolic dispersion near K. At the magic angle of 1.16° (and also at smaller twist angles) the bands no longer form a Dirac cone. The low-energy bands in AtABA are not isolated in energy from the remote bands because they are intersected by a pair of linear bands whose Fermi velocity is similar to that of monolayer graphene. These bands form a second Dirac cone at K which exhibits a

---

[*] The structure was generated from LAMMPS, as outlined in the Methods. The tight-binding parameters for these calculations were $a = 1.39$ Å, $d = 3.35$ Å, $q_\pi = 7.43$ and $q_\pi = 3.14$, with a spherical Heaviside step function with cut-off of 10 Å being used to truncate hopping parameters.

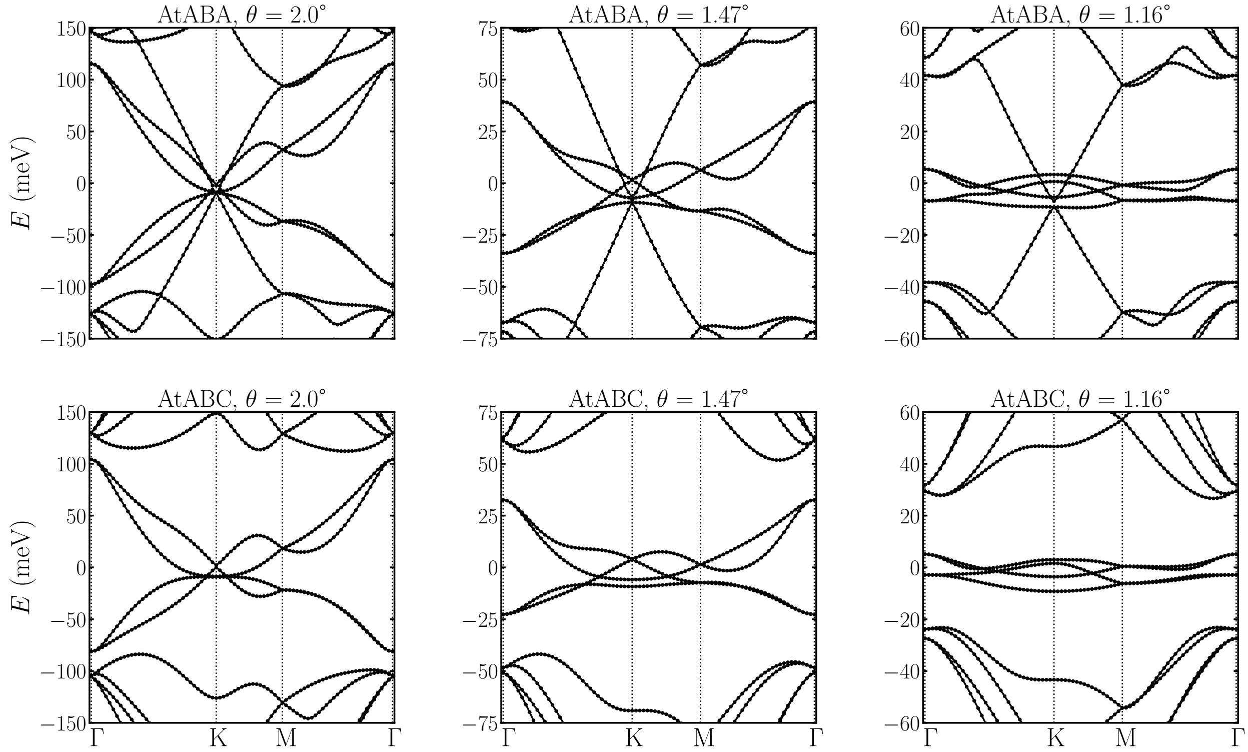

Figure 5.14: Tight-binding band structure of AtABA and AtABC at three twist angles: 2.0°, 1.47° and the magic-angle of 1.16°.

small gap of $\sim 1-5$ meV.

Additional insight can be gained by comparing the band structure of AtABA to that of the constituent ABA trilayer. The latter system features a set of parabolic bands which are also intersected by a Dirac cone [305]. This suggests that the addition of the twisted graphene monolayer on top of the ABA trilayer induces the “flat” Dirac cone (whose Dirac point lies is slightly higher in energy than that of the dispersive Dirac cone) and also modifies the band width of the parabolic bands. Finally, it is also interesting to note that the band structure of AtABA is quite similar to that of twisted trilayer graphene in which the middle layer of an AAA-stacked trilayer is twisted relative to the outer layers [126, 187, 190, 191]. Figure 5.14 (bottom panels) also shows the band structure of AtABC as a function of twist angle. For this system we also find a set of four flat bands near the Fermi level. Whilst these bands look qualitatively similar to those of AtABA, there are some important differences. As in AtABA, the low-energy electronic structure of AtABC has one pair of bands that form a Dirac cone at K at twist angles larger than the magic angle. The other pair of bands, however, now has a cubic dispersion near K, and there is no additional Dirac cone that intersects these bands,

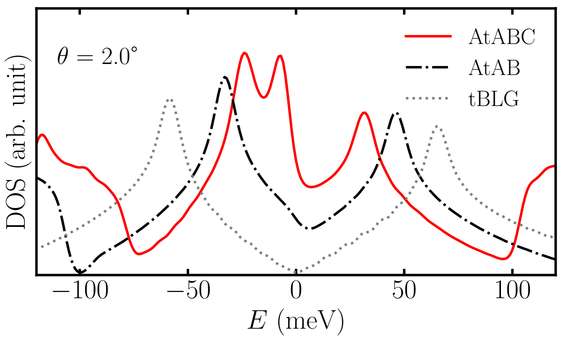

Figure 5.15: Density of states (DOS) as a function of energy for AtABC, AtAB and tBLG at a twist angle of 2.0°. The zero of energy is set to the Fermi level at charge neutrality for each system, and the zero in the DOS is at the bottom of the y-axis.

which are entirely separated from the remote bands in this system near the magic angle.

Again, it is instructive to compare the band structure of AtABC to that of the constituent parts. In ABC trilayer graphene, there is a set of cubic bands near the Fermi level [306], which AtABC retains in the the low-energy dispersion of the isolated bands with the twist angle controlling their width. Finally, it is worth noting that the band structure of AtABC is similar to that of twisted monolayer-AB bilayer graphene (AtAB), with the important difference that the dispersion in AtAB is parabolic [182] instead of cubic at the K point.

This difference in the power law of the dispersion has important consequences for the DOS. In Fig. 5.15, we show the DOS of the flat bands of AtABC, AtAB and tBLG at an angle of 2.0°. All systems have a pair of van Hove singularities at an energy corresponding to a doping level of ±2 electrons (relative to charge neutrality) per moiré unit cell. The linear dispersion of the tBLG bands close to charge neutrality gives rise to a linear DOS close to the Dirac point where the DOS vanishes. In contrast, for AtAB, the DOS is always finite and exhibits a step-like feature at approximately -5 meV where the parabolic bands touch. Importantly, the AtABC system has an additional van Hove singularity arising from the bands with a cubic dispersion.

Based on the tight-binding calculations, AtABC is clearly a promising candidate for hosting strongly correlated electrons in isolated flat bands. We therefore study the effect of electron-electron interactions in this system. To capture the effect of long-ranged Coulomb interactions, self-consistent atomistic Hartree theory calculations at integer doping levels per moiré unit cell were carrier out. However, in contrast to tBLG and tTLG, such interactions only have a negligible effect on the electronic band structure of AtABC, as seen in Fig. 5.16.

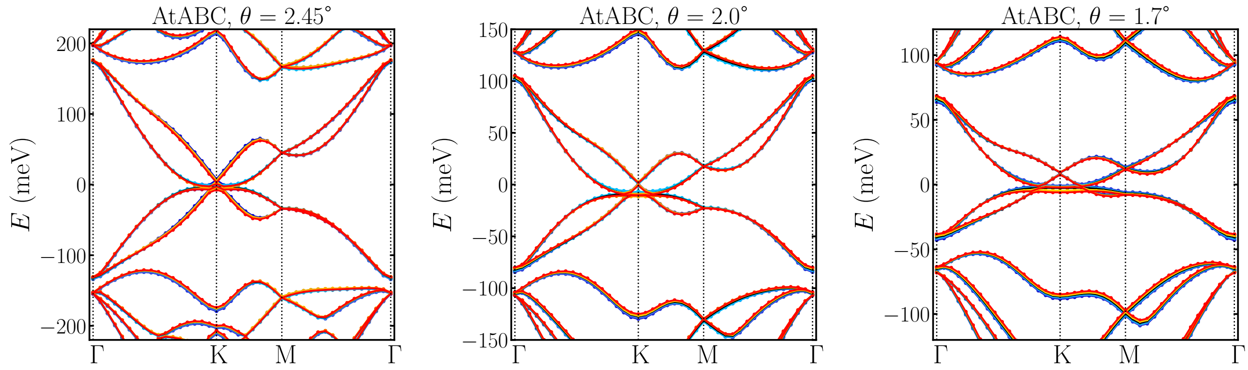

Figure 5.16: Hartree theory band structures of AtABC at 1.7° for integer doping levels per moiré unit cell from $\nu = 3$ (blue) to $\nu = -3$ (red).

This can be understood by analysing the spatial character of the wavefunctions at different points in the first Brillouin zone. In tBLG [136] and tTLG [126], it was shown that there is a strong correlation between a state's position in k-space and its localisation in real space. For example, the states at the edge of the hexagonal Brillouin zone are localised on the AA regions while states at the centre of the Brillouin zone are localised on the AB regions. When the occupancy of these states changes due to electron or hole doping a highly inhomogeneous charge density is induced which in turn results in a strong Hartree potential. In contrast, we do not observe a similar correlation between k-space position and real-space localisation of states in AtABC and as a consequence the charge density induced by doping is relatively uniform resulting in a much weaker Hartree potential. This result is consistent with other Hartree calculations of moiré materials containing untwisted graphene layers [178].

In the absence of significant Hartree interactions, we next consider the effect of exchange interactions. It is well known that the exchange interaction should be screened [231] which reduces its strength and modifies its spatial form. In moiré materials, the presence of flat bands greatly enhances the internal screening [255, 256], and external screening arising from the presence of nearby metallic gates further suppresses long-ranged interactions [114]. As a consequence of screening, the range of the exchange interaction is significantly shorter than the moiré length scale and we therefore employ an atomic Hubbard interaction for electrons in the carbon p_z-orbitals [11, 107, 125, 126, 205, 208, 287] to calculate the interacting spin susceptibility using the random phase approximation (RPA) as function of doping, twist angle and value of the Hubbard U parameter. This approach was also employed in Ref. 125 for tBLG,

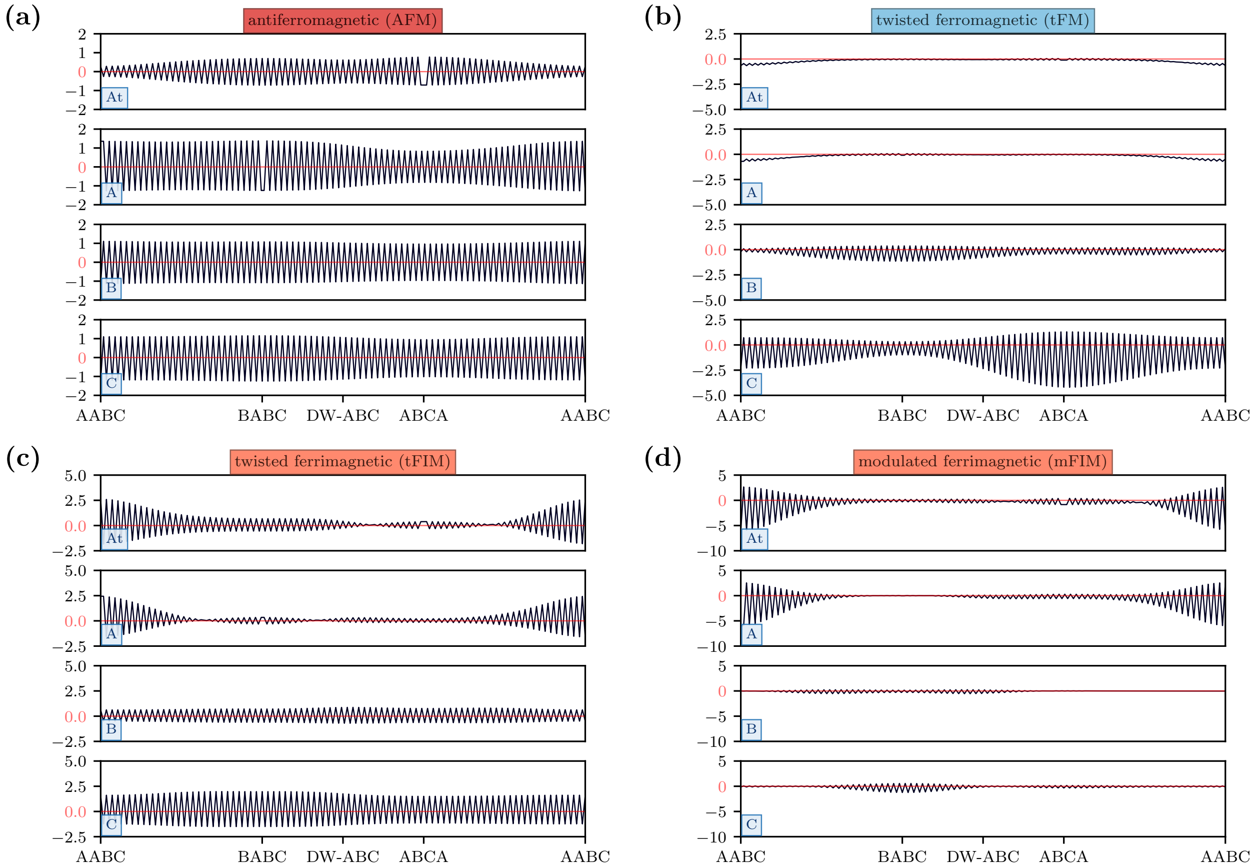

Figure 5.17: Layer-resolved line-cuts of the normalised magnetisation for different magnetic instabilities of AtABC along the diagonal of the moiré unit cell at the magic angle of $\theta = 1.16°$. The local stacking sequence is shown at the bottom of each panel, where DW stands for the domain wall region of the moiré pattern. (a) Anti-ferromagnetic state with mild modulations on the moiré scale. (b) A state with ferromagnetic order in the twisted layers and ferrimagnetic order in the lower layers. (c) A state with modulated ferrimagnetic order in the twisted layers and relatively uniform anti-ferromagnetic order in the lower layers. (d) A state with modulated ferrimagnetic order in all layers.

where excellent agreement between the experimental and theoretical phase diagram was found, and functional renormalisation group calculations [307] have shown that the phase diagram is not sensitive to the range of interactions provided it is short. Therefore, we are confident that this approach can reliably identify the onset of broken symmetry phases in graphitic moiré systems.

From these RPA calculations, we identify the critical value of the Hubbard parameter U_c at which the susceptibility diverges [125, 208]. If U_c is smaller than the physical value of the Hubbard parameter, we expect the system to undergo a phase transition into a magnetically ordered state whose spatial structure is determined by the leading eigenvector of the spin response function. In this work, we use a Hubbard value of $U = 4$ eV, which has been shown

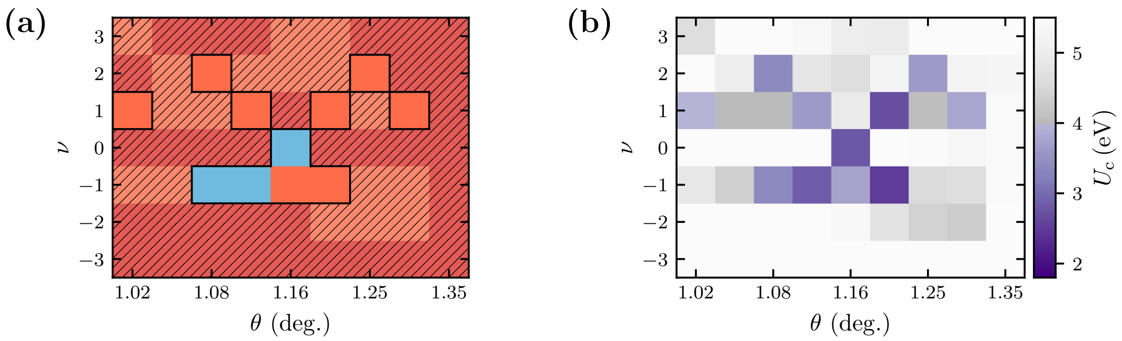

Figure 5.18: (a) - Magnetic phase diagram of AtABC as a function of twist angle θ and integer doping level ν per moiré unit cell. Blue corresponds to ferromagnetic order, orange corresponds to ferrimagnetic order, and red corresponds to anti-ferromagnetic order. Regions where the critical value of the Hubbard parameter is smaller than its physical value are hatched. (b) - Critical interaction strength U_c required for the onset of magnetic instabilities in AtABC as a function of twist angle θ and integer doping levels in the flat bands ν.

to be a realistic value of the onsite Hubbard interaction of graphene [109, 236]. Moreover, in Ref. 125, it was shown that $U = 4$ eV for tBLG yields good agreement with the available experimental data.

Figure 5.17 shows the structure of various low-energy magnetic states of AtABC at the magic-angle of 1.16°. In each of the plots, we display a normalised eigenvector from the magnetic susceptibility calculations as a function of position along the diagonal of the moiré unit cell (different stacking regions are indicated on the x-axis). Other leading instabilities were also found, but they are either variations of the ones shown in Fig. 5.17 with a different nodal structure or mixtures of these orderings. Overall, we find that there is a rich variety of magnetic ordering tendencies that can either be dominant in the twisted layers or in the untwisted layers.

Figure 5.17(a) shows an antiferromagnetic (AFM) state which is mostly uniform over the whole AtABC structure and only exhibits a mild modulation on the moiré scale. The magnetisation differs slightly in each layer with the largest variations occurring in the graphene sheet that is twisted on top of the ABC trilayer. This layer also exhibits a somewhat smaller magnitude of the magnetisation than in the other layers, suggesting that this AFM state is inherited from the AFM state of the ABC trilayer which "spills" into the top layer.

Figure 5.17(b) shows a state with a modulated ferromagnetic (FM) structure in the top two layers and ferrimagnetic structure in the bottom two layers. We refer to this ordering as tFM (for twisted FM, as the FM order is found in the twisted layers). In the upper layers the magnetisation has peaks in the AABC regions which are separated by a node. A similar state has been found in tBLG [125, 208]. Finally, Figs. 5.17(c) and (d) show two examples of ferrimagnetic (FIM) states. The state in Fig. 5.17(c) is mostly AFM with some FIM character and exhibits nodes in the top two layers. We shall refer to this ordering as tFIM (for twisted FIM, as the FIM order is mainly in the twisted layers). The state in Fig. 5.17(d) is predominantly FIM and has significant modulations in each layer, which we refer to as mFIM (for modulated FIM).

Having described in detail the different types of magnetic states in AtABC, we now discuss the magnetic phase diagram as function of twist angle and doping, denoted by ν for the number of additional electrons/holes per moiré unit cell, shown in Fig. 5.18(a). Magnetic states with $U_\mathrm{c} < U = 4$ eV are found for a range of doping levels and twist angles. When $U_\mathrm{c} > U = 4$ eV, we hatch over the magnetic order to indicate that we do not expect it to occur. In Fig. 5.18(b) we plot the corresponding value of U_c for each $\theta - \nu$ combination and if $U_\mathrm{c} > U = 4$ eV we use a grey scale. The FM state is only found at the magic angle at charge neutrality or at slightly smaller twist angles for $\nu = -1$ (i.e., when one hole is added per moiré unit cell). Interestingly, the character of the FM state for $\nu = -1$ slowly transitions from purely FM to a mixture of FM and FIM as a function of the twist angle.

The other broken symmetry states in the phase diagram are of FIM type and occur at $\nu = -1$ at and very close to the magic-angle, but also for the electron doped systems ($\nu = 1$ or $\nu = 2$) over a range of twist angles. In contrast, AFM order is never found in the phase diagram. While this type of order is the leading instability for a range of $\theta - \nu$ values, the corresponding critical values of the Hubbard parameter are always larger than the physical value ($U_\mathrm{c} > U = 4\,\mathrm{eV}$) and therefore this order is not realised. This can be attributed to the fact that the AFM order is inherited from the parent ABC trilayer system which has a high value of U_c [291].

Having presented the band structure, effects of electron-electron interactions and magnetic order of AtABC, a natural question to ask is: how promising is AtABC for the observation of strong correlation phenomena in comparison to other graphitic moiré materials? Among the graphene-based moiré materials that have been studied experimentally to date, only tBLG

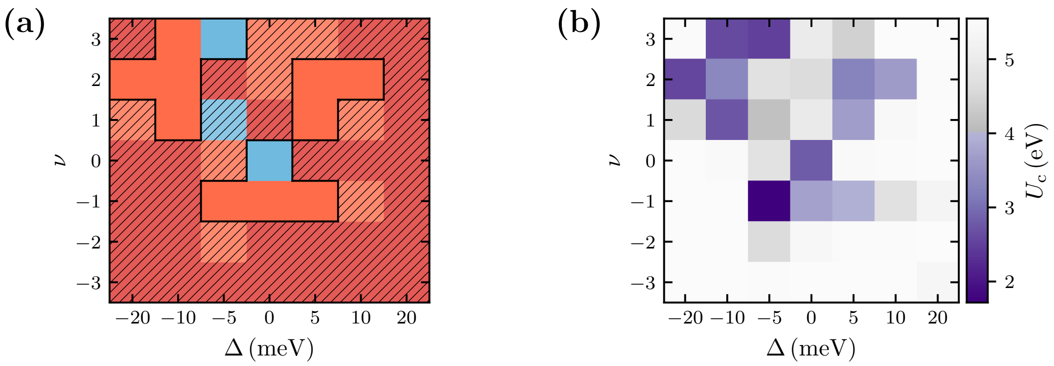

Figure 5.19: (a) - Magnetic phase diagram of 1.16° AtABC as a function of potential difference between adjacent layers Δ (which is proportional to a perpendicular electric field) and integer doping level ν per moiré unit cell. Blue corresponds to ferromagnetic order, orange corresponds to ferrimagnetic order, and red corresponds to anti-ferromagnetic order. Regions where the critical value of the Hubbard parameter is smaller than its physical value are hatched. (b) - Critical interaction strength U_c required for the onset of magnetic instabilities in 1.16° AtABC as a function of layer-dependent onsite potential difference Δ and integer doping levels in the flat bands ν.

and tTLG exhibit robust superconductivity [89, 196]. In contrast to AtABC, the long-ranged Coulomb interaction plays an important role in these systems and enlarges the size of the region in the $\theta - \nu$ phase diagram where broken symmetry states occur [125, 293]. Based on this empirical evidence, one could argue that moiré systems that do not contain any untwisted pairs of neighbouring layers [186] are more promising candidates for the observation of strongly correlated phases than moiré materials that contain untwisted layers [199]. While this might be true in the absence of electric fields, recent reports suggest that magic-angle mono-bilayer (AtAB) graphene exhibits both correlated insulating states [183] as well as signatures of superconductivity when an electric field is applied perpendicular to the layers [185]. Our analysis reveals that these systems, AtAB and AtABC, exhibit qualitatively electronic structure, which suggests that AtABC may also be a promising candidate for the observation of strong correlation phenomena in the presence of applied electric fields.

To put this prediction on a stronger footing, we calculated the interacting spin susceptibility of magic-angle (1.16°) AtABC as a function of applied electric field and doping, as shown in Fig. 5.19. A perpendicular electric field introduces an additional onsite potential, which is approximately constant within a layer, but that varies linearly between the layer. We define Δ as the potential difference between two adjacent layers, such that the onsite potential of layer l (where $l = 1, 2, 3, 4$ with 1 corresponding to the twisted monolayer) is given by $-\Delta \cdot l$. Negative values of Δ mean that the potential energy of the electrons is lowest in the twisted monolayer. This potential difference is directly proportional to the applied electric field, with values of $|\Delta| = 30$ meV being well within experimental reach [126].

In the absence of a field, we only expect magnetic order to occur at charge neutrality or $\nu = -1$ at 1.16° [see Fig. 5.18(a)]. Upon applying an electric field which lowers the energy of electrons in the twisted layers ($\Delta < 0$), we find that the system is more susceptible to magnetic ordering. Overall, we find mainly FIM order in electron-doped systems, but the hole-doped systems do not generally become more susceptible to magnetic ordering, with the exception of $\nu = -1$ at $\Delta = -5$ meV [see Fig. 5.19(b)]. Therefore, the electron-hole asymmetry of the magnetic phase diagram becomes more pronounced in an electric field which lowers the energy of the electrons in the twisted layers relative to the other layers. On the other hand, electric fields which increase the energy of the electrons in the twisted layers ($\Delta > 0$) generally cause the system to be less susceptible to magnetic ordering. For electron-doped $\Delta > 0$ systems in a small field, we find that FIM occurs at $\nu = 1, 2$, but for larger field strengths this magnetic order disappears. In experiments on magic-angle AtAB performed by Chen *et al.* [183], there were similar trends in terms of where the correlated insulating states occur in the space of doping level and electric field. For an electric field which lowers the energy of the monolayer (relative to the AB bilayer), correlated insulating states were found at all integer electron doping levels, similar to tBLG [183]. Whereas, for an electric field which lowers the energy of the AB stacked bilayer (relative to the monolayer), a correlated insulating state was only observed at $\nu = 2$, similar to tDBLG [183]. As we have found that AtABC has a similar electronic structure and electron interactions to AtAB, this also suggests similarities in their broken symmetry phases.

Chapter 6

Conclusions and Outlook

The observation of correlated insulating states and superconductivity in magic-angle tBLG generated tremendous interest in the field of twistronics. This motivated many to further investigate and understand tBLG, and other moiré graphene multilayers. In what follows, a brief summary of the contributions made to this field in this thesis shall be given. The chapter and publication in which the finding was presented shall be indicted.

To understand these correlated phases of tBLG, it is useful to have a minimal model of the low-energy physics. Near this magic angle of 1.1°, the (Fermi) velocity of the electrons become vanishingly small (creating extremely flat electronic bands). In such a regime, the kinetic energy of these electrons, described by the hopping parameter t, is greatly diminished and the potential energy, described by the Hubbard interaction U, prevails as the dominant energy scale. I found that these Hubbard interaction parameters change linearly with the twist angle and that there is a twist angle window in which these emergent electronic phases are expected to be observable [Chapter 3; Goodwin *et al.* PRB 100:121106(R) 2019]. Moreover, in experiments tBLG resides in proximity to metallic gates, which can affect how electrons in tBLG interact with each other. I studied how the distances from tBLG to these metallic gates affect the Hubbard parameters [Chapter 3; Goodwin *et al.* PRB 101:165110 2020]. I found the scale of the potential energy reduces upon bringing tBLG closer to the metallic gates, and if the correlated insulating states and superconductivity are independent phases which compete, I predicted there should no longer be correlated insulating phases and the superconducting state should be stabilised. Shortly after, experimentalists confirmed my predictions with the observation of higher superconductivity transition temperatures without correlated insulators when the gates were close enough to tBLG.

The electronic screening from internal degrees of freedom must also be accounted for in the low-energy model of tBLG [Chapter 3; Goodwin *et al.* PRB 100:235424 2019]. Screening from tBLG dramatically increases as the twist angle is reduced towards the magic angle, as it scales with the inverse of the Fermi velocity. I found near the magic angle, the screened interaction between electrons changes from being purely repulsive, to one with attractive regions too. I proposed that this attractive interaction between electrons, of a purely electronic origin, could act as the glue which binds the electrons into a superconducting phase.

At the magic angle, "off-the-shelf" *ab initio* methods cannot efficiently investigate the electronic properties of tBLG because the system is too large. I developed self-consistent electronic structure codes to investigate different phases in tBLG. I found, in agreement with previous work, strong distortions to the low-energy physics occurs upon adding/removing electrons from tBLG [Chapter 4; Goodwin *et al.* Electron. Struct. 2:034001 2020]. This results in a special, and quite unusual, type of pinning of electronic states that was observed in pioneering scanning tunnelling experiments of tBLG. These long-ranged Hartree interactions are responsible for extending the range of twist angles in which tBLG exhibits emergent, correlated phases [Chapter 4 and Klebl, Goodwin *et al.* PRB 103:195127 2021].

Using these methods, I investigated other moiré graphene multilayers beyond tBLG [Chapter 5; Liang, Goodwin *et al.* PRB 102:155146 2020]. When the moiré material has twist angles of the same magnitude but alternating sign between adjacent graphene layers, such as twisted trilayer graphene [Chapter 5; Fischer, Goodwin *et al.* arXiv:2104.10176] and double twisted bilayer graphene, the effects of long-ranged electron-electron interactions are found to be analogous to tBLG. Specifically, these interactions cause a sensitive doping-dependence to the electronic structure, which pins the van Hove singularities. In contrast, moiré graphene multilayers in which there is at least one set of adjacent layers that are aligned, such as twisted double bilayer graphene [Chapter 5; Cheung, Goodwin *et al.* arXiv:2111.03019] and mono-trilayer graphene [Chapter 5; Goodwin, Klebl *et al.* PRM 5:084008 2021], there is little effect of these long-ranged electron-electron interactions on the electronic structure. These trends could prove to be important in explaining experimental differences between different moiré graphene multilayers.

These calculations were entirely performed with atomistic methods. In this approach, there are two well defined length scales: the length scale associated with the carbon-carbon bond of graphene, and the moiré length scale from twisting the graphene sheets relative to each other. The interplay between these two lengths scales has been evident in our results. The long-ranged electron-electron interactions, on the length scale of the moiré pattern, can cause the onset of magnetic order which modulates on the scale of the carbon-carbon bond length. Conversely, such antiferromagnetic order on the honeycomb lattice of graphene can cause the AB and BA regions of the moiré unit cell to become inequivalent, resulting in gaps to form at charge neutrality in the low-energy electronic structure of tBLG. On the other hand, simply by aligning two adjacent graphene sheets in a moiré graphene multilayer, such there are sublattice variations in the underlying aligned graphene layers, the effect of long-ranged electron-electron (Hartree) interactions on the moiré length scale can be almost completely suppressed.

Looking forward, there are myriad directions in which the field of twistronics could expand into. One of the main questions which the field must answers for tBLG is the mechanism of superconductivity and the role of electron interactions for this phase. Within the work presented here, there are a number of avenues of research which directly follow on.

The internal screening response of tBLG is extremely important in predicting the phases using a beyond mean-field method. Therefore, it would be highly interesting to use the screened Hubbard parameters in methods such as exact diagonalization or quantum Monte Carlo. Alternatively, the dielectric function in momentum space could be used for an interaction vertex in momentum space which could, for example, be used in a functional renormalisation group approach.

The developed Hartree+U theory yielded good agreement with experiments in terms of where broken symmetry phases were expected in the doping and twist angle space. However, it had limitations in its predictions of the broken symmetry phases, especially in terms of correlated insulating states at doping levels away from charge neutrality. Therefore, further development of this theory in the direction of a screened Hartree-Fock theory would be highly promising. The screened interaction in real space from the internal electronic degrees of freedom of the moiré graphene multilayer could be used to screen the exchange interaction in a Hartree-Fock approach. Computing the dielectric function in each iteration of the self-consistent cycle would be computationally extremely expensive. Instead, a more phenomenological approach based on fits to analytical polarizability functions from the electronic structure could provide a computationally cheaper route to investigate these effects.

The role of these long-ranged Hartree interactions could also be highly interesting to investigate in the context of superconductivity. For example, in the context of the conventional mechanism, these long-ranged electron interactions induce additional band flattening which can enhance the density of states (DOS). This is obviously favourable for the conventional mechanism, and it could cause the peak of the superconducting dome to occur away from half-filling as the Hartree interactions can peak the DOS away from this doping level. Alternatively, and perhaps more promising, is a spin-fluctuation mechanism. We demonstrated that these long-ranged electron-electron interactions clearly increase the prevalence of magnetic order in tBLG, and therefore, also the possibility for spin fluctuation superconductivity. Moreover, in this mechanism, the highest transition temperatures always occur away from integer doping levels, which is what is known from experiments.

Finally, further research on moiré graphene multilayers would also be quite fruitful. Here a qualitative difference between systems with alternating twist angle structures to those with at least one set of adjacent graphene layers that are aligned were identified in terms of the long-ranged Hartree interactions. It would be interesting to see if any general trends emerge with multiple twist angles, for example. Only by further investigating these different moiré graphene multilayers with different methodologies will the extent of the difference between these two classes of moiré graphene multilayers be revealed.

Bibliography

[1] A. H. Castro Neto, F. Guinea, N. M. R. Peres, K. S. Novoselov, and A. K. Geim. The electronic properties of graphene. *Rev. Mod. Phys.*, 81:109–162, 2009.

[2] M. I. Katsnelson. Graphene: carbon in two dimensions. *Mater. Today*, 10:20–27, 2007.

[3] H. Lu and S.-D. Li. Two-dimensional carbon allotropes from graphene to graphyne. *J. Mater. Chem. C*, 1:3677, 2013.

[4] K. S. Novoselov, A. K. Geim, S. V. Morozov, D. Jiang, Y. Zhang, S. V. Dubonos, I. V. Grigorieva, and A. A. Firsov. Electric field effect in atomically thin carbon films. *Science*, 306:666–669, 2004.

[5] P. R. Wallace. The band theory of graphite. *Phys. Rev.*, 71:622, 1947.

[6] C. Honerkamp. Density waves and Cooper pairing on the honeycomb lattice. *Phys. Rev. Lett.*, 100:14604, 2008.

[7] V. N. Kotov, B. Uchoa, V. M. Pereira, F. Guinea, and A. H. Castro Neto. Electron-electron interactions in graphene: Current status and perspectives. *Rev. Mod. Phys.*, 84:1067–1125, 2012.

[8] H-K. Tang, E. Laksono, J. N. B. Rodrigues, P. Sengupta, F. F. Assaad, and S. Adam. Interaction-driven metal-insulator transition in strained graphene. *Phys. Rev. Lett.*, 115:186602, 2015.

[9] J. Jung and A. H. MacDonald. Enhancement of nonlocal exchange near isolated band crossings in graphene. *Phys. Rev. B*, 84:085446, 2011.

[10] H.-K. Tang, J. N. Leaw, J. N. B. Rodrigues, I. F. Herbut, P. Sengupta, F. F. Assaad, and S. Adam. The role of electron-electron interactions in two-dimensional Dirac fermions. *Science*, 361:570–574, 2018.

[11] L. A. Gonzalez-Arraga, J. L. Lado, F. Guinea, and P. San-Jose. Electrically controllable magnetism in twisted bilayer graphene. *Phys. Rev. Lett.*, 119:107201, 2017.

[12] Y. Wang *et al.* Observing atomic collapse resonances in artificial nuclei on graphene. *Science*, 340:734–737, 2013.

[13] C.-H. Park, L. Yang, Y.-W. Son, and M. L. Cohen abd S.G. Louie. Anisotropic behaviours of massless Dirac fermions in graphene under periodic potentials. *Nat. Phys.*, 4:213–217, 2008.

[14] J. Mao *et al.* Evidence of flat bands and correlated states in buckled graphene superlattices. *Nature*, 584:215–220, 2020.

[15] D. C. Elias, R. V. Gorbachev, A. S. Mayorov, S. V. Morozov, P. Blake A. A. Zhukov, L. A. Ponomarenko, I. V. Grigorieva, K. S. Novoselov, F. Guinea, and A. K. Geim. Dirac cones reshaped by interaction effects in suspended graphene. *Nat. Phys.*, 7:701–704, 2011.

[16] J. Chae *et al.* Renormalization of the graphene dispersion velocity determined from scanning tunneling spectroscopy. *Phys. Rev. Lett.*, 109:116802, 2012.

[17] B. Hunt *et al.* Massive Dirac Fermions and Hofstadter butterfly in a van der Waals heterostructure. *Science*, 340:1427–1430, 2013.

[18] C. R. Dean *et al.* Hofstadter's butterfly and the fractal quantum Hall effect in moiré superlattices. *Nature*, 497:598–602, 2013.

[19] P. Moon and M. Koshino. Electronic properties of graphene/hexagonal-boron-nitride moiré superlattice. *Phys. Rev. B*, 90:155406, 2014.

[20] N. R. Finney, M. Yankowitz, L. Muraleetharan, K. Watanabe, T. Taniguchi, C. R. Dean, and J. Hone. Tunable crystal symmetry in graphene–boron nitride heterostructures with coexisting moiré superlattices. *Nat. Nanotechnol*, 14:1029–1034, 2019.

[21] Zihao Wang *et al.* Composite super-moiré lattices in double-aligned graphene heterostructures. *Sci. Adv.*, 5:eaay8897, 2019.

[22] J. B. Oostinga, H. B. Heersche, X. Liu, A. F. Morpurgo, and L. M. K. Vandersypen. Gate-induced insulating state in bilayer graphene devices. *Nat. Mater.*, 7:151–157, 2008.

[23] Y. Zhang, T.-T. Tang, C. Girit, Z. Hao, M. C. Martin, A. Zettl, M. F. Crommie, Y. R. Shen, and F. Wang. Direct observation of a widely tunable bandgap in bilayer graphene. *Nature*, 459:820–823, 2009.

[24] A. V. Rozhkov, A. O. Sboychakov, A. L. Rakhmanov, and F. Nori. Electronic properties of graphene-based bilayer systems. *Phys. Rep.*, 648:1–104, 2016.

[25] K. S. Novoselov, E. Mccann, S. V. Morozov, V. I. Fal'ko, M. I. Katsnelson, U. Zeitler, D. Jiang, F. Schedin, and A. K. Geim. Unconventional quantum Hall effect and Berry's phase of 2π in bilayer graphene. *Nat. Phys.*, 2(3):177, 2006.

[26] W. Bao *et al.* Stacking-dependent band gap and quantum transport in trilayer graphene. *Nat. Phys.*, 7:948–952, 2011.

[27] K. Zou, F. Zhang, C. Clapp, A. H. MacDonald, and J. Zhu. Transport studies of dual-gated abc and aba trilayer graphene: Band gap opening and band structure tuning in very large perpendicular electric fields. *Nano Lett.*, 13:369–373, 2013.

[28] P. Maher, C. R. Dean, A. F. Young, T. Taniguchi, K.Watanabe, K. L. Shepard, J. Hone, and P. Kim. Evidence for a spin phase transition at charge neutrality in bilayer graphene. *Nat. Phys.*, 9:154–158, 2013.

[29] J. M. B. Lopes dos Santos, N. M. R. Peres, and A. H. Castro Neto. Graphene bilayer with a twist: Electronic structure. *Phys. Rev. Lett.*, 99:256802, 2007.

[30] S. Carr, S. Fang, and E. Kaxiras. Electronic-structure methods for twisted moiré layers. *Nat. Rev. Mater*, 5:748–763, 2020.

[31] S. J. Ahn *et al.* Dirac electrons in a dodecagonal graphene quasicrystal. *Science*, 361:782–786, 2018.

[32] G. Trambly de Laissardière, D. Mayou, and L. Magaud. Localization of Dirac electrons in rotated graphene bilayers. *Nano Lett.*, 10:804–808, 2010.

[33] R. Bistritzer and A. H. MacDonald. Moiré bands in twisted double-layer graphene. *PNAS*, 108:12233–12237, 2010.

[34] J. M. B. Lopes dos Santos, N. M. R. Peres, and A. H. Castro Neto. Continuum model of the twisted graphene bilayer. *Phys. Rev. B*, 86:155449, 2012.

[35] E. Y. Andrei and A. H. MacDonald. Graphene bilayers with a twist. *Nat. Mater.*, 19:1265–1275, 2020.

[36] J. Jung, A. Raoux, Z. Qiao, and A. H. MacDonald. *Ab initio* theory of moiré superlattice bands in layered two-dimensional materials. *Phys. Rev. B*, 89:205414, 2014.

[37] G. Trambly de Laissardière, D. Mayou, and L. Magaud. Numerical studies of confined states in rotated bilayers of graphene. *Phys. Rev. B*, 86:125413, 2012.

[38] G. Tarnopolsky, A. J. Kruchkov, and A. Vishwanath. Origin of magic angles in twisted bilayer graphene. *Phys. Rev. Lett.*, 122:106405, 2019.

[39] S. Shallcross, S. Sharma, E. Kandelaki, and O. A. Pankratov. Electronic structure of turbostratic graphene. *Phys. Rev. B*, 81:165105, 2010.

[40] E. Suárez Morell, J. D. Correa, M. Pacheco P. Vargas, and Z. Barticevic. Flat bands in slightly twisted bilayer graphene: Tight-binding calculations. *Phys. Rev. B*, 82:121407(R), 2010.

[41] A. O. Sboychakov, A. L. Rakhmanov, A. V. Rozhkov, and Franco Nori. Electronic spectrum of twisted bilayer graphene. *Phys. Rev. B*, 92:075402, 2015.

[42] A. Oshiyama, J.-I. Iwata, K. Uchida, and Y.-I. Matsushita. Large-scale real-space density-functional calculations: Moiré-induced electron localization in graphene. *J. Appl. Phys.*, 117:112811, 2015.

[43] S.Fang and E. Kaxiras. Electronic structure theory of weakly interacting bilayers. *Phys. Rev. B*, 93:235153, 2016.

[44] G. Li, A. Luican, J. M. B. Lopes dos Santos, A. H. Castro Neto, A. Reina, J. Kong, and E. Y. Andrei. Observation of van Hove singularities in twisted graphene layers. *Nat. Phys.*, 6:109, 2010.

[45] I. Brihuega, P. Mallet, H. González-Herrero, G. Trambly de Laissardiére, M. M. Ugeda, L. Magaud, J. M. Gómez-Rodríguez, F. Ynduráin, and J.-Y. Veuillen. Unraveling the intrinsic and robust nature of Van Hove singularities in twisted bilayer graphene by scanning tunneling microscopy and theoretical analysis. *Phys. Rev. Lett.*, 109:196802, 2012.

[46] W. Yan, M. Liu, R.-F. Dou, L. Meng, L. Feng, Z.-D. Chu, Y. Zhang, Z. Liu, J.-C. Nie, and L. He. Angle-dependent van Hove singularities in a slightly twisted graphene bilayer. *Phys. Rev. Lett.*, 109:126801, 2012.

[47] V. Cherkez, G. Trambly de Laissardiére, P. Mallet, and J.-Y. Veuillen. Van Hove singularities in doped twisted graphene bilayers studied by scanning tunneling spectroscopy. *Phys. Rev. B*, 91:155428, 2015.

[48] Dillon Wong *et al.* Local spectroscopy of moiré-induced electronic structure in gate-tunable twisted bilayer graphene. *Phys. Rev. B*, 92:155409, 2015.

[49] S.-Y. Li, K.-Q. Liu, L.-J. Yin, W.-X. Wang, W. Yan, X.-Q. Yang, J.-K. Yang, H. Liu, H. Jiang, and L. He. Splitting of van Hove singularities in slightly twisted bilayer graphene. *Phys. Rev. B*, 96:155416, 2017.

[50] K. Uchida, S. Furuya, J.-I. Iwata, and A. Oshiyama. Atomic corrugation and electron localization due to moiré patterns in twisted bilayer graphenes. *Phys. Rev. B*, 90:155451, 2014.

[51] M. Neek-Amal, P. Xu, D. Qi, P. M. Thibado, L. O. Nyakiti, V. D. Wheeler, R. L. Myers-Ward, Jr. C. R. Eddy, D. K. Gaskill, and F. M. Peeters. Membrane amplitude and triaxial stress in twisted bilayer graphene deciphered using first-principles directed elasticity theory and scanning tunneling microscopy. *Phys. Rev. B*, 90:064101, 2014.

[52] G. Cantele, D. Alfè, F. Conte, V. Cataudella, D. Ninno, and P. Lucignano. Structural relaxation and low energy properties of twisted bilayer graphene. *Phys. Rev. Research*, 2:043127, 2020.

[53] P. Lucignano, D. Alfé, V. Cataudella, D. Ninno, and G. Cantele. Crucial role of atomic corrugation on the flat bands and energy gaps of twisted bilayer graphene at the magic angle. *Phys. Rev. B*, 99:195419, 2019.

[54] M. M. van Wijk, A. Schuring, M. I. Katsnelson, and A. Fasolino. Relaxation of moiré patterns for slightly misaligned identical lattices: graphene on graphite. *2D Mater.*, 2:034010, 2015.

[55] S. K. Jain, V. Juričić, and G. T. Barkema. Structure of twisted and buckled bilayer graphene. *2D Mater.*, 4:015018, 2017.

[56] F. Gargiulo and O. V. Yazyev. Structural and electronic transformation in low-angle twisted bilayer graphene. *2D Mater.*, 5:015019, 2018.

[57] M. Wen, S. Carr, S. Fang, E. Kaxiras, and E. B. Tadmor. Dihedral-angle-corrected registry-dependent interlayer potential for multilayer graphene structures. *Phys. Rev. B*, 98:235404, 2018.

[58] N. N. T. Nam and M. Koshino. Lattice relaxation and energy band modulation in twisted bilayer graphene. *Phys. Rev. B*, 96:075311, 2017.

[59] X. Liang, Z. A. H. Goodwin, V. Vitale, F. Corsetti, A.A. Mostofi, and J. Lischner. Effect of bilayer stacking on the atomic and electronic structure of twisted double bilayer graphene. *Phys. Rev. B*, 102:155146, 2020.

[60] S. Dai, Y. Xiang, and D. J. Srolovitz. Twisted bilayer graphene: Moiré with a twist. *Nano Lett.*, 16:5923–5927, 2016.

[61] H. Yoo *et al.* Atomic and electronic reconstruction at van der Waals interface in twisted bilayer graphene. *Nat. Mater.*, 18:448–453, 2019.

[62] N. P. Kazmierczak, M. V. Winkle, C. Ophus, K. C. Bustillo, S. Carr, H. G. Brown, J. Ciston, T. Taniguchi, K. Watanabe, and D. K. Bediako. Strain fields in twisted bilayer graphene. *Nat. Mater.*, 20:956–963, 2021.

[63] J. Liu, J. Liu, and X. Dai. Pseudo Landau level representation of twisted bilayer graphene: Band topology and implications on the correlated insulating phase. *Phys. Rev. B*, 99:155415, 2019.

[64] M. Angeli, D. Mandelli, A. Valli, A. Amaricci, M. Capone, E. Tosatti, and M. Fabrizio. Emergent D_6 symmetry in fully-relaxed magic-angle twisted bilayer graphene. *Phys. Rev. B*, 98:235137, 2018.

[65] Y. W. Choi and H. J. Choi. Strong electron-phonon coupling, electron-hole asymmetry, and nonadiabaticity in magic-angle twisted bilayer graphene. *Phys. Rev. B*, 98:241412(R), 2018.

[66] M. Xie and A. H. MacDonald. On the nature of the correlated insulator states in twisted bilayer graphene. *Phys. Rev. Lett.*, 124:097601, 2020.

[67] F. Guinea and N. R. Walet. Continuum models for twisted bilayer graphene: the effects of lattice deformation and hopping parameters. *Phys. Rev. B*, 99:205134, 2019.

[68] M. Koshino, N. F. Q. Yuan, T. Koretsune, M. Ochi, K. Kuroki, and L. Fu. Maximally localized Wannier orbitals and the extended Hubbard model for twisted bilayer graphene. *Phys. Rev. X*, 8:031087, 2018.

[69] S. Carr, S. Fang, Z. Zhu, and E. Kaxiras. Minimal model for low-energy electronic states of twisted bilayer graphene. *Phys. Rev. Research*, 1:013001, 2019.

[70] N. Marzari, A. A. Mostofi, J. R. Yates, I. Souza, and D. Vanderbilt. Maximally localized Wannier functions: Theory and applications. *Rev. Mod. Phys.*, 84:1419–1475, 2012.

[71] N. F. Q. Yuan and L. Fu. Model for the metal-insulator transition in graphene superlattices and beyond. *Phys. Rev. B*, 98:045103, 2018.

[72] H. C.Po, L. Zou, A. Vishwanath, and T. Senthil. Origin of Mott insulating behavior and superconductivity in twisted bilayer graphene. *Phys. Rev. X*, 8:031089, 2018.

[73] J. Kang and O. Vafek. Symmetry, maximally localized Wannier states, and low energy model for the twisted bilayer graphene narrow bands. *Phys. Rev. X*, 8:031088, 2018.

[74] K. Seo, V. N. Kotov, and B. Uchoa. Ferromagnetic Mott state in twisted graphene bilayers at the magic angle. *Phys. Rev. Lett.*, 122:246402, 2019.

[75] Z. A. H. Goodwin, F. Corsetti, A. A. Mostofi, and J. Lischner. Twist-angle sensitivity of electron correlations in moiré graphene bilayers. *Phys. Rev. B*, 100:121106(R), 2019.

[76] R. Sakuma. Symmetry-adapted Wannier functions in the maximal localization procedure. *Phys. Rev. B*, 87:235109, 2013.

[77] H. C. Po, H. Watanabe, and A. Vishwanath. Fragile topology and Wannier obstructions. *Phys. Rev. Lett.*, 121:12604, 2018.

[78] L. Zou, H. C. Po, A. Vishwanath, and T. Senthil. Band structure of twisted bilayer graphene: Emergent symmetries, commensurate approximants, and Wannier obstructions. *Phys. Rev. B*, 98:085435, 2018.

[79] J. Cano, B. Bradlyn, Z. Wang, L. Elcoro, M. G. Vergniory, C. Felser, M. I. Aroyo, and B. Andrei Bernevig. Topology of disconnected elementary band representations. *Phys. Rev. Lett.*, 120:266401, 2018.

[80] H. C. Po, L. Zou, T. Senthil, and A. Vishwanath. Faithful tight-binding models and fragile topology of magic-angle bilayer graphene. *Phys. Rev. B*, 99:195455, 2019.

[81] S. Carr, S. Fang, H. C. Po, A. Vishwanath, and E. Kaxiras. Derivation of Wannier orbitals and minimal-basis tight-binding Hamiltonians for twisted bilayer graphene: a first-principles approach. *Phys. Rev. Research*, 1:033072, 2019.

[82] H. Schmidt, J. C. Rode, D.Smirnov, and R. J. Haug. Superlattice structures in twisted bilayers of folded graphene. *Nat. Commun.*, 5:5742, 2014.

[83] J. C. Rode, D. Smirnov, C. Belke, H. Schmidt, and R. J. Haug. Twisted bilayer graphene: Interlayer configuration and magnetotransport signatures. *Ann. Phys. (Berlin)*, 529:1700025, 2017.

[84] K. Kim *et al.* van der Waals heterostructures with high accuracy rotational alignment. *Nano Lett.*, 16:1989–1995, 2016.

[85] L. Wang *et al.* One-dimensional electrical contact to a two-dimensional material. *Science*, 342:614–617, 2003.

[86] Y. Cao, J. Y. Luo, V. Fatemi, S. Fang, J. D. Sanchez-Yamagishi, K. Watanabe, T. Taniguchi, E. Kaxiras, and P. Jarillo-Herrero. Superlattice-induced insulating states and valley-protected orbits in twisted bilayer graphene. *Phys. Rev. Lett.*, 117:116804, 2016.

[87] K. Kim, A. DaSilva, S. Huang, B. Fallahazad, S. Larentis, T. Taniguchi, K. Watanabe, B. J. LeRoy, A. H. MacDonald, and E. Tutuca. Tunable moiré bands and strong correlations in small-twist-angle bilayer graphene. *PNAS*, 114:3364–3369, 2017.

[88] Y. Cao *et al.* Correlated insulator behaviour at half-filling in magic-angle graphene superlattices. *Nature*, 556:80–84, 2018.

[89] Y. Cao, V. Fatemi, S. Fang, K. Watanabe, T. Taniguchi, E. Kaxiras, and P. Jarillo-Herrero. Unconventional superconductivity in magic-angle graphene superlattices. *Nature*, 556:43–50, 2018.

[90] P. A. Lee, N. Nagaosa, and X.-G. Wen. Doping a Mott insulator: Physics of high-temperature superconductivity. *Rev. Mod. Phys.*, 78:17–85, 2006.

[91] Y. Cao, D. Chowdhury, D. Rodan-Legrain, O.Rubies-Bigordà, K. Watanabe, T. Taniguchi, T. Senthil, and P. Jarillo-Herrero. Strange metal in magic-angle graphene with near Planckian dissipation. *Phys. Rev. Lett.*, 124:076801, 2019.

[92] H. Polshyn, M. Yankowitz, S. Chen, Y. Zhang, K. Watanabe, T. Taniguchi, C. R. Dean,

and A. F. Young. Large linear-in-temperature resistivity in twisted bilayer graphene. *Nat. Phys.*, 15:1011–1016, 2019.

[93] M. Yankowitz, S. Chen, H. Polshyn, Y. Zhang, K. Watanabe, T. Taniguchi, D. Graf, A. F. Young, and C. R. Dean. Tuning superconductivity in twisted bilayer graphene. *Science*, 363:1059–1064, 2019.

[94] B. Padhi, C. Setty, and P. W. Phillips. Doped twisted bilayer graphene near magic angles: Proximity to Wigner crystallization, not Mott insulation. *Nano Lett.*, 18:6175–6180, 2018.

[95] F. Guinea and N. R. Walet. Electrostatic effects, band distortions, and superconductivity in twisted graphene bilayers. *PNAS*, 115:13174–13179, 2018.

[96] J. Kang and O.Vafek. Strong coupling phases of partially filled twisted bilayer graphene narrow bands. *Phys. Rev. Lett.*, 122:246401, 2018.

[97] M. Ochi, M. Koshino, and K. Kuroki. Possible correlated insulating states in magic-angle twisted bilayer graphene under strongly competing interactions. *Phys. Rev. B*, 98:081102(R), 2018.

[98] L. Balents, C. R. Dean, D. K. Efetov, and A. F. Young. Superconductivity and strong correlations in moiré flat bands. *Nat. Phys.*, 16:725–733, 2020.

[99] J. Sólyom. *Fundamentals of the phyiscs of solids*, volume Volume III Normal, Broken-Symmetry, and Correlated Systems. Springer, 2010.

[100] F. Wu, A. H. MacDonald, and I. Martin. Theory of phonon-mediated superconductivity in twisted bilayer graphene. *Phys. Rev. Lett.*, 121:257001, 2018.

[101] F. Wu. Topological chiral superconductivity with spontaneous vortices and supercurrent in twisted bilayer graphene. *Phys. Rev. B*, 99:195114, 2019.

[102] F. Schrodi, A. Aperis, and P. M. Oppeneer. Prominent Cooper pairing away from the Fermi level and its spectroscopic signature in twisted bilayer graphene. *Phys. Rev. Research*, 2:012066(R), 2020.

[103] T. J. Peltonen, R. Ojajärvi, and T. T. Heikkilä. Mean-field theory for superconductivity in twisted bilayer graphene. *Phys. Rev. B*, 98:220504(R), 2018.

[104] B. Roy and V. Juričić. Unconventional superconductivity in nearly flat bands in twisted bilayer graphene. *Phys. Rev. B*, 99:121407(R), 2019.

[105] G. Sharma, M. Trushin, O. P. Sushkov, G. Vignale, and S. Adam. Superconductivity from collective excitations in magic angle twisted bilayer graphene. *Phys. Rev. Research*, 2:022040(R), 2020.

[106] J. González and T. Stauber. Kohn-Luttinger superconductivity in twisted bilayer graphene. *Phys. Rev. Lett.*, 122:026801, 2019.

[107] A. Fischer, L. Klebl, C. Honerkamp, and D. M. Kennes. Spin-fluctuation-induced pairing in twisted bilayer graphene. *Phys. Rev. B*, 103:L041103, 2021.

[108] D. M. Kennes, J. Lischner, and C. Karrasch. Strong correlations and d+id superconductivity in twisted bilayer graphene. *Phys. Rev. B*, 98:241407(R), 2018.

[109] M. Schüler, M. Rösner, T. O. Wehling, A. I. Lichtenstein, and M. I. Katsnelson. Optimal hubbard models for materials with nonlocal Coulomb interactions: Graphene, silicene, and benzene. *Phys. Rev. Lett.*, 111:036601, 2013.

[110] S. Carr, D. Massatt, S. Fang, P. Cazeaux, M. Luskin, and E. Kaxiras. Twistronics: Manipulating the electronic properties of two-dimensional layered structures through their twist angle. *Phys. Rev. B*, 95:075420, 2017.

[111] D. M. Kennes, M. Claassen, L. Xian, A. Georges, A. J. Millis, J. Hone, C. R. Dean, D. N. Basov, A. Pasupathy, and A. Rubio. Moiré heterostructures: a condensed matter quantum simulator. *Nat. Phys.*, 17:155–163, 2021.

[112] S. Carr, S. Fang, P. Jarillo-Herrero, and E. Kaxiras. Pressure dependence of the magic twist angle in graphene superlattices. *Phys. Rev. B*, 98:085144, 2018.

[113] T. Cea, P. A. Pantaleón, and F. Guinea. Band structure of twisted bilayer graphene on hexagonal boron nitride. *Phys. Rev. B*, 102:155136, 2020.

[114] Z. A. H. Goodwin, V. Vitale, F. Corsetti, D. Efetov, A. A. Mostofi, and J. Lischner. Critical role of device geometry for the phase diagram of twisted bilayer graphene. *Phys. Rev. B*, 101:165110, 2020.

[115] Y. Tang *et al.* Simulation of Hubbard model physics in WSe_2/WS_2 moiré superlattices. *Nature*, 597:353–358, 2020.

[116] D.M. Kennes, L. Xian, M. Claassen, and A. Rubio. One-dimensional flat bands in twisted bilayer germanium selenide. *Nat. Commun.*, 11:1124, 2020.

[117] B. L. Chittari, N. Leconte, S. Javvaji, and J. Jung. Pressure induced compression of flatbands in twisted bilayer graphene. *Electron. Struct.*, 1:015001, 2018.

[118] G. Trambly de Laissardiére, O. F. Namarvar, D. Mayou, and L. Magaud. Electronic properties of asymmetrically doped twisted graphene bilayers. *Phys. Rev. B*, 93:235135, 2016.

[119] A. O. Sboychakov, A. V. Rozhkov, A. L. Rakhmanov, and F. Nori. Externally controlled magnetism and band gap in twisted bilayer graphene. *Phys. Rev. Lett.*, 120:266402, 2018.

[120] X. Lu *et al.* Superconductors, orbital magnets, and correlated states in magic angle bilayer graphene. *Nature*, 574:653–657, 2019.

[121] Y. Saito, J. Ge, K. Watanabe, T. Taniguchi, and A. F. Young. Independent superconductors and correlated insulators in twisted bilayer graphene. *Nat. Phys.*, 16:926–930, 2020.

[122] P. Stepanov, I. Das, X. Lu, A. Fahimniya, K. Watanabe, T. Taniguchi, F. H. L. Koppens, J. Lischner, L. Levitov, and D. K. Efetov. Untying the insulating and superconducting orders in magic-angle graphene. *Nature*, 583:375–378, 2020.

[123] X. Liu, Z. Wang, K. Watanabe, T. Taniguchi, O. Vafek, and J. I. A. Li. Tuning electron correlation in magic-angle twisted bilayer graphene using coulomb screening. *Science*, 371:1261–1265, 2021.

[124] H. S. Arora *et al.* Superconductivity in metallic twisted bilayer graphene stabilized by WSe_2. *Nature*, 583:379–384, 2020.

[125] L. Klebl, Z. A. H. Goodwin, A. A. Mostofi, D. M. Kennes, and J. Lischner. Importance of long-ranged electron-electron interactions for the magnetic phase diagram of twisted bilayer graphene. *Phys. Rev. B*, 103:195127, 2021.

[126] A. Fischer, Z.A. H. Goodwin, A. A. Mostofi, J. Lischner, D. M. Kennes, and L. Klebl. Unconventional superconductivity in magic-angle twisted trilayer graphene. *arXiv:2104.10176*, 2021.

[127] A. L. Sharpe, E. J. Fox, A. W. Barnard, J. Finney, K. Watanabe, T. Taniguchi, M. A. Kastner, and D. Goldhaber-Gordon. Emergent ferromagnetism near three-quarters filling in twisted bilayer graphene. *Science*, 365:605–608, 2019.

[128] M. Serlin, C. L. Tschirhart, H. Polshyn, Y. Zhang, J. Zhu, K. Watanabe, T. Taniguchi, L. Balents, and A. F. Young. Intrinsic quantized anomalous Hall effect in a moiré heterostructure. *Science*, 367:900–903, 2020.

[129] A. Kerelsky *et al.* Maximized electron interactions at the magic angle in twisted bilayer graphene. *Nature*, 572:95–100, 2019.

[130] Y. Xie, B. Lian, B. Jäck, X. Liu, C.-L. Chiu, K. Watanabe, T. Taniguchi, B. A. Bernevig, and A. Yazdani. Spectroscopic signatures of many-body correlations in magic-angle twisted bilayer graphene. *Nature*, 572:101–105, 2019.

[131] Y. Jiang, X. Lai, K. Watanabe, T. Taniguchi, K. Haule, J. Mao, and E. Y. Andrei. Charge order and broken rotational symmetry in magic-angle twisted bilayer graphene. *Nature*, 573:91–95, 2019.

[132] S. Zhang *et al.* Abnormal conductivity in low-angle twisted bilayer graphene. *Sci. Adv.*, 6:eabc5555, 2020.

[133] Y.-W. Liu *et al.* Tunable lattice reconstruction, triangular network of chiral one-dimensional states, and bandwidth of flat bands in magic angle twisted bilayer graphene. *Phys. Rev. Lett.*, 125:236102, 2020.

[134] A. Grüneis, C. Attaccalite, L. Wirtz, H. Shiozawa, R. Saito, T. Pichler, and A. Rubio. Tight-binding description of the quasiparticle dispersion of graphite and few-layer graphene. *Phys. Rev. B*, 78:205425, 2008.

[135] T. Cea, N. R. Walet, and F. Guinea. Electronic band structure and pinning of Fermi energy to van Hove singularities in twisted bilayer graphene: A self-consistent approach. *Phys. Rev. B*, 100:205113, 2019.

[136] L. Rademaker, D. A. Abanin, and P. Mellado. Charge smoothening and band flattening due to Hartree corrections in twisted bilayer graphene. *Phys. Rev. B*, 100:205114, 2019.

[137] Z. A. H. Goodwin, V. Vitale, X. Liang, A. A. Mostofi, and J. Lischner. Hartree theory calculations of quasiparticle properties in twisted bilayer graphene. *Electron. Struct.*, 2:034001, 2020.

[138] M.J. Calderón and E. Bascones. Interactions in the 8-orbital model for twisted bilayer graphene. *Phys. Rev. B*, 102:155149, 2020.

[139] Y. Choi *et al.* Electronic correlations in twisted bilayer graphene near the magic angle. *Nat. Phys.*, 15:1174–1180, 2019.

[140] Z. Zhang, R. Myers, K. Watanabe, T. Taniguchi, and B. J. LeRoy. Probing the wavefunctions of correlated states in magic angle graphene. *Phys. Rev. Research*, 2:033181, 2020.

[141] Y. Cao, D. Rodan-Legrain, J. M. Park, F. N. Yuan, K. Watanabe, T. Taniguchi, R. M. Fernandes, L. Fu, and P. Jarillo-Herrero. Nematicity and competing orders in superconducting magic-angle graphene. *Science*, 372:264–271, 2021.

[142] R. M. Fernandes and J. W. F. Venderbos. Nematicity with a twist: Rotational symmetry breaking in a moiré superlattice. *Sci. Adv.*, 6:eaba8834, 2020.

[143] S. Liu, E. Khalaf, J. Yeon Lee, and A. Vishwanath. Nematic topological semimetal and insulator in magic angle bilayer graphene at charge neutrality. *Phys. Rev. Research*, 3:013033, 2021.

[144] K. P. Nuckolls, M. Oh, D. Wong, B. Lian, K. Watanabe, T. Taniguchi, B. A. Bernevig, and A. Yazdani. Strongly correlated Chern insulators in magic-angle twisted bilayer graphene. *Nature*, 588:610–615, 2020.

[145] Y. Choi *et al.* Correlation-driven topological phases in magic-angle twisted bilayer graphene. *Nature*, 589:536–541, 2021.

[146] A. T. Pierce *et al.* Unconventional sequence of correlated Chern insulators in magic-angle twisted bilayer graphene. *Nat. Phys.*, 17:1210–1215, 2021.

[147] I. Das, X. Lu, J. Herzog-Arbeitman, Z.-D. Song, K. Watanabe, T. Taniguchi, B. A. Bernevig, and D. K. Efetov. Symmetry broken Chern insulators and "magic series" of Rashbalike Landau level crossings in magic angle bilayer graphene. *Nat. Phys.*, 17:710–714, 2021.

[148] S. Wu, Z. Zhang, K. Watanabe, T. Taniguchi, and E. Y. Andrei. Chern insulators, van Hove singularities and topological flat bands in magic-angle twisted bilayer graphene. *Nat. Mater.*, 21:488–494, 2020.

[149] Y. Xie *et al.* Fractional chern insulators in magic-angle twisted bilayer graphene. *Nature*, 600:439–443, 2021.

[150] P. Stepanov, M. Xie, T. Taniguchi, K. Watanabe, X. Lu, A. H. MacDonald, B. A. Bernevig, and D. K. Efetov. Competing zero-field Chern insulators in superconducting twisted bilayer graphene. *Phys. Rev. Lett.*, 127:197701, 2021.

[151] D. Wong, K. P. Nuckolls, M. Oh, B. Lian, Y. Xie, S. Jeon, K. Watanabe, T. Taniguchi, B. A. Bernevig, and A. Yazdani. Cascade of electronic transitions in magic-angle twisted bilayer graphene. *Nature*, 582:198–202, 2020.

[152] U. Zondiner *et al.* Cascade of phase transitions and Dirac revivals in magic-angle graphene. *Nature*, 582:203–208, 2020.

[153] A. Rozen *et al.* Entropic evidence for a Pomeranchuk effect in magic-angle graphene. *Nature*, 592:214–219, 2021.

[154] Y. Saito, F. Yang, J. Ge, X. Liu, T. Taniguchi, K. Watanabe, J. I. A. Li, E. Berg, and A. F. Young. Isospin Pomeranchuk effect in twisted bilayer graphene. *Nature*, 592:220–224, 2021.

[155] I. Pomeranchuk. On the theory of liquid 3-He. *Zh. Eksp. Teor. Fiz*, 20:919–926, 1950.

[156] A. Uri *et al.* Mapping the twist-angle disorder and Landau levels in magic-angle graphene. *Nature*, 581:47–52, 2020.

[157] C. L. Tschirhart *et al.* Imaging orbital ferromagnetism in a moire Chern insulator. *Science*, 372:1323–1327, 2021.

[158] S. Lisi *et al.* Observation of flat bands in twisted bilayer graphene. *Nat. Phys.*, 17:189–193, 2021.

[159] M. Iqbal Bakti Utama *et al.* Visualization of the flat electronic band in twisted bilayer graphene near the magic angle twist. *Nat. Phys.*, 17:184–188, 2021.

[160] N. C.H. Hesp *et al.* Observation of interband collective excitations in twisted bilayer graphene. *Nat. Phys.*, 17:1162–1168, 2021.

[161] P. S. Mahapatra, B. Ghawri, M. Garg, S. Mandal, K. Watanabe, T. Taniguchi, M. Jain, S. Mukerjee, and A. Ghosh. Misorientation-controlled cross-plane thermoelectricity in twisted bilayer graphene. *Phys. Rev. Lett.*, 125:226802, 2020.

[162] A. Vela, M. V. O. Moutinho, F. J. Culchac, P. Venezuela, and R. B. Capaz. Electronic structure and optical properties of twisted multilayer graphene. *Phys. Rev. B*, 98:155135, 2018.

[163] F. Haddadi, Q. Wu, A. J. Kruchkov, and O. V. Yazyev. Moiré flat bands in twisted double bilayer graphene. *Nano Lett.*, 20:2410–2415, 2020.

[164] P. Rickhaus *et al.* Gap opening in twisted double bilayer graphene by crystal fields. *Nano lett.*, 19:8821–8828, 2019.

[165] F. J. Culchac, R. R. Del Grande, Rodrigo B. Capaz, Leonor Chico, and E. Surez Morell. Flat bands and gaps in twisted double bilayer graphene. *Nanoscale*, 12:5014–5020, 2020.

[166] M. Koshino. Band structure and topological properties of twisted double bilayer graphene. *Phys. Rev. B*, 99:235406, 2019.

[167] Y.W. Choi and H.J. Choi. Intrinsic band gap and electrically tunable flat bands in twisted double bilayer graphene. *Phys. Rev. B*, 100:201402(R), 2019.

[168] N. Chebrolu, B. Chittari, and J. Jung. Flat bands in twisted double bilayer graphene. *Phys. Rev. B*, 99:235417, 2019.

[169] C. Shen *et al.* Correlated states in twisted double bilayer graphene. *Nat. Phys.*, 16:520–525, 2020.

[170] X. Liu, Z. Hao, E. Khalaf, J. Y. Lee, K. Watanabe, T. Taniguchi, A. Vishwanath, and P. Kim. Tunable spin-polarized correlated states in twisted double bilayer graphene. *Nature*, 583:221–225, 2020.

[171] Burg G. W, J. Zhu, T. Taniguchi, K. Watanabe, A. H. MacDonald, and E. Tutuc. Correlated insulating states in twisted double bilayer graphene. *Phys. Rev. Lett.*, 123:197702, 2019.

[172] Y. Cao, D. Rodan-Legrain, O. Rubies-Bigorda, J. M. Park, K. Watanabe, T. Taniguchi, and P. Jarillo-Herrero. Tunable correlated states and spin-polarized phases in twisted bilayer–bilayer graphene. *Nature*, 583:215–220, 2020.

[173] F. Wu and S. Sarma. Ferromagnetism and superconductivity in twisted double bilayer graphene. *Phys. Rev. B*, 101:155149, 2020.

[174] J. Y. Leey, E. Khalaf, S. Liu, X. Liu, Z. Hao, P. Kim, and A. Vishwanath. Theory of correlated insulating behaviour and spin-triplet superconductivity in twisted double bilayer graphene. *Nat. Commun.*, 10:5333, 2019.

[175] C. Zhang *et al.* Visualizing delocalized correlated electronic states in twisted double bilayer graphene. *Nat. Commun.*, 12:2516, 2021.

[176] X. Liu, C.-L. Chiu, J. Y. Lee, G. Farahi, K. Watanabe, T. Taniguchi, A. Vishwanath, and A. Yazdani. Spectroscopy of a tunable moiré system with a correlated and topological flat band. *Nat. Commun.*, 12:2732, 2021.

[177] C.Rubio-Verdú *et al.* Moiré nematic phase in twisted double bilayer graphene. *Nat. Phys.*, pages https://doi.org/10.1038/s41567–021–01438–2, 2021.

[178] P. A. Pantaleón, T. Cea, R. Brown, N. R. Walet, and F. Guinea. Narrow bands and electrostatic interactions in graphene stacks. *2D Mater.*, 8:044006, 2020.

[179] A. Kerelsky *et al.* Moiré-less correlations in abca graphene. *PNAS*, 118:e2017366118, 2021.

[180] P. Rickhaus *et al.* Correlated electron-hole state in twisted double-bilayer graphene. *Science*, 373:1257–1260, 2021.

[181] L. Rademaker, I. Protopopov, and D. Abanin. Topological flat bands and correlated states in twisted monolayer-bilayer graphene. *Phys. Rev. Research*, 2:033105, 2020.

[182] Y. Park, B. L. Chittari, and J. Jung. Gate-tunable topological flat bands in twisted monolayer-bilayer graphene. *Phys. Rev. B*, 102:035411, 2020.

[183] S. Chen *et al.* Electrically tunable correlated and topological states in twisted monolayer–bilayer graphene. *Nat. Phys.*, 17:374–380, 2021.

[184] H. Polshyn *et al.* Nonvolatile switching of magnetic order by electric fields in an orbital Chern insulator. *Nature*, 588:66–70, 2020.

[185] Y. Shi *et al.* Tunable van Hove singularities and correlated states in twisted trilayer graphene. *Nat. Phys.*, 17:619–626, 2021.

[186] E. Khalaf, A. J.Kruchkov, G. Tarnopolsky, and A. Vishwanath. Magic angle hierarchy in twisted graphene multilayers. *Phys. Rev. B*, 100:085109, 2019.

[187] Z. Zhu, S. Carr, D. Massatt, M. Luskin, and E. Kaxiras. Twisted trilayer graphene: A precisely tunable platform for correlated electrons. *Phys. Rev. Lett.*, 125:116404, 2020.

[188] W.-J. Zuo, J.-B. Qiao, D.-L. Ma, L.-J. Yin, G. Sun, J.-Y. Zhang, L.-Y. Guan, and L. He. Scanning tunneling microscopy and spectroscopy of twisted trilayer graphene. *Phys. Rev. B*, 97:035440, 2018.

[189] Xi Zhang, Kan-Ting Tsai, Ziyan Zhu, Wei Ren, Yujie Luo, Stephen Carr, Mitchell Luskin, Efthimios Kaxiras, and Ke Wang. Correlated superconducting and insulating states in twisted trilayer graphene moire of moire superlattices. *Phys. Rev. Lett.*, 127:166802, 2021.

[190] S. Carr, C. Li, Z. Zhu, E. Kaxiras, S. Sachdev, and A. Kruchkov. Ultraheavy and Ultrarelativistic dirac quasiparticles in sandwiched graphenes. *Nano Lett.*, 20:3030–3038, 2020.

[191] X. Li, F. Wu, and A. H. MacDonald. Electronic structure of single-twist trilayer graphene. *arXiv:1907.12338*, 2019.

[192] A. Lopez-Bezanilla and J. L. Lado. Electrical band flattening, valley flux, and superconductivity in twisted trilayer graphene. *Phys. Rev. Research*, 2:033357, 2020.

[193] C. Lei, L. Linhart, W. Qin, F. Libisch, and A. H. MacDonald. Mirror symmetry breaking and stacking-shift dependence in twisted trilayer graphene. *Phys. Rev. B*, 104:035139, 2021.

[194] J. Shin, B. L. Chittari, and J. Jung. Stacking and gate tunable topological at bands, gaps and anisotropic strip patterns in twisted trilayer graphene. *Phys. Rev. B*, 104:045413, 2021.

[195] Z. Wu, Z. Zhan, and S. Yuan. Lattice relaxation, mirror symmetry and magnetic field effects on ultraflat bands in twisted trilayer graphene. *arXiv:2012.13741*, 2021.

[196] J. M. Park, Y. Cao, K. Watanabe, T. Taniguchi, and P. Jarillo-Herrero. Tunable strongly coupled superconductivity in magic-angle twisted trilayer graphene. *Nature*, 590:249–255, 2021.

[197] Z. Hao, A. M. Zimmerman, P. Ledwith, E. Khalaf, D. H. Najafabadi, K. Watanabe, T. Taniguchi, A. Vishwanath, and P. Kim. Electric field tunable superconductivity in alternating twist magic-angle trilayer graphene. *Science*, 371:1133–1138, 2021.

[198] Y. Cao, J. M. Park, K. Watanabe, T. Taniguchi, and P. Jarillo-Herrero. Large Pauli limit violation and reentrant superconductivity in magic-angle twisted trilayer graphene. *Nature*, 595:526–531, 2021.

[199] Y. W. Choi and H. J. Choi. Dichotomy of electron-phonon coupling in graphene moiré flat bands. *Phys. Rev. Lett.*, 127:167001, 2021.

[200] T. Cea, N. R. Walet, and F. Guinea. Twists and the electronic structure of graphitic materials. *Nano Lett.*, 19:8683–8689, 2019.

[201] L. Xian, A. Fischer, M. Claassen, J. Zhang, A. Rubio, and D. M. Kennes. Engineering three dimensional moiré flat bands. *Nano Lett.*, 21:7519–7526, 2021.

[202] J. H. Wilson, Y. Fu, S. Das Sarma, and J. H. Pixley. Disorder in twisted bilayer graphene. *Phys. Rev. Research*, 2:023325, 2020.

[203] L. Huder, A. Artaud, T. L. Quang, G. Trambly de Laissardière, A. G.M. Jansen, G. Lapertot, C. Chapelier, and V. T. Renard. Electronic spectrum of twisted graphene layers under heterostrain. *Phys. Rev. Lett.*, 120:156405, 2018.

[204] J.-B. Qiao, L.-J. Yin, and L. He. Twisted graphene bilayer around the first magic angle engineered by heterostrain. *Phys. Rev. B*, 98:235402, 2018.

[205] A. Ramires and J. L. Lado. Impurity-induced triple point fermions in twisted bilayer graphene. *Phys. Rev. B*, 99:245118, 2019.

[206] D. T. Larson, S. Carr, G. A. Tritsaris, and E. Kaxiras. Effects of lithium intercalation in twisted bilayer graphene. *Phys. Rev. B*, 101:075407, 2020.

[207] M. Andelković, S. P. Milovanović, L. Covaci, and F. M. Peeters. Double moiré with a twist: Supermoiré in encapsulated graphene. *Nano lett.*, 20:979–988, 2020.

[208] L. Klebl and C. Honerkamp. Inherited and flatband-induced ordering in twisted graphene bilayers. *Phys. Rev. B*, 100:155145, 2019.

[209] J. Sólyom. *Fundamentals of the phyiscs of solids*, volume Volume I Structure and Dynamics. Springer, 2010.

[210] J.-K. Lee *et al.* The nature of metastable AA' graphite: Low dimensional nano and single-crystalline forms. *Sci. Rep.*, 6:39624, 2016.

[211] T. C. O'Connor, J. Andzelm, and M. O. Robbins. Airebo-m: A reactive model for hydrocarbons at extreme pressures. *J. Chem. Phys.*, 142:024903, 2015.

[212] S. J. Stuart, A. B. Tutein, and J. A. Harrison. A reactive potential for hydrocarbons with intermolecular interactions. *J. Chem. Phys.*, 112:6472–6486, 2000.

[213] Aleksey N. Kolmogorov and Vincent H. Crespi. Registry-dependent interlayer potential for graphitic systems. *Phys. Rev. B*, 71:235415, 2005.

[214] S. Plimpton. Fast parallel algorithms for short-range molecular dynamics. *J. Comp. Phys.*, 117:1–19, 1995.

[215] E. Bitzek, P. Koskinen, F. Gähler, M. Moseler, and P. Gumbsch. Structural relaxation made simple. *Phys. Rev. Lett.*, 97:170201, 2006.

[216] M. L. Cohen and S. G. Louie. *Fundamentals of Condensed Matter Physics.* Cambridge University Press, 2016.

[217] J. Hafner, C. Wolverton, and G. Ceder. Toward computational materials design: The impact of density functional theory on materials research. *MRS Bulletin*, 31:659–668, 2006.

[218] W. Kohn and L. J. Sham. Self-consistent equations including exchange and correlation effects. *Phys. Rev.*, 140:A1133, 1965.

[219] L. Hedin. New method for calculating the one-paticle Green's function with application to the electron-gas problem. *Phys. Rev.*, 139:A796, 1965.

[220] K. Burke. Perspective on density functional theory. *J. Chem. Phys.*, 136:150901, 2012.

[221] C.-K. Skylaris, P. D. Haynes, A. A. Mostofi, and M. C. Payne. Introducing onetep: Linear-scaling density functional simulations on parallel computers. *J. Chem. Phys.*, 122:084119, 2005.

[222] E. Prodan and W. Kohn. Nearsightedness of electronic matter. *PNAS*, 102:11635–11638, 2005.

[223] C. Brouder, G. Panati, M. Calandra, C. Mourougane, and N. Marzari. Exponential localization of Wannier functions in insulators. *Phys. Rev. Lett.*, 98:046402, 2007.

[224] Joseph C. A. *et al.* Prentice. The onetep linear-scaling density functional theory program. *J. Chem. Phys.*, 152(17):174111, 2020.

[225] J. P. Perdew, K. Burke, and M. Ernzerhof. Generalized gradient approximation made simple. *Phys. Rev. Lett.*, 77:3865–3868, 1996.

[226] P. E. Blöchl. Projector augmented-wave method. *Phys. Rev. B*, 50:17953–17979, 1994.

[227] F. Jollet, M. Torrent, and N. Holzwarth. Generation of projector augmented-wave atomic data: A 71 element validated table in the xml format. *Comput. Phys. Commun.*, 185:1246–1254, 2014.

[228] À. Ruiz-Serrano and C. K. Skylaris. A variational method for density functional theory calculations on metallic systems with thousands of atoms. *J. Chem. Phys.*, 139:054107, 2013.

[229] N. Marzari, D. Vanderbilt, and M. C. Payne. Ensemble density-functional theory for *ab initio* molecular dynamics of metals and finite-temperature insulators. *Phys. Rev. Lett.*, 79:1337–1340, 1997.

[230] L. E. Ratcliff, G. J. Conduit, N. D. M. Hine, and P. D. Haynes. Band structure interpolation using optimized local orbitals from linear-scaling density functional theory. *Phys. Rev. B*, 98:125123, 2018.

[231] N. W. Ashcroft and N. D. Mermin. *Solid State Physics.* Holt-Saunders, 1976.

[232] J. Sólyom. *Fundamentals of the phyiscs of solids*, volume Volume II Electronic Properties. Springer, 2010.

[233] J. C. Slater and G. F. Koster. Simplified LCAO method for the periodic potential problem. *Phys. Rev.*, 94:1498–1524, 1954.

[234] G. Stefanucci and R. Van Leeuwen. *Nonequilibrium many-body theory of quantum systems a modern introduction.* Cambridge University Press, 2013.

[235] K. W.-K. Shung. Dielectric function and plasmon structure of stage-1 intercalated graphite. *Phys. Rev. B*, 34:979–993, 1986.

[236] T. O. Wehling, E. Şaşıoğlu, C. Friedrich, A. I. Lichtenstein, M. I. Katsnelson, and S. Blügel. Strength of effective Coulomb interactions in graphene and graphite. *Phys. Rev. Lett.*, 106:236805, 2011.

[237] T. M. R. Wolf, J. L. Lado, G. Blatter, and O. Zilberberg. Electrically tunable flat bands and magnetism in twisted bilayer graphene. *Phys. Rev. Lett.*, 123:096802, 2019.

[238] G.Pizzi *et al.* Wannier90 as a community code: new features and applications. *J. Phys.: Condens. Matter*, 32:165902, 2019.

[239] N. Marzari and D. Vanderbilt. Maximally localized generalized Wannier functions for composite energy bands. *Phys. Rev. B*, 56:12847–12865, 1997.

[240] R. Wang, E. A. Lazar, H. Park, A. J. Millis, and C. A. Marianetti. Selectively localized Wannier functions. *Phys. Rev. B*, 90:165125, 2014.

[241] F. Aryasetiawan, K. Karlsson, O. Jepsen, and U. Schönberger. Calculations of Hubbard U from first-principles. *Phys. Rev. B*, 74:125106, 2006.

[242] I. V. Solovyev and M. Imada. Screening of Coulomb interactions in transition metals. *Phys. Rev. B*, 71:045103, 2005.

[243] F. Aryasetiawan, A. Georges M. Imada, S. Biermann G. Kotliar, and A. I. Lichtenstein. Frequency-dependent local interactions and low-energy effective models from electronic structure calculations. *Phys. Rev. B*, 70:195104, 2004.

[244] A. Laturia, M. L. Van de Put, and W. G. Vandenberghe. Dielectric properties of hexagonal boron nitride and transition metal dichalcogenides: from monolayer to bulk. *NPJ 2D Mater. Appl.*, 2:6, 2018.

[245] R. E. Throckmorton and O. Vafek. Fermions on bilayer graphene: Symmetry breaking for b = 0 and v = 0. *Phys. Rev. B*, 86:115447, 2012.

[246] T. Ando. Screening effect and impurity scattering in monolayer graphene. *J. Phys. Soc. Jpn.*, 75:074716, 2006.

[247] J.H. Ho, C.P. Chang, and M.F. Lin. Electronic excitations of the multilayered graphite. *Phys. Lett. A*, 352:446–450, 2006.

[248] J.-Y. Wu, G. G., and M.-F. Lin. Combined effect of stacking and magnetic field on plasmon excitations in bilayer graphene. *Phys. Rev. B*, 89:165407, 2014.

[249] R. Roldán and L. Brey. Dielectric screening and plasmons in AA-stacked bilayer graphene. *Phys. Rev. B*, 88:115420, 2013.

[250] T. Ando, A. B. Fowler, and F. Stern. Electronic properties of two-dimensional systems. *Rev. Mod. Phys.*, 54:437–672, 1982.

[251] K. Andersen, S. Latini, and K. S. Thygesen. Dielectric genome of van der Waals heterostructures. *Nano Lett.*, 15:4616–4621, 2015.

[252] M. S. Hybertsen and S. C. Louie. *Ab initio* static dielectric matrices from the density-functional approach. I. formulation and application to semiconductors and insulators. *Phys. Rev. B*, 35:5585–5601, 1987.

[253] Gonçalo Filipe Santos Catarina. Twisted bilayer graphene - electronic and optical properties. Master's thesis, Técnico Lisboa, 2017.

[254] C. Honerkamp, H. Shinaoka, F. F. Assaad, and P. Werner. Limitations of constrained random phase approximation downfolding. *Phys. Rev. B*, 98:235151, 2018.

[255] J. M. Pizarro, M. Rosner, R. Thomale, R. Valent, and T. O. Wehling. Internal screening and dielectric engineering in magic-angle twisted bilayer graphene. *Phys. Rev. B*, 100:161102(R), 2019.

[256] Z. A. H. Goodwin, F. Corsetti, A. A. Mostofi, and J. Lischner. Attractive electron-electron interactions from internal screening in magic angle twisted bilayer graphene. *Phys. Rev. B*, 100:235424, 2019.

[257] M. Zahn. Point charge between two parallel grounded planes. *Am. J. Phys.*, 44:1132, 1976.

[258] N. Bultinck, E. Khalaf, S. Liu, S. Chatterjee, A. Vishwanath, and M. P. Zaletel. Ground state and hidden symmetry of magic angle graphene at even integer filling. *Phys. Rev. X*, 10:031034, 2020.

[259] Y. Zhang, K. Jiang, Z. Wang, and F. Zhang. Correlated insulating phases of twisted bilayer graphene at commensurate filling fractions: A Hartree-Fock study. *Phys. Rev. B*, 102:035136, 2020.

[260] J. Liu and X. Dai. Theories for the correlated insulating states and quantum anomalous hall effect phenomena in twisted bilayer graphene. *Phys. Rev. B*, 103:035427, 2021.

[261] T. Cea and F. Guinea. Band structure and insulating states driven by coulomb interaction in twisted bilayer graphene. *Phys. Rev. B*, 102:045107, 2020.

[262] T. Stauber and H. Kohler. Quasi-flat plasmonic bands in twisted bilayer graphene. *Nano Lett.*, 16:6844–6849, 2016.

[263] X. Yan, X. K. T. Law, and P. A. Lee. Kekulé valence bond order in an extended Hubbard model on the honeycomb lattice with possible applications to twisted bilayer graphene. *Phys. Rev. B*, 98:121406(R), 2018.

[264] F. Corsetti, A. A Mostofi, and J. Lischner. First-principles multiscale modelling of charged adsorbates on doped graphene. *2D Mater.*, 4:025070, 2017.

[265] L. V. Keldysh. Coulomb interaction in thin semiconductor and semimetal films. *JETP Lett.*, 29:658–660, 1979.

[266] M. Aghajanian, A. A. Mostofi, and J. Lischner. Tuning electronic properties of transition-metal dichalcogenides via defect charge. *Sci. Rep.*, 8:13611, 2018.

[267] K. Ohno. Some remarks on the pariser-parr-pople method. *Theoret. chim. Acta*, 2:219–227, 1964.

[268] B. Wunsch, T. Stauber, F. Sols, and F. Guinea. Dynamical polarization of graphene at finite doping. *New J. Phys.*, 8:318, 2006.

[269] J. Lischner. Multiscale modelling of charged impurities in two-dimensional materials. *Comput. Mater. Sci.*, 160:368–373, 2019.

[270] L. Yang, J. Deslippe, C.-H. Park, M. L. Cohen, and S. G. Louie. Excitonic effects on the optical response of graphene and bilayer graphene. *Phys. Rev. Lett.*, 103:186802, 2009.

[271] W. Kohn and J. M. Luttinger. New mechanism for superconductivity. *Phys. Rev. Lett.*, 15:524–526, 1965.

[272] A. V. Chubukov. Kohn-Luttinger effect and the instability of a two-dimensional repulsive Fermi liquid at T=0. *Phys. Rev. B*, 48:1097–1104, 1993.

[273] W. A. Little. Possibility of synthesizing an organic superconductor. *Phys. Rev.*, 134:A1416–A1424, 1964.

[274] A. Hamo, A. Benyamini, I. Shapir, I. Khivrich, J. Waissman, K. Kaasbjerg, Y. Oreg, F. von Oppen, and S. Ilani. Electron attraction mediated by coulomb repulsion. *Nature*, 535:395–400, 2016.

[275] J. E. Hirsch and D. J. Scalapino. Enhanced superconductivity in quasi two-dimensional systems. *Phys. Rev. Lett.*, 56:2732–2735, 1986.

[276] B. Uchoa and A. H. Castro Neto. Superconducting states of pure and doped graphene. *Phys. Rev. Lett.*, 98:146801, 2007.

[277] X. Gu, C. Chen, J. Ning Leaw, E. Laksono, V. M. Pereira, G. Vignale, and S. Adam. Antiferromagnetism and chiral d-wave superconductivity from an effective t-J-D model for twisted bilayer graphene. *Phys. Rev. B*, 101:180506(R), 2020.

[278] C.-C. Liu, L.-D. Zhang, W.-Q. Chen, and F. Yang. Chiral spin density wave and d+id superconductivity in the magic-angle-twisted bilayer graphene. *Phys. Rev. Lett.*, 121:217001, 2018.

[279] H. Guo, X. Zhu, S. Feng, and R. T. Scalettar. Pairing symmetry of interacting fermions on a twisted bilayer graphene superlattice. *Phys. Rev. B*, 97:235453, 2018.

[280] T. C. Lang, Z. Y. Meng, M. M. Scherer, S. Uebelacker, F. F. Assaad, A. Muramatsu, C. Honerkamp, and S. Wessel. Antiferromagnetism in the Hubbard model on the Bernal-stacked honeycomb bilayer. *Phys. Rev. Lett.*, 109:126402, 2012.

[281] J. Hubbard. Electron correlations in narrow energy bands. *Proc. R. Soc. Lond. A*, 276:237–259, 1963.

[282] J. Hubbard. Electron correlations in narrow energy bands. II. the degenerate band case. *Proc. R. Soc. Lond. A*, 277:238–257, 1964.

[283] P. B. Allen and R. C. Dynes. Transition temperature of strong-coupled superconductors reanalyzed. *Phys. Rev. B*, 12:905, 1975.

[284] J. Vahedi, R. Peters, A. Missaoui, A. Honecker, and G. Trambly de Laissardiére. Magnetism of magic-angle twisted bilayer graphene. *SciPost Phys.*, 11:083, 2021.

[285] J. González and T. Stauber. Time-reversal symmetry breaking versus chiral symmetry breaking in twisted bilayer graphene. *Phys. Rev. B*, 102:081118(R), 2020.

[286] J. González and T. Stauber. Magnetic phases from competing Hubbard and extended Coulomb interactions in twisted bilayer graphene. *Phys. Rev. B*, 104:115110, 2021.

[287] A. O. Sboychakov, A. V. Rozhkov, A. L. Rakhmanov, and F. Nori. Many-body effects in twisted bilayer graphene at low twist angles. *Phys. Rev. B*, 100:045111, 2019.

[288] A. O. Sboychakov, A. V. Rozhkov, A. L. Rakhmanov, and F. Nori. Spin density wave and electron nematicity in magic-angle twisted bilayer graphene. *Phys. Rev. B*, 102:155142, 2020.

[289] Louk Rademaker and Paula Mellado. Charge-transfer insulation in twisted bilayer graphene. *Phys. Rev. B*, 98:235158, 2018.

[290] T. Cea and F. Guinea. Coulomb interaction, phonons, and superconductivity in twisted bilayer graphene. *PNAS*, 118:e2107874118, 2021.

[291] M. M. Scherer, S. Uebelacker, D. D. Scherer, and C. Honerkamp. Interacting electrons on trilayer honeycomb lattices. *Phys. Rev. B*, 86:155415, 2012.

[292] Y. Choi *et al.* Interaction-driven band flattening and correlated phases in twisted bilayer graphene. *Nat. Phys.*, 17:1375–1381, 2021.

[293] C. Lewandowski, S. Nadj-Perge, and D. Chowdhury. Does filling-dependent band renormalization aid pairing in twisted bilayer graphene? *arXiv:2102.05661*, 2021.

[294] Alejandro Lopez-Bezanilla. Emergence of flat-band magnetism and half-metallicity in twisted bilayer graphene. *Phys. Rev. Materials*, 3:054003, 2019.

[295] A. L. Rakhmanov, A. V. Rozhkov, A. O. Sboychakov, and F. Nori. Instabilities of the AA-stacked graphene bilayer. *Phys. Rev. Lett.*, 109:206801, 2012.

[296] H. Ochoa. Strain-induced excitonic instability in twisted bilayer graphene. *Phys. Rev. B*, 102:201107(R), 2020.

[297] C. S. Cheung, Z. A. H. Goodwin, V. Vitale, J. Lischner, and A. A. Mostofi. Hartree theory and crystal field of twisted double bilayer graphene near the magic-angle. *arXiv:2111.03019*, 2021.

[298] Z. A. H. Goodwin, L. Klebl, V. Vitale, X. Liang, V. Gogtay, X. van Gorp, D. M. Kennes, A. A. Mostofi, and J. Lischner. Flat bands, electron interactions, and magnetic order in magic-angle mono-trilayer graphene. *Phys. Rev. Materials*, 5:084008, 2021.

[299] X. Lin, H. Zhu, and J. Ni. Pressure-induced gap modulation and topological transitions in twisted bilayer and twisted double bilayer graphene. *Phys. Rev. B*, 101:155405, 2020.

[300] E. J. G. Santos and E. Kaxiras. Electric-field dependence of the effective dielectric constant in graphene. *Nano Lett.*, 13:898–902, 2013.

[301] Nikita V. Tepliakov, QuanSheng Wu, and Oleg V. Yazyev. Crystal field effect and electric field screening in multilayer graphene with and without twist. *Nano Lett.*, 21:4636–4642, 2021.

[302] G. Chen *et al.* Signatures of tunable superconductivity in a trilayer graphene moiré superlattice. *Nature*, 572:215–219, 2019.

[303] G. Chen *et al.* Evidence of a gate-tunable Mott insulator in a trilayer graphene moiré superlattice. *Nat. Phys.*, 15:237–241, 2019.

[304] G. Chen *et al.* Tunable correlated Chern insulator and ferromagnetism in a moiré superlattice. *Nature*, 579:56–61, 2020.

[305] M. G. Menezes, R. B. Capaz, and S. G. Louie. *Ab initio* quasiparticle band structure of ABA and ABC-stacked graphene trilayers. *Phys. Rev. B*, 89:035431, 2014.

[306] H. Min and A. H. MacDonald. Electronic structure of multilayer graphene. *Prog. Theor. Phys., Suppl.*, 176:227–252, 2008.

[307] L. Klebl, D. M. Kennes, and C. Honerkamp. Functional renormalization group for a large moiré unit cell. *Phys. Rev. B*, 102:085109, 2020.